Measurement and Modelling of Human Car Driving with Steering Torque Feedback

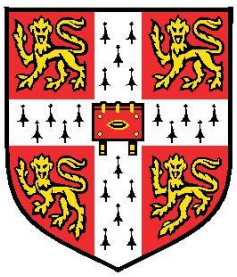

Tenghao Niu

Department of Engineering
University of Cambridge

This thesis is submitted for the degree of
Doctor of Philosophy

Christ's College September 2021

Declaration

I hereby declare that this thesis is the result of my own work and includes nothing which is the outcome of work done in collaboration except as declared in the Preface and specified in the text. I further state that no substantial part of my thesis has already been submitted, or, is being concurrently submitted for any such degree, diploma or other qualification at the University of Cambridge or any other University or similar institution except as declared in the Preface and specified in the text. It does not exceed the prescribed word limit for the Engineering Degree Committee.

Tenghao Niu

September 2021

Measurement and Modelling of Human Car Driving with Steering Torque Feedback

Tenghao Niu

Abstract

Steering feel, or steering torque feedback, is an important aspect of a vehicle's dynamic behaviour and may become more significant in the transition between conventional and automated control. However, there is very little theoretical understanding of its role. The evaluation of steering feel mainly relies on subjective-objective correlation, which turns the subjective ratings of steering feel into objectively measurable metrics. Consequently, this aspect of vehicle development is time consuming, expensive, and probably suboptimal. Therefore, the aim of the research is to improve theoretical understanding of steering feel by measuring, understanding, and modelling a driver's subjective and objective responses to steering torque feedback. This work builds upon and complements earlier work that investigated the role of vestibular feedback in car driving.

A new driver-steering-vehicle model incorporating steering torque feedback is developed for both linear and nonlinear steering dynamics. The underlying hypothesis is that a human driver obtains an internal mental model of the steering and vehicle dynamics, the neuromuscular dynamics, and the sensory systems, which plays a significant role in sensory perception, cognitive control, and neuromuscular action. The effects of the model parameters on the dynamic behaviour of the driver-steering-vehicle system are demonstrated through a comprehensive parameter study.

Experiments are devised and performed on a fixed-base driving simulator to identify the unknown parameters of the model so that the driver model is enabled to represent realistic driving behaviours. The objective and subjective experimental data are analysed using rigorous statistical methods to obtain a fundamental understanding of the driver's steering control behaviour with different steering properties and driving conditions. In general, it is found that with an increase in steering system friction level, the driver's steering control performance deteriorates, and the subjective evaluation of steering feel is perceived as worse.

An identification procedure is initially developed to fit the linear model predictions to measured steering responses in the linear phase of the experiments. The model is found to fit the measured results well under a wide range of conditions, and the identified parameter values are found to be physically plausible. The validity of the identification procedure to find accurate model parameters and the validity

of the model structure to describe realistic driver steering control behaviours are checked against experimental and simulation results.

The identification and validation procedures are then adjusted to account for challenges of finding parameter values for the nonlinear model. The model structure is found to accurately predict the deterministic component of a driver' steering control of a vehicle with nonlinear steering system friction. The identified process noise level is found to increase with the increase in steering system friction. However, the possibility that drivers may use an intermittent and threshold-driven control strategy which might explains the identified increasing trend is not examined. A series of simulations is used to investigate the correlations between the model and the driver's subjective assessment of the vehicle steering quality. It is shown that the model has the potential to explain and predict the driver's subjective and objective responses to steering torque feedback.

Acknowledgements

First and foremost, I would like to thank my supervisor, Professor David Cole, for his dedicated support and guidance. David continuously provided encouragement and was always willing and enthusiastic to assist in any way he could during this research project. Without him, I would not have been able to complete my PhD study and this thesis. I would also like to thank my advisor, Professor David Cebon, for his constructive comments on my first-year report and valuable advice on my research project.

Many thanks go to Toyota Motor Europe, who supported my research financially during my time at Cambridge, and especially Dr Xabier Carrera Akutain and Andrea Michelle Rios Lazcano, who provided me with professional advice from an industry perspective and generously supported my experiments under the COIVD-19 restrictions.

And my biggest thanks to my family for all the support they have shown me through my research, the culmination of four years of distance learning.

Finally, I would like to thank the members of the Driver-Vehicle Dynamics Research Group, Dynamics and Vibration Research Group and Transportation Research Group, especially Dr Christopher Rosier, Dr Xiaoxiang Na, Dr Xuan Zuo Liu, Yan Ke, Samer Abdelmoeti, James McBride, Dr Matthew de Brett, Dr Luis Andrade Acosta, Tisal Edirisinghe, Dr Sam Brockie, Dr Jiannan Yang, Dr David Hawes, Tobias Carrigan, Dr Demetris Demetriou, Dr Naoki Onozato, and Dr John Hickey for their friendship and help.

Supervisor: Professor David Cole

Advisor: Professor David Cebon

Examiners: Professor David Cebon

Professor Fredrik Bruzelius

Contents

List of Figures

List of Tables

Nomenclature

Roman letters

Upper case

$\widehat{\mathbf{A}}_R$	Nonlinear reduced plant state function
$\widehat{\mathbf{A}}_{msv}$	Nonlinear muscle-steering-vehicle state function
$\widehat{\mathbf{A}}_n$	Jacobian of $\widehat{\mathbf{A}}_R$ at time step n during controller prediction
$\widehat{\mathbf{Q}}_{\mathrm{KF}}$	Process noise covariance on states
$\dot{T}_f$	Steering system friction torque change rate
$\widehat{\mathbf{A}}$	Nonlinear plant state function
$\mathbf{A}_{\mathbf{H}}$	Hessian of $\widehat{\mathbf{A}}$
$\mathbf{A}_{\mathbf{J}}$	Jacobian of $\widehat{\mathbf{A}}$
$\mathbf{A}_R$	Reduce plant state matrix
$\mathbf{A}_a$	Muscle activation state matrix
$\mathbf{A}_{fF}$	Lateral force disturbance filter state matrix
$\mathbf{A}_{fM}$	Yaw moment disturbance filter state matrix
$\mathbf{A}_{fT}$	Column torque disturbance state matrix
$\mathbf{A}_{fr}$	Target path state matrix
$\mathbf{A}_{msv}$	Muscle-steering-vehicle state matrix
$\mathbf{A}_{\tau\theta_a}$	Muscle angle sensory delay state matrix
$\mathbf{A}_{\tau r}$	Stretch reflex state matrix
$\mathbf{A}_{\tau vi}$	Visual delay state matrix
$\mathbf{B}_R$	Reduced plant input matrix
$\mathbf{B}_a$	Muscle activation input matrix
$\mathbf{B}_{fF}$	Lateral force disturbance filter input matrix
$\mathbf{B}_{fM}$	Yaw moment disturbance filter input matrix
$\mathbf{B}_{fT}$	Column torque disturbance input matrix
$\mathbf{B}_{fr}$	Target path input matrix
$\mathbf{B}_{msv}$	Muscle-steering-vehicle input matrix
$\mathbf{B}'_{msv}$	Nonlinear muscle-steering-vehicle input matrix
$\mathbf{B}_{\tau\theta_a}$	Muscle angle sensory delay input matrix
$\mathbf{B}_{\tau r}$	Stretch reflex input matrix
$\mathbf{B}_{\tau vi}$	Visual delay input matrix
$\mathbf{C}_R$	Reduced plant output matrix
$\mathbf{C}_{Rmsv}$	Reduced muscle-steering-vehicle output matrix
$\mathbf{C}_a$	Muscle activation output matrix
$\mathbf{C}_{fF}$	Lateral force disturbance filter output matrix
$\mathbf{C}_{fM}$	Yaw moment disturbance filter output matrix
$\mathbf{C}_{fT}$	Column torque disturbance output matrix
$\mathbf{C}_{fr}$	Target path output matrix
$\mathbf{C}_{msv}$	Muscle-steering-vehicle output matrix
$\mathbf{C}_{\tau\theta_a}$	Muscle angle sensory delay output matrix
$\mathbf{C}_{\tau r}$	Stretch reflex output matrix

$\mathbf{C}_{\tau vi}$	Visual delay output matrix
$\mathbf{G}_F$	Lateral force plant input matrix
$\mathbf{G}_M$	Yaw moment plant input matrix
$\mathbf{G}_{RF}$	Lateral force reduced plant input matrix
$\mathbf{G}_{RM}$	Yaw moment reduced plant input matrix
$\mathbf{G}_{RT}$	Column torque reduced plant input matrix
$\mathbf{G}_T$	Column torque plant input matrix
$\mathbf{G}_r$	Target path plant input matrix
$\mathbf{K}_{\mathrm{LQ}}$	LQR gain vector
$\mathbf{M}_x$	Innovation gain matrix
$\mathbf{M}_y$	Innovation gain matrix
$\mathbf{Q}_{\mathrm{KF}}$	Process noise covariance
$\mathbf{Q}_{\mathrm{LQ}}$	Controller cost function matrix
$\mathbf{R}_{\mathrm{KF}}$	Measurement noise covariance
$\mathbf{R}_{\mathrm{LQ}}$	Controller cost function matrix
B_i	Box-Jenkins numerator polynomial, where i is selected from F_y, M_z, T_d or r
C_{boost}	Boost curve coefficient
C_f	Lateral front tyre stiffness
C_r	Lateral rear tyre stiffness
C_{sw}	Box-Jenkins noise model numerator polynomial
$C_{sw}{}'$	Equivalent damping of steering system friction
D_r	Stretch reflex delay block
D_{sw}	Box-Jenkins noise model denominator polynomial
F_{F_y}	Box-Jenkins denominator polynomial, where i is selected from F_y, M_z, T_d or r
F_{hi}	Load cell calibration force in i direction, where i is is selected from x, y or z
F_C	Friction torque magnitude
F_y	Lateral force disturbance
F_{yf}	Front tyre force
F_{yr}	Rear tyre force
H_a	Muscle activation process transfer function
H_{fF}	Lateral force disturbance filter transfer function
H_{fM}	Yaw moment disturbance filter transfer function
H_{fT}	Column torque disturbance filter transfer function
H_{fr}	Target path filter transfer function
H_{fw}	Process noise filter transfer function
H_{ms}	Muscle steering dynamics transfer function
H_n	Box-Jenkins noise model transfer function
H_r	Stretch reflex gain transfer function
H_v	Vehicle dynamics transfer function
I_{arm}	Arm inertia
I_c	Inertia of the rack and the front wheels referred to the pinion
I_{sw}	Inertia of the steering wheel
M_{hi}	Load cell calibration torque in i direction, where i is selected from x, y or z
M_z	Yaw moment disturbance
N_p	Number of time steps of prediction horizon
$N_{v\theta_a}$	Number of time steps of muscle sensory delay
N_{vi}	Number of time steps of visual delay
R^2	Coefficient of determination
$\hat{R}$	Normalised subjective rating
$\bar{R}$	Mean subjective rating
R	Subjective rating

T_1	Time constant
$T_{a(exp)}$	Actual muscle activation torque
T_a	Muscle activation torque
T_d	Column torque disturbance
$T_{demand(exp)}$	Recorded torque demand signal
$T_{demand(sim)}$	Simulated torque demand signal
T_f	Steering system friction torque
T_m	Assist torque
T_p	Prediction horizon
T_s	Sample time
T_{sw}	Steering torque
T_t	Controller time shift
T_w	Self-aligning moment
V_{θ_a}	Standard deviation of measurement noise on the muscle angle θ_a
V_e	Standard deviation of measurement noise on the lateral deviation of the vehicle from the target path e
V_i	Voltage outputs from the i_{th} strain gauge set
V_ψ	Standard deviation of measurement noise on the vehicle yaw angle ψ
W_d	Energy dissipated by damping
W_f	Energy dissipated by friction
$\boldsymbol{W}_{\alpha\beta}^{(l)}$	LSTM weightings, where α is selected from r or h, and β is selected from f, i, o or c
$\boldsymbol{X}_{R0}$	State trajectory
H	Controller state matrix
I	Identity matrix
K	Kalman gain
L	A gain matrix
P	State covariance matrix
S	Controller discrete Riccati equation solution
F	F value of statistical tests
G	Steering gear ratio
I	Vehicle yaw moment of inertia
J	Cost function
U	Vehicle longitudinal speed
W	Process noise standard deviation
X	Load cell calibration matrix

Roman letters

Lower case

a_y	Vehicle lateral acceleration
c_{hw}	Handwheel damping
c_a	Damping resisting stretching of the muscle fibre
c_p	Intrinsic muscle damping
c_{sw}	Damping of the steering system (of the bearings) and steering system friction
c_t	Torsion bar damping
f_{cF}	Cut-off frequency for the low-pass filter H_{fF}
f_{cM}	Cut-off frequency for the low-pass filter H_{fM}
f_{cT}	Cut-off frequency for the low-pass filter H_{fT}
f_{crh}	Cut-off frequency for the high-pass filter in H_{fr}
f_{crl}	Cut-off frequency for the low-pass filter in H_{fr}
k_{hw}	Handwheel stiffness term
k_a	Tendon stiffness

k_p	Intrinsic muscle stiffness
k_r	Reflex gain
k_{sw}	Stiffness of the steering system due to the kingpin axes (inclination and scrub radius)
k_t	Steering column stiffness
n_d	Number of drivers
n_i	Number of time steps, where i is selected from 1, 2 or 3
q_e	Controller cost function weight on path-following error
q_α	Controller cost function weight on control action
w_F	Lateral force disturbance white noise
w_M	Yaw moment disturbance white noise
w_T	Column torque disturbance white noise
w_r	Target path white noise
$w_{sw(sim)}$	Simulated steering wheel angle noise
$w_{\alpha(sim)}$	Simulated filtered process noise
w_α	Filtered process noise
y_s	Reduced plant output
$\boldsymbol{b}_\beta$	LSTM bias vector, where β is selected from f, i, o or c
$\boldsymbol{c}_\tau^{(l)}$	LSTM cell state at layer l and time step τ
$\boldsymbol{h}_\tau^{(l)}$	LSTM hidden state at layer l and time step τ
$\boldsymbol{x}_L$	Linearisation states
$\boldsymbol{x}_R$	Reduced plant states
$\boldsymbol{x}_a$	Muscle activation states
$\boldsymbol{x}_{fF}$	Lateral force disturbance filter states
$\boldsymbol{x}_{fM}$	Yaw moment disturbance filter states
$\boldsymbol{x}_{fT}$	Column torque disturbance states
$\boldsymbol{x}_{fr}$	Target path states
$\boldsymbol{x}_{msv}$	Muscle-steering-vehicle states
$\boldsymbol{x}'_{msv}$	Nonlinear muscle-steering-vehicle states
$\boldsymbol{x}_e$	Plant state estimate
$\boldsymbol{x}_{\tau\theta_a}$	Muscle angle sensory delay states
$\boldsymbol{x}_{\tau e}$	Path-following error visual delay states
$\boldsymbol{x}_{\tau r}$	Stretch reflex states
$\boldsymbol{x}_{\tau\psi}$	Yaw angle visual delay states
a	Distance of front tyres from the centre of mass of the vehicle
b	Distance of rear tyres from the centre of mass of the vehicle
c	tanh function slope
d	Trail (Pneumatic and caster)
e	Path-following error
i	Index
k	Time step index
l	LSTM layer index
m	Vehicle mass/ Number of LSTM layers
p	Probability
q	Time-shift operator
r	Correlation coefficient/ Target path lateral position
s	Laplace transform parameter
t	Time
v	Vehicle lateral velocity
w	Process noise
$\boldsymbol{v}$	Measurement noise
$\boldsymbol{x}$	Plant states
$\boldsymbol{z}$	Plant output

Greek letters

Upper case

Θ_{sw}	Steering wheel angle amplitude
$\boldsymbol{\Gamma}_f$	LSTM forgot gate output
$\boldsymbol{\Gamma}_i$	LSTM input gate output
$\boldsymbol{\Gamma}_o$	LSTM output gate output
Δ	Small change in value
$\boldsymbol{\Theta}$	MPC input matrix

Greek letters

Lower case

$\dot{\theta}_{a(exp)}$	Actual muscle angular velocity
$\dot{\theta}_a$	Muscle angular velocity
$\dot{\theta}_c$	Steering column angular velocity
$\dot{\theta}_{c0}$	Friction model angular velocity
$\dot{\theta}_{ct}$	Friction model angular velocity
$\dot{\theta}_{sw}$	Steering angular velocity
α_{sim}	Simulated alpha activation signal
$\theta_{a(exp)}$	Actual muscle angle
θ_a	Muscle angle
θ_c	Steering column angle
$\theta_{sw(exp)}$	Measured steering wheel angle
$\theta_{sw(sim)}$	Simulated steering wheel angle
θ_{sw}	Steering wheel angle
τ_{θ_a}	Muscle angle sensory delay
τ_1	Motor neurons lag time constant
τ_2	Muscle activation and deactivation lag time constant
τ_r	Reflex delay
τ_{vi}	Visual delay
$\boldsymbol{\alpha}_0$	Nominal control sequence
α	Alpha activation signal
δ	Front tyres steer angle
ε	Weighted prediction error
σ	Standard deviation/Sigmoid function
τ	LSTM time step index
ψ	Vehicle yaw angle
ω	Vehicle yaw rate
$\boldsymbol{\alpha}$	Control sequence

Numerals

$\mathbf{0}$	Matrix of zeros

Others

$(:, j)$	Entire *j*th column
$(i, :)$	Entire *i*th row
(i, j)	*i*th row and *j*th column
$[i, j]$	Containing *i* rows and *j* columns

Abbreviations

CI	confidence interval
CNS	central nervous system
CUAC	Cambridge University Automobile Club
CUED	Cambridge University Engineering Department
EHPS	electro-hydraulic power steering
EKF	extended Kalman filter
EKF1	first-order extended Kalman filter
EKF2	second-order extended Kalman filter
EPS	electric power steering
HPS	hydraulic power steering
LMPC	linear model predictive control
LQG	linear quadratic Gaussian
LQR	linear quadratic regulator
LR	linear regression
LSTM	Long Short-Term Memory
MLE	maximum likelihood estimate
MPC	model predictive control
NMPC	nonlinear model predictive control
RMS	Root-Mean-Square
RNN	Recurrent Neural Network
SBW	steer-by-wire
SNR	signal-to-noise ratio
SRR	steering reversal rate
TME	Toyota Motor Europe
VAF	variance accounted for
ZOH	zero-order hold

Chapter 1

Introduction

Steering feel, or steering torque feedback, is important aspect of dynamic properties of vehicles and has been devoted significant attention to by vehicle manufacturers. The vehicle steering system mainly serves two functions: enabling the tracking and road holding abilities of the vehicle through a steering effort from the driver and informing the driver about the driving environment and vehicle response. During vehicle steering, lateral forces generated by the tyres on the front axle are communicated to the driver through torque at the steering wheel, and this can give the driver useful information about the vehicle states. Steering feel, resulting from the interaction between the driver and the vehicle through the steering wheel, not only influences the ability of the driver to control the vehicle accurately and safely, but also affects the driver's subjective assessment of the vehicle's dynamic qualities upon steering through sensation of steering control, vehicle response and haptic feedback [1].

Although autonomous steering control is a maturing technology, the dynamic interaction between the human occupants and the vehicle is still important because the human driver is likely to retain a role in controlling the vehicle for at least part of its operating cycle. In fact, steering torque feedback may play a more significant role in the transition between conventional and automated vehicles [2]. Advanced Driver Assistance Systems (ADAS) with partial level of automation have been widely implemented to improve driving safety over the years [3]. However, the automated steering system always leads to unsatisfactory steering feel in the human-automation haptic shared steering control driving scenario as the behaviour of the driving assist system is difficult to be captured by the human driver [4]. In addition, driving a vehicle equipped ADAS normally requires transition between full automated control and full human control. During this transition, the human driver must undergo a period of adaptation to become familiar with the dynamics of the vehicle and settle on a stable control strategy, and this adaptation process is significantly affected by the human driver's subjective steering feel [5].

Despite the importance of steering feel, or steering torque feedback, the subjective nature makes it difficult to be quantified. The subjective-objective correlation method is the most established technique used to evaluate steering feel in the automotive industry. Objective metrics are normally extracted from the results of objective assessments based on standard manoeuvres. Subjective ratings are typically gained from expert drivers according to questionnaires. The recorded objective metrics are then correlated with the subjective ratings by using linear regression or nonlinear analysis to provide a method of predicting the human driver's subjective assessment of steering feel. Typical examples of this technique are seen in [6] [7] [8] [9] [10] etc. Although some strong correlations were found between subjective ratings and objective metrics, they are limited to the range of experimental conditions and there is lack of theoretical understanding of these correlations. In addition, the wide range of objective parameters, subjective parameters and test conditions make the studies difficult to be evaluated. Sharp [11] criticized the subjective-objective correlation technique by listing noticeable difficulties and warned that the findings from these studies can subsequently been proven unreliable. In addition, Cole [2] pointed out that continual vehicle chassis technology development is expanding the vehicle performance envelope to a range where the extrapolation of current correlation models are inaccurate. Consequently, this aspect of vehicle development is time consuming, expensive and suboptimal. The on-centre regime of operation is experienced by most drivers most of the time, and therefore contributes significantly to the human driver's subjective assessment of feel.

Based on the background information, the main aim of the research is:

to improve theoretical understanding of the subjective assessment of steering feel, or steering torque feedback by measuring, understanding and modelling a driver's subjective and objective responses to steering torque feedback, especially for on-centre steering.

It is advocated that a driver model capable of representing the driver's cognitive and physiological processes can potentially provide insight into subjective assessment of steering feel [2]. With such a model, the unreliability of subjective-objective correlation method can be avoided, and the present or future chassis technology can be optimized mathematically in the design phase. In this research, a mathematical closed-loop driver-vehicle model incorporating steering torque feedback is developed based on previous work on developing physiologically-based models of the driver to predict the driver-vehicle closed loop system behaviour such as [12] [13] [14] [15] [16] [17] [18] [19] [20] etc. The underlying hypothesis of the research is that a human driver obtains an internal mental model of the steering and vehicle dynamics with the driver's neuromuscular dynamics and sensory systems, which is used in sensory perception, cognitive control, and neuromuscular action.

Based on the aim of this research, the reminder of the thesis is organised as follows:

Chapter 2 reviews the relevant literature regarding current methods for evaluating the human driver's perception of steering feel, including the objective assessment, the subjective assessment and the

correlations between the subjective and objective data, and the techniques for modelling the steering system and the driver for developing the closed-loop physiologically-based driver-steering-vehicle model. The objectives of the research are defined based on the literature review.

Chapter 3 presents the novel mathematical driver-steering-vehicle model incorporating steering feel with a comprehensive parameter study to confirm correct operation of the developed model. Initially, a linear model for the linear steering and vehicle dynamics is developed by taking all the essential parts into account. The model is then extended to account for nonlinear steering dynamics, especially nonlinear steering system friction.

Chapter 4 describes the development of a fixed-base driving simulator and a series of driving experiments performed on the simulator. The results of the driving simulator experiments are analysed by using rigorous statistical methods to investigate the effects of steering torque feedback and the nonlinear steering dynamics on the human driver's steering control performance and the subjective evaluation of steering properties of the vehicle.

Chapter 5 presents an identification procedure used to find the unknown parameter values for the linear driver model by fitting the driver-steering-vehicle model predictions to the results of the linear phase of the driving simulator experiments. The validity of the identified linear driver model in replicating realistic driver steering control behaviours and the validity of the identification procedure in converging to the correct model parameter values are also examined.

Chapter 6 presents the identification of the driver model structure controlling a vehicle with nonlinear steering dynamics and demonstrates the ability of the model to predict the human drover's objective and subjective responses of steering torque feedback. Limitations of the model are also pointed out.

Chapter 7 summarises the main findings and conclusions and presents future work.

Chapter 2

Literature Review

2.1 Introduction

In this chapter, published literature relevant to the human driver's perception of the steering quality of the vehicle is reviewed, mainly regarding but not limited to the on-centre regime of operation. On-centre steering is associated with the vehicle travelling in a nominally straight line, and steering inputs are such that lateral accelerations of the vehicle are normally no greater than about $2ms^{-2}$. This regime of operation is perhaps experienced by most drivers most of the time in daily life and thus may contribute significantly to the human driver's assessment of the steering and vehicle quality. Outside of this regime, the steering operates in the off-centre and limit handling regimes. The steering system has been considered a much more significant factor in the on-centre region than the other operating conditions due to the high-steering system compliance because of the small amount of power assistance. This review focuses on literature that considers the conventionally mechanical steering system, normally consisting of a steering hand wheel connected via a shaft (column) to a rack and pinion, usually with power assist elements (hydraulic or electric). Nowadays, the exponential growth of the development of advanced steering technologies such as steer-by-wire (SBW) and four-wheel steer has allowed the vehicle responses to the steering inputs to be adjusted with more freedom. However, the limited theoretical understanding of the interaction between the steering and vehicle system and the steering torque feedback has prevented high-quality design of these systems.

Section 2.2 describes the methods for the objective assessment of steering feel, or steering quality of the vehicle. The methods for the subjective assessment of steering feel and the correlation between the objective and subjective data are reviewed in Section 2.3 and Section 2.4, respectively. The method combining the analytical steering system model and the vehicle dynamics for the investigation of the steering quality at low acceleration has been appreciated by many researchers. Therefore, a

comprehensive review of the use of mathematical models in predicting steering characteristics has been carried out in Section 2.5. Mathematical models representing the human driver's physiological behaviour are summarised in Section 2.6. Finally, conclusions along with shortcomings of current approaches and objectives for this research are presented in Section 2.7. The aim of this chapter is to critically review the most relevant published literature and summarise existing knowledge in order to provide a basis for further study into the objective and subjective assessments of steering feel, or steering torque feedback under on-centre steering regime.

2.2 Objective Assessment

In this section, objective methods for the evaluation of steering quality are reviewed. Specifically, this section concerns both on-centre steering and off-centre steering of passenger cars. Some studies about other vehicle types and research purposes, such as heavy vehicles or handling properties, are also included. Although they are not within the scope of the research, it is helpful to identify the vehicle manoeuvres employed, the measurements recorded, and the performance metrics derived in the general field of the research.

2.2.1 Test Vehicles

Different vehicle types and the numbers of test vehicles employed in the investigation contribute to the diversity of previous studies. For example, Jaksch [21] and Farrer [22] only used two passenger cars in their studies. However, adjustments were made to provide a wide range of on-centre handling properties. By contrast, Harrer's study [8] involved over twenty passenger cars, instead of using a small number of vehicles with various configurations, concentrating on vehicle handling and steering feel. Additionally, a wide range of test vehicles varying from heavy trucks to driving simulators is covered, although passenger cars are the most common test vehicles. Rothhämel [23] [24] investigated the steering feel and vehicle handling characteristics of trucks by using a moving-base driving simulator, to test sixteen steering systems with variation in the inertia, stiffness, damping and friction. He justified the use of a driving simulator as a practical solution to investigating large variations in vehicle and steering parameters. However, he also admitted that a simulator (even a moving-base simulator) never feels exactly like an actual vehicle because there are always limitations to the reproduced motions. A similar conclusion was drawn by Aurell [25]. Even within the type of passenger cars, some researchers also distinguished different vehicles classes (e.g., the C-, D-, E- and SUV-classes and the sport cars), by considering that different vehicle dynamic behaviours are expected, such as Kim [26] and Nybacka [9] [27].

2.2.2 Test Manoeuvres

Objective testing manoeuvres were normally well defined by standards from vehicle dynamics communities. This section summarises several representative examples from previous studies. However, there is a lack of clarity with respect to interpreting the results, and it is also necessary to note that a number of studies have not explained the objective testing manoeuvres used.

Segel [28] performed one of the earliest studies of driver-vehicle interaction in steering activities, and he employed a steady turn of 0.2g lateral acceleration and fast passing manoeuvres on narrow (8-feet wide) lanes. Jaksch [21] of Volvo reported extensively on several experimental and theoretical studies to understand steering control quality in a transient steering manoeuvre. The manoeuvre consisted of an ISO lane change with maximum lateral accelerations higher than $2ms^{-2}$. Therefore, the steering was not limited to the on-centre region, but this work is referenced by many later studies of on-centre steering quality.

Norman [29] of General Motors identified on-centre steering behaviour as requiring special attention, and he described a weave test that is widely used today. The test involves driving at a fixed speed of 100km/h along a nominal straight line and then applying a sinusoidal steering wheel angle at a specified frequency (0.2Hz) and an amplitude ($2ms^{-2}$). A weave test is now defined in an ISO standard [30]. Farrer [22] and Somerville [31] also performed a weave test with a steering frequency of 0.2Hz. Maximum lateral acceleration of $1ms^{-2}$ was chosen to keep the hysteresis end-effects away from the on-centre region of interest ($0.5ms^{-2}$). (Farrer's definition of the on-centre region ($0.5ms^{-2}$) differs considerably from that of Norman ($2ms^{-2}$). The use of weave tests was also reported in Sato et al [32], Harnett [33], Harrer [8], Rothhämel [24], Dang [34]'s work, and a series of papers by engineers from Honda [35] [36] [37] [38], although the frequencies and amplitudes of the steering inputs may differ from each other.

In addition to a weave test, Farrer [22] and Somerville [31] also performed a transition test that involved turning the steering wheel slowly away from the straight-ahead position until the rate of change of steering hand wheel torque and the vehicle response had stabilised with respect to steering hand wheel angle, typically 2Nm and 2degree/s. Both tests were performed at a vehicle speed of 100km/h. Farrer [22] argued that the transition test allowed features of on-centre steering quality that could not be identified from the weave test to be identified. A transient test was also incorporated into an ISO standard [39]. Harnett [33] included the transition tests defined in ISO standard to exam the off-centre region of vehicle handling.

Siegler [40] included four tests: steady-state circle test, ramp steer test, and on-centre and off-centre sinusoidal steering hand wheel angle input tests. In more recent studies, Nybacka [9] [27] and Gil Gomez [10] performed a combination of a great number of ISO standardised tests and classified them

into several groups: straight-ahead controllability tests, cornering controllability tests, and low-speed manoeuvring tests.

It is important to note that there are two classifications of the manoeuvres: open-loop and closed-loop manoeuvres. Harrer [8] argued that closed-loop manoeuvres such as lane-changes are unsuitable for the objective assessment of steering quality, since the human driver's mental compensation significantly affects the measured results, and therefore used a steering robot and demonstrated much better consistency and accuracy than achievable by a test driver. Siegler [40], Nybacka [9] [27] and Gil Gomez [10] also reported having used steering robots in their objective steering quality assessment investigation. Obviously, not every researcher has access to this technology, and closed-loop tests have been used for these objective tests by researchers other than those specifically mentioned above. However, it is also possible for human drivers to perform an open-loop test in principle, such as by shutting the eyes.

2.2.3 Objective Measurements and Metrics

Not all the published literature clearly stated which data or how the data were measured/recorded. However, this is understandable due to the large amount of data to be gathered from the tests. The following measurements form a basic set of data reported in most of the previous literature: vehicle lateral velocity, vehicle lateral acceleration, vehicle yaw rate, vehicle side slip angle, vehicle roll angle and/or roll rate, steering wheel angle and angular velocity, and steering wheel torque.

Once the data have been collected or calculated from measurements, a variety of describing parameters or say metrics are created to be correlated with subjective assessment results such as the averaged values, the gradients, the peak values with the corresponding positions, the overshoot values and the corresponding positions, the delays and the rising times from various plots of the data.

Segel [28] noted that the objective metric of the steering behaviour was the gradient of steering torque to lateral acceleration in a steady turn. Jaksch [21] realised the importance of steering torque and calculated steering hand wheel angle gradient (angle/lateral acceleration) and steering hand wheel torque gradient (torque/lateral acceleration). Steering effort was defined as the product of these two quantities. He also found that steering effort and response time of yaw velocity to hand wheel angle are the most significant response variables in determining subjective steering quality.

In Norman's study [29], objective metrics of steering performance were determined from 'cross-plots' of the measured responses. The four plots used were: steering hand wheel angle vs. vehicle lateral acceleration, steering hand wheel torque vs. vehicle lateral acceleration, steering hand wheel torque vs. steering hand wheel angle, and steering work vs. vehicle lateral acceleration. Each plot was approximately a closed curve exhibiting hysteresis characteristics. About thirteen performance metrics

were derived from these plots. For example, the steering torque gradient at $0ms^{-2}$ was obtained from the steering hand wheel torque vs. lateral acceleration plot. Although Norman [29] just focused on using these performance metrics to identify differences in steering behaviour between classes of vehicle rather than to correlate the metrics with subjective assessments of steering quality, these cross-plots techniques have been widely used alongside his weave tests by many studies such as [32] [22] [31] [25] [33] [8] [23] [34] etc. In Harrer's study [8], forty-five objective metrics were determined from the results of the weave tests, from six different cross-plots of torque, angle, yaw velocity, lateral acceleration, and sideslip and then were used to correlate with subjective criteria.

Misaji et al. [35] argued that the established practice of determining discrete values of hysteresis, gradients and intercepts from the multiple cross-plots of measured responses results in too many parameters, such that the correlation with subjective assessment results is complicated. Extension of the method to higher frequency steering inputs (the importance of which was recognised earlier in [41]) compounds the problems. To address these problems, the authors instead fitted equivalent linear stiffness and damping values to the cross-plot of steering hand wheel torque vs. steering wheel angle, using a method previously utilised to model the hysteresis behaviour of rubber vibration isolators. Tokunaga et al. [36] [37] extended the method by calculating the ratio of equivalent damping to stiffness. These parameters were then correlated with subjective criteria. In addition, in Aurell's study [25], it was found that many of the objective metrics were strongly correlated with each other, and five were selected as being independent, which are yaw rate mean gain, yaw rate phase time at 0.5Hz, maximum steering wheel torque gradient, steering wheel torque gradient at $1ms^{-2}$ and steering wheel torque hysteresis.

Koide and Kawakami [41] measured the frequency response (steering torque, yaw velocity, and lateral acceleration in response to steering wheel angle up to a frequency of about 2.5Hz). The frequency response measurement recognises that steering feel cannot be fully characterised by measurements made only at low frequency (0.2Hz). Peppler [42] used the measured data to fit a simple nonlinear model of steering hand wheel torque, consisting of linear stiffness and damping elements and a Coulomb friction element, all in parallel. The identified stiffness, damping, and friction terms were used as objective metrics to correlate with subjective criteria.

In more recent studies, Nybacka [9] [27] employed 28 objective metrics and Gil Gomez [10] employed 27 objective metrics classified into several groups based on the tests performed: straight-head controllability, cornering controllability, and first impression. The definitions of these objective metrics are corresponding to SAE and ISO standards.

2.3 Subjective Assessment

In the previous section, published literature regarding objective methods for assessing the steering quality of the vehicle is reviewed. However, many of these studies also included a subjective assessment exercise. In this section, relevant literature in which subjective assessment of steering feel forms a significant part is reviewed, mainly regarding but not limited to on-centre steering.

2.3.1 Test Subjects

One main question in these subjective tests is whether to use average drivers, say customers, or expert drivers. Although both kinds of subjects have been adopted in some previous studies (e.g., Hoffman and Joubert [43]), subjective assessments are mostly chosen to be performed by expert drivers. Farrer [22] stated that the problem should be analysed statistically, and a large number of drivers with mixed background and ages should be used. However, he noticed that it is inappropriate for this problem due to the highly technical nature of research. Harrer [8] also noted that attempts to involve customers in steering feel investigation tests led to inconsistency between the subjects and difficulty in interpreting the descriptions of subjective assessments and, therefore, suggested only including experienced vehicle dynamics engineers with advanced driving training. Dang [34] explained that experts are required as they can understand the questions thoroughly and relate the sensations to them in the tests. Additionally, to avoid age preferences, the largest age gap was set as ten years. Chen [6] used expert drivers because the level of consistency of their subjective assessment results could be higher, and in addition, they can still have enough mental capability for subjective evaluation of steering feel while performing advanced manoeuvres. Although expert drivers were used, Crolla [7] indicated that the subjective ratings often revealed poor consistency between drivers. Gil Gomez [44] also noticed a large spread in drivers' ratings in their study.

The number of test drivers, varying from one to forty in previous studies, is another primary consideration in these tests. Gil Gomez [45] mentioned that four hundred random subjects would be necessary in order to obtain statistically significant experimental results. However, engaging a great number of drivers is not feasible and would extend the test time significantly. Considering that, Chen [6] used ten test drivers and Gil Gomez [10] selected twenty-two expert drivers participating in their studies .

2.3.2 Test Manoeuvres

In contrast to objective tests dominated by open-loop manoeuvres, subjective assessments are determined by closed-loop manoeuvres, which can be conducted using predefined courses or letting the driver drive freely. For instance, some researchers used predefined manoeuvres such as steady turns,

fast passing manoeuvres, weave test, double lane change, straight lane etc. (Segel [28], Koide [41], Sato [32], Farrer [22], Somerville [31], Xin [2008], Rothhämel [23], Dang [34] etc.), although not every study followed the exact standard. In addition, a pre-training test for the drivers is usually included to let the drivers get familiar with the test manoeuvres, if predefined manoeuvres are chosen for the tests. Crolla and Chen [7], Harnett [33], Nybacka [9] [27], et al. decided to let the drivers drive freely, which means that the drivers were not constrained to follow standard manoeuvres. They claimed that a more representative methodology would exclude rigidly specific procedures, although standardisation is a logical approach to evaluate various drivers and cars in a comparable way. Some researchers even employed both methods, such as Aurell [25] and Gil Gomez [10]. Gil Gomez [10] performed the study with both a short predefined manoeuvre for first impression and free driving afterwards, and showed that short predefined manoeuvres and long free driving gave similar subjective assessment results. Usually, no matter what kind of manoeuvres are chosen, random and blind tests (drivers are not told the condition of the test vehicles) are always considered as the best practice, and a reference vehicle is also recommended.

2.3.3 Subjective Questionnaires

The main method of producing the subjective assessment results is to generate right questions for the test subjects. However, there is a lack of consistency about the most relevant and vital subjective feelings in evaluating the steering quality of a vehicle; and how to describe them. Therefore, not every study included the same subjective questions, and the number of the questions also varies a lot. For example, Segel [28] generated three general questions for the steady turn test and another four questions for the fast passing manoeuvre test. Farrer [22] produced a questionnaire containing fifteen questions related to on-centre handling quality. Crolla and Chen [7] presented forty-nine well-designed questions in their subjective questionnaire.

In addition, even in some studies where the same set of questions is used, the test drivers may interpret them differently. Crolla and Chen [7] stated that this could be the main reason for the high spread observed in their subjective assessment results. Therefore, they suggested that the test drivers must participate in designing the questions. Rothhämel [23] investigated the ‘word pool’ method to generate the questionnaire to make the questions conform to test driver’s parlance and then used five-word combination dimensions as the subjective questions.

Another example of designing the questionnaire is given by Farrer [22], the questions in whose work were split into two parts: the first part assessing each quality of interest and the second asking the test drivers’ preferred level. This design technique has also been used in Somerville [31], Kim [26]’s work. In addition, Gil Gomez [44] designed two types of subjective questions for the test drivers: the estimation type for judging how the magnitude of each criterion of interest and the evaluation type for

judging how good/bad the characteristics are, and categorised the questions into five levels, with each subsequent level defined in more details.

Overall, the following questions or characteristics are the most commonly used evaluation criteria, which indicate a concentration on steering feel, for these kinds of studies: steering response, steering precision, steering sensitivity, steering torque demand, steering wheel angle demand, steering stiffness, roll motion, road feel, steering effort, roll motion velocity, steering returnability, steering friction and overall steering feel/steering torque feedback etc.

2.3.4 Rating Scale

After defining the subjective questions, a strategy should be determined for answering the questions. Segel [28] did not numerically quantify the subjective data, and Sato [14] just asked the drivers to rate the subjective criteria as excellent, good or poor. These methods make it challenging to find the relationship between the subjective assessment results and objective metrics and therefore, a numerical rating scale is always used to perform statistical analysis and find a mathematical correlation.

The most commonly used scale is the 1-10 scale defined in SAE standard J1441 [46], which has been employed by Farrer [22], Somerville [31], Harrer [8], Zschocke [47], Nybacka [9] [27] and Gil Gomez [10] et al. Harrer [8] modified the scale slightly by adding a plus or minus sign to indicate which side of the ideal level the assessed criterion lay. Zschocke [47] used the 1-10 scale for evaluation (very poor-excellent) and another 1-6 scale for quantification (low-high). Gil Gomez [10] classified the subjective questions into different levels as mentioned above and also employed two scales: a 1-10 rating scale for vehicle handling was used for the subjective assessments of level 2 to 4, and a 1-5 scale with different paired anchor descriptions in the extremes was used for level-5 subjective assessments. Examples of the descriptors used are: ‘narrow to wide’, ‘weak to strong’, and ‘non-sticky to sticky’, respectively, for the cross-plot deadband, steering wheel torque build-up magnitude and steering friction feel.

The second most commonly used scale is the 1-7 scale, which was used by Chen [6], Crolla and Chen [7], Aurell [25] and Rothhämel [23]. Normally, in these studies, a reference vehicle is used with a score four. Gil Gomez [45] stated that using reference vehicles might simplify the research initially, but make the study results difficult to compare because different references are used in different studies.

Apart from the two common scales mentioned above, there are also other scales used in previous studies. For example, Tokunaga et al. [36] [37] used a scale of 1 to 5. Dang [34] adopted three different scales: 1 to 5, 1 to 9 and -4 to 4.

2.4 Correlation between Subjective and Objective Data

Once the objective metrics and the subjective assessment results are gathered, the correlation between them is to be found, which could provide a method to predict the subjective assessment results from the objective metrics so that guidelines for the design of the steering and vehicle system can be proposed without relying on tests on the physical vehicle. Although some studies have applied non-mathematical ways (for example, Harnett [33] just compared the objective and subjective data visually), this section focus on summarising mathematical correlation methods from linear regression to nonlinear analysis such as fuzzy logic and neural network.

2.4.1 Data Qualification

To prepare high quality subjective and objective data so that reliable correlations can be found, some researchers have applied multiple techniques, including self-correlation analysis, data selection and normalisation, to process the raw data.

Correlation analysis within the dataset, or say self-correlation analysis, is a common method to ensure the independence of each objective metric or subjective question and to remove redundant data. For example, Aurell [25] found that many of the objective metrics were strongly correlated with each other after conducting a linear regression, and therefore only selected five independent ones to correlate with subjective questions. Zschocke and Albers [47] found that there is no difference between the initial and the holding steering torque in terms of human perception. Rothhämel [23] explained that the answers to two questions with a high correlation coefficient indicates that the drivers have rated the same metric twice, even though the formatting of the questions may be different.

Drivers' evaluation and subjective data selection can be conducted by analysing the mean value for all the drivers' ratings and the spread in the ratings. Gil Gomez [44] [48] and Nykacka [9] [27] have identified drivers' rating tendencies. Dang [34] provided a detailed procedure on eliminating the drivers whose subjective data are unreliable following fundamental statistical analysis: step 1: for each evaluation, a driver's ratings are eliminated if the correlation coefficient between this driver's ratings and the average ratings is too low; low correlation coefficient means that the driver's rating tendency is quite different from the accurate ratings, that is to say, the driver's rating is not reliable; step 2: for each evaluation item, a driver's ratings are eliminated if the driver's ratings are particularly far from the average; step 3: after steps 1 and 2, outliers are eliminated according to Chauvenet's criterion that outliers in the sample were rejected if their value is at least one and a half times the interquartile range away from the 25th or 75th percentile; step 4: obtain the average ratings of each evaluation for each characteristic based on the remaining ratings after steps 1, 2, and 3. Then the average ratings are used for the correlation analysis.

Data normalisation is another common practice for qualifying the data and has been widely used in previous studies such as [7] [47] [10]. Crolla and Chen [7] stated that before correlation, the objective metrics and the subjective data should be normalised to a dataset with a zero mean and a variance of one because of human differences in judging the scale and rating scale range difference. Gil Gomez [10] commented that this method should be used with care by considering whether the assumption can be made that the data from the drivers can form a normal distribution by using a small sample. Zschocke and Albers [47] used a Lillefors test for checking whether their data can fit a normal distribution or not before employing Z-transformation to normalise the data, and non-parametric statistical tools were used such as Spearman's approach instead of a student's approach if it failed. Gil Gomez [44] eventually used a modified version of the normalisation method that the normalisation is applied per criterion after noticing that the distribution of subjective ratings for all the questions is not exactly normal.

2.4.2 Linear Regression

Jaksch [21], Aurell [25], Misaji [35], Harrer [8], Zschocke and Albers [47], Nybacka [9] [27] and Kim [26] used simple linear regression to correlate the subjective assessment results with the objective metrics. The simplicity of linear regression could be the main reason for its popularity. Simple linear regression generates a linear model relating one objective metric to one subjective variable. The correlation coefficient r ($r \in [-1,1]$) is widely adopted as a measure of the strength of the linear relationship. An $|r|$ value of 1 indicates the strongest correlation. If $|r|$ is smaller than a certain value, e.g., 0.7 in Nykacka [27]'s study, the correlation is considered as invalid. Jaksch [21] employed a Bravais-Pearson linear regression analysis and Harrer [8] indicated that the Pearson correlation coefficient should be larger than 0.8054 for a valid correlation.

Instead of or besides a simple linear regression analysis, Koide [41], Crolla and Chen [7], Harrer [8], Dang [34], Rothhämel [23], Nybacka [9] [27] used multiple linear regression. In this case, more than one objective metric is related to one subjective variable. The coefficient of determination R^2 ($R^2 \in [0,1]$) is used to measure the accuracy of the multiple linear regression model. F-statistics is commonly used to check the significance of the regression equation and each regression coefficient in the equation. For example, to judge whether the correlation and the equations are valid, Crolla [7] used R^2, correlation coefficients, the *F*-statistics and t-values for each regression coefficient, with the t-values indicating the significance of the regressor for the equation and assumed that a correlation is not valid if $R^2 < 0.7$ and t-value $< 95\%$. In Harrer [8]'s study, a confidence level of 90% was regarded as necessary to identify a valid correlation for a multiple linear regression. Rothhämel [23] also used R^2, the *F*-statistics and t-values to check the correlation quality and the uncertainty is quantified by the lower and upper limits of the 95% confidence level.

2.4.3 Nonlinear Analysis Methods

Ash [49] stated that because there is potential for both the subjective ratings and the steering and vehicle system to exhibit non-linear characteristics, a nonlinear method to build up links between the objective and subjective data should also be considered. In addition, Nybacka [27] argued that linear correlation analysis could only show that some objective metrics probably have a monotonically positive or negative effect on the corresponding subjective assessment, while a nonlinear method can enable a preferred range of an objective metric to be identified and nonlinear relationships that cannot be easily found by linear regression to be detected.

Neural network (NN) is a common nonlinear method that has been used by several researchers (Ash [49], Rothhämel [50], Nybacka [9] [27], Gil Gomez [10]). A neural network is a kind of data-driven black-box mathematical structure consisting of interconnected artificial neurons that imitate how a biological neural system works (e.g., the human brain). The neural network is capable of learning nonlinear relationships between different parameters or variables from data, and a typical multi-layer neural network consists of an input layer, one or several hidden layers and an output layer of neurons. An example of the neural network structure for exploring nonlinear subjective-objective links is shown in Figure 2.1.

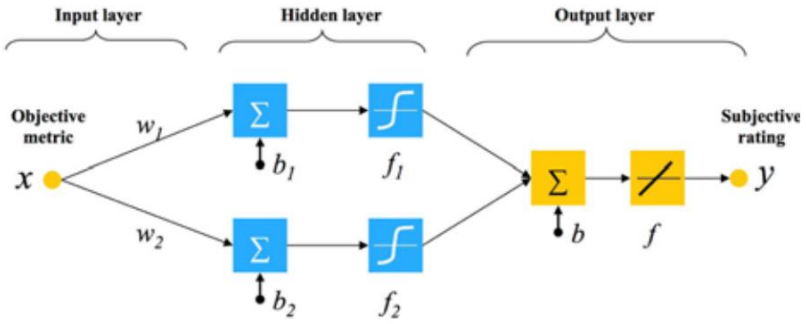

Figure 2.1: Single-input-single-output (SISO) neural network with one hidden layer with two tan-sigmoid activation neurons and a linear transfer function in the output layer [10].

Some other researchers (Ash [49] and Chen [51]) have utilised fuzzy logic for establishing nonlinear relationships between the subjective and objective data. Fuzzy logic is a superset of conventional Boolean logic that has been extended to handle the concept of partial truth to truth values between ‘completely true’ and ‘completely false’. Ash [49] stated that the fuzzy logic method lends itself to this type of data well due to the nature of subjective data collected by humans which scientifically is not precise data; and that can be used to model non-linear functions or arbitrary complexity.

According to Nybacka [9], although both fuzzy logic and neural network can be used to find nonlinear correlations between different parameters, the former can be adopted for non-metric subjective

assessment, such as ‘good/bad’ or ‘heavy/medium/soft’ while the latter can be used when the subjective assessment is in a numbered form.

2.4.4 Correlation Results

Previous studies have made some contributions to the subjective-objective correlation research. For example, Crolla and Chen [7] found that the subjective ratings for steering feel were consistent with objective metrics of steering hand wheel torque and rate of steering hand wheel torque, and good and consistent correlations were often associated with objective metrics that describe the higher frequency behaviour of the vehicle (that is, beyond the steady-state). Harrer [8] concluded that the steering hand wheel torque gradient and the lateral acceleration or yaw rate gradient at low steering wheel angles are the most significant objective metrics affecting steering feel. An example of detailed correlations in his study is shown in Table 2.1 and Table 2.2. In addition, Gil Gomez [10] identified a set of preferred ranges for the objective metrics by using a neural network, as shown in Table 2.3, which also include findings from Nybacka [9] [27] and King [52].

Despite some correlations were identified, Crolla and Chen [7] concluded that it was unclear how the mathematical regression results could provide physical insight into the subjective-objective link. The authors also noticed that the drivers’ subjective ratings often revealed a poor degree of consistency. Additionally, Gil Gomez [10] admitted that correlations are difficult as these data are not fully compatible by noticing drivers’ wide rating spread and their different use of the rating scale. In addition, the method for transforming subjective assessment into numerical values is not optimal and therefore still needs to be improved.

Table 2.1: Linear correlation results [8]

TEST	#	Assessment Criterion	#	Objective Parameter
Weave	1	Steering Torque on centre (80km/h)	1	Steering Stiffness
			41	Peak value of steering torque
	2	Steering Torque on centre (120km/h)	5	Ratio torque/angle
			41	Peak value of steering torque
	5	Centre feel at 80 km/h < 5°	1	Steering stiffness
			2	Steering stiffness at zero steer
	6	Centre feel at 120 km/h < 5°	1	Steering stiffness
			2	Steering stiffness at zero steer
	7	Steering friction	6	Specific area torque/angle
	8	Steering Response from the middle (80km/h)	11	Ratio yaw velocity/angle
			19	Steering sensitivity at 0 deg
	9	Steering precision	8	Yaw velocity response gain
	10	Steering angle demand Low speed (80km/h)	11	Ratio yaw velocity/angle
			24	Ratio lat. acceleration / angle
	11	Steering angle demand High speed (120km(h)	11	Ratio yaw velocity/angle
			24	Ratio lat. acceleration / angle

Table 2.2: Multiple linear regression criteria and corresponding parameters [8]

TEST	#	Assessment Criterion	#	Objective Parameter 1	#	Objective Parameter 2
Weave	5	Centre feel at 80 km/h < 5°	1	Steering stiffness	24	Ratio lat. acceleration / angle
			1	Steering stiffness	39	Peak value of lateral acceleration
	6	Centre feel at 120 km/h < 5°	1	Steering stiffness	24	Ratio lat. acceleration / angle
			1	Steering stiffness	39	Peak value of lateral acceleration
	7	Steering friction	1	Steering stiffness	17	Minimum steering sensitivity
	8	Steering response from the middle (80km/h)	29	Torque at 1m/s²	16	Steering sensitivity
	10	Steering angle demand Low speed (80km/h)	5	Ratio torque/angle	14	Ratio yaw velocity/angle
			5	Ratio torque/angle	37	Ratio torque / lat acceleration
	11	Steering angle demand High speed (120km(h)	5	Ratio torque/angle	14	Ratio yaw velocity/angle
			5	Ratio torque/angle	37	Ratio torque / lat acceleration

Table 2.3: Identified preferred objective metrics [10]

No	Objective measure	All DS	DS2	DS1	King *et al.* (2002)
1	Window (°)	< 3.5 Lv.5 [4]	< 3.7		
2	Response gain straight path (°/s/100°SWA)	> 25	29.5 ~ 33.5	25 ~ 30	20 ~ 25
3	Lateral acc. resp. gain (g/100°SWA) low speed	> 1.1	> 1.125		> 1.25
4	Lateral acc. resp. gain (g/100°SWA) high speed	> 1.7	> 1.8		
5	Gain linearity (-)	(< 1.4)			
7	Roll control straight path (°/s/g)	< 31.25	< 30.5		
8	Torque deadband (°)	1.2 ~ 2.0 Lv.5 [2]	< 1.6	< 2.2	
9	Torque build-up (Nm/100°SWA)	30 ~ 40 [31.5]	30 ~ 38		
10	Friction feel (Nm)	1.2 ~ 1.7 Lv.5 [2.2]			
11	Yaw response gain (°/s/100°SWA)	> 28	30.5 ~ 34	28 ~ 32	12 ~ 20
12	Response gain understeer (°/g)	< 2.75 (1.5 ~ 2.0)	1.6 ~ 2.1		> 0
13	Yaw gain linearity (%)	< 100 (85 ~ 100)			
14	Rel. yaw gain @ Max. lat. acc. (°/s/100°SWA)	(> 55)			
15	Yaw - SWA phase time lag @ 4 m/s²	(70 ~ 90)	62 ~ 75		
16	Ay-SWA phase time lag @ 4 m/s²	> 80 (80 ~ 150)			
17	Ay – Yaw phase time lag @ 4 m/s²	< 30			
18	Roll control cornering (°/g)	(< 4.6)	< 4.2		
19	Torque build-up into corner (Nm/100°SWA)	> 18 Lv.5 [16]	> 16.5		
20	Torque build-up cornering (Nm/g)	> 2.5 Lv.5 [2.1]	> 2.7	4-6	
21	On-centre hysteresis (°)	-	11.5 ~ 14.5		
22	Off-centre hysteresis (Nm)	1.5 ~ 2.6	2.1 ~ 2.6	1.5 ~ 2.2	
23	Effort level (Nm)	3.7 ~ 4.3	4.2 ~ 4.8	3.6 ~ 4.5	
24	Low speed response gain (°/s/100°SWA)	(> 28)	> 25.5		20 ~ 25
25	Low speed torque build-up (Nm/100°SWA)	14-20			
26	Parking effort standstill (Nm)	< 3.7	< 4	< 3.3	
27	Parking effort rolling (Nm)	< 2.8 (1-2.8)	< 3.2	> 1.5	

2.5 Mathematical Modelling of Steering System

The steering system can be modelled with different levels of complexity depending on the research purpose, and rich literature exists in this field. Preferably, the model should not be unnecessarily complex since it will increase computational time and become more difficult to analyse. This section focuses on the literature that considers mechanical system modelling of conventional manual steering system, hydraulic power steering system, electro-hydraulic power steering and electric power steering system and that predicts steering characteristics themselves. In addition, controller implementation is highly related to the dynamic performance of steering for power assist steering systems. Therefore, some studies considering steering system modelling for controller design are also reviewed.

2.5.1 Mechanical System Modelling for Manual Steering System, Hydraulic Power Steering (HPS) and Electro-hydraulic Power Steering (EHPS)

Modelled as a 2 degree-of-freedom system in most cases (that is, the steering hand wheel with column and the rack), the steering system can be considered to include up to 5 degree-of-freedom where the basic inertia of each component is taken into account. Baxter [53] just used a simple model to improve the definitions of steering stiffness and steering feel and argued that the boost level should be minimised in the on-centre region, in order that the driver can detect the small fluctuations in tyre forces occurring in this region. Norman [29] drew a similar conclusion when comparing the power steering characteristics of US and European cars. Wohnhaas and Essers [54] used a 4 degree-of-freedom system to model a manual rack and pinion steering system, with concentration on the stick-slip friction in the gear mechanism for predicting the steering system behaviour. The model was able to predict the measured fluctuation in steering column torque arising from the tooth meshing process during sinusoidal steering hand wheel inputs. However, this mechanism of column torque fluctuation does not feature in the other steering models reviewed in this section. Post and Law [55] developed both a high degree-of-freedom and a simplified 2 degree-of-freedom steering system model to predict on-centre handling and implemented the steering system models with a vehicle model. The importance of modelling the nonlinear components in the steering system such as friction in the steering gear and king-pin axes, hydraulic boost characteristics and other nonlinear compliances in accurately reproducing the steering system behaviours has been shown. Neureder [56] studied vibrations in the steering hand wheel, and a 4 degree-of-freedom steering system model was used for this. Ueda [57] of Nissan also modelled the steering system with 4 degree-of-freedom and with multiple friction elements for the prediction of on-centre handling characteristics, and the model has been found to fit the measurement quite well. The validated steering system model was then used to investigate the influence of steering design parameters variation (such as friction and torsion bar stiffness). Harnett [33] developed a 2 degree-of-freedom steering system model by taking account of steering wheel inertia and

front tyres inertia about the steering axis with great details including column friction, column play, column stiffness and damping, rack friction and damping, servo force, fixed pneumatic/mechanical trail, tyre lateral force and aligning moment (nonlinear functions of slip angle). The simulation of the model agreed with the measured responses of the test vehicle well, especially in the linear region of the tyres. Pfeffer [58] proposed a rather complicated 5 degree-of-freedom model, shown as an example in Figure 2.2, for a hydraulic rack and pinion model in order to analyse steering feel. However, a simplified 2 degree-of-freedom model was also developed, and it was found that the two models performed similarly in vehicle dynamics simulation and investigating steering feel.

Apart from predicting steering characteristics themselves, some studies focused on designing the controller for the steering system when the power assistance unit is introduced, such as [59] [60] [61] etc. In these studies, lower-order models were normally preferred in order to reduce the computational load of the controller.

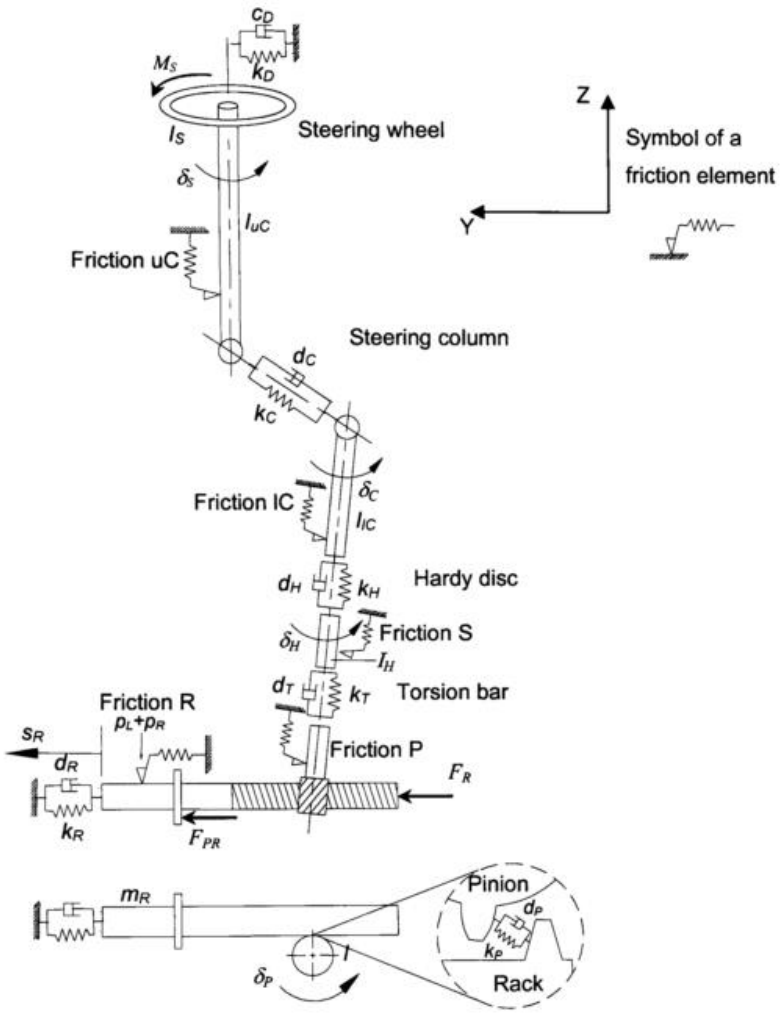

Figure 2.2: 5 degree-of-freedom model of steering system [58].

2.5.2 Mechanical System Modelling for Electric Power Steering (EPS)

The modelling of the mechanical system of the electric power-assist steering system is similar to that of the manual or hydraulic power-assist steering system, with the rotational motion of the electric motor always being considered as an extra degree-of-freedom. Zaremba and Davis [62] and Zaremba [63] did one of the earliest studies on modelling the steering mechanism of a rack-assisted EPS. They used a 3 degree-of-freedom system consisting of steering column inertia, rack mass and assist motor inertia to analyse the stability of EPS in the frequency domain, taking nonlinear elements into account, such as friction and backlash. Badawy and Zuraski [64] used both a full order model and a reduced model to model a column-type EPS for the purpose of developing an optimised EPS, and it was found that the two models performed similarly. Based on a basic model with 4 degree-of-freedom, Dannöhl [65] developed a 6 degree-of-freedom detailed model with comprehensive nonlinear components including friction, nonlinear belt stiffness and backlash in the ball screw drive to represent the mechanical structure of a rack-assisted EPS for analysing the reasons for the discontinuities of steering torque. Tamura et al. [66] proposed a nonlinear model with 8 degree-of-freedom, as shown in Figure 2.3, for the analysis of the static and dynamic performance of a column-type EPS, taking the basic inertia, stiffness and damping properties of each component into consideration. The static and dynamic responses of the model agreed well with the experimental data of normal and inverse input.

Like the manual and hydraulic power-assist steering system modelling, a lower-order or simplified mechanical model is often chosen for controller design due to easy implementation, such as [67] [68] [69] [70] [71]. Song [72] developed a full steering model with 5 degree-of-freedom firstly and simplified the model to just include one degree-of-freedom, that is, the total inertia referred to the pinion axis. The simulation results for the full steering system model and the simplified model are similar, although there is a slight difference in vehicle response. Dannöhl [65] also derived a reduced model based on his 4 degree-of-freedom basic steering system model for the convenience of controller implementation.

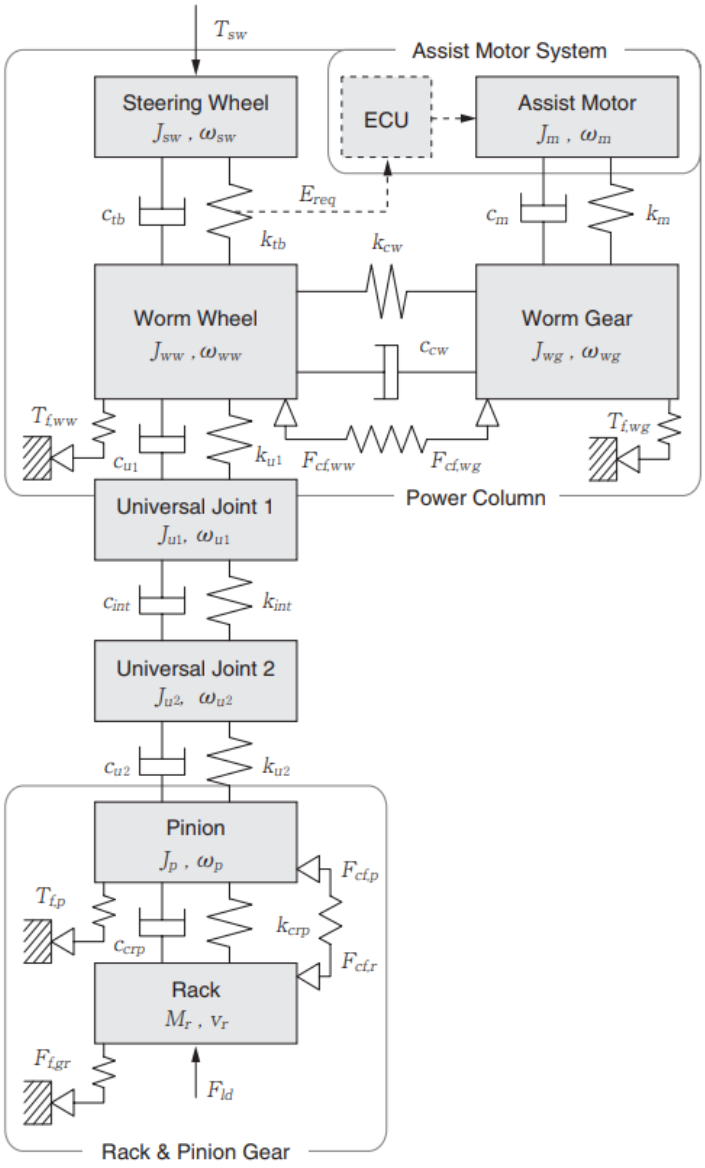

Figure 2.3: 8 degree-of-freedom column-type EPS model [66].

2.5.3 Friction Modelling

An appropriate friction model is necessary for steering system model development as it is an important aspect in describing the steering system properly and predicting steering performance accurately. Friction occurs in various positions of the steering system, such as the column, the rack, the gear meshing, the yoke, the bearings and the steering valve sealing. Coulomb friction is one of the most common practices to represent friction and is usually modelled by using a hyperbolic tangent function to avoid the discontinuities in the calculation. Segel [73] implemented a Coulomb friction in the steering system model and emphasised that it is essential to include friction in the steering system to stabilise the vehicle. Post and Law [55] also developed a specialised friction model based on Coulomb friction

and demonstrated the importance of including nonlinear components in the model. The practice of using Coulomb friction to represent steering system friction characteristics is also seen in the studies conducted by Zhang [74] and Dannöhl [65]. However, Neureder [56] suggested that the steering system friction behaves differently than a Coulomb friction. It was found that the vehicle exhibits vibrations with small forces, which contradicts the characteristics of Coulomb friction. Viscous damping is another simple method for representing friction, being directly adopted by Yamamoto [70] and being used as a linearisation method in the studies conducted by Sakai [75] and Govender and Müller [69]. Govender and Müller [69] demonstrated that it is an acceptable approach for modelling friction to some extent, although the nonlinear characteristics are rarely reproduced.

Wohnhaas and Essers [54] concentrated on the stick-slip friction in the gear mechanism and suggested a very detailed friction model, which is load and position dependent. The model was then found to be able to predict the measured fluctuation in steering column torque arising from tooth meshing, and it might be concluded that the tooth meshing friction is of secondary importance.

To better represent the hysteresis characteristic of the friction, Harnett [33] modelled the friction by using Dahl's Friction Model, which depends on the relative velocity $\dot{x}$ between the two parts involved. The model is given by (2.1).

$$\dot{F}_{Fr} = \sigma\dot{x}\left|-\frac{F_{Fr}}{F_c}\text{sign}[\dot{x}]\right|^{i_D}.\text{sign}\left(1-\frac{F_{Fr}}{F_c}\text{sign}[\dot{x}]\right) \tag{2.1}$$

where σ and i_D determine the shape of the hysteresis loop, F_c is the Coulomb friction magnitude, and F_{Fr} is the friction.

Ueda [57] developed an empirical friction model comprising three-spring coulomb friction elements in parallel connection in order to produce a more realistic hysteresis curve. In this case, the friction behaves like a spring up to a limit, after which the force remains constant. The friction model was implemented in five places in the steering model. As expected, it was shown that increasing the magnitude of each friction element tends to widen hysteresis in the cross-plots.

Pfeffer [58] generated another empirical friction model based on a similar idea. The friction element involves an exponential spring in series with a friction glider, as shown in Figure 2.4. The hysteresis curve consists of rising and falling branches, with the rising branch being described by (2.2) and (2.3).

$$F_{SF} = F_{lim}\left(1-e^{-f_{ESF}x}\right) \tag{2.2}$$

$$f_{ESF} = \frac{F_{lim}}{k_{ESF}} \tag{2.3}$$

where k_{ESF} is the spring stiffness at zero force and F_{lim} is the force limit, which is dependent on system pressure or speed. The friction model was then enhanced by connecting a nonlinear Maxwell element

(series spring-damper) in parallel to cover dynamic effects, as shown in Figure 2.5. The exponential spring k_M is to limit the dynamic effects at high speeds while the damper c_M is to reduce the spring force especially at low speeds. The overall friction is the summation of the forces represented by the two parallel elements. Dell' Amico [60] [61] adopted the same approach for friction modelling.

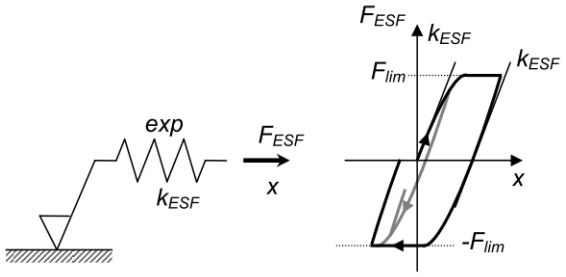

Figure 2.4: Exponential-Spring-Friction-Element (ESF-Element) [58].

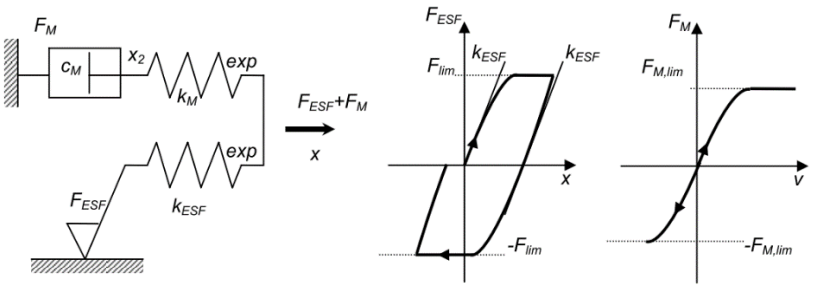

Figure 2.5: Exponential-Spring-Friction-Element with Maxwell-Element (ESFM-Element) [58].

Tamura et al. [66] argued that previous models such as Coulomb friction and combinations of friction elements and Maxwell have discontinuous characteristics theoretically and therefore are slow for numerical computation. Instead, they employed the LuGre friction model [76] [77], which represents friction accurately with a continuous state formulation and can capture more friction characteristics including stiction and Stribeck effects besides hysteresis. Basically, it is based on a representation of the average deflection force of elastic bristles at the friction surface, and the friction coefficient μ is given by (2.4), (2.5) and (2.6).

$$\mu = \sigma_0 p + \sigma_1 \dot{p} + \sigma_2 v \tag{2.4}$$

$$\dot{p} = v - \sigma_0 \frac{|v|}{g(v)} p \tag{2.5}$$

$$g(v) = \mu_c + (\mu_{ba} - \mu_c) e^{-\left(\frac{|v|}{v_{sb}}\right)^2} \tag{2.6}$$

where μ_c is the Coulomb friction coefficient, μ_{ba} is the peak friction coefficient, v_{sb} is the Stribeck velocity, σ_0 and σ_1 are the contact stiffness and damping coefficients in the tangential direction, respectively, σ_2 is the viscous friction coefficient, p is the bristle deflection, and v is the slip. The friction model was applied at the gear meshing, the bearings and the rack guides.

Specker [78] criticised the disadvantage of previous static and dynamic friction models in causing instability for lower sample frequencies and applications with nonlinear state observers due to the usage of stepping functions crossing zero velocity and developed a new dynamic friction model based on a static friction model and a linear parameter-varying first-order low-pass filter to address these problems. The static model considers viscous, Coulomb, and Stribeck friction features and is defined by continuous functions, yielding a smooth force transition at standstill. The adaptive filter changes its time constant dependent on the actual velocity and supplements the static model with hysteresis and memory effect. The complete dynamic friction model is given by (2.10) with the terms $\tilde{F}_v(v)$, $\tilde{F}_c(v)$ and $\tilde{F}_\Delta(v)$ given by (2.7), (2.8) and (2.9), respectively.

$$\tilde{F}_v(v) = dv \tag{2.7}$$

$$\tilde{F}_c(v) = \hat{F}_C \tanh\left(\frac{v}{v_t}\right) \tag{2.8}$$

$$\tilde{F}_\Delta(v) = \left(\hat{F}_S - \hat{F}_C \tanh\left(\frac{v_{sp}}{v_t}\right) - dv_{sp}\right)\left(\frac{v}{v_{sp}} e^{-\left(\frac{v}{\sqrt{2}v_{sp}}\right)^2 + \frac{1}{2}}\right) \tag{2.9}$$

$$\dot{F}_{Fr}(v) = \frac{1 - e^{-\left(\frac{v}{v_0}\right)^2}}{T_1}\left(\tilde{F}_v(v) + \tilde{F}_c(v) + \tilde{F}_\Delta(v) - F_{Fr}(v)\right) \tag{2.10}$$

where d is a damping coefficient, $\hat{F}_C$ is the peak of the Coulomb friction force, v_t is the transition velocity of the hyperbolic tangent function, $\hat{F}_S$ is the Stribeck peak force and v_{sp} is the Stribeck peak velocity defining the friction delay (not the Stribeck velocity). The new dynamic friction model has been shown to be capable of reproducing nonlinear friction characteristics with a high accuracy using small sample rates and therefore is suitable for practical control and state observation algorithms.

2.6 Driver Modelling

In order to accurately predict a driver's subjective assessment of steering feel, or steering torque feedback, a validated mathematical model that can represent the human driver's physiological behaviour precisely is necessary. This section presents a thorough review of driver modelling techniques in terms of cognition process, neuromuscular system, and human driver perception.

2.6.1 Cognition

Increased knowledge of human driving behaviour has led to progress in modelling the driver's cognitive process. A variety of driver steering control models have been proposed due to distinctive demands, and an extensive review of driver cognitive modelling with respect to different applications and methodical methods was given by Plochl and Edelmann [79]. This section focuses on path-following steering control at constant vehicle forward speed, especially regarding the on-centre regime of operation.

McRuer and Krendel [80] [81], who described human regulation steering tasks as a form of close-loop compensatory control, proposed 'cross-over models' as shown in Figure 2.6. It suggests that the human driver performs a tracking task by using a compensator $H(s)$ to maintain an invariant form for the open-loop system $H(s)G(s)$ in the vicinity of the cross-over frequency. The combined system is represented as:

$$H(s)G(s) = \frac{\omega_c}{s} e^{-\tau_r s} \tag{2.11}$$

where ω_c is the cross-over frequency and τ_r is the effective system dead time.

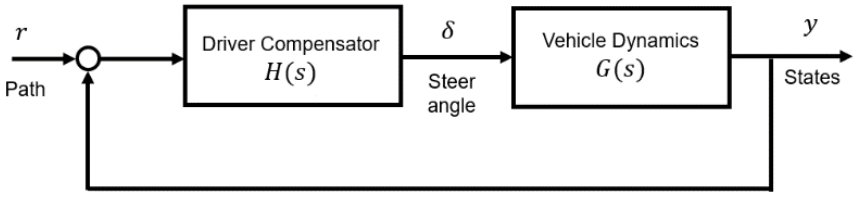

Figure 2.6: Simple feedback compensator driver model.

In contrast to cross-over models, which do not consider driver predictive concepts, more modern preview/predictive models suggest that the driver predicts the path of the vehicle based on current vehicle states and a previewed path to follow with the knowledge of the vehicle dynamics. Then the driver will determine an appropriate steer angle guiding the vehicle along the proceeding path according to the prediction. The earliest attempt for this kind of preview model was made by Kondo [82]. However, the simplest model just included one sight point as the preview location. Yosimoto [83], Guo [84] and Renski [85] also used the single point review concept.

In contrast to single preview point, the concept that the full information of the previewed road path and vehicle trajectory is available to the driver has been used in more recent studies. MacAdam [86] [87] gave the first example of an optimal control model of driver steering control, calculating the optimal steer angle minimising the difference between previewed road path and predicted vehicle trajectory

over a previewed distance using a continuous cost function. Peng [88] extended MacAdam's use of model predictive control (MPC) theory to include path-following yaw angle error in the cost function for the minimisation. In a separate development, Sharp and Valtetsiotis [89] proposed linear quadratic regulator (LQR) to solve linear vehicle control problems. As opposed to MacAdam's model, the controller is generated in the discrete-time domain. Cole et al. [90] compared the application of MPC and LQR for linear driver modelling and demonstrated that for controlling a linear time-invariant vehicle without constraints, the MPC and LQR approaches are identical, provided that the preview and control horizons are long enough. Keen [16] [91] and Odhams [14] [92] [93] used an instrumented vehicle operating in the linear regime and a fixed-base driving simulator separately to identify the MPC steering controller, and both studies found that the model fitted the measured data well.

Keen and Cole [94] then extended the MPC approach to account for nonlinear vehicle dynamics by proposing a multiple linear model structure for the driver's internal mental model. Specifically, a set of learnt linear models are derived by linearising the nonlinear vehicle model (nonlinear tyre) at every operating point of the vehicle for MPC controller formulation. Kim [18] and Kim and Cole [95] adopted this multiple linear model structure for nonlinear vehicle dynamics (nonlinear tyre and tyre-road friction) in the investigation of the role of steering torque feedback in providing the driver with road information, with a specific driver internal mental model selection algorithm. The simulation results showed the importance of steering torque feedback in helping the driver improve path-following accuracy, evidenced by the better identification results of the vehicle-road system with selecting the correct linearised model.

2.6.2 Neuromuscular System

Pick and Cole [12] [96] [97] [98] [99] [100] [101] did a series of studies to understand and model the driver's neuromuscular system in steering control tasks. In experiments, electromyography (EMG) was employed to identify the arm muscles that contribute to generating torques at the steering wheel. The muscles were then lumped together into one linear muscle model that generates torques on the steering wheel [98]. As a result, a driver-vehicle model incorporating the driver's neuromuscular system, which comprises arm inertia, muscle dynamics and stretch reflex, was proposed in [101]. In this study, the output from the steering controller is assumed to be the neuron signal arising from the human brain that activates the muscle fibres to generate torque. It was found that human drivers tend to stiffen their arms, which is called muscle co-contraction, to stabilise the vehicle and reject external disturbances.

Hoult [102] [17] extended the neuromuscular model developed by Pick and Cole [101] to include intrinsic muscle dynamics and identified the intrinsic dynamics of test subjects experimentally through a transfer function. Cole [103] subsequently fitted the identified transfer function with a lumped model and found that the addition of an intrinsic damping term improved the fit.

Droogendijk [104] and Katzourakis [105] from TU Delft proposed a series of driver models including neuromuscular system. In these models, the simultaneous alpha and gamma motoneurons co-activation was represented by using an inverse model.

Cole [103] further extended the neuromuscular model developed by Hoult [17] to include the alpha and gamma co-activation and cognitive delay by introducing a forward model, instead of the inverse model used in Droogendijk [104], Katzourakis [105] and Pick and Cole [97]'s studies.

The role of each block in the neuromuscular system model was investigated in a series of studies carried out by Pick and Cole [101] and Cole [106] [103]. Generally, it was found that the stretch reflex loop plays an important role in the response of the model to unexpected disturbances.

2.6.3 Perception

The understanding of the human driver's perception of vehicle states and the environment, arising from human sensory systems, should be a prerequisite for modelling the driver-vehicle close-loop system. However, there is a limited number of studies considering human perception in driver modelling. MacAdam [107] did an early study on including sensory limitations and noise in the driver model. However, the issue of sensory integration was not considered in depth. The most recent comprehensive reviews of existing knowledge of sensory dynamics, delays, thresholds and integration in the application of modelling driver steering task are given by Bigler and Cole [108] and Nash [109].

Bigler [19] and Bigler and Cole [108] proposed a sensory model structure, shown in Figure 2.7, specifically for driver modelling based on the theory provided by Harris and Wolpert [110] and Kang [111]. In this model, the additive and Signal-dependent noise (SDN) can represent two important sensory performance criteria, respectively, that is, a threshold level, which is the minimum stimulus that can be detected and the just-noticeable differences (JNDs) between two stimuli can be measured. The JND is assumed to be proportional to the stimulus amplitude, which is known as Weber's Law. The time delay for the sensory organs processing the stimulus was also included.

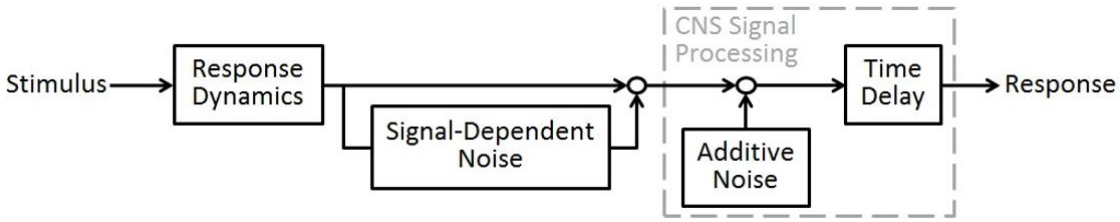

Figure 2.7: Generic sensor model proposed by Bigler and Cole [108].

In terms of sensory dynamics, the visual system, the vestibular organs and the somatosensors are the main modalities used in vehicle steering control [109]. Visual perception typically has two functions in driving tasks: perception of self-motion and perception of road path geometry. Bigler [19] investigated the frequency response of perception of self-motion and found that the visual dynamics can be reasonably described by a model introduced by Soyka [112] [113], which is described as a low-pass filter with a cut-off frequency ω_{vi}:

$$H_{vi}(s) = \frac{\omega_{vi}}{s + \omega_{vi}} \tag{2.12}$$

Like human cognitive process modelling, visual perception of road path geometry can be represented by a preview controller. Nash and Cole [114] [20] adopted the model of 'preview' of upcoming target path given by Sharp and Valtetsiotis [89] and Cole et al. [90], which is shown in Figure 2.8.

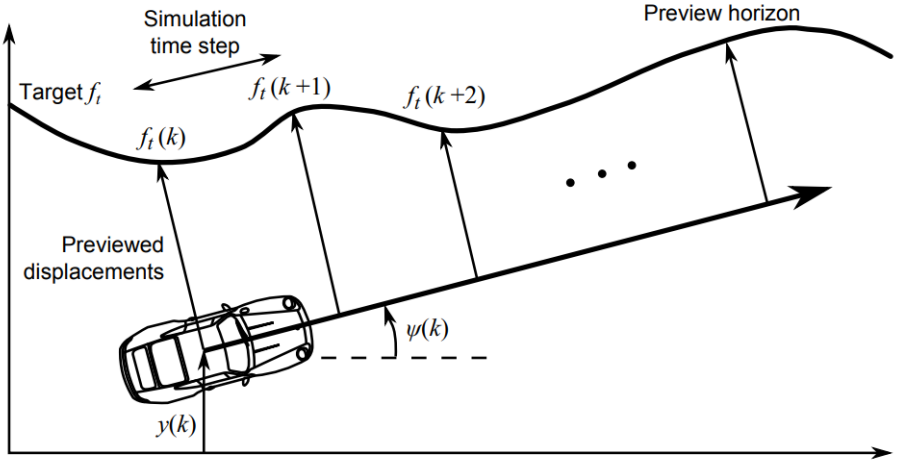

Figure 2.8: Model of 'preview' for visual perception of road path.

Nash and Cole [114] [20] also incorporated the two main vestibular organs: the otoliths H_{oto} perceiving vehicle lateral acceleration and semi-circular canals (SCCs) H_{SCC} perceiving vehicle yaw rate into the driver-vehicle model. The transfer functions for these two organs are given by (2.13) and (2.14). The dynamic behaviour of somatosensory system was not modelled in Nash and Cole [114] [20]'s study.

$$H_{oto}(s) = \frac{0.4(1 + 10s)}{(1 + 5s)(1 + 0.016s)} \tag{2.13}$$

$$H_{scc}(s) = \frac{5.73(80s^2)}{(1 + 80s)(1 + 5.73s)} \tag{2.14}$$

With respect to sensory integration, the Kalman filter was found to be capable of representing the ability of the human driver to estimate the states of the controlled system with an internal model of the system

[109] [115]. Nash and Cole [20] proposed a novel complete driver-vehicle model incorporating sensory dynamics, a simplified neuromuscular system, additive and signal noise, a state estimator and a controller. For a linear plant to be controlled, a LQG algorithm was applied (that is, a LQR controller and a time-invariant Kalman filter to estimate the states from noisy measurement optimally). Both the Kalman filter and the LQR controller were assumed to obtain a linear internal model of the neuromuscular, vehicle and sensory dynamics, and the process and measurement noise were modelled as zero-mean Gaussian noise processed by forcing functions. The model was then extended to include nonlinear vehicle (nonlinear tyre) dynamics and human driver limitations. In that case, several extended Kalman filters were selected as the state estimator, and MPC controllers with constraints were chosen. The structure of the model is shown in Figure 2.9 and Figure 2.10. The complete model was identified and validated from a series of moving-base driving simulator experiments using non-parametric and parametric identification methods. It was shown that the validated new driver-vehicle model is satisfactory for analysing the role of the sensory organs in driving [116]. Nash and Cole [117] then extended the study to investigate the effect of sensory conflicts on driver steering control.

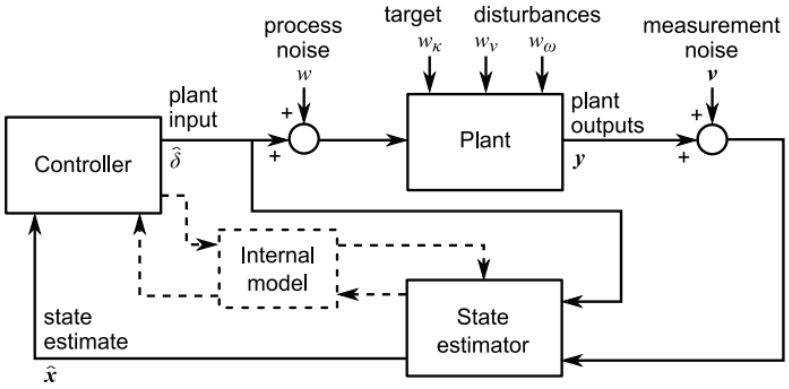

Figure 2.9: Overall structure of the driver-vehicle model [20].

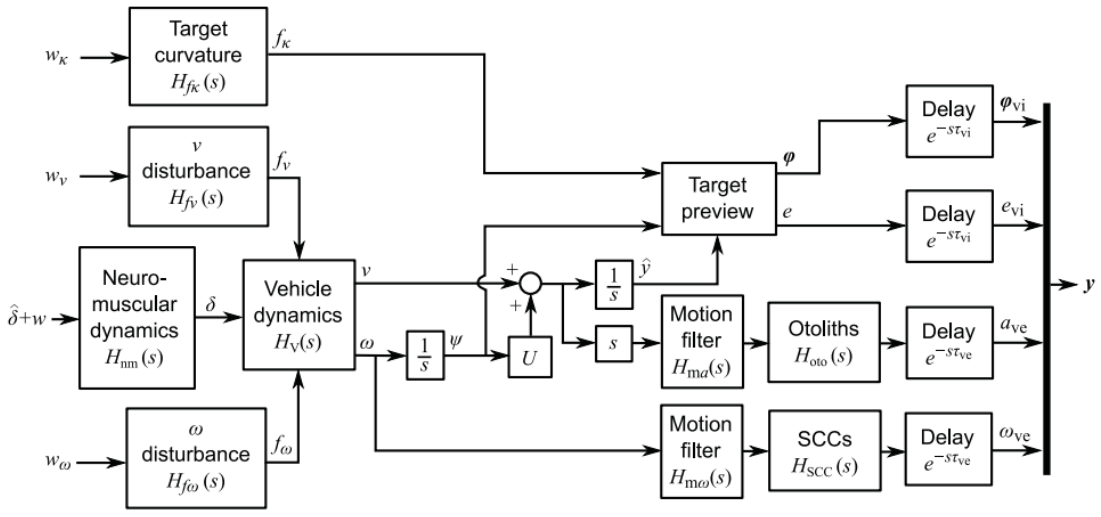

Figure 2.10: Block diagram of the plant controlled by the driver [20].

2.6.4 Subjective Assessment

A neuroscience study conducted by Blakemore [118] into tickliness found that the subjective feeling of humans is reflected by the discrepancy between the human's own prediction and actual sensory feedback. An internal forward model of the motor system predicts the sensory consequences of a movement based on the motor command. However, the prediction made by the internal forward model may be different from the actual sensory feedback human can receive. This study demonstrated that as the discrepancy between predicted and actual sensory feedback increases, there is a concomitant decrease in the level of subjective satisfaction. These results provide insight into a possible theoretical description of a driver's subjective assessment of steering feel. However, no previous study has incorporated this effect in driver modelling.

2.7 Conclusions and Research Objectives

According to the review of existing steering feel assessment methods, steering system modelling techniques, and work on driver models, findings are summarised as follows:

- Objective assessments are normally conducted with open-loop steering inputs. The weave test introduced by Norman [29] remains the basis of objective assessments of steering feel, especially for the on-centre region. The addition of frequency analysis, other standard manoeuvres and the use of steering robots aid the objective assessments. The increasing number of objective metrics extracted from the results of objective measurements has made interpretation difficult, and several researchers have proposed methods such as self-correlation analysis to find the independent metrics.

- Subjective assessments of steering feel are typically made by expert human drivers through closed-loop control inputs. The wide range of assessment questions and rating scales, the statistically insufficient number of test drivers, and the big variation in test drivers' ratings make the standardisation a challenging task.

- The subjective-objective correlation method is the most established technique used to evaluate steering feel. Some data qualification techniques are often employed to ensure good correlations to be found. The correlation methods can range from simple linear regression to nonlinear methods such as neural network. Although some strong correlations are identified, the physical reasons are not clear, and it is not reliable to extrapolate these correlations beyond test conditions. In addition, a wide range of parameters to be correlated, test conditions and correlation methods make the comparison of different studies difficult to undertake.

- The steering system can be modelled with different levels of complexity depending on the trade-off between computational efficiency and prediction accuracy. Nonlinearities in the steering system such as friction require attention to reproduce realistic steering system characteristics. The development of advanced friction models has enabled steering system friction to be computationally efficiently simulated with a high accuracy.

- Extensive research has been carried out on modelling the driver's behaviour in vehicle steering control including cognition, neuromuscular action, and perception. The validated models have the potential to provide insight for predicting the human driver's subjective assessment of steering feel mathematically with the aid of neuroscience knowledge.

Based on the literature review, the following research objectives are identified:

i. Develop a mathematical driver-steering-vehicle model incorporating steering feel, or steering torque feedback. The model will include a nonlinear and reasonably precise steering mechanism and will account for the possibility that the complexity of the internal mental model is limited.

ii. Devise and perform experiments using a fixed-base driving simulator with a randomly moving target path and random disturbances to provide the subjective and objective data necessary to identify and validate the developed driver-steering-vehicle model.

iii. Use the measured data to identify the unknown parameters of the mathematical model and the human driver's internal mental model.

iv. Determine the relationship between: the subjective quality of steering torque feedback; the ability of the driver to learn an accurate internal model of the steering system and generate optimal steering control actions; and the steering control performance that the human driver can achieve.

Chapter 3

Driver-Steering-Vehicle Modelling

3.1 Introduction

With the increasing need to reduce vehicle development time and cost, there is significant motivation for developing closed-loop mathematical driver-vehicle models to assess objective and subjective dynamic qualities of the vehicle without relying on extensive track tests and subjective feedback from test drivers. A thorough review of earlier driver steering models was conducted by Ploechl and Edelmann [79]. However, most of the studies only modelled the driver as an ideal controller and put little emphasis on the understanding of the human driver's limitations in the perception of vehicle states and the environments, arising from human sensory systems. As explained by Donges [119], the steering behaviour of human drivers can be explained by a 'two-level' model, with an open-loop controller to calculate steering actions to follow the previewed target trajectory from the visual system and a closed-loop controller to compensate for disturbances around the planned trajectory based on the estimate of vehicle states. Steering torque feedback plays an important role in the feedback task.

In this chapter, a new mathematical model of driver-steering-vehicle system is developed, taking account of steering torque feedback. The model comprises the vehicle and steering dynamics, the neuromuscular system, the sensory delays, and the human brain functions. The underlying hypothesis is that a human driver learns an internal mental model of the steering and vehicle dynamics with the driver's neuromuscular dynamics and sensory systems, which plays a significant role in sensory perception, cognitive path following control, and neuromuscular action. This work builds on and complements the previous work of Nash and Cole [20], who designed a new driver model incorporating visual and vestibular sensory systems.

The aim of this work is to develop a mathematical driver-steering-vehicle model incorporating steering torque feedback, in order to provide a theoretical understanding of how the subjective quality of a

vehicle's steering torque characteristic relates to how accurately an internal mental model can be learnt and how accurately the steering control actions can be generated. The model is then used to make accurate predictions of the steering torque response and to understand the extent to which the steering torque is informative about the states and parameters of the vehicle. A new linear driver-steering-vehicle is developed first to enable a fundamental understanding of torque feedback to be obtained. The derivations of this linear model have been reported in [120] and are presented in Section 3.2 in this chapter. Next, a comprehensive analysis of the linear model behaviour is conducted through simulation studies of the various parameters and the results are presented in Section 3.3. However, it is necessary to consider the nonlinear steering dynamics for investigating steering torque feedback. Friction in the steering mechanism is always present to some extent, and it is thought that lower friction levels lead to a subjectively better steering feel. However, there is no predictive tool to assess steering friction at the design stage at present. The new driver-steering-vehicle model is therefore extended to account for the nonlinear steering system friction by using the techniques used by Nash and Cole [20] to model human drivers' state estimation and cognitive control of a vehicle with nonlinear tyre dynamics. The derivation of this nonlinear model is presented in Section 3.4. The performance of the nonlinear model is then compared with that of the linear model in Section 3.5. The main conclusions are given in Section 3.6.

3.2 Linear Driver-Steering-Vehicle Model

In this section, a new mathematical model of driver-steering-vehicle system incorporating steering torque feedback is presented. To enable a fundamental understanding of the role of steering torque feedback while reducing the computational cost involved in simulating the model, linear dynamics are used to model the driver-steering-vehicle system. Various simplifying assumptions and omissions are made with the aim of devising the simplest possible model that predicts the responses of interest. These assumptions can be relaxed in the future once more is known about the role of steering torque feedback in the steering control task. The scope of the model does not extend to speed choice or control. Therefore, only vehicles travelling at constant longitudinal speed are considered, although the principles behind this model could be extended to include variable-speed vehicles. The driver is assumed to follow a given target path of negligible thickness. A minimal set of human sensory measurements is assumed: visual perception organs and the arm muscle proprioceptors. The modelling of the vestibular organs is omitted to reduce the complexity of the model and for compatibility with fixed-base driving simulator experiments described in Chapter 4. These assumptions are addressed in detail in later sections of this chapter.

The steering task described by the model is represented in Figure 3.1. The driver follows a randomly moving target path used in [20] in the linear operating regime while compensating for random disturbances acting on the steering and vehicle system. The target path r is straight but randomly varies

its lateral displacement from the centreline of the road, which means that the driver does not have any preview of the target path displacement. The aim of this is to ensure that the driver's control action is entirely feedback in nature (no feed-forward) and thus emphasise the role steering torque feedback. The random disturbances acting on the steering-vehicle system specifically refer to column torque disturbance T_d acting on the steering system, lateral force F_y and yaw moment M_z disturbances acting on the centre of mass of the vehicle. It is assumed that the aim of the driver is to minimise the tracking error between the vehicle lateral displacement and the randomly moving target path.

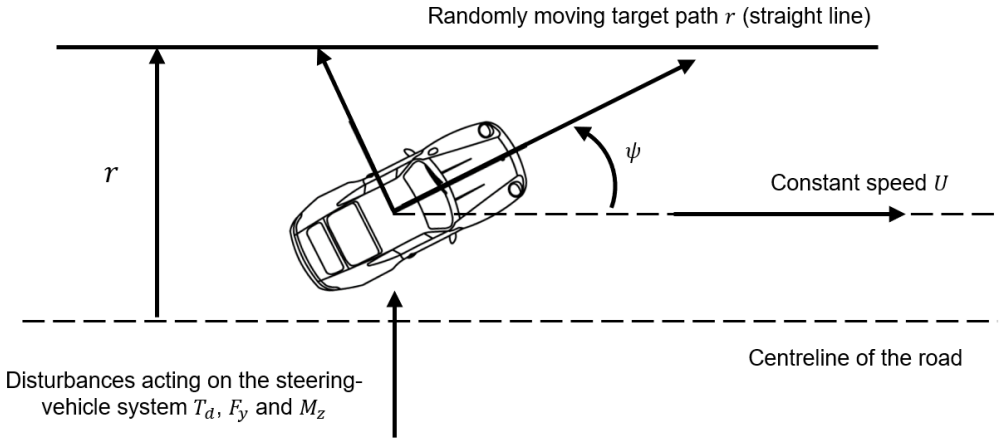

Figure 3.1: Steering control task described by the new driver model. The driver is to follow the randomly moving target path r while rejecting disturbances acting on the steering-vehicle system T_d, F_y and M_z

A schematic structure of the new driver-steering-vehicle model built upon the previous research of Nash and Cole [20] is shown in Figure 3.2. The model is developed based on the hypothesis that the driver is trying to minimise the lateral deviation of the vehicle from the randomly moving target path by using the optimal estimated states of the plant and the environment from the noisy sensory measurements. The driver's primary control output is the alpha muscle activation signal. The driver's control strategy follows the linear quadratic Gaussian (LQG) framework, combining a linear quadratic regulator (LQR) with a Kalman filter to give statistically optimal control actions and state estimates based on the driver's internal model of the plant. A Kalman filter uses an internal model to achieve optimal state estimation in the presence of additive white noise. However, there is also a muscle stretch reflex action, a stretch reflex (H_r and D_r) controller is therefore also included in this model. The plant shown in Figure 3.3 describes the plant controlled by the driver in detail, including models of the muscle activation process (H_a), the muscle dynamics (part of H_{ms}), the vehicle (H_v) and steering dynamics (the other part of H_{ms}), human sensory delays and disturbance filters (H_{fT}, H_{fF}, H_{fM} and H_{fr}). The perceived states by the driver are the visually-sensed vehicle lateral deviation with respect to the target path e, the yaw angle ψ, and the proprioceptively-sensed muscle angle θ_a.

The driver-steering-vehicle model is implemented in state-space form, in discrete time with a sample time T_s so that time delays can be easily implemented using shift registers. All continuous transfer functions $H(s)$ are converted to discrete state-space matrices (**A**, **B**, **C**, **D**) with states $\boldsymbol{x}$ and subscripts matching the name of that transfer function. The discretisation is based on a zero-order hold (ZOH) method, which could achieve accurate simulation results without adding too much complexity for the implementation, as suggested by Nash and Cole [20]. In most cases, this is approximated in the form $\mathbf{A} = \mathbf{I} + T_s\mathbf{A}_c$, $\mathbf{B} = T_s\mathbf{B}_c$, where $\mathbf{A}_c$ and $\mathbf{B}_c$ are continuous-time state-space matrices. The time step index is denoted by k.

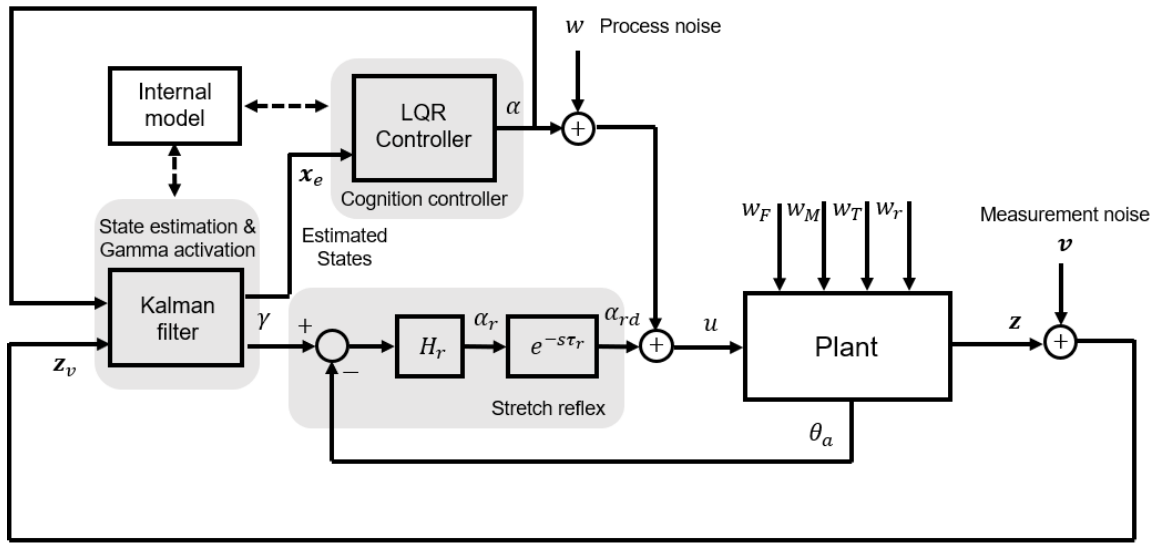

Figure 3.2: Schematic diagram of the linear driver-steering-vehicle model. Disturbance signals are input as white noise w_F, w_M, w_T and w_r then filtered in the plant. The plant input α and outputs $\boldsymbol{z}$ are perturbed with process and measurement noise w and $\boldsymbol{v}$, so a Kalman filter estimates the plant states $\boldsymbol{x_e}$. An LQR controller computes an optimal plant input α.

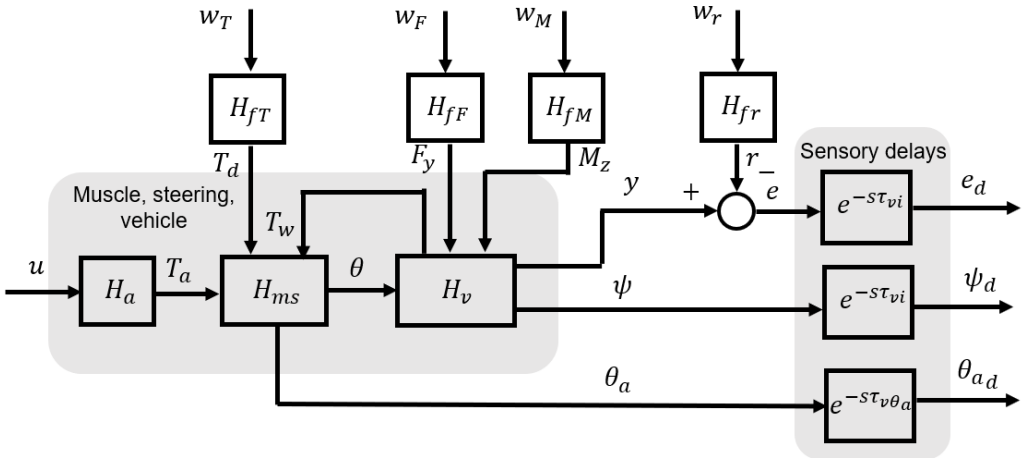

Figure 3.3: Structure of plant in the new driver-steering-vehicle model. The plant describes the dynamics controlled by the human driver, including muscle activation H_a, muscle and steering dynamics H_{ms}, vehicle dynamics H_v, human sensory delays and disturbance filters H_{fT}, H_{fF}, H_{fM} and H_{fr}.

3.2.1 Vehicle Model

The vehicle dynamics H_v are represented using the two degree-of-freedom lateral-yaw single-track 'bicycle' model moving at a constant speed for simplicity, as shown in Figure 3.4. The model captures the two dominating motions, that is, vehicle yaw and lateral motions, with lateral velocity v measured along the lateral axis of the vehicle to the centre of mass of the vehicle and yaw rate ω defined with respect to ground. The yaw angle ψ is defined as the angle between the longitudinal axis of the vehicle and the global x-axis. δ is the front tyres steer angle. The roll and pitch effects of the vehicle are not modelled.

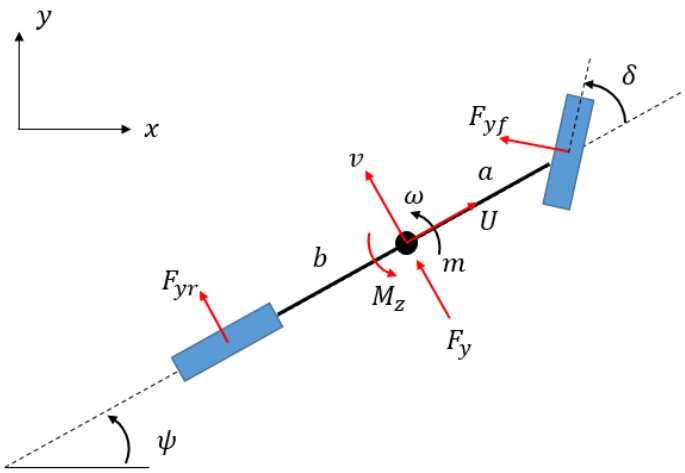

Figure 3.4: The two degree-of-freedom lateral-yaw vehicle model with disturbance force and moment.

For constant longitudinal speed and small-angle assumptions, the equations of motion of the vehicle model are:

$$m\big(\dot{v}(t) + U\omega(t)\big) = F_{yf}(t) + F_{yr}(t) + F_y(t) \tag{3.1}$$

$$I\dot{\omega}(t) = aF_{yf}(t) - bF_{yr}(t) + M_z(t) \tag{3.2}$$

where U denotes the constant longitudinal speed of the vehicle, m and I denote the vehicle mass and yaw moment of inertia, respectively. a and b denote the distance of front and rear tyres from the centre of mass of the vehicle, respectively. F_{yf} and F_{yr} are front and rear tyre forces acting on the vehicle lateral axis. A lateral force F_y and a yaw moment M_z applied at the centre of mass of the vehicle act as disturbances, such as might arise from road roughness or wind gusts. For the on-centre regime of operation considered, the lateral tyre forces F_{yf} and F_{yr} are assumed to be proportional to tyre slip angles. Therefore, the lateral forces of the front and rear tyres are:

$$F_{yf}(t) = 2C_f\left(\delta(t) - \frac{v(t) + a\omega(t)}{U}\right) \tag{3.3}$$

$$F_{yr} = 2C_r\left(-\frac{v(t) - b\omega(t)}{U}\right) \tag{3.4}$$

where C_f and C_r are constant cornering stiffness of each front tyre and each rear tyre, respectively. The continuous-time state-space equations of the vehicle model are:

$$\begin{Bmatrix} \dot{y}(t) \\ \dot{v}(t) \\ \dot{\psi}(t) \\ \dot{\omega}(t) \end{Bmatrix} = \begin{bmatrix} 0 & 1 & U & 0 \\ 0 & -\frac{2C_f + 2C_r}{mU} & 0 & -U - \frac{2C_f a - 2C_r b}{mU} \\ 0 & 0 & 0 & 1 \\ 0 & -\frac{2C_f a - 2C_r b}{IU} & 0 & -\frac{2a^2 C_f + 2b^2 C_r}{IU} \end{bmatrix} \begin{Bmatrix} y(t) \\ v(t) \\ \psi(t) \\ \omega(t) \end{Bmatrix}$$
$$+ \begin{bmatrix} 0 & 0 & 0 \\ \frac{2C_f}{m} & \frac{1}{m} & 0 \\ 0 & 0 & 0 \\ \frac{2C_f a}{I} & 0 & \frac{1}{I} \end{bmatrix} \begin{Bmatrix} \delta(t) \\ F_y(t) \\ M_z(t) \end{Bmatrix} \tag{3.5}$$

3.2.2 Muscle Dynamics and Steering Model

The muscle dynamics and the steering system are strongly coupled by the torques and angles exchanged through the steering wheel, so they are modelled together as H_{ms}, with the structure shown in Figure 3.5. The steering dynamics with an assist torque are represented by a two degree-of-freedom system, with the steering wheel angle denoted as θ_{sw} and the steering column angle denoted as θ_c. The linear steering dynamics interact with the driver through the introduction of the muscle angle of the arms θ_a, which is the angle between the active elements of the muscle and the tendon, and results from muscle activation driven by neurons. The inertia of the rack and the front wheels referred to the pinion is denoted by I_c. This inertia is connected to the vehicle ground by a torsional stiffness k_{sw} that represents self-centering stiffness (typically arising from the tyre forces acting through the steering geometry) and a parallel torsional damping term c_{sw} that represents damping in the steering mechanism with respect to the steering wheel axis. The inertia of the steering handwheel is denoted as I_{sw} and the inertia of the driver's arm I_{arm} is assumed to be rigidly connected to the steering wheel, which is denoted by the dashed line between I_{arm} and I_{sw}. The resulting summation of the inertia of the arms I_{arm} and the inertia of the steering wheel I_{sw} are connected with the inertia of the rack and the front wheels I_c by steering column with stiffness k_t and a torsion bar with damping c_t in parallel. Moreover, any additional stiffness and damping effects that may result from the steering mechanism referred to the steering wheel are represented by k_{hw} and c_{hw}.

The muscle dynamics considers both the muscle activation and intrinsic dynamics [103]. The mechanical response of the muscle due to change in the steering wheel angle and from muscle activation

torque is represented by a linearized Hill's muscle model [121], which is a series combination of a contractile element (parallel combination of torque from the muscle activation signal T_a and a dashpot c_a which resists stretching of the muscle fibre) and spring k_a representing the elasticity of the tendons. The details of the generation of muscle activation signal T_a are described in later sections. The internal stiffness and damping of the muscles and joints, which are known as muscle intrinsic properties, are represented by k_p and c_p, respectively.

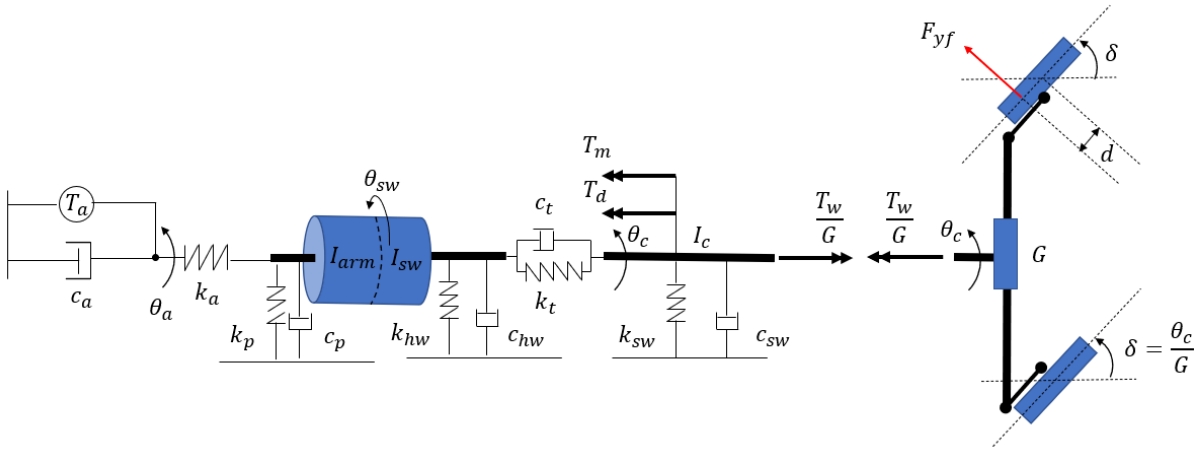

Figure 3.5: Muscle and steering system model with steering column torque disturbance. The springs and dampers act in rotation.

The equations of motion of the muscle dynamics and steering model are:

$$T_a(t) = c_a\dot{\theta}_a(t) + k_a\big(\theta_a(t) - \theta_{sw}(t)\big) \tag{3.6}$$

$$\begin{aligned} &k_a\big(\theta_a(t) - \theta_{sw}(t)\big) - c_t\left(\dot{\theta}_{sw}(t) - \dot{\theta}_c(t)\right) - k_t\big(\theta_{sw}(t) - \theta_c(t)\big) \\ &\qquad = (I_{sw} + I_{arm})\ddot{\theta}_{sw}(t) + \big(c_{hw} + c_p\big)\dot{\theta}_{sw}(t) + \big(k_{hw} + k_p\big)\theta_{sw}(t) \end{aligned} \tag{3.7}$$

$$\begin{aligned} &T_d(t) + c_t\big(\dot{\theta}_{sw}(t) - \dot{\theta}_c(t)\big) + k_t(\theta_{sw}(t) - \theta_c(t)) + T_m(t) - \frac{T_w(t)}{G} \\ &\qquad = I_c\ddot{\theta}_c(t) + c_{sw}\dot{\theta}_c(t) + k_{sw}\theta_c(t) \end{aligned} \tag{3.8}$$

Besides the torque applied by the arm muscles due to muscle activation, the steering model includes the self-aligning moment T_w, the torque input from the driving assist system T_m and the equivalent steering column torque disturbance resulting from the rack. The self-aligning moment T_w due to the torque generated about the king-pin axes by the lateral axle force is given by:

$$T_w(t) = F_{yf}(t)d \tag{3.9}$$

where the front tyre trail distance, consisting of both the pneumatic and mechanical trail, is denoted by d. The assist torque applied at the steering column T_m by the driving assist system, assumed to be based on a linear boost curve with boost coefficient C_{boost}, is given by:

$$T_m(t) = C_{boost}c_t\left(\dot{\theta}_{sw}(t) - \dot{\theta}_c(t)\right) + C_{boost}k_t(\theta_{sw}(t) - \theta_c(t)) \tag{3.10}$$

Finally, the steering gear ratio G transforms the steering column angle into the front tyre steering angle by:

$$\delta(t) = \frac{\theta_c(t)}{G} \tag{3.11}$$

Therefore, the continuous-time state-space equations of the muscle-steering-vehicle are:

$$\begin{Bmatrix} \dot{y}(t) \\ \dot{v}(t) \\ \dot{\psi}(t) \\ \dot{\omega}(t) \\ \dot{\theta}_{sw}(t) \\ \ddot{\theta}_{sw}(t) \\ \dot{\theta}_c(t) \\ \ddot{\theta}_c(t) \\ \dot{\theta}_a(t) \end{Bmatrix} = \begin{bmatrix} 0 & 1 & U & 0 & 0 & 0 & 0 & 0 & 0 \\ 0 & -\frac{2C_f + 2C_r}{mU} & 0 & -U - \frac{2C_f a - 2C_r b}{mU} & 0 & 0 & \frac{2C_f}{Gm} & 0 & 0 \\ 0 & 0 & 0 & 1 & 0 & 0 & 0 & 0 & 0 \\ 0 & -\frac{2C_f a - 2C_r b}{IU} & 0 & -\frac{2a^2C_f + 2b^2C_r}{IU} & 0 & 0 & \frac{2C_f a}{GI} & 0 & 0 \\ 0 & 0 & 0 & 0 & 0 & 1 & 0 & 0 & 0 \\ 0 & 0 & 0 & 0 & F_2 & F_3 & F_4 & F_5 & F_1 \\ 0 & 0 & 0 & 0 & 0 & 0 & 0 & 1 & 0 \\ 0 & G_1 & 0 & G_2 & G_3 & G_4 & G_5 & G_6 & 0 \\ 0 & 0 & 0 & 0 & \frac{k_a}{c_a} & 0 & 0 & 0 & -\frac{k_a}{c_a} \end{bmatrix} \begin{Bmatrix} y(t) \\ v(t) \\ \psi(t) \\ \omega(t) \\ \theta_{sw}(t) \\ \dot{\theta}_{sw}(t) \\ \theta_c(t) \\ \dot{\theta}_c(t) \\ \theta_a(t) \end{Bmatrix} + \begin{bmatrix} 0 & 0 & 0 & 0 \\ 0 & \frac{1}{m} & 0 & 0 \\ 0 & 0 & 0 & 0 \\ 0 & 0 & \frac{1}{I} & 0 \\ 0 & 0 & 0 & 0 \\ 0 & 0 & 0 & 0 \\ 0 & 0 & 0 & 0 \\ 0 & 0 & 0 & \frac{1}{I_c} \\ 0 & 0 & 0 & 0 \end{bmatrix} \begin{Bmatrix} T_a(t) \\ F_y(t) \\ M_z(t) \\ T_d(t) \end{Bmatrix} \tag{3.12}$$

$$\begin{Bmatrix} y(t) \\ \psi(t) \\ \theta_a(t) \end{Bmatrix} = \begin{bmatrix} 1 & 0 & 0 & 0 & 0 & 0 & 0 & 0 & 0 \\ 0 & 0 & 1 & 0 & 0 & 0 & 0 & 0 & 0 \\ 0 & 0 & 0 & 0 & 0 & 0 & 0 & 0 & 1 \end{bmatrix} \begin{Bmatrix} y(t) \\ v(t) \\ \psi(t) \\ \omega(t) \\ \theta(t) \\ \dot{\theta}(t) \\ \theta_c(t) \\ \dot{\theta}_c(t) \\ \theta_a(t) \end{Bmatrix} \tag{3.13}$$

where $G_1 = \frac{2C_f d}{GUI_c}$, $G_2 = \frac{2C_f ad}{GUI_c}$, $G_3 = \frac{(1+C_{boost})k_t}{I_c}$, $G_4 = \frac{(1+C_{boost})c_t}{I_c}$, $G_5 = -\left[\frac{(1+C_{boost})k_t+k_{sw}}{I_c} + \frac{2C_f d}{G^2 I_c}\right]$, $G_6 = -\frac{(1+C_{boost})c_t+c_{sw}}{I_c}$, $F_1 = \frac{k_a}{I_{arm}+I_{sw}}$, $F_2 = -\frac{k_a+k_{hw}+k_p+k_t}{I_{arm}+I_{sw}}$, $F_3 = -\frac{c_{hw}+c_p+c_t}{I_{arm}+I_{sw}}$, $F_4 = \frac{k_t}{I_{arm}+I_{sw}}$, $F_5 = \frac{c_t}{I_{arm}+I_{sw}}$

Converted to discrete-time state-space equations with sample time T_s, the above equations become:

$$\boldsymbol{x}_{msv}(k+1) = \mathbf{A}_{msv}\boldsymbol{x}_{msv}(k) + \mathbf{B}_{msv}\{T_a(k) \quad F_y(k) \quad M_z(k) \quad T_d(k)\}^T \tag{3.14}$$

$$\{y(k) \quad \psi(k) \quad \theta_a(k)\}^T = \mathbf{C}_{msv}\boldsymbol{x}_{msv}(k) \tag{3.15}$$

3.2.3 Muscle Activation

The muscle activation signal T_a arises from the neural activation of the muscle [103]. There are two processes associated with the activation process block H_a shown in Figure 3.3. Activation begins with a signal u sent to alpha motor neurons in the spine that in turn activate the muscle fibres. The dynamics associated with the motor neurons are represented by a first-order lag with time constant τ_1, normally in the range 20-50ms [17]. There is also a lag associated with the activation and deactivation of the muscle fibres. Previous twitch tests found that depending on the muscle size, the activation time constant is 5-15ms, while the deactivation time constant is typically in the range 20-60ms [17]. Cole [103] mentioned that it is a necessary approximation for a linear model that a single first-order lag with a time constant τ_2 is used for both activation and deactivation of muscle fibres. The series combination of the two first-order lags forms the H_a block shown in Figure 3.3. Therefore, the muscle activation torque T_a relating the signal u is given by the transfer function:

$$H_a(s) = \frac{1}{(\tau_1 s + 1)(\tau_2 s + 1)} \tag{3.16}$$

Converted to state-space form, the muscle activation block H_a is:

$$\begin{Bmatrix} \dot{x}_{H_a}(t) \\ \dot{T}_a(t) \end{Bmatrix} = \begin{bmatrix} 0 & -\frac{1}{\tau_1\tau_2} \\ 1 & -\frac{\tau_1+\tau_2}{\tau_1\tau_2} \end{bmatrix} \begin{Bmatrix} x_{H_a}(t) \\ T_a(t) \end{Bmatrix} + \begin{bmatrix} \frac{1}{\tau_1\tau_2} \\ 0 \end{bmatrix} u(t) \tag{3.17}$$

$$T_a(t) = [0 \quad 1] \begin{Bmatrix} x_{H_a}(t) \\ T_a(t) \end{Bmatrix} \tag{3.18}$$

Written in matrix notations and converted to discrete-time with sample time T_s, the above state-space equations become:

$$\boldsymbol{x}_a(k+1) = \mathbf{A}_a \boldsymbol{x}_a(k) + \mathbf{B}_a u(k) \tag{3.19}$$

$$T_a(k) = \mathbf{C}_a \boldsymbol{x}_a(k) \tag{3.20}$$

3.2.4 Sensory Systems

Various sensory systems are used by the driver to infer the states of the vehicle and its surrounding. The main senses used by the driver in the steering control task are the visual system, the vestibular system and the somatosensors [109]. A minimal set of human sensory measurements is assumed for visual perception organs and the proprioceptors; the modelling of the vestibular organs is considered out of the scope of the research. The visual system is not only used for detecting the target path, but also used in perceiving self-motion of the vehicle relative to the surrounding environment. In this work, the perceived states by the visual system are the vehicle lateral deviation with respect the randomly moving target path e and the yaw angle of the vehicle ψ. Proprioceptors are a subset of somatosensors and are used for sensing the motion and forces of the joints and muscle, which is an important means the driver has to sense the angle and torque of the steering wheel resulting from the steering dynamics and the contact between the front tyres and the road. In this work, the muscle angle θ_a is included as another measurement. The perceived states are subject to a visual delay τ_{vi} and a muscle sensory delay $\tau_{v\theta_a}$, consisting of $N_{vi} = \tau_{vi}/T_s$ and $N_{v\theta_a} = \tau_{v\theta_a}/T_s$ time steps, respectively. The time delay of cognitive processing is assumed to be lumped together with the sensory delays and not modelled separately. The sensory delays in Figure 3.3 are implemented using shift registers. The delayed values of the vehicle lateral deviation with respect to the randomly moving target path e_d are found by (3.21) and (3.22) as an example.

$$\begin{Bmatrix} e(k) \\ \vdots \\ e(k-N_{vi}+1) \end{Bmatrix} = \begin{bmatrix} \mathbf{0}_{[1,N_{vi}-1]} & 0 \\ \mathbf{I}_{[N_{vi}-1,N_{vi}-1]} & \mathbf{0}_{[N_{vi}-1,1]} \end{bmatrix} \begin{Bmatrix} e(k-1) \\ \vdots \\ e(k-N_{vi}) \end{Bmatrix} + \begin{bmatrix} 1 \\ \mathbf{0}_{[N_{vi}-1,1]} \end{bmatrix} e(k) \tag{3.21}$$

$$e(k-N_{vi}) = [\mathbf{0}_{[1,N_{vi}-1]} \quad 1] \begin{Bmatrix} e(k-1) \\ \vdots \\ e(k-N_{vi}) \end{Bmatrix} \tag{3.22}$$

where **I** is the identity matrix, **0** is a matrix of zeros, and $\mathbf{M}_{[i,j]}$ is a matrix with i rows and j columns. Converted to discrete-time state-space equations with sample time T_s, the above equations become:

$$\boldsymbol{x}_{\tau e}(k+1) = \mathbf{A}_{\tau vi}\boldsymbol{x}_{\tau e}(k) + \mathbf{B}_{\tau vi}e(k) \tag{3.23}$$

$$e(k - N_{vi}) = \mathbf{C}_{\tau vi}\boldsymbol{x}_{\tau e}(k) \tag{3.24}$$

Similarly, delayed values of vehicle yaw angle ψ and muscle angle θ_a are given by the following discrete-time state-space equations:

$$\boldsymbol{x}_{\tau\psi}(k+1) = \mathbf{A}_{\tau vi}\boldsymbol{x}_{\tau\psi}(k) + \mathbf{B}_{\tau vi}\psi(k) \tag{3.23}$$

$$\psi(k - N_{vi}) = \mathbf{C}_{\tau vi}\boldsymbol{x}_{\tau\psi}(k) \tag{3.24}$$

$$\boldsymbol{x}_{\tau\theta_a}(k+1) = \mathbf{A}_{\tau\theta_a}\boldsymbol{x}_{\tau\theta_a}(k) + \mathbf{B}_{\tau\theta_a}\theta_a(k) \tag{3.25}$$

$$\theta_a\left(k - N_{v\theta_a}\right) = \mathbf{C}_{\tau\theta_a}\boldsymbol{x}_{\tau\theta_a}(k) \tag{3.26}$$

The perceived states of the vehicle and its surrounding by the sensory system are then sent to the central nervous system (CNS), subject to measurement noise. These noisy signals are used to estimate the states of the plant. The detailed derivation of the state estimator is presented in later sections.

3.2.5 Disturbance Filtering

The steering task described by the model is mentioned in the preamble of Section 3.2. The vehicle moves at constant longitudinal speed U and the driver is asked to follow a randomly moving target path while compensating for disturbances acting on the steering-vehicle system, as shown in Figure 3.3. The target r and disturbances T_d, F_y and M_z are generated by filtering Gaussian white noise to ensure that the closed-loop driver-steering-vehicle system is not excited beyond the frequencies of interest [20]. White noise signals w_r w_F, w_M and w_T are generated in discrete time by choosing random numbers from a zero-mean normal distribution. The corresponding variances W_r^2 W_F^2, W_M^2 and W_T^2 of the signals could be adjusted based on different simulation conditions. Specifically, vehicle lateral force disturbance F_y, vehicle yaw moment disturbance M_z and steering column torque disturbance T_d are generated by passing the noise inputs through second-order low pass filters with a cut-off frequency f_{cF}, f_{cM} and f_{cT}, respectively. The second-order low pass filter described by (3.27) is shown as an example.

$$H_{fF}(s) = \left(\frac{f_{cF}}{s + f_{cF}}\right)^2 \tag{3.27}$$

Converted to state-space form, the low pass filter H_{fF} is:

$$\begin{Bmatrix} \dot{x}_{H_{fF}}(t) \\ \dot{F}_y(t) \end{Bmatrix} = \begin{bmatrix} 0 & -f_{cF}^2 \\ 1 & -2f_{cF} \end{bmatrix} \begin{Bmatrix} x_{H_{fF}}(t) \\ F_y(t) \end{Bmatrix} + \begin{bmatrix} f_{cF}^2 \\ 0 \end{bmatrix} w_F(t) \tag{3.28}$$

$$F_y(t) = [0 \quad 1] \begin{Bmatrix} x_{H_{fF}}(t) \\ F_y(t) \end{Bmatrix} \tag{3.29}$$

Written in matrix notations and converted to discrete-time with sample time T_s, the above state-space equations become:

$$\boldsymbol{x}_{fF}(k+1) = \mathbf{A}_{fF}\boldsymbol{x}_{fF}(k) + \mathbf{B}_{fF}w_F(k) \tag{3.30}$$

$$F_y(k) = \mathbf{C}_{fF}\boldsymbol{x}_{fF}(k) \tag{3.31}$$

Similarly, the other second-order low pass filters H_{fM} and H_{fT} are given by:

$$\boldsymbol{x}_{fM}(k+1) = \mathbf{A}_{fM}\boldsymbol{x}_{fM}(k) + \mathbf{B}_{fM}w_M(k) \tag{3.32}$$

$$M_z(k) = \mathbf{C}_{fF}\boldsymbol{x}_{fM}(k) \tag{3.33}$$

$$\boldsymbol{x}_{fT}(k+1) = \mathbf{A}_{fT}\boldsymbol{x}_{fT}(k) + \mathbf{B}_{fT}w_T(k) \tag{3.34}$$

$$T_d(k) = \mathbf{C}_{fT}\boldsymbol{x}_{fT}(k) \tag{3.35}$$

The random target path r is generated by passing the noise input w_r through a function combining a second-order low-pass filter with a cut-off frequency f_{rl} and a second-order high-pass filter with a cut-off frequency f_{rh} [20]:

$$H_{fr}(s) = \left(\frac{s}{s+f_{rh}}\right)^2 \left(\frac{f_{rl}}{s+f_{rl}}\right)^2 \tag{3.36}$$

Similarly, converted to discrete-time state-space form, the filter H_{fr} becomes:

$$\boldsymbol{x}_{fr}(k+1) = \mathbf{A}_{fr}\boldsymbol{x}_{fr}(k) + \mathbf{B}_{fr}w_r(k) \tag{3.37}$$

$$r(k) = \mathbf{C}_{fr}\boldsymbol{x}_{fr}(k) \tag{3.38}$$

3.2.6 Complete Plant

Combining blocks developed from Section 3.2.1 to 3.2.5 gives the complete plant, written in the discrete-time state-space form:

$$\begin{aligned} \boldsymbol{x}(k+1) &= \mathbf{A}\boldsymbol{x}(k) + \mathbf{B}\alpha(k) \\ &\quad + [\mathbf{B} \quad \mathbf{G}_r \quad \mathbf{G}_F \quad \mathbf{G}_M \quad \mathbf{G}_T]\{w(k) \quad w_r(k) \quad w_F(k) \quad w_M(k) \quad w_T(k)\}^T \end{aligned} \tag{3.39}$$

$$\boldsymbol{z}(k) = \mathbf{C}\boldsymbol{x}(k) \tag{3.40}$$

where $\boldsymbol{x}(k) =$

$\{\boldsymbol{x}_{fr}(k) \quad \boldsymbol{x}_{fF}(k) \quad \boldsymbol{x}_{fM}(k) \quad \boldsymbol{x}_{fT}(k) \quad \boldsymbol{x}_{msv}(k) \quad \boldsymbol{x}_{a}(k) \quad \boldsymbol{x}_{\tau\psi}(k) \quad \boldsymbol{x}_{\tau\theta_a}(k) \quad \boldsymbol{x}_{\tau e}(k)\}^T,$

$\boldsymbol{z}(k) = \left\{e(k - N_{vi}) \quad \psi(k - N_{vi}) \quad \theta_a\left(k - N_{v\theta_a}\right)\right\}^T,$

$$\mathbf{A} = \begin{bmatrix} \mathbf{A}_{fr} & \mathbf{0} & \mathbf{0} & \mathbf{0} & \mathbf{0} & \mathbf{0} & \mathbf{0} & \mathbf{0} & \mathbf{0} \\ \mathbf{0} & \mathbf{A}_{fF} & \mathbf{0} & \mathbf{0} & \mathbf{0} & \mathbf{0} & \mathbf{0} & \mathbf{0} & \mathbf{0} \\ \mathbf{0} & \mathbf{0} & \mathbf{A}_{fM} & \mathbf{0} & \mathbf{0} & \mathbf{0} & \mathbf{0} & \mathbf{0} & \mathbf{0} \\ \mathbf{0} & \mathbf{0} & \mathbf{0} & \mathbf{A}_{fT} & \mathbf{0} & \mathbf{0} & \mathbf{0} & \mathbf{0} & \mathbf{0} \\ \mathbf{0} & \mathbf{B}_{msv(:,2)}\mathbf{C}_{fF} & \mathbf{B}_{msv(:,3)}\mathbf{C}_{fM} & \mathbf{B}_{msv(:,4)}\mathbf{C}_{fT} & \mathbf{A}_{msv} & \mathbf{B}_{msv(:,1)}\mathbf{C}_{a} & \mathbf{0} & \mathbf{0} & \mathbf{0} \\ \mathbf{0} & \mathbf{0} & \mathbf{0} & \mathbf{0} & \mathbf{0} & \mathbf{A}_{a} & \mathbf{0} & \mathbf{0} & \mathbf{0} \\ \mathbf{0} & \mathbf{0} & \mathbf{0} & \mathbf{0} & \mathbf{B}_{\tau vi}\mathbf{C}_{msv(2,:)} & \mathbf{0} & \mathbf{A}_{\tau vi} & \mathbf{0} & \mathbf{0} \\ \mathbf{0} & \mathbf{0} & \mathbf{0} & \mathbf{0} & \mathbf{B}_{\tau\theta_a}\mathbf{C}_{msv(3,:)} & \mathbf{0} & \mathbf{0} & \mathbf{A}_{\tau\theta_a} & \mathbf{0} \\ -\mathbf{B}_{\tau vi}\mathbf{C}_{fr} & \mathbf{0} & \mathbf{0} & \mathbf{0} & \mathbf{B}_{\tau vi}\mathbf{C}_{msv(1,:)} & \mathbf{0} & \mathbf{0} & \mathbf{0} & \mathbf{A}_{\tau vi} \end{bmatrix}$$

$\mathbf{B} = [\mathbf{0} \quad \mathbf{0} \quad \mathbf{0} \quad \mathbf{0} \quad \mathbf{0} \quad \boldsymbol{B}_a \quad \mathbf{0} \quad \mathbf{0} \quad \mathbf{0}]^T$

$\mathbf{G}_r = [\mathbf{B}_{fr} \quad \mathbf{0} \quad \mathbf{0} \quad \mathbf{0} \quad \mathbf{0} \quad \mathbf{0} \quad \mathbf{0} \quad \mathbf{0} \quad \mathbf{0}]^T$

$\mathbf{G}_F = [\mathbf{0} \quad \mathbf{B}_{fF} \quad \mathbf{0} \quad \mathbf{0} \quad \mathbf{0} \quad \mathbf{0} \quad \mathbf{0} \quad \mathbf{0} \quad \mathbf{0}]^T$

$\mathbf{G}_M = [\mathbf{0} \quad \mathbf{0} \quad \mathbf{B}_{fM} \quad \mathbf{0} \quad \mathbf{0} \quad \mathbf{0} \quad \mathbf{0} \quad \mathbf{0} \quad \mathbf{0}]^T$

$\mathbf{G}_T = [\mathbf{0} \quad \mathbf{0} \quad \mathbf{0} \quad \mathbf{B}_{fT} \quad \mathbf{0} \quad \mathbf{0} \quad \mathbf{0} \quad \mathbf{0} \quad \mathbf{0}]^T$

$$\mathbf{C} = \begin{bmatrix} \mathbf{0} & \mathbf{0} & \mathbf{0} & \mathbf{0} & \mathbf{0} & \mathbf{0} & \mathbf{0} & \mathbf{0} & \mathbf{C}_{\tau vi} \\ \mathbf{0} & \mathbf{0} & \mathbf{0} & \mathbf{0} & \mathbf{0} & \mathbf{0} & \mathbf{C}_{\tau vi} & \mathbf{0} & \mathbf{0} \\ \mathbf{0} & \mathbf{0} & \mathbf{0} & \mathbf{0} & \mathbf{0} & \mathbf{0} & \mathbf{0} & \mathbf{C}_{\tau\theta_a} & \mathbf{0} \end{bmatrix},$$

$\mathbf{0}$ is a matrix of zeros, $\mathbf{M}_{(i,j)}$ indicates the ith row and jth column of matrix $\mathbf{M}$ and ':' represents the entire row or column of the matrix.

3.2.7 Stretch Reflex Control

The muscle activation is considered to come from the alpha motor neurons in the spine. The alpha motor neurons receive signals from two main sources [103]. Signals can be sent directly from the motor cortex in the brain; in Figure 3.2 this signal is labelled α. In addition, the alpha motor neurons can be signalled by the reflex action, which is predominantly a closed-loop feedback control of muscle length known as the stretch reflex. Gamma motor neurons in the spine activate special fibres in the muscle called spindles. The gamma motor neurons adjust the length of the spindles according to the muscle displacement angle (or steering wheel angle) expected by the brain. If the muscle angle differs from the expected angle, the spindles are strained and send a signal to the alpha motor neurons, activating the muscle to achieve the

expected muscle angle. The function of the muscle spindles is represented in Figure 3.2 by the summation circle, which calculates the difference between the expected angle γ and the actual angle θ_a. The generation of the expected muscle angle γ is presented in later sections. The difference is then operated upon by a reflex gain block H_r and a delay block D_r before activating the muscle via the alpha motor neuron.

In this work, the reflex behaviour is modelled to be sensitive to muscle displacement angle; therefore, the reflex gain block H_r contains a stiffness gain k_r. The reflex delay is primarily a function of neural conduction velocities and the distance of the muscle from the motor neurons in the spine. It is modelled as a discrete-time shift register with a parameter τ_r representing the delay time, consisting of $N_r = \tau_r/T_s$ time steps.

$$\begin{Bmatrix} \alpha_r(k) \\ \vdots \\ \alpha_r(k-N_r+1) \end{Bmatrix} = \begin{bmatrix} \mathbf{0}_{[1,N_r-1]} & 0 \\ \mathbf{I}_{[N_r-1,N_r-1]} & \mathbf{0}_{[N_r-1,1]} \end{bmatrix} \begin{Bmatrix} \alpha_r(k-1) \\ \vdots \\ \alpha_r(k-N_r) \end{Bmatrix} + \begin{bmatrix} 1 \\ \mathbf{0}_{[N_r-1,1]} \end{bmatrix} \alpha_r(k) \quad (3.41)$$

$$\alpha_{rd}(k) = \alpha_r(k-N_r) = [\mathbf{0}_{[1,N_{vi}-1]} \quad 1] \begin{Bmatrix} \alpha_r(k-1) \\ \vdots \\ \alpha_r(k-N_r) \end{Bmatrix} \quad (3.42)$$

Converted to discrete-time state-space equations with sample time T_s, the above equations become:

$$\boldsymbol{x}_{\tau r}(k+1) = \mathbf{A}_{\tau r}\boldsymbol{x}_{\tau r}(k) + \mathbf{B}_{\tau r}k_r[\gamma(k) - \theta_a(k)] \quad (3.43)$$

$$\alpha_{rd}(k) = \mathbf{C}_{\tau r}\boldsymbol{x}_{\tau r}(k) \quad (3.44)$$

3.2.8 Kalman Filter for State Estimation and Gamma Activation

The optimal controller requires the full plant state vector $\boldsymbol{x}$ to calculate the optimal plant input. The sensory systems described in Section 3.2.4 provide the central nervous system (CNS) with measurements $\boldsymbol{z}$ of the plant, perturbed by measurement noise $\boldsymbol{v}$, and it is assumed that the CNS carries out sensory measurement integration using statistically optimal methods to estimate the states of the plant. Similar to the driver model developed by Nash and Cole [20], the process of estimating the states of the plant is represented by using a Kalman filter, based on an internal mental model of the plant derived in Section 3.2.6, the measurement of noise-free plant input α and noisy measurement $\boldsymbol{z} + \boldsymbol{v}$ of the plant. The theory of Kalman filtering is given by [122] [123]. Initially, an estimate of the states $\boldsymbol{x}_e(k+1|k)$ is predicted by propagating the current input $\alpha(k)$ and state estimate $\boldsymbol{x}_e(k)$ through the internal mental model of the plant:

$$\boldsymbol{x}_e(k+1|k) = \mathbf{A}\boldsymbol{x}_e(k) + \mathbf{B}\alpha(k) \quad (3.45)$$

A correction is then added based on the error between the previously estimated output $\mathbf{C}\boldsymbol{x}_e(k|k-1)$ and measured output $\boldsymbol{z}(k)+\boldsymbol{v}(k)$, weighted by the 'Kalman gain' $\mathbf{K}(k)$

$$\boldsymbol{x}_e(k)=\boldsymbol{x}_e(k|k-1)+\mathbf{K}(k)\{\boldsymbol{z}(k)+\boldsymbol{v}(k)-\mathbf{C}\boldsymbol{x}_e(k|k-1)\} \tag{3.46}$$

The time-varying Kalman gain $\mathbf{K}(k)$ is calculated to give a statistically optimal minimum-variance estimate based on the concept of 'maximum likelihood estimate' (MLE), weighting the estimates based on the covariances of the Gaussian noise w, w_r, w_F, w_M, w_T and $\boldsymbol{v}$. In this work, the covariances are assumed to be time-invariant. Therefore, a steady-state Kalman filter is implemented to estimate the states of the plant optimally. The estimate of the plant states $\boldsymbol{x}_e$ is given by:

$$\boldsymbol{x}_e(k+1|k)=[\mathbf{A}-\mathbf{LC}]\boldsymbol{x}_e(k|k-1)+[\mathbf{B}\quad\mathbf{L}]\begin{Bmatrix}\alpha(k)\\ \boldsymbol{z}(k)+\boldsymbol{v}(k)\end{Bmatrix} \tag{3.47}$$

$$\boldsymbol{x}_e(k)=[\mathbf{I}-\mathbf{M}_x\mathbf{C}]\boldsymbol{x}_e(k|k-1)+[\mathbf{0}\quad\mathbf{M}_x]\begin{Bmatrix}\alpha(k)\\ \boldsymbol{z}(k)+\boldsymbol{v}(k)\end{Bmatrix} \tag{3.48}$$

where gain matrix $\mathbf{L}$ and the innovation gains $\mathbf{M}_x$ and $\mathbf{M}_y$ are:

$$\mathbf{L}=\mathbf{APC}^T(\mathbf{CPC}^T+\mathbf{R}_{\mathrm{KF}})^{-1} \tag{3.49}$$

$$\mathbf{M}_x=\mathbf{PC}^T(\mathbf{CPC}^T+\mathbf{R}_{\mathrm{KF}})^{-1} \tag{3.50}$$

$$\mathbf{M}_y=\mathbf{CPC}^T(\mathbf{CPC}^T+\mathbf{R}_{\mathrm{KF}})^{-1} \tag{3.51}$$

and $\mathbf{P}$ is given by solving the following discrete Riccati equation:

$$\mathbf{A}^T\mathbf{PA}-\mathbf{P}-\mathbf{A}^T\mathbf{PC}(\mathbf{C}^T\mathbf{PC}+\boldsymbol{R}_{KF})^{-1}\mathbf{C}^T\mathbf{PA}+\widehat{\mathbf{Q}}_{\mathrm{KF}}=\mathbf{0} \tag{3.52}$$

where $\widehat{\mathbf{Q}}_{\mathrm{KF}}=[\mathbf{B}\quad\mathbf{G}_r\quad\mathbf{G}_F\quad\mathbf{G}_M\quad\mathbf{G}_T]\mathbf{Q}_{\mathrm{KF}}[\mathbf{B}\quad\mathbf{G}_r\quad\mathbf{G}_F\quad\mathbf{G}_M\quad\mathbf{G}_T]$

The process and measurement noise covariance matrices $\mathbf{Q}_{\mathrm{KF}}$ and $\mathbf{R}_{\mathrm{KF}}$ are given by:

$$\mathbf{Q}_{\mathrm{KF}}=\mathrm{diag}([W^2\quad W_r^2\quad W_F^2\quad W_M^2\quad W_T^2]) \tag{3.53}$$

$$\mathbf{R}_{\mathrm{KF}}=\mathrm{diag}\left(\left[V_e^2\quad V_\psi^2\quad V_{\theta_a}^2\right]\right) \tag{3.54}$$

where W^2 denotes the variance of the process noise w, W_r^2 W_F^2, W_M^2 and W_T^2 denote the variances of the disturbances w_r, w_F, w_M and w_T, respectively, and V_e^2, V_ψ^2 and $V_{\theta_a}^2$ denote the variances of the measurement noise added to the plant outputs e, ψ, and θ_a, respectively.

The generation of the expected muscle angle, labelled as γ in Figure 3.2, is known as gamma activation, which is also based on an internal mental model of the plant derived in Section 3.2.6. Specifically, the expected muscle angle γ is calculated by processing the internal mental model of the plant forwardly

with the current input $\alpha(k)$ and state estimate $\boldsymbol{x}_e(k)$, which is essentially the prediction step of Kalman filter. Therefore, the gamma activation process is incorporated into the Kalman filter.

As mentioned in Chapter 2, a neuroscience study conducted by Blakemore [118] into tickliness found that as the discrepancy between predicted and actual sensory feedback increases, there is a concomitant decrease in the level of subjective satisfaction. Compared with the theory of Kalman filter, this discrepancy is reflected by the prediction error $\boldsymbol{z}(k) + \boldsymbol{v}(k) - \mathbf{C}\boldsymbol{x}_e(k|k-1)$. Therefore, the Kalman filtering theory provides the new driver-steering-vehicle model with the possibility of predicting the human driver's subjective assessment of steering feel. Specifically, it is hypothesised that subjective rating of steering feel is related to the driver's ability to predict the steering torque feedback using their internal model and their known control inputs. A larger error means that steering feel is subjectively worse. This hypothesis is tested in Chapter 6.

3.2.9 Cognitive Controller

Similar to the driver model developed by Nash and Cole [20], for the linear plant derived in Section 3.2.6, a linear quadratic regulator (LQR) optimal controller is used to represent the driver's cognitive control behaviour to follow the randomly moving target path based on the same internal mental model as the one in state estimation and gamma activation. The effect of cognitive delay is accounted for in the sensory delay blocks and thus is not considered in this section.

In the LQR algorithm, a gain vector $\mathbf{K}_{\mathrm{LQ}}$ processing the estimated plant states $\boldsymbol{x}_e$ is calculated based on the minimisation of a cost function J to generate an optimal control action α. The additive Gaussian white noise w_r w_F, w_M and w_T are not considered since these are not driver control actions. In this work, it is assumed that the driver aligns a different part of the vehicle with the randomly moving target path instead of the centre of vehicle, as illustrated in Figure 3.6. A time shift constant T_t is included in the model to account for this effect and therefore the cost function J includes costs on the shifted lateral deviation of the vehicle from the target path and the plant input α and weights the two terms by q_e and q_α, respectively:

$$J = \sum_{k=0}^{\infty} \{q_e[y(k) - r(k) + U\psi(t)T_t]^2 + q_\alpha \alpha(k)^2\}$$

$$= \sum_{k=0}^{\infty} \left\{\boldsymbol{x}(k)^T \mathbf{Q}_{\mathrm{LQ}} \boldsymbol{x}(k) + \alpha(k)^T \mathbf{R}_{\mathrm{LQ}} \alpha(k)\right\} \tag{3.55}$$

where

$$\mathbf{Q}_{\mathrm{LQ}} = \mathbf{H}^T q_e \mathbf{H} \tag{3.56}$$

$$\mathbf{H} = \begin{bmatrix} \mathbf{C}_{fr} & \mathbf{0}_{[1,N_{fy}]} & \mathbf{0}_{[1,N_{fz}]} & \mathbf{0}_{[1,N_{fd}]} & 1\ 0\ UT_t & \mathbf{0}_{[1,N_{msv}-3]} & \mathbf{0}_{[1,N_{vi}]} & \mathbf{0}_{[1,N_{v\theta_a}]} & \mathbf{0}_{[1,N_{vi}]} \end{bmatrix} \quad (3.57)$$

$$\mathbf{R}_{\mathrm{LQ}} = q_\alpha \quad (3.58)$$

where $\mathbf{0}$ is a matrix of zeros, $\mathbf{M}_{[i,j]}$ is a matrix with i rows and j columns, N_i is the number of states in the state vector $\boldsymbol{x}_i(k)$. Several previous studies took account of vehicle yaw angle error in the cost function [89] [90], and it is also possible to include other elements such as the first derivative of the control action and the integral of tracking error. However, only two elements are considered here for simplicity. Different combinations of the values of the weightings can represent a range of driving strategies, in particular indicating the trade-off between the path-following accuracy and the control activity to accomplish a driving manoeuvre.

The time-invariant LQR control is of the form [90]:

$$\alpha(k) = -\mathbf{K}_{\mathrm{LQ}}\boldsymbol{x}_e(k) \quad (3.59)$$

where

$$\mathbf{K}_{\mathrm{LQ}} = \left(\mathbf{B}^T\mathbf{S}\mathbf{B} + \mathbf{R}_{\mathrm{LQ}}\right)^{-1}\mathbf{B}^T\mathbf{S}\mathbf{A} \quad (3.60)$$

and $\mathbf{S}$ is given by solving the following discrete Riccati equation:

$$\mathbf{A}^T\mathbf{S}\mathbf{A} - \mathbf{S} - \mathbf{A}^T\mathbf{S}\mathbf{B}\left(\mathbf{B}^T\mathbf{S}\mathbf{B} + \mathbf{R}_{\mathrm{LQ}}\right)^{-1}\mathbf{B}^T\mathbf{S}\mathbf{A} + \mathbf{Q}_{\mathrm{LQ}} = \mathbf{0} \quad (3.61)$$

Matlab's *dlqr* function can be used to evaluate $\mathbf{K}_{\mathrm{LQ}}$ given the costs and the plant being controlled by the human driver.

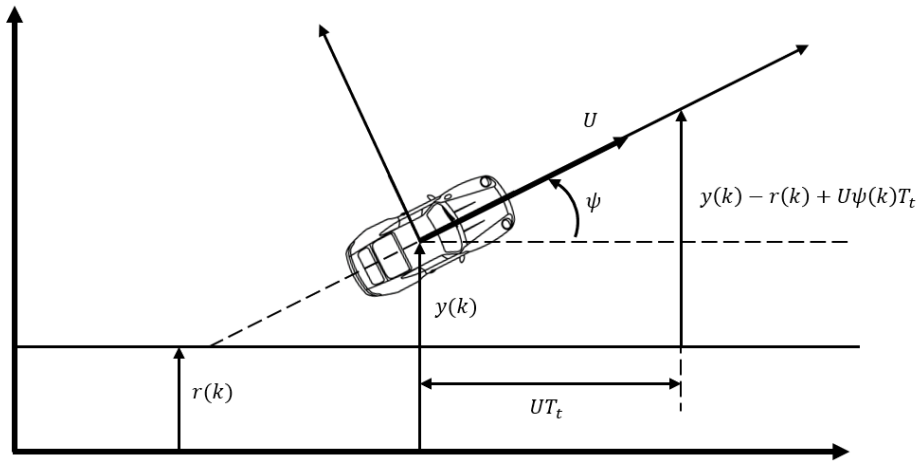

Figure 3.6: Geometry of driver's viewpoint, a different part of the vehicle is aligned with the randomly moving target path instead of the centre of vehicle.

3.2.10 Parameters of the Driver-Steering-Vehicle Model

In total, there are more than forty parameters in the closed-loop driver-steering-vehicle model, including the parameters of the vehicle model, the steering model, and the driver model. Explanations of how all the parameter values are determined are provided below.

Regarding the steering model and the vehicle model, most of these parameters are directly given by Toyota Motor Europe (TME) [124] with a small number of them are chosen based on the measured data provided by TME and preliminary stability analysis. More details of the justification of the chosen parameter values are given in Chapter 4. The amplitudes of the applied Gaussian white noise and their corresponding filters are given by the driving simulator experimental conditions described in Chapter 4. It is necessary to keep the steering and vehicle model identical to that used in the experiments.

It is assumed that the internal model exactly matches the actual plant controlled by the driver based on the findings from Nash and Cole [116] that the human driver is capable of obtaining an accurate model if the system dynamics are linear. The driver model parameters relate to the physical properties of the human driver, and therefore, most of the parameters of the driver model are identified using the experimental results. However, some of the parameters can be fixed in advance using data from the relevant literature. To be specific, the muscle activation blocks H_a consists of two time constants in the series of first-order lags τ_1 and τ_2. It has been found that these two time constants are independent of the muscle activation level [17], which means values of them are not affected by the states of the muscle, whether relaxed or tensed. Therefore, it is reasonable to fix their values. In this work, a value of 30ms is used for τ_1 and the value of τ_2 is chosen as 20ms, taking the advice of Cole [103]. The reflex delay is also not affected by the muscle activation level and is set to 40ms as suggested by Hoult [42]. The intrinsic dynamics is related to the flesh of arms, and the values of intrinsic stiffness k_p and damping c_p are simply set to $0\mathrm{Nm/rad}$ and $0\mathrm{Nms/rad}$, respectively, following the suggestions of Cole [103] because of the difficulty of identifying experimentally the separate contributions of the intrinsic, reflex and cognitive dynamics. The value of tendon stiffness k_a is set to $30\mathrm{Nm/rad}$ [121]. The values of the LQR controller cost function weightings allow the trade-off between path-following accuracy and control activity to be determined, and influence the path-following bandwidth of the driver model [17]. This means different driving styles of the driver could be represented by varying the weightings of the cognitive controller cost function. However, it is only the relative weightings that influence the controller performance. Therefore, q_e is fixed to $1\mathrm{m}^{-2}$ and q_α is varied. The names, symbols, units, and sources of the vehicle model parameters, the steering system parameters, the disturbance filters parameters and the fixed driver model parameters are summarised in Table 3.1. Except the parameters discussed above, various other parameters values must be found by fitting the model to experimental data using an identification procedure. The identified parameters are: the damping c_a resisting stretching of the muscle fibre, the arm inertia I_{arm}, the reflex controller gain k_r, the noise standard

deviation W, V_e, $V_\psi$and V_{θ_a}, the visual sensory delay τ_{vi}, the muscle angle sensory delay τ_{θ_a}, the cognitive controller cost on the shifted lateral deviation of the vehicle from the target path q_e and the controller time shift T_t.

Table 3.1: Driver-steering-vehicle model parameters

	Description	Parameter	Value	Unit	Source
Vehicle Model	Vehicle mass	m	1370	kg	[124]
	Vehicle yaw moment of inertia	I	1840	kg m^2	[124]
	Lateral front tyre stiffness	C_f	41.8×10^3	N/rad	[124]
	Lateral rear tyre stiffness	C_r	62.2×10^3	N/rad	[124]
	Distance from CoM to front axle	a	0.98	m	[124]
	Distance from CoM to rear axle	b	1.49	m	[124]
	Longitudinal velocity	U	16.7	m/s	[124]
Steering Model	Steering gear ratio	G	16		[124]
	Trail (Pneumatic and caster)	d	0.059	m	[124]
	Stiffness of the steering system due to the kingpin axes (inclination and scrub radius)	k_{sw}	0.516	Nm/rad	[124]
	Moment of inertia of the steering wheel	I_{sw}	0.0264	kg m^2	/
	Damping coefficient of the steering system (of the bearings) and steering system friction	c_{sw}	0.2	Nms/rad	/
	Boost curve coefficient	C_{boost}	0		/
	Steering column stiffness	k_t	115	Nm/rad	[1]
	Inertia of the rack and the front wheels referred to the pinion	I_c	$\frac{1.7}{G^2}$	kg m^2	[1]
	Damping coefficient of the torsion bar	c_t	1.74	Nms/rad	[1]
	Handwheel stiffness term	k_{hw}	0	Nm/rad	/
	Handwheel damping term	c_{hw}	0	Nms/rad	/

Table 3.1(continued): Driver-steering-vehicle model parameters

	Description	Parameter	Value	Unit	Source
Driver Model	Intrinsic muscle stiffness	k_p	0	Nm/rad	[103]
	Intrinsic muscle damping	c_p	0	Nms/rad	[103]
	Tendon stiffness	k_a	30	Nm/rad	[121]
	Motor neurons lag time constant	τ_1	30	ms	[103]
	Muscle activation and deactivation lag time constant	τ_2	20	ms	[103]
	Reflex delay	τ_r	40	ms	[17]
	Cost function weight on control input α	q_α	1		/
	Cut-off frequency for the low-pass filter H_{fF}	f_{cF}	6.28	rad/s	
	Cut-off frequency for the low-pass filter H_{fM}	f_{cM}	6.28	rad/s	
	Cut-off frequency for the low-pass filter H_{fT}	f_{cT}	62.8	rad/s	
	Cut-off frequency for the low-pass filter in H_{fr}	f_{crl}	1	rad/s	
	Cut-off frequency for the high-pass filter in H_{fr}	f_{crh}	0.05	rad/s	

3.3 Simulation Study of Linear Model Parameters

Based on the formulation of the new driver-steering-vehicle model, a parameter study is conducted to enable a fundamental understanding of steering torque feedback. This section firstly describes the effects of steering system parameters on the steering properties of the vehicle to get a better understanding of the objective assessment of steering feel. As mentioned in Section 3.2.10, there are eleven driver model parameters which are neither fixed in advance from relevant literature nor taken from the experimental conditions. Then a parameter analysis on the eleven parameters that influence the drivers' steering control performance is conducted. Baseline values of these parameters are found by conducting preliminary identification based on experiments over a range of conditions with details are given in [125] and are updated following the identification results presented in Figure 5.4 in Chapter 5. The identified values of these eleven parameters are given in Table 3.2. Nash [126] found that the process noise and measurement noise standard deviations in the Kalman filter depend on the RMS values of the equivalent signals in the driver-steering-vehicle model. However, these signals are not known until after the simulation has been run, so an iterative procedure would be needed to find the RMS signal values for each condition. To save computational time, these noise standard deviations are simply fixed at the values shown in Table 3.2 for the baseline simulations in this section.

Table 3.2: Driver model parameters used in the simulations.

Description	Parameter	Value	Unit
Damping resisting stretching of the muscle fibre	c_a	3.37	Nms/rad
Arm inertia	I_{arm}	0.0973	kgm^2
Reflex gain	k_r	24.9	Nm/rad
Process noise standard deviation	W	13.3	Nm
Standard deviation of measurement noise on the lateral deviation of the vehicle from the target path e	V_e	0.147	m
Standard deviation of measurement noise on the vehicle yaw angle ψ	V_ψ	0.0744	rad
Standard deviation of measurement noise on the muscle angle θ_a	V_{θ_a}	0.863	rad
Visual delay	τ_{vi}	0.110	s
Muscle angle sensory delay	τ_{θ_a}	0.360	s
Cognitive controller cost on the shifted lateral deviation of the vehicle from the target path	q_e	1000	m^{-2}
Controller time shift	T_t	0.0229	s

3.3.1 Simulation Study of Steering System Parameters

In this section, the steering system is decoupled from the muscle dynamics and then combined with the vehicle model so that the open-loop steering-vehicle dynamics can be simulated. A diagram showing the steering system model only together with a steering wheel torque input from the driver T_{sw} is presented in Figure 3.7. It is also assumed that there is no steering column torque disturbance.

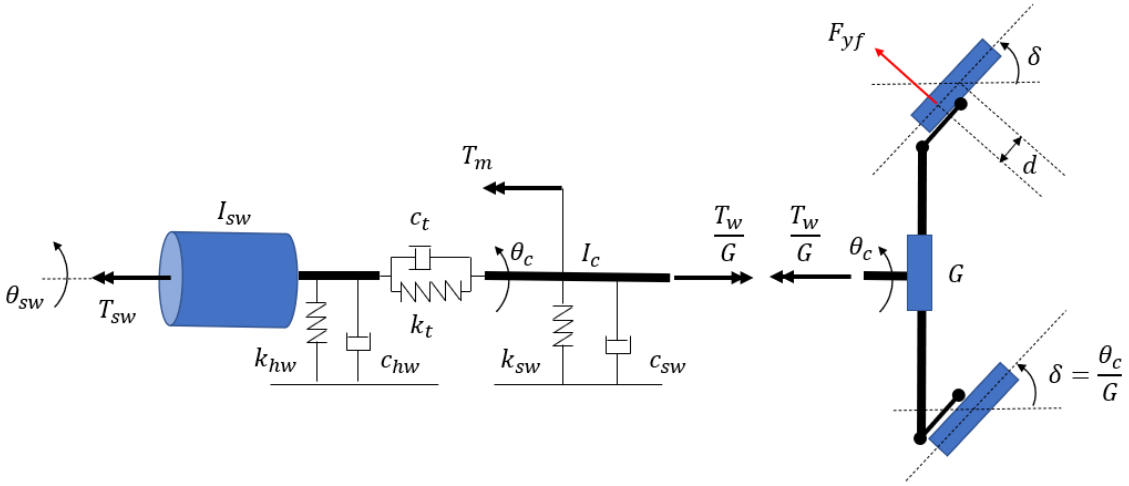

Figure 3.7: Steering system model with external steering wheel torque input. The springs and dampers act in rotation.

The parameters shown in Table 3.3 are investigated. In this table, the values in bold are called baseline values, which are used as the baseline for the parameter analysis. The values other than the baseline values are used in the simulation to understand how the variation of these steering parameters affect the responses of the steering-vehicle system and the objective assessment of steering feel. In the analysis, only one parameter is varied each time while the others are fixed at the baseline values. The other parameters of the steering-vehicle model are given in Table 3.1.

To investigate the on-centre region specifically, the steering-vehicle system model is subject to a sinusoidal steering wheel torque input with an amplitude of 2.2Nm and a frequency of 0.2Hz so that the maximum lateral acceleration is within the range from -2ms^{-2} to 2ms^{-2} to ensure on-centre regime.

$$T_{sw} = 2.2\sin(0.4\pi t) \tag{3.62}$$

Frequency responses of the steering-vehicle system are plotted to investigate vehicle steering performance. Several cross-plots, including vehicle lateral acceleration a_y versus steering wheel torque T_{sw}, vehicle lateral acceleration a_y versus steering wheel angle θ, steering wheel angle θ versus steering wheel torque T_{sw} and steering wheel angle θ versus vehicle yaw rate ω are generated since they are useful tools for analysing objective assessment of steering feel. Returnability, on-centre feel,

torque stiffness and steering sensitivity are representative objective steering feel characteristics that can be illustrated by the cross-plots. The definitions of them are [29]:

- Returnability: the lateral acceleration at zero steering wheel torque
- On-centre feel: the slope of steering wheel torque to lateral acceleration between -0.5ms^{-2} and 0.5ms^{-2} in lateral acceleration
- Torque stiffness: steering wheel torque gradient at zero steering wheel angle
- Steering sensitivity: the reciprocal of steering wheel angle gradient at 1ms^{-2} lateral acceleration

Table 3.3: Parameter values of the steering model in the parameter study

Description	Parameter	Value	Unit
Stiffness of the steering system due to the kingpin axes (inclination + scrub radius)	k_{sw}	0.344 **0.516** 0.688	Nm/rad
Damping coefficient of the steering system (of the bearings) and steering system friction	c_{sw}	0.1 **0.2** 0.3	Nms/rad
Moment of inertia of the steering handwheel	I_{sw}	0.01 **0.0264** 0.04	kgm^2
Steering column stiffness	k_t	28.8 **115** 230	Nm/rad
Torsion bar damping	c_t	0.1 **1.74** 10	Nms/rad
Boost curve coefficient	C_{boost}	**0** 1	
Steering gear ratio	G	8 **16** 24	
Trail (Pneumatic + Caster)	d	0.01 **0.059** 0.1	m

Figure 3.8 shows the frequency response of the steering-vehicle system with various values of steering gear ratio G. The frequency is plotted up to 10^4rad/s in order to confirm the correct operation of the model. In practice, the human driver would not be expected to apply torques at frequencies above 30rad/s. Discernible differences are noticed when examining the plots at low frequencies such as 0.2Hz (1.2566rad/s) that the magnitudes of all the three system states are relatively larger for larger values of steering gear ratio G. This is because, at low frequencies, the torque applied to the steering wheel by the driver T_{sw} is mainly reacted by the steering system stiffness k_{sw} and by the self-aligning torque resulting from front tyres lateral force F_{yf} acting through the trail distance d and steering gear ratio G. For a larger value of steering gear ratio, a larger lateral tyre force is required to react the steering wheel torque; this is achieved by a larger front tyres steer angle, with corresponding increases in vehicle lateral velocity v, vehicle yaw rate ω and steering wheel angle θ_{sw}. At very high frequencies, the gain roll-off for the two vehicle states v and ω is 80dB/decade, which arises from the combined second-order steering system model with the second-order vehicle model (40dB/decade each), while the gain roll-off

for the steering wheel angle θ_{sw} is 40dB/decade, arising just from the second-order steering system model. It is shown that there is also a slight decrease in gain at high frequencies for vehicle lateral velocity v and vehicle yaw rate ω with the increase in steering gear ratio G. There is because that the increased value of the steering gear ratio leads to increased equivalent inertia of the rack and the front wheels. The corner frequencies of the system correspond to the resonance of the vehicle system, followed by the resonance of the steering system. It is easy to distinguish the two separate resonances when the steering gear ratio G is 8. However, they are getting close to each other with the increase of steering gear ratio G. The exact values of the damped natural frequencies of the system are the imaginary parts of the eigenvalues of the system, as shown in Figure 3.9. Figure 3.10 shows the cross-plots of four states of the steering-vehicle system, illustrating the effects of changing steering gear ratio on objective steering feel characteristics. Firstly, discernible differences are noticed when examining the characteristics of steering wheel angle θ_{sw} versus steering wheel torque T_{sw}, and vehicle lateral acceleration a_y versus steering wheel torque T_{sw}. It is seen that as the steering gear ratio increases, less steering wheel torque is required to achieve the same steering wheel angle or vehicle lateral acceleration. This is consistent with findings from the frequency responses of the system shown in Figure 3.8. Additionally, the changes of characteristic parameters describing objective assessment of steering feel due to steering gear ratio variation are summarised in Table 3.4. In summary, the steering gear ratio G influences steering sensitivity, returnability, on-centre feel and torque stiffness.

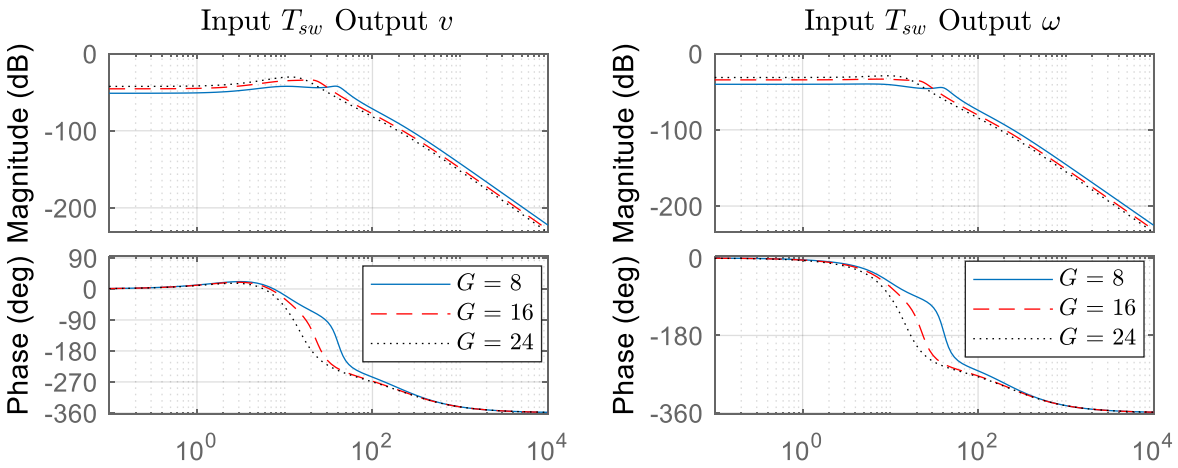

Figure 3.8: Frequency responses of the steering-vehicle system with different values of steering gear ratio G. The x-axis for the three plots is frequency in rad/s.

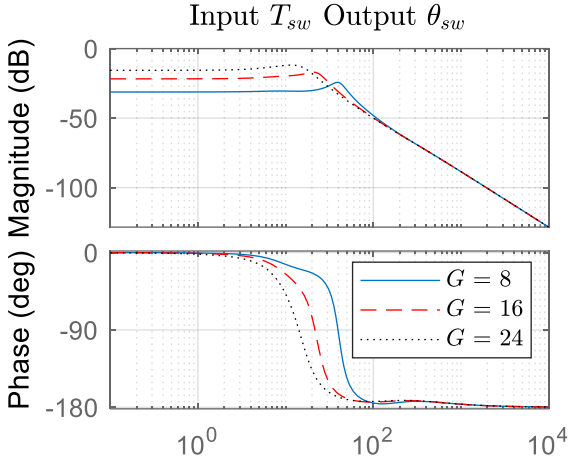

Figure 3.8(continued): Frequency responses of the steering-vehicle system with different values of steering gear ratio G. The x-axis for the three plots is frequency in rad/s.

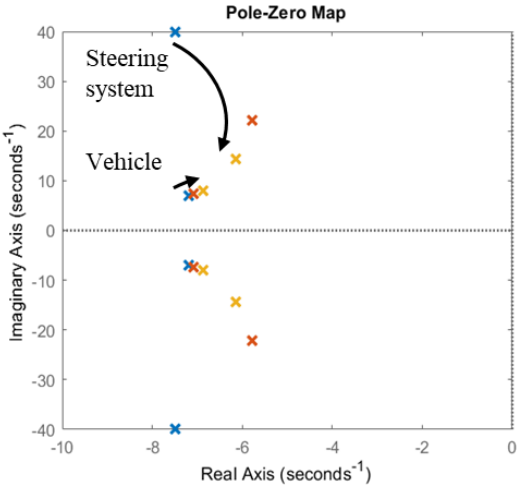

Figure 3.9: Eigenvalues of the steering-vehicle system. The direction of the arrow indicates increasing G.

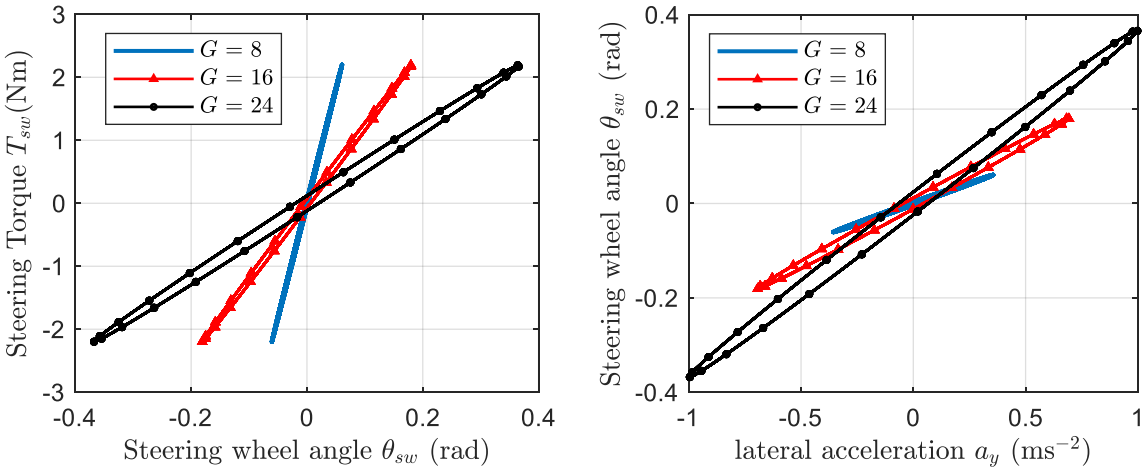

Figure 3.10: Cross-plots of the states of the steering-vehicle system. The hysteresis loops are formed clockwise.

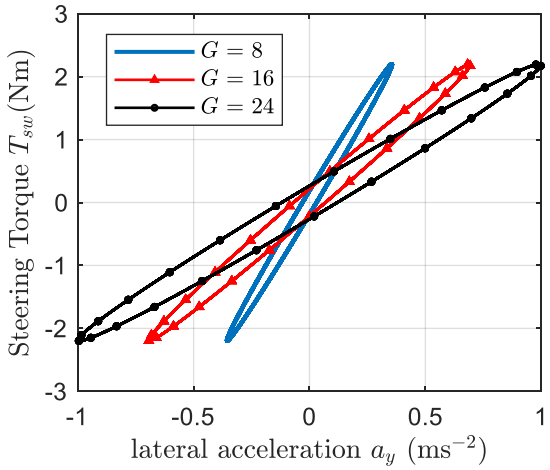

Figure 3.10(continued): Cross-plots of the states of the steering-vehicle system. The hysteresis loops are formed clockwise.

Figure 3.11 shows the frequency response of the steering-vehicle system with various values of front tyres trail distance d. The decreases in the frequency response magnitudes of all the three states vehicle lateral velocity v, vehicle yaw rate ω and steering wheel angle θ_{sw} are noticed in normal operation frequencies (low frequencies) such as 0.2Hz (1.2566rad/s) when the front tyres trail distance d increases, indicating an increase in equivalent stiffness of the steering-vehicle. The values of the damped natural frequencies of the system are the imaginary parts of the eigenvalues of the system, as shown in Figure 3.12. Figure 3.13 shows the cross-plots of four states of the steering-vehicle system, illustrating the effects of changing front tyres trail distance d on objective steering feel characteristics. These cross-plots highlight the effect of increasing tyre trail distance by shortening the horizontal width of the plots involving steering wheel torque T_{sw}. As the front tyres trail distance d increases, the resistance torque generated by the front tyres force acting through the trail distance becomes large and therefore needs to be compensated by a larger steering wheel torque T_{sw}. In addition, when the front tyres trail distance d is set to 0.01m, there is little torque feedback from the front tyres and the maximum lateral acceleration and steering wheel angle are unrealistically large. The changes of the characteristic parameters describing objective assessment of steering feel due to front tyres trail distance d variation are also summarized in Table 3.4, and basically, the front tyres trail distance d has an influence on returnability, on-centre feel and torque stiffness.

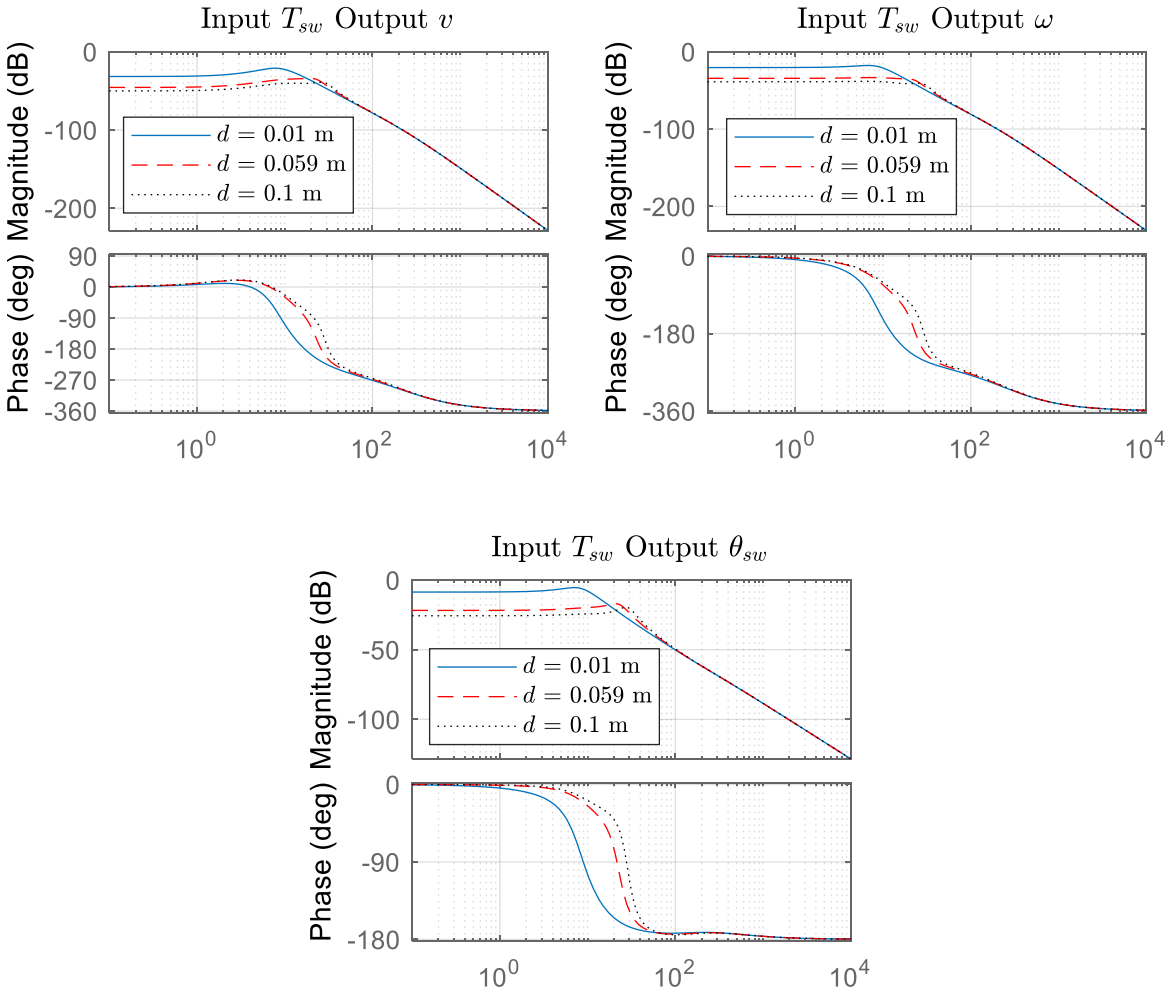

Figure 3.11: Frequency responses of the steering-vehicle system with different values of front tyres trail distance d. The x-axis for the three plots is frequency in rad/s.

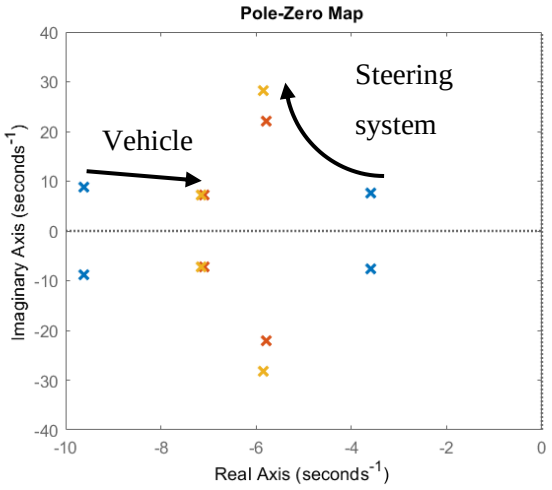

Figure 3.12: Eigenvalues of the steering-vehicle system. The direction of the arrow indicates increasing d.

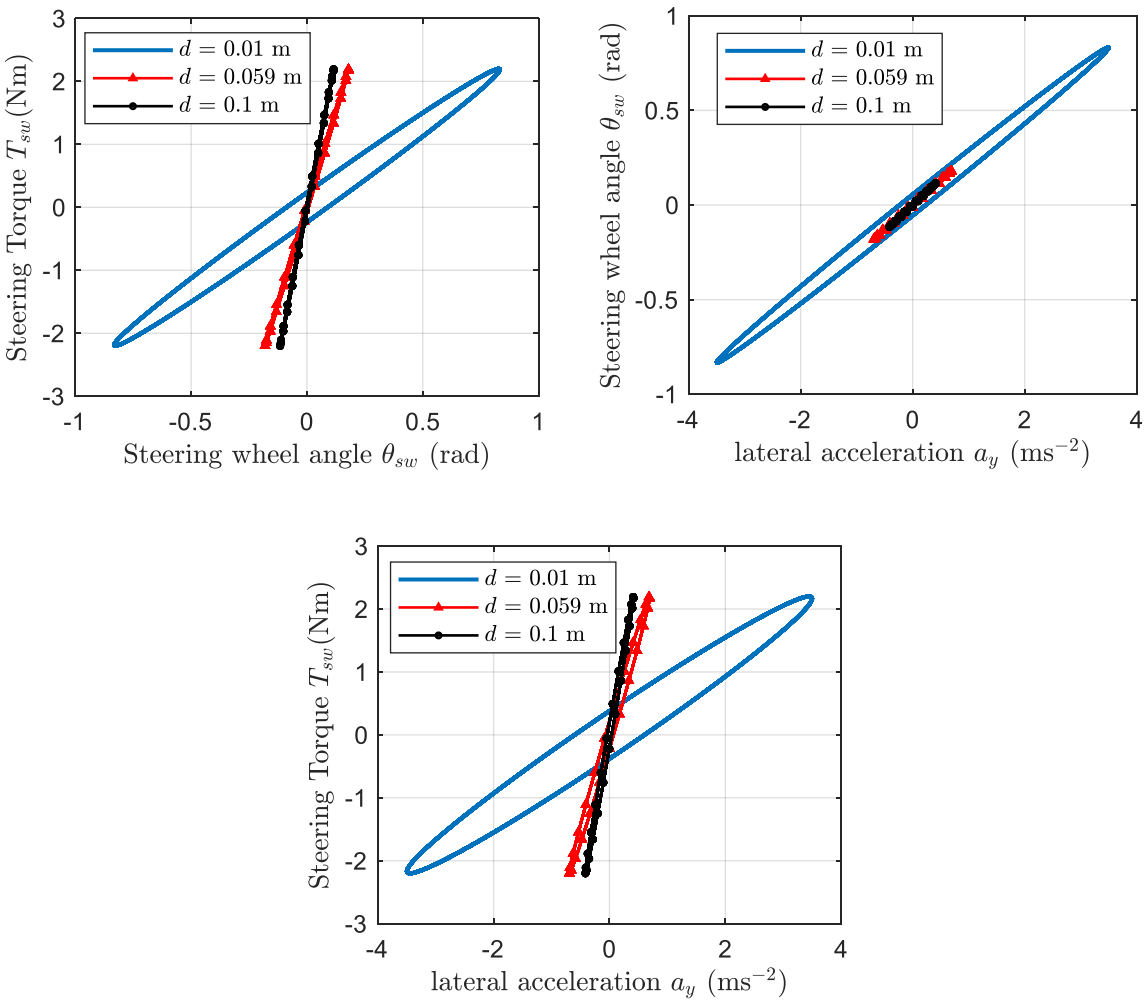

Figure 3.13: Cross-plots of the states of the steering-vehicle system. The hysteresis loops are formed clockwise.

Figure 3.14 shows the frequency response of the steering-vehicle system with and without assist torque. The gain for all the three states vehicle lateral velocity v, vehicle yaw rate ω and steering wheel angle θ_{sw} at low frequencies increases when there is assist torque. This is ascribed to the greater torque applied on the steering-vehicle system. However, at high frequencies, the increase in the gain is only seen for the two vehicle states. This is because the assist torque is directly applied at the inertia of the rack and the front wheels, which is directly connected with the vehicle and the change of the torque across the torsion bar and the steering column is negligible at high frequencies. The values of the damped natural frequencies of the system are the imaginary parts of the eigenvalues of the system, as shown in Figure 3.15. Figure 3.16 shows the cross-plots of four states of the steering-vehicle system. It is shown that when an assist torque is applied at the steering system, the required steering wheel torque to achieve the same steering wheel angle, vehicle yaw rate, and vehicle lateral acceleration is smaller, as expected. The effects of the assist torque on the characteristic parameters describing objective

assessment of steering feel are also illustrated by these cross plots and are summarized. In general, the existence of the assist torque influences steering sensitivity, returnability, on-centre feel and torque stiffness.

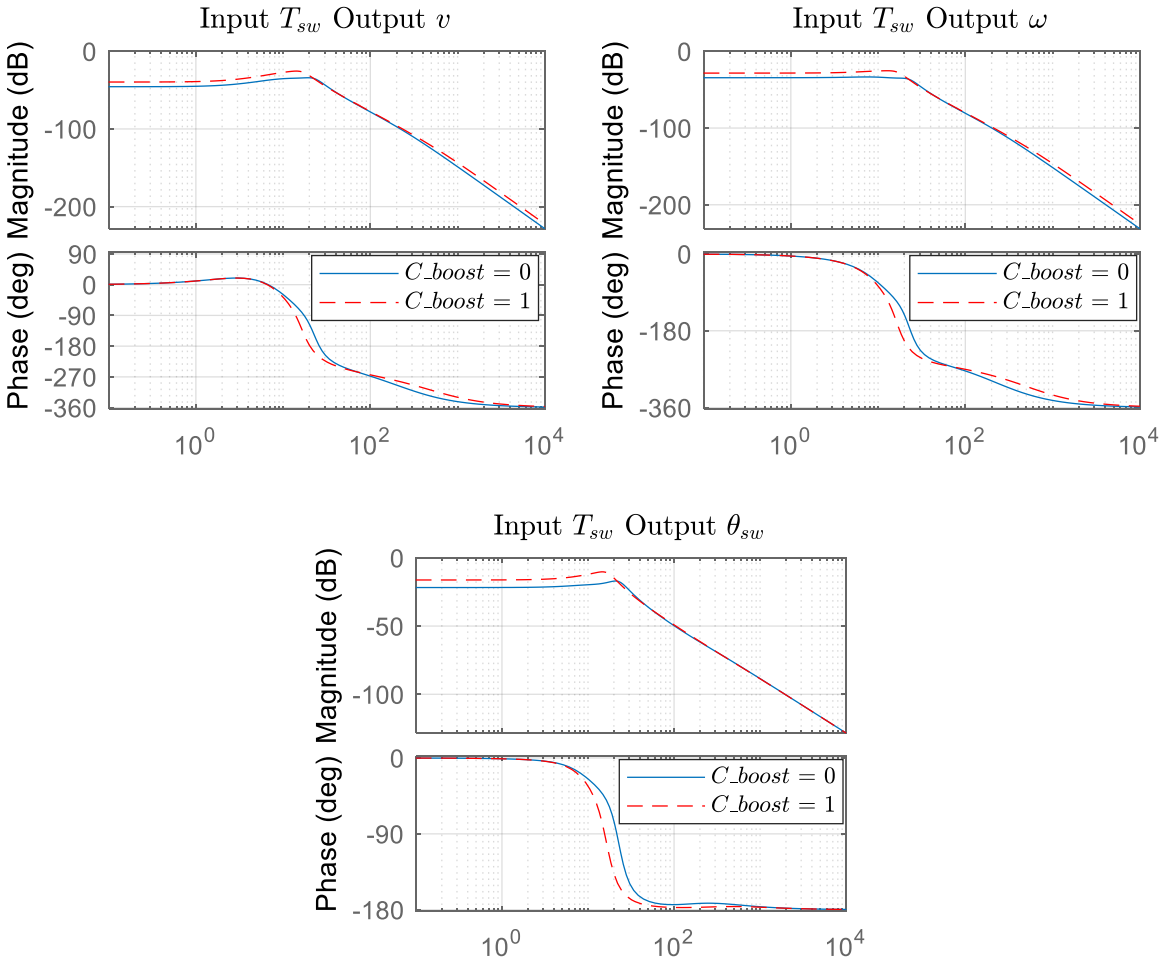

Figure 3.14: Frequency responses of the steering-vehicle system with and without assist torque from driving assistant system. The x-axis for the three plots is frequency in rad/s.

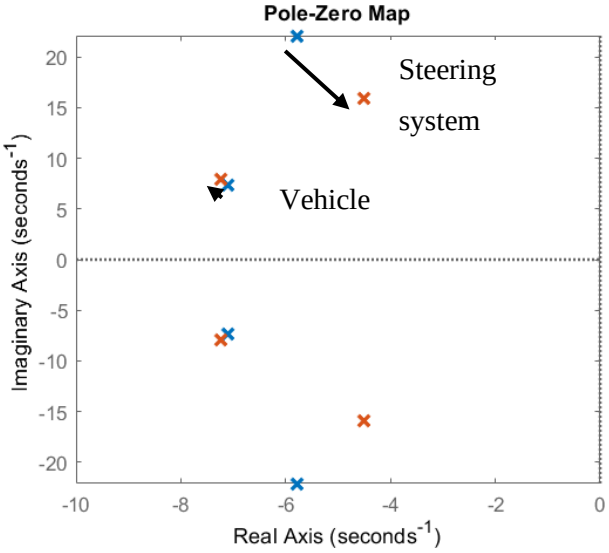

Figure 3.15: Eigenvalues of the steering-vehicle system. The direction of the arrow indicates increasing C_{boost}.

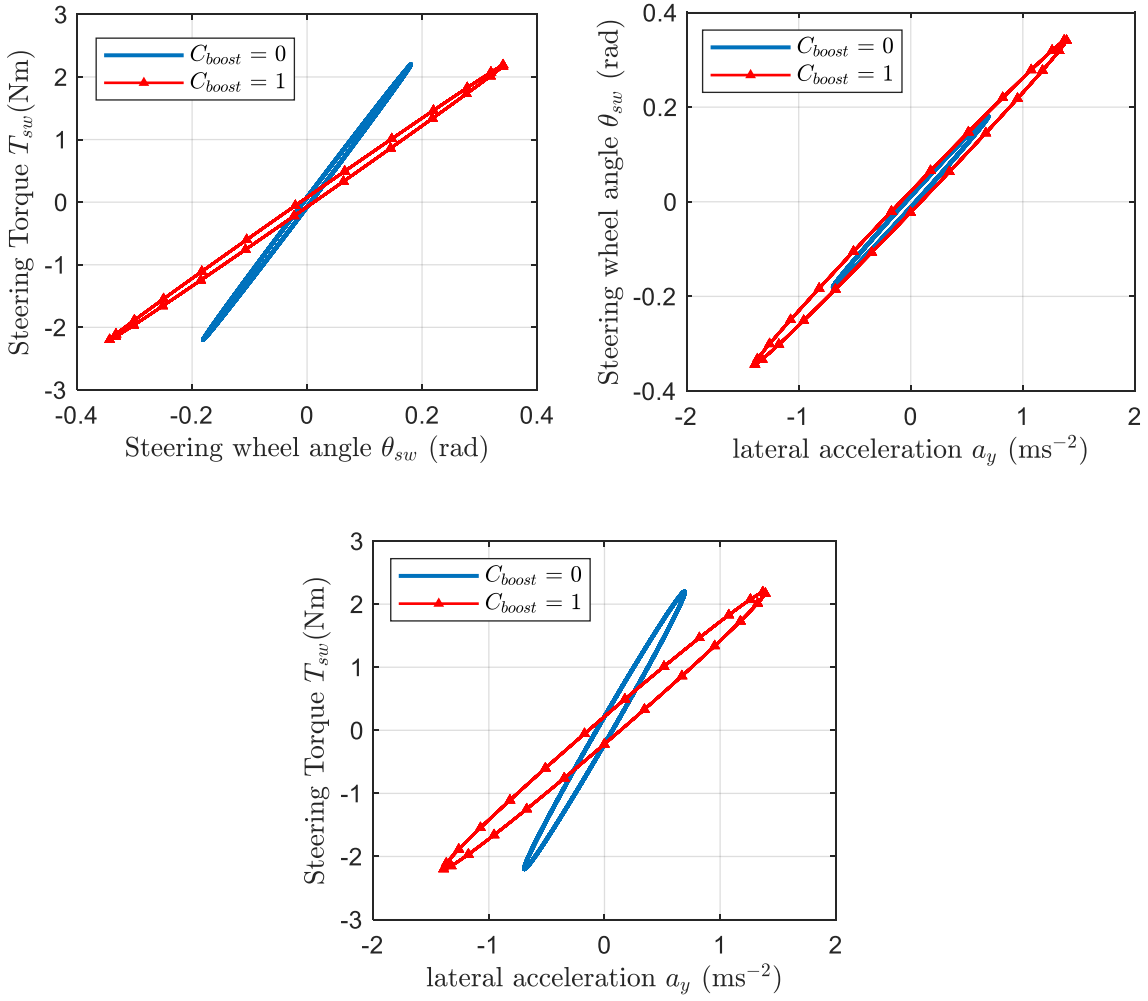

Figure 3.16: Cross-plots of the states of the steering-vehicle system. The hysteresis loops are formed clockwise.

The effects of the other steering system parameters listed in Table 3.3 are on the dynamic behaviour of the steering-vehicle system are predictable and obvious. Therefore, the detailed analysis regarding the frequency response plots and the cross-plots is not shown. Specifically, the increase of steering column stiffness k_t reduces the magnitude of steering system responses at low frequencies, and the lower value of torsion bar damping c_t gives lower magnitudes in vehicle responses at high frequencies. In addition, the increase of self-centering stiffness k_{sw} reduces the magnitude of steering and vehicle responses at low frequencies, the increase of steering system damping c_{sw} reduces the resonance peak related to the steering system, while the increase of steering wheel inertia I_{sw} results in lower magnitude of the steering and vehicle responses at high frequencies and lower value of resonance frequency of the steering system. The effects of these parameters on the characteristic parameters describing objective assessment of steering feel are also shown in Table 3.4. In general, the observed effects shown in Table 3.4 are consistent with the findings of published literature reviewed in Section 2.2.3.

Table 3.4: Effects of the increase of steering system parameters on steering feel parameters

Steering system parameter	Steering sensitivity	Returnability	On-centre feel	Torque stiffness
Steering gear ratio G	$-$	$+$	$-$	$-$
Front tyres trail distance d	/	$-$	$+$	$+$
Boost curve coefficient C_{boost}	$+$	$+$	$-$	$-$
Steering column stiffness k_t	$+$	/	/	$+$
Torsion bar damping c_t	/	/	/	/
Steering wheel inertia I_{sw}	/	/	/	/
Steering system damping c_{sw}	/	$+$	/	/
Self-centering stiffness k_{sw}	/	/	$+$	$+$

Note:'+' indicates 'increase', '-' indicates 'decrease' and '/' indicates negligible change

3.3.2 Simulation Study of Neuromuscular Parameters

In this section, the open-loop muscle-steering-vehicle model, which are the blocks H_{ms} and H_v shown in Figure 3.3, is simulated to investigate the effects of the neuromuscular parameters on the model performance. Figure 3.17 shows the frequency response of the steering wheel angle θ_{sw} for various values of arm inertia I_{arm} with muscle activation torque input T_a. At high frequencies, the gain roll-off is 60dB/decade, which is the combination effect of the first-order Hill's muscle model (20dB/decade) and the second-order steering system model (40dB/decade). It is shown that there is a noticeable decrease in gain at high frequencies with the increase of arm inertia since the response in this frequency

region is dominated by the inertia of the arms and steering wheel. The roll-off frequency is affected by the inertia value, with an increase in the inertia value leading to a lower roll-off frequency.

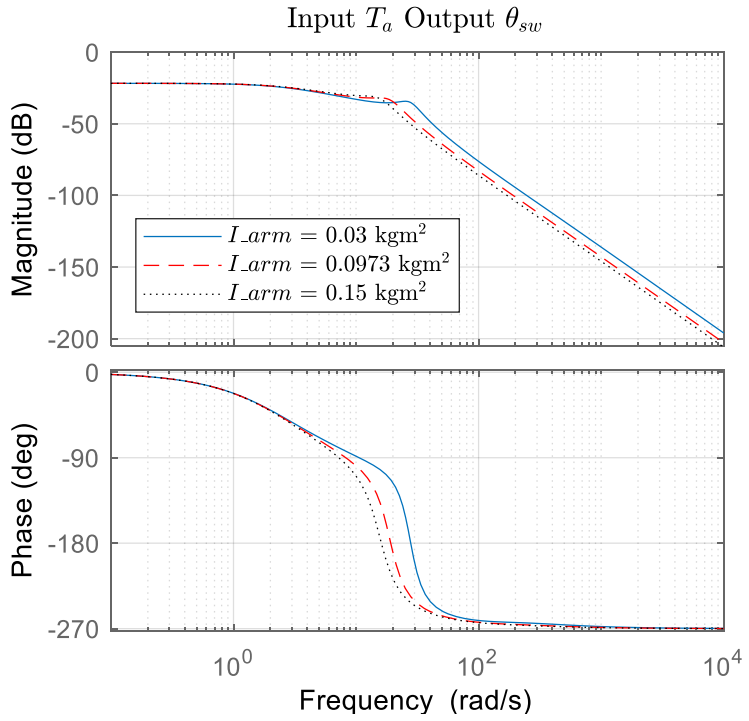

Figure 3.17: Frequency response of the open-loop muscle-steering-vehicle system with different values of arm inertia I_{arm}, specifically of steering wheel angle θ_{sw} to muscle activation torque input T_a.

Figure 3.18 shows frequency response of the steering wheel angle θ_{sw} with various frequencies of muscle activation torque T_a for several values of damping resisting stretching of the muscle fibre c_a. When the damping resisting stretching of the muscle fibre c_a is increased, which arises when the extent to which the muscle is tensed is larger, some muscle activation is damped out by the muscle, leading to a reduced magnitude of the steering wheel angle at intermediate or high frequencies. Moreover, the slope of the phase change is also influenced by the change of damping resisting stretching of the muscle fibre c_a. Figure 3.19 shows the frequency response of the steering wheel angle θ_{sw} with various frequencies of muscle activation torque T_a for several values of tendon stiffness k_a. It is shown that the gain of steering wheel angle increases when the tendon stiffness k_a is increased. This is ascribed to the greater torque transmitted by the muscle to the steering wheel when the muscle is activated. The corner frequency corresponding to the Hill's muscle model is reflected by the time constant, the ratio of k_a to c_a.

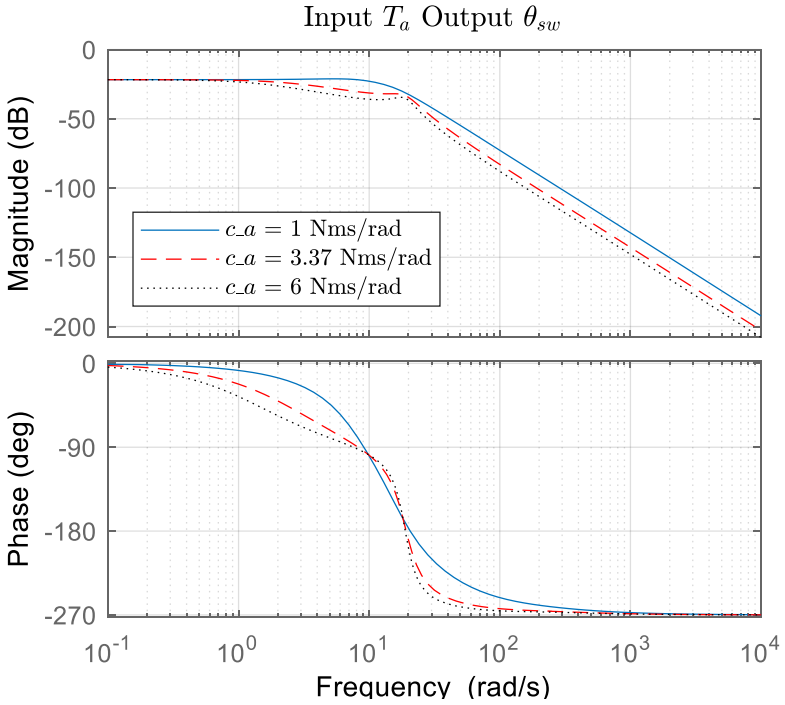

Figure 3.18: Frequency response of the open-loop muscle-steering-vehicle system with different values of damping resisting stretching of the muscle fibre c_a, specifically of steering wheel angle θ_{sw} to muscle activation torque T_a.

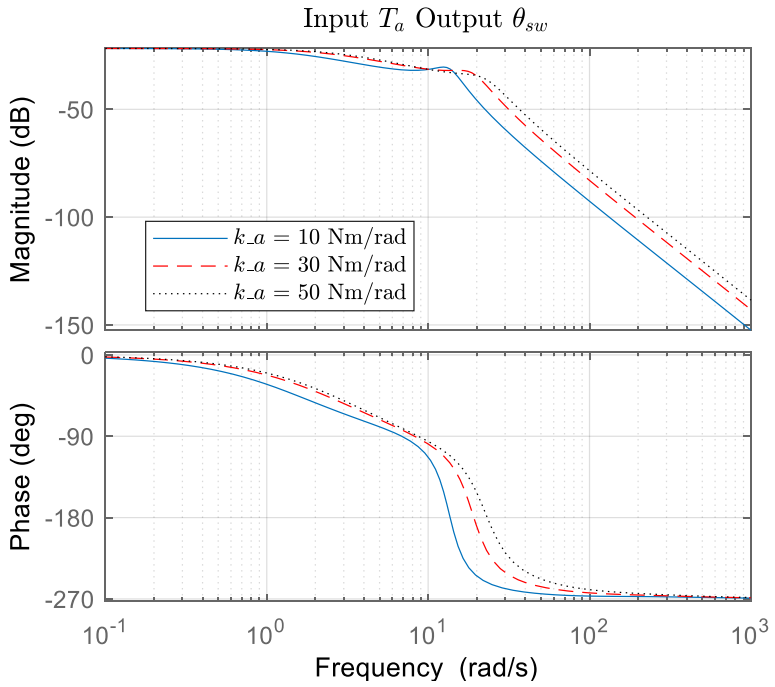

Figure 3.19: Frequency response of the open-loop muscle-steering-vehicle system with different values of tendon stiffness k_a, specifically of steering wheel angle θ_{sw} to muscle activation torque T_a.

To investigate the effect of stretch reflex control action, the open-loop muscle-steering-vehicle model, formed by the series combination of the blocks H_a, H_{ms} and H_v shown in Figure 3.3, is simulated with and without the reflex control loop. The transfer function of the muscle-steering-vehicle model only is represented as the solid line shown in Figure 3.20. The input is the alpha activation signal α arising from the brain of the human driver, and the output is the steering wheel angle θ_{sw}. At low frequencies, the system behaves like inertia on a spring. The gain in this frequency range is therefore determined by the stiffness of the system. At high frequencies, the gain roll-off is 100dB/decade, arising from the second-order steering system (40dB/decade), the first-order Hill's muscle model (20dB/decade) and the two first-order lags (20dB/decade each) related to the muscle activation block in the path from α to θ_{sw}. The changes in the slope in the intermediate frequency range are consistent with the time lags and corner frequencies of the system. The transfer function of the muscle-steering-vehicle model with the stretch reflex loop is shown as the dashed line in Figure 3.20. The gamma activation signal γ, which is the expected muscle angle from the human brain in this study, is set to zero. Compared with the transfer function without the stretch reflex loop, it is seen that at low frequencies down to zero, the gains are smaller because the stretch reflex loop provides additional stiffness. When there is the presence of input to the plant, the actual muscle angle θ_a will differ from the expected angle γ, which is zero here. The alpha motor neurons in turn send a signal α_r to activate the muscle to achieve the expected muscle angle γ. Therefore, the magnitude of steering wheel angle is reduced with the stretch reflex control action. As high value of stretch reflex gain k_r corresponds to a more tensed muscle state, the frequency responses here are consistent with the results found by [103] that human drivers tend to stiffen the arms to compensate for the unknown disturbances acting on the vehicle. However, the stretch reflex loop also results in a lightly damped resonance at about 10rad/s, the properties of which are strongly influenced by the reflex gain H_r and delay D_r. The frequency of the resonance increases with the gain and the damping ratio tends to reduce as the delay and gain increase. At frequencies above the resonance, the response of the system is similar to that without the additional stretch reflex loop.

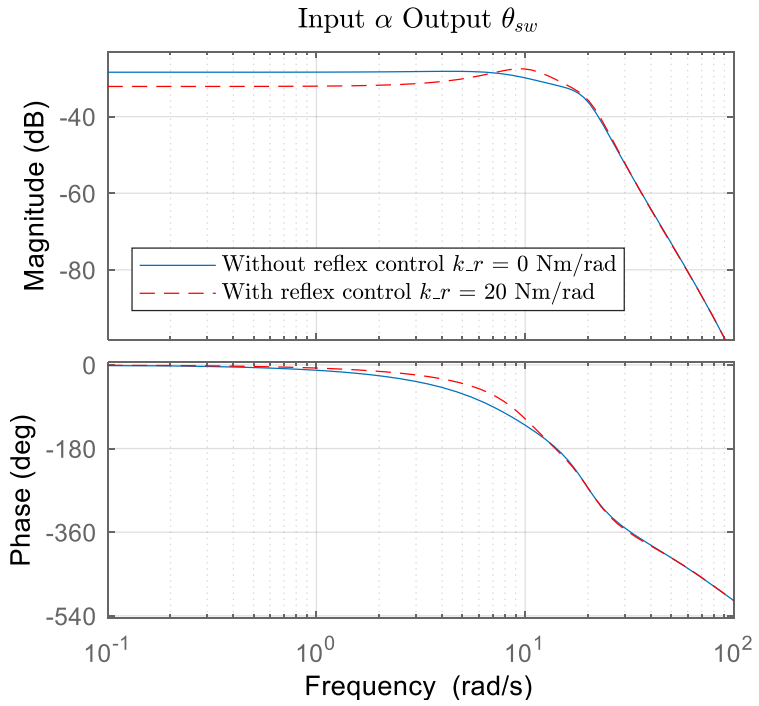

Figure 3.20: Frequency responses of the open-loop muscle-steering-vehicle system with and without stretch reflex loop, specifically of steering wheel angle θ_{sw} to alpha activation signal α.

3.3.3 Simulation Study of Kalman Filter Parameters

A Kalman filter is used in this model to represent the driver's integration of sensory measurements. The measurements are combined to give a state estimate based on an internal mental model of the plant controlled by the human driver and estimates of the process and measurement noise standard deviations. The values of the process and measurement noise covariance matrices in the Kalman filter $\mathbf{Q}_{\mathrm{KF}}$ and $\mathbf{R}_{\mathrm{KF}}$ indicate how the process noise and the measurement noise are weighted in the state estimation. Previous studies [123] and preliminary simulation results found that the most important aspect of the Kalman filter is in the determination of the process and measurement noise covariance matrices $\mathbf{Q}_{\mathrm{KF}}$ and $\mathbf{R}_{\mathrm{KF}}$. Therefore, it is worth investigating how the variation of these noise covariance matrices, especially the ratio between them, influences Kalman filtering performance by simulating the closed-loop driver-steering-vehicle system with process and measurement noise. Different from Section 3.2.7, the values of $\mathbf{Q}_{\mathrm{KF}}$ and $\mathbf{R}_{\mathrm{KF}}$ are modified as:

$$\mathbf{Q}_{\mathrm{KF}} = \mathrm{diag}([C_w W^2 \quad W_r^2 \quad W_F^2 \quad W_M^2 \quad W_T^2]) \tag{3.63}$$

$$\mathbf{R}_{\mathrm{KF}} = \mathrm{diag}\left(\left[C_e V_e^2 \quad C_\psi V_\psi^2 \quad C_{\theta_a} V_{\theta_a}^2\right]\right) \tag{3.64}$$

where W^2, V_e^2, V_ψ^2 and $V_{\theta_a}^2$ still denote the actual variances of the noise, W_r^2 W_F^2, W_M^2 and W_T^2 denote the variances of the disturbances w_r, w_F, w_M and w_T, respectively, and C_w, C_e, C_ψ and C_{θ_a} are called

scaling factors. The standard deviations of the noise used in the simulations are shown in Table 3.5 and the standard deviations of the disturbances w_r, w_F, w_M and w_T are all set to zero in the simulations.

Table 3.5: Standard deviations of the process and measurement noise in the simulations

Description	Parameter	Value	Unit
Standard deviation of the process noise w	W	13.3	Nm
Standard deviation of the measurement noise v_e	V_e	0.147	m
Standard deviation of the measurement noise v_ψ	V_ψ	0.0744	rad
Standard deviation of the measurement noise v_{θ_a}	V_{θ_a}	0.863	rad

To investigate how the use of each sensory measurement is varied with the scaling factors, a technique similar to that used by Nash [126], who studied the effects of sensory measurements on the driver's control action, is applied. Transfer functions between each sensory measurement and the simulated steering wheel angle are found by splitting the contribution to the steering wheel angle for each measurement following the linear superposition principle. The RMS values of the simulated steering wheel angle contribution for each sensory measurement are calculated using a spectral analysis theory approach [20]. The ratios of these values to the total RMS value of the simulated steering wheel angle are then calculated to represent the relative weighting of each sensory measurement. The relative weightings of the sensory measurements for different scaling factors associated with the process and measurement noise are shown in Figure 3.21. The summation of these weightings may be larger than one because the contributions of the different measurements are not always in phase with each other. When the process noise scaling factor C_w is increased while the others are fixed at 1, the measurements are weighted more in the steering control task. In all the other cases, as the scaling factor increases, the corresponding sensory measurement is weighted less. The reason is that when the Kalman filter assumes that the noise from a particular sensory measurement is large, the corresponding sensory measurement will not be trusted much, and the Kalman filter will rely on the other sensory measurements for state estimation.

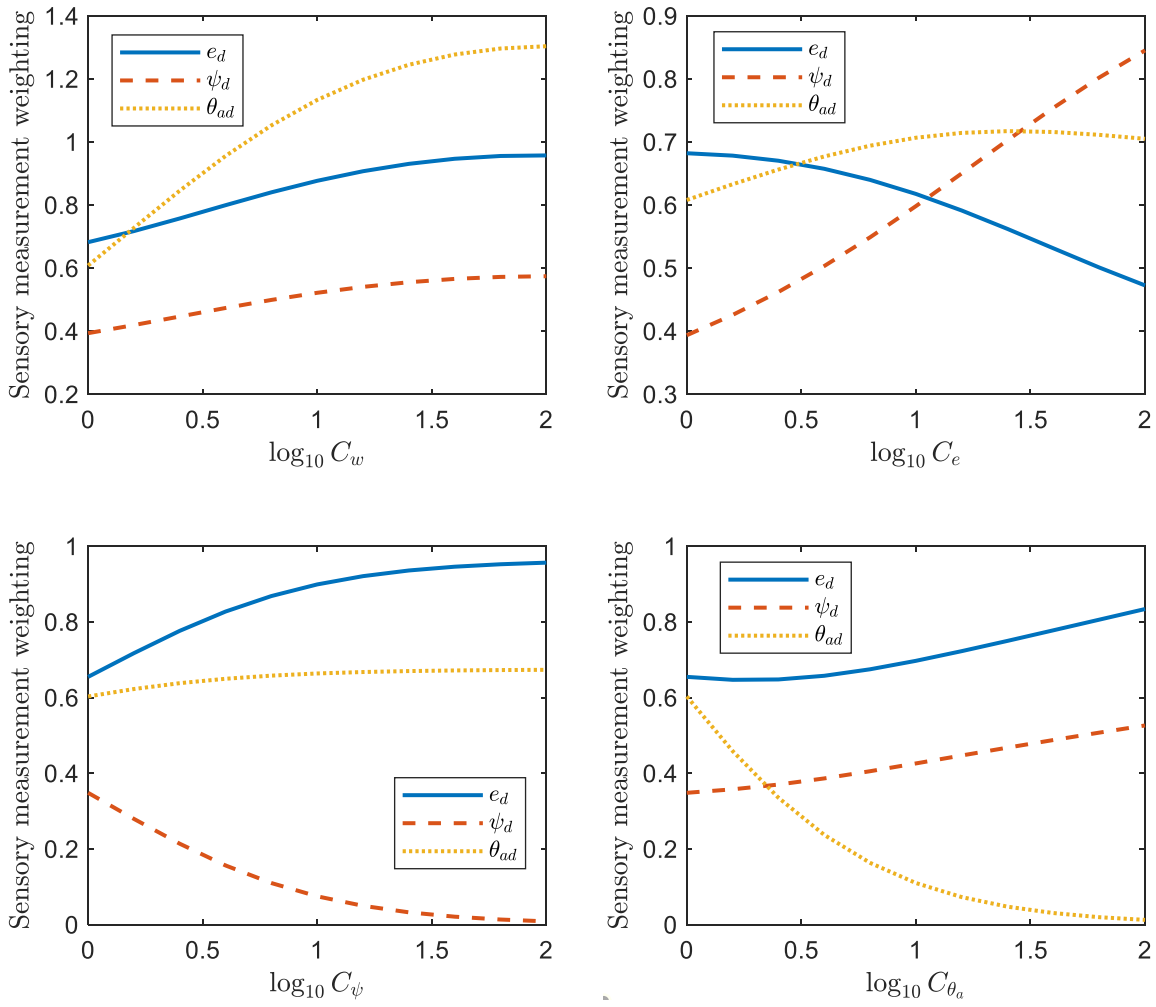

Figure 3.21: Sensory weightings with various scaling factors. Weightings show the proportion of steering wheel angle RMS resulting from each sensory measurement.

3.3.4 Simulation Study of Controller Parameters

The task described by the driver-steering-vehicle model is to follow the randomly moving target path by steering the vehicle. Therefore, the evaluation of the path-following performance of the modelled driver not only depends on the RMS value of path-following error e, but also relies on the driver's control effort, which can be quantified as the RMS value of the alpha signal α from the brain. When putting more weightings minimising the path-following errors, the steering effort level will increase. On the other hand, the path-following accuracy is sacrificed to minimise the steering effort level. This trade-off is reflected by the values of LQR controller cost function weights on e and α, specifically q_e and q_α. The values of RMS tracking error and RMS alpha signal for various values of q_e are shown in Figure 3.22. As expected, the general trend is that the path-following error decreases as the steering effort increases. Figure 3.23 shows the frequency response of the closed-loop driver-steering-vehicle model with different values of q_e.

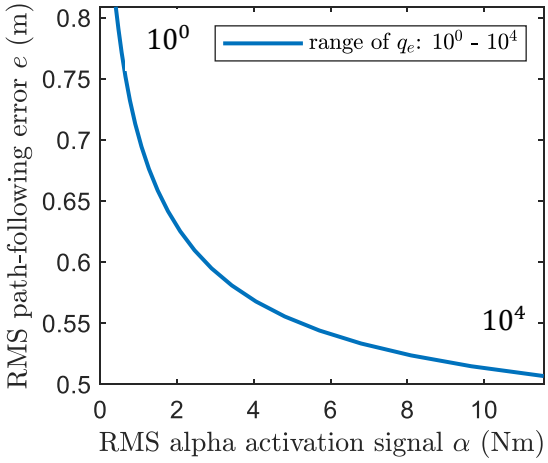

Figure 3.22: Trade-off plot showing the variation of RMS tracking errors and RMS control effort (alpha signal) with a range of values of q_e (from left to right: 10^0 to 10^4).

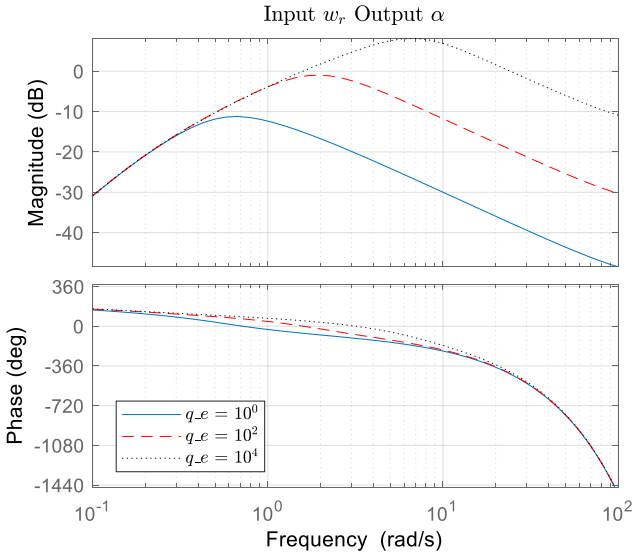

Figure 3.23: Frequency responses of the closed-loop driver-steering-vehicle system with different values of q_e, specifically of alpha signal α to randomly moving target path w_r.

3.4 Nonlinear Driver-Steering-Vehicle Model

A new driver-steering-vehicle model incorporating steering torque feedback and state estimation has been developed in Section 3.2. The new driver model is derived for a linear steering-vehicle system operating at on-centre operating regime. However, nonlinearities are always present to some extent in the steering mechanism, and previous research [1] [22] [33] [58] has revealed that on-centre steering feel is significantly affected by the nonlinear steering system friction. Therefore, it is necessary to develop a closed-loop driver-steering-vehicle model that can describe a human driver's control of a vehicle with nonlinear components, especially steering system friction, to better understand steering torque feedback in on-centre regime.

Nonlinear steering control algorithms have been increasingly developed for autonomous driving and semi-autonomous driving, as reviewed by [127] [128] [129]. However, the objective of these algorithms is to find an optimal control performance instead of mimicking the human driver's control behaviour. Various studies have attempted to model a human driver's control of nonlinear vehicles [79] [89] [130], and Nash and Cole [20] have developed a realistic nonlinear driver-vehicle model that takes account of the nonlinear vehicle dynamics, specifically nonlinear tyres, and sensory dynamics in a recent study.

In this section, the linear mathematical model of the driver-steering-vehicle system presented in Section 3.2 is extended to control a constant-speed vehicle with nonlinear steering dynamics, especially steering system friction. This requires modifications of the plant, state estimator and controller. Nonlinear state estimation and optimal control are much more complicated than the linear ones. Nash and Cole [20] implemented various combinations of state estimators and controllers by approximating nonlinear dynamics to simplify the task and have compared the performance of the different approaches. The results of the study of Nash and Cole [20] are used as the initial guidance of the choice of the state estimator and controller for a steering-vehicle system with nonlinear steering system friction. A schematic structure of the nonlinear driver-steering-vehicle model is shown in Figure 3.24. The model still comprises the vehicle and steering dynamics, the neuromuscular system, the sensory delays, and the human brain functions. However, the linear quadratic Gaussian (LQG) framework used in the linear driver-steering-vehicle model is replaced by an extended Kalman filter (EKF) and a model predictive control (MPC) method.

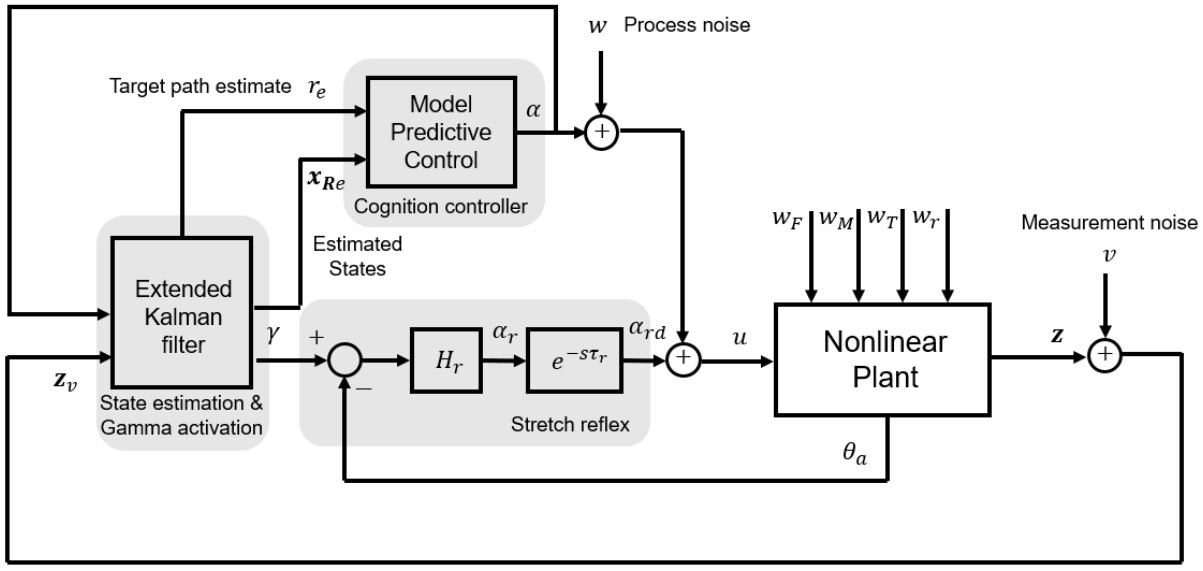

Figure 3.24: Schematic diagram of the nonlinear driver-steering-vehicle model. Disturbance signals are input as white noise w_F, w_M, w_T and w_r then filtered in the plant. The plant input α and outputs $\boldsymbol{z}$ are perturbed with process and measurement noise w and $\boldsymbol{v}$, so an extended Kalman filter estimates the plant states $\boldsymbol{x_e}$. An MPC controller computes an optimal plant input α.

3.4.1 Nonlinear Plant

The plant for the nonlinear driver-steering-vehicle model is similar to the plant derived for the linear driver-steering-vehicle model in Section 3.2. Compared to the linear plant, the nonlinear friction torque is applied to the steering system in the nonlinear plant. The structure of the muscle dynamics and steering system with nonlinear steering friction T_f is shown in Figure 3.25. The friction element T_f is placed at the steering column and below the torsion, in consistent with the two degree-of-freedom steering system model in [131].

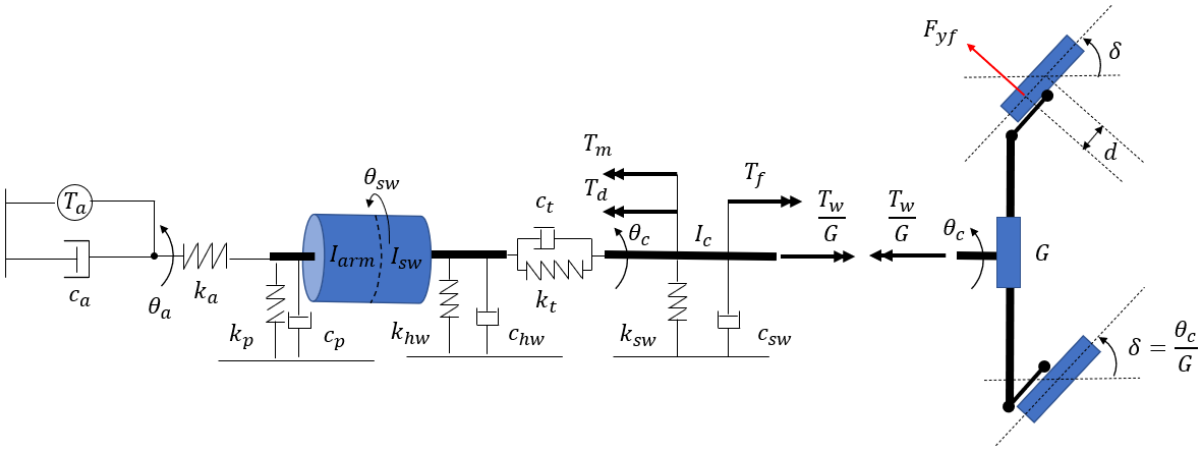

Figure 3.25: Muscle and steering system model with steering column torque disturbance and steering system friction. The springs and dampers act in rotation.

The state-space representation of the muscle-steering-vehicle dynamics is now given by the general equation:

$$\boldsymbol{x}'_{msv}(k+1) = \widehat{\mathbf{A}}_{msv}\boldsymbol{x}'_{msv}(k) + \mathbf{B}'_{msv}\{T_{a(k)} \quad F_y(k) \quad M_z(k) \quad T_d(k)\}^T \tag{3.65}$$

where $\boldsymbol{x}'_{msv}(k) = \{y(k) \quad v(k) \quad \psi(k) \quad \omega(k) \quad \theta(k) \quad \dot{\theta}(k) \quad \theta_c(k) \quad \dot{\theta}_c(k) \quad \theta_a(k) \quad T_f(k)\}^T$, $\widehat{\mathbf{A}}_{msv}$ is a nonlinear function. The derivation of the muscle-steering-vehicle dynamics without steering system friction is not repeated here. The steering system friction T_f shown in Figure 3.25 is represented by a dynamic friction model introduced by Specker [78] and is dependent on the steering column angular velocity $\dot{\theta}_c$. This model is based on a static friction model and a linear parameter-varying first-order low-pass filter. Simple friction models such as a hyperbolic tangent function and more or less complex combinations of Maxwell [132] and friction elements require small values of sample time T_s to achieve accurate representation of the friction, which leads to impractical computational time. In contrast, Specker's friction model provides a good qualitative representation of the friction for relatively large values of sample time T_s, making it applicable for control and state estimation tasks. The complete dynamic friction model results in the following equation:

$$\dot{T}_f(t) = \frac{1 - e^{-\left(\frac{\dot{\theta}_c(t)}{\dot{\theta}_{c0}}\right)^2}}{T_1}\left(F_C \tanh\left(\frac{\dot{\theta}_c(t)}{\dot{\theta}_{ct}}\right) - T_f(t)\right) \tag{3.66}$$

where constant T_1 and $\dot{\theta}_{c0}$ determine the hysteresis of the friction, $\dot{\theta}_{ct}$ determines the friction torque slope at standstill and F_C determines the magnitude of the friction. The three parameters T_1, $\dot{\theta}_{c0}$ and $\dot{\theta}_{ct}$ are tuned through preliminary simulations to ensure high precision of friction replication which is comparable to reputable friction models while making the computation numerical stable for a reasonable range of operating frequencies. The comparison of the friction-velocity characteristics between Specker's friction model and a simple Coulomb friction model, which is a hyperbolic tangent function with a slope of 50Nms/rad, as described by (3.67), is shown in Figure 3.26, and the chosen parameter values for Specker's friction model are given in Table 3.6.

$$T_f(t) = F_C \tanh\left(50\dot{\theta}_c(t)\right) \tag{3.67}$$

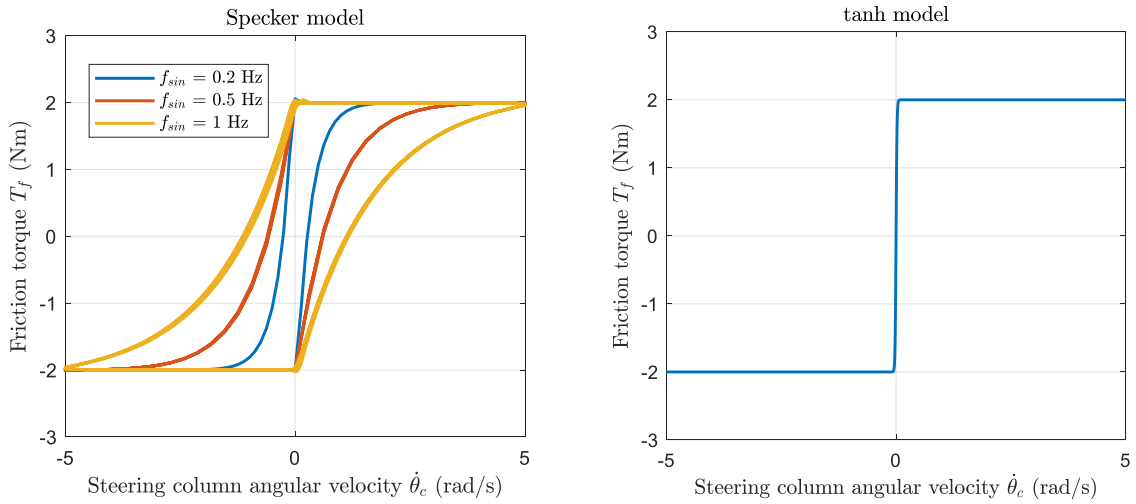

Figure 3.26: Nonlinear friction-velocity characteristics with various frequencies.

Table 3.6: Specker's friction model parameter values

Parameters	$\dot{\theta}_{ct}$	$\dot{\theta}_{c0}$	T_1	F_c
Units	rad/s	rad/s	s	Nm
Values	0.02	0.05	0.05	2

3.4.2 Extended Kalman Filter for State Estimation and Gamma Activation

An extended Kalman filter, which works on the same principles as the linear Kalman filter, is used to estimate the states of the nonlinear plant. In the extended Kalman filter algorithm, the nonlinear plant

dynamics are approximated by linearisation or other transformations through Taylor Series. Nash and Cole [4] implemented several variations of the extended Kalman filter and found that a first-order extended Kalman filter (EKF1), which calculates the first-order linearised approximation to the plant states at each time step, is the most appropriate one in terms of accuracy and computational speed. Although this could serve as an initial guideline for selecting the state estimator, by accounting for the difference in the nonlinearities, both a first-order extended Kalman filter (EKF1) and a second-order extended Kalman filter (EKF2) are implemented.

Detailed descriptions of EKF1 and EKF2 for generic problems can be found in [133]. Similar to the linear Kalman filter, the algorithm is formed by two stages at each time step: the predict stage involves predicting a new state estimate using the previous estimate processing the internal model of the plant, followed by the update stage, which involves updating the estimate by incorporating the difference between predicted and measured plant outputs.

For EKF1, initially, an estimate of the states $\boldsymbol{x}_e(k+1|k)$ is predicted by propagating the current input $\alpha(k)$ and state estimate $\boldsymbol{x}_e(k)$ through the internal mental model:

$$\boldsymbol{x}_e(k+1|k) = \widehat{\mathbf{A}}\big(\boldsymbol{x}_e(k)\big) + \mathbf{B}\alpha(k) \tag{3.68}$$

The prediction error state covariance matrix $\mathbf{P}(k+1|k)$ is given by:

$$\mathbf{P}(k+1|k) = \mathbf{A}_\mathbf{J}\big(\boldsymbol{x}_e(k)\big)\mathbf{P}(k)\mathbf{A}_\mathbf{J}^T\big(\boldsymbol{x}_e(k)\big) + \widehat{\mathbf{Q}}_{\mathrm{KF}}(k) \tag{3.69}$$

where $\widehat{\mathbf{A}}$ is a general nonlinear function. The nonlinear function $\widehat{\mathbf{A}}$ is linearised about state estimate $\boldsymbol{x}_e(k)$ by expanding Taylor Series and retaining $\mathbf{A}_\mathbf{J}$, which is the Jacobian $\mathrm{d}\widehat{\mathbf{A}}/\mathrm{d}\boldsymbol{x}$ evaluated at $\boldsymbol{x}_e(k)$.

The correction is then added based on the error between the previous estimated output $\mathbf{C}\boldsymbol{x}_e(k+1|k)$ and measured output $\boldsymbol{z}(k+1) + \boldsymbol{v}(k+1)$, weighted by the 'Kalman gain' $\mathbf{K}(k+1)$

$$\boldsymbol{x}_e(k+1) = \boldsymbol{x}_e(k+1|k) + \mathbf{K}(k+1)\{\boldsymbol{z}(k+1) + \boldsymbol{v}(k+1) - \mathbf{C}\boldsymbol{x}_e(k+1|k)\} \tag{3.70}$$

where the 'Kalman gain' $\mathbf{K}(k+1)$ is calculated by achieving a statistically optimal minimum-variance estimate based on the concept of MLE:

$$\mathbf{K}(k+1) = \mathbf{P}(k+1|k)\mathbf{C}\big(\mathbf{C}\mathbf{P}(k+1|k)\mathbf{C}^T + \mathbf{R}_{\mathrm{KF}}(k+1)\big)^{-1} \tag{3.71}$$

and the state covariance matrix $\mathbf{P}(k+1)$ is updated through:

$$\mathbf{P}(k+1) = (\mathbf{I} - \mathbf{K}(k+1)\mathbf{C})\mathbf{P}(k+1|k) \tag{3.72}$$

It is seen that unlike the steady-state linear Kalman filter used in Section 3.2.8, the covariance matrix $\mathbf{P}$ changes with time. The prediction error state covariance matrix $\mathbf{P}(1|0)$ is chosen as the one calculated in the linear Kalman filter and is then updated through the update stage. EKF2 is implemented by

finding a quadratic approximation to the plant states at each time step, which is achieved by retaining one more term of the Taylor series expansions. In EKF2, $\mathbf{A_H}$, which is the Hessian $\mathrm{d}\widehat{\mathbf{A}}^2/\mathrm{d}^2\boldsymbol{x}$ evaluated at $\boldsymbol{x}_e(k)$, needs to be calculated.

It is assumed that the covariances of the process and measurement noise are time-invariant, therefore $\widehat{\mathbf{Q}}_{\mathrm{KF}}$ and $\mathbf{R}_{\mathrm{KF}}$ are always set to the covariance matrices used in the linear driver-steering-vehicle model.

Like Section 3.2.8, the gamma activation process is still incorporated into the extended Kalman filter. The expected muscle angle is extracted from the predict stage using the internal model of the plant.

3.4.2 Model Predictive Control

The model predictive control (MPC) method is designed to calculate an optimal plant input α using the internal model of the plant. To save computation time, the system dynamics is linearised, as suggested by Nash and Cole [4]. The linearised MPC (LMPC) calculates an optimal control sequence $\boldsymbol{\alpha}$ up to the prediction horizon T_p ($N_p = T_p/T_s$ time steps), then applies the first element of the optimal control sequence to the plant, at which point a new optimal control sequence is calculated, and the process continues.

To reduce the computational load of the MPC method, a reduced plant is defined, which includes only the states required by the controller, as shown in Figure 3.27. The target path is implemented as a reference without being included in the reduced plant. The controller minimises a cost function weighting the shifted lateral deviation of the vehicle from the target path (path following error) and the plant input α. Therefore, any part of the plant which does not feed into the shifted path following error is ignored.

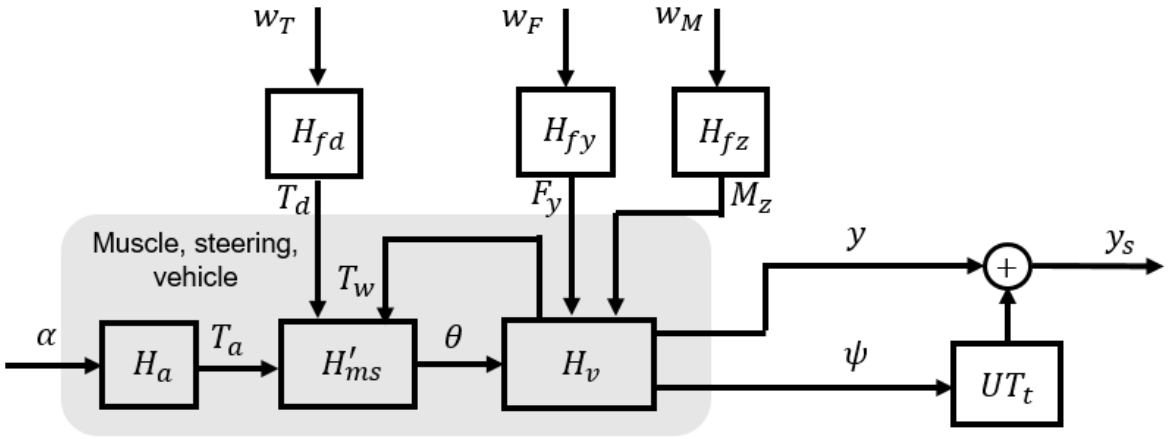

Figure 3.27: Structure of the reduced plant used for MPC in the new nonlinear driver-steering-vehicle model. H'_{ms} represents muscle dynamics and steering system with nonlinear steering friction. The definitions of all the other blocks are unchanged from those in Section 3.2.

The discrete-time state-space form of the reduced plant shown in Figure 3.35 without the nonlinear friction (setting the steering system friction to zero but keeping involving T_f notation in the state-space equation) is given by:

$$\boldsymbol{x}_R(k+1) = \mathbf{A}_R\boldsymbol{x}(k) + \mathbf{B}_R\alpha(k) + [\mathbf{B}_R \quad \mathbf{G}_{RF} \quad \mathbf{G}_{RM} \quad \mathbf{G}_{RT}]\{w(k) \quad w_F(k) \quad w_M(k) \quad w_T(k)\}^T \tag{3.73}$$

$$y_s(k) = \mathbf{C}_R\boldsymbol{x}(k) \tag{3.74}$$

where $\boldsymbol{x}(k) = \{\boldsymbol{x}_{fy}(k) \quad \boldsymbol{x}_{fz}(k) \quad \boldsymbol{x}_{fd}(k) \quad \boldsymbol{x}'_{msv}(k) \quad \boldsymbol{x}_a(k)\}^T$,

$$\mathbf{A}_R = \begin{bmatrix} \mathbf{A}_{fy} & \mathbf{0} & \mathbf{0} & \mathbf{0} & \mathbf{0} \\ \mathbf{0} & \mathbf{A}_{fz} & \mathbf{0} & \mathbf{0} & \mathbf{0} \\ \mathbf{0} & \mathbf{0} & \mathbf{A}_{fd} & \mathbf{0} & \mathbf{0} \\ \mathbf{B}'_{msv(:,2)}\mathbf{C}_{fy} & \mathbf{B}'_{msv(:,3)}\mathbf{C}_{fz} & \mathbf{B}'_{msv(:,4)}\mathbf{C}_{fd} & \mathbf{A}_{msv} & \mathbf{B}'_{msv(:,1)}\mathbf{C}_a \\ \mathbf{0} & \mathbf{0} & \mathbf{0} & \mathbf{0} & \mathbf{A}_a \end{bmatrix}$$

$\mathbf{B}_R = [\mathbf{0} \quad \mathbf{0} \quad \mathbf{0} \quad \mathbf{0} \quad \mathbf{B}_a]^T$

$\mathbf{G}_{RF} = [\mathbf{B}_{fy} \quad \mathbf{0} \quad \mathbf{0} \quad \mathbf{0} \quad \mathbf{0}]^T$

$\mathbf{G}_{RM} = [\mathbf{0} \quad \mathbf{B}_{fz} \quad \mathbf{0} \quad \mathbf{0} \quad \mathbf{0}]^T$

$\mathbf{G}_{RT} = [\mathbf{0} \quad \mathbf{0} \quad \mathbf{B}_{fd} \quad \mathbf{0} \quad \mathbf{0}]^T$

$\mathbf{C}_R = [\mathbf{0} \quad \mathbf{0} \quad \mathbf{0} \quad \mathbf{C}_{Rmsv} \quad \mathbf{0}]$ and $\mathbf{C}_{Rmsv} = [1 \quad 0 \quad UT_t \quad 0 \quad 0 \quad 0 \quad 0 \quad 0 \quad 0 \quad 0]$

$\mathbf{0}$ is a matrix of zeros, $\mathbf{M}_{(i,j)}$ indicates the ith row and jth column of matrix $\mathbf{M}$ and ':' represents the entire row or column of the matrix. Ignoring any Gaussian white noise and adding the nonlinear friction in the system, the discrete-time state-space form of the nonlinear reduced plant is given by:

$$\boldsymbol{x}_R(k+1) = \widehat{\mathbf{A}}_R\big(\boldsymbol{x}_R(k)\big) + \mathbf{B}_R\alpha(k) \tag{3.75}$$

$$y_s(k) = \mathbf{C}_R\boldsymbol{x}_R(k) \tag{3.76}$$

where $\widehat{\mathbf{A}}_R$ is a general nonlinear function. The nonlinear function $\widehat{\mathbf{A}}_R$ can be linearised about states $\boldsymbol{x}_L$ with the approximation:

$$\widehat{\mathbf{A}}_R\big(\boldsymbol{x}_R(k+n)\big) \approx \widehat{\mathbf{A}}_R\big(\boldsymbol{x}_L(k+n)\big) + \widehat{\mathbf{A}}_n\big(\boldsymbol{x}_R(k+n) - \boldsymbol{x}_L(k+n)\big) \tag{3.77}$$

where $\widehat{\mathbf{A}}_n$ is the Jacobian $\mathrm{d}\widehat{\mathbf{A}}_R/\mathrm{d}\boldsymbol{x}$ evaluated at $\boldsymbol{x}_L(k+n)$. The reduced state vector $\boldsymbol{x}_R(k)$ and the reference trajectory $r_e(k)$ can be extracted directly from the corresponding states in $\boldsymbol{x}_e(k)$.

Nash and Cole [20] implemented several simplified controllers by linearising the plant to different extents and found that the LPF (Linearising the system about the predicted state at each time step up to the full prediction horizon) controller provides the best trade-off between control performance and

control speed. Therefore, the LMPC in this work is derived based on the LPF algorithm. Although the driver does not know the future target path in this work, it is assumed that the driver's visual system previews $(N_p + 1)$ points of the current target lateral position. However, to compensate for the human driver's visual delay, the controller only evaluates the reduced plant equations from the current time step k to $(k + N_p - N_{vi} + 1)$. The control horizon is set equal to the prediction horizon for simplicity. The solution of the LMPC, a sequence of the optimal control sequence $\boldsymbol{\alpha}$, starts from a nominal control sequence $\boldsymbol{\alpha}_0$, which is the previous optimal control sequence shifted by one time step, with a corresponding state trajectory $\boldsymbol{X}_{R0} = [\boldsymbol{x}_{R0}\,(k)\ \ldots\ \boldsymbol{x}_{R0}\,(k + N_p - N_{vi} + 1)]$. The linearised matrix $\widehat{\mathbf{A}}_n$ is calculated about each nominal state $\boldsymbol{x}_L\,(k + n) = \boldsymbol{x}_{R0}\,(k + n)$. The controller aims to minimise the cost function over the full prediction horizon:

$$J = \sum_{k=1}^{N_p - N_{vi} + 1} \{q_e[y_s(k + n) - r_e(k)]^2 + q_\alpha \alpha(k + n)^2\} \tag{3.78}$$

Writing the values of r_e, y_s and α over the prediction horizon as vectors $\boldsymbol{r}_e$, $\boldsymbol{y}_s$ and $\boldsymbol{\alpha}$, and removing the r_e^2 term which is not affected the control input, (3.78) is written as:

$$J = q_e \boldsymbol{y}_s^T \boldsymbol{y}_s - 2q_e \boldsymbol{r}_e^T \boldsymbol{y}_s + q_\alpha \boldsymbol{\alpha}^T \boldsymbol{\alpha} \tag{3.79}$$

Substituting a nominal sequence $\boldsymbol{\alpha}_0$ and a small change $\Delta\boldsymbol{\alpha}$ for the control sequence $\boldsymbol{\alpha}$, and similarly for $\boldsymbol{y}_s$, gives

$$J = q_e(\boldsymbol{y}_{s0} + \Delta\boldsymbol{y}_s)^T(\boldsymbol{y}_{s0} + \Delta\boldsymbol{y}_s) - 2q_e \boldsymbol{r}_e^T(\boldsymbol{y}_{s0} + \Delta\boldsymbol{y}_s) + q_\alpha(\boldsymbol{\alpha}_0 + \Delta\boldsymbol{\alpha})^T(\boldsymbol{\alpha}_0 + \Delta\boldsymbol{\alpha}) \tag{3.80}$$

Simplifying (3.80) and removing the independent terms result in:

$$J = q_e \Delta\boldsymbol{y}_s{}^T \Delta\boldsymbol{y}_s + 2q_e(\boldsymbol{y}_{s0} - \boldsymbol{r}_e)^T \Delta\boldsymbol{y}_s + q_\alpha \Delta\boldsymbol{\alpha}^T \Delta\boldsymbol{\alpha} + 2q_\alpha \boldsymbol{\alpha}_0^T \Delta\boldsymbol{\alpha} \tag{3.81}$$

The linearised dynamics give the approximate relationship $\Delta\boldsymbol{y}_s = \boldsymbol{\Theta}\Delta\boldsymbol{\alpha}$. (3.81) is then modified to a quadratic program form:

$$J = \Delta\boldsymbol{\alpha}^T\left(q_e \boldsymbol{\Theta}^{\mathrm{T}}\boldsymbol{\Theta} + q_\alpha \mathbf{I}\right)\Delta\boldsymbol{\alpha} + 2(q_e(\boldsymbol{y}_{s0} - \boldsymbol{r}_e)^T \boldsymbol{\Theta} + q_\alpha \boldsymbol{\alpha}_0^T)\Delta\boldsymbol{\alpha} \tag{3.82}$$

Similar to the linear MPC derivation in [7], with the linearised matrices $\widehat{\mathbf{A}}_n$ predicted n time steps ahead of the current time step k, $\boldsymbol{\Theta}$ is found from:

$$\boldsymbol{\Theta}(k) = \begin{bmatrix} \mathbf{C}_{\mathrm{R}}\mathbf{B}_{\mathrm{R}} & \mathbf{0} & \mathbf{0} & \cdots & \mathbf{0} \\ \mathbf{C}_{\mathrm{R}}\widehat{\boldsymbol{A_1}}\mathbf{B}_{\mathrm{R}} & \mathbf{C}_{\mathrm{R}}\mathbf{B}_{\mathrm{R}} & \mathbf{0} & \cdots & \mathbf{0} \\ \mathbf{C}_{\mathrm{R}}\widehat{\boldsymbol{A_2}}\widehat{\boldsymbol{A_1}}\mathbf{B}_{\mathrm{R}} & \mathbf{C}_{\mathrm{R}}\widehat{\boldsymbol{A_2}}\mathbf{B}_{\mathrm{R}} & \mathbf{C}_{\mathrm{R}}\mathbf{B}_{\mathrm{R}} & \cdots & \mathbf{0} \\ \vdots & \vdots & \vdots & \ddots & \vdots \\ \mathbf{C}_{\mathrm{R}}\left(\prod_{i=1}^{N_p - N_{vi}} \widehat{\boldsymbol{A_\iota}}\right)\mathbf{B}_{\mathrm{R}} & \mathbf{C}_{\mathrm{R}}\left(\prod_{i=2}^{N_p - N_{vi}} \widehat{\boldsymbol{A_\iota}}\right)\mathbf{B}_{\mathrm{R}} & \mathbf{C}_{\mathrm{R}}\left(\prod_{i=3}^{N_p - N_{vi}} \widehat{\boldsymbol{A_\iota}}\right)\mathbf{B}_{\mathrm{R}} & \cdots & \mathbf{C}_{\mathrm{R}}\mathbf{B}_{\mathrm{R}} \end{bmatrix} \tag{3.83}$$

$\boldsymbol{y}_{s0}$ is obtained by evaluating the nonlinear plant equations (3.75) and (3.76) over the prediction horizon using $\boldsymbol{\alpha}_0$. Equation (3.82) is solved by using a quadratic programming solver such as Matlab's *quadprog* function. Alternatively, this can be solved by using QR decomposition as in [90].

Besides the LMPC, a fully nonlinear MPC (NMPC) method is also implemented with the goal of finding a solution that fully incorporates the nonlinear dynamics of the plant without any approximation. In the NMPC method, Matlab's *fminunc* function is chosen as the nonlinear optimisation solver. However, other commercial nonlinear optimisation solvers, such as IPOPT [134], can also be used. The optimal control sequence is formed by a nominal sequence $\boldsymbol{\alpha}_0$ plus a small change $\Delta\boldsymbol{\alpha}$. In the optimisation, the cost function is iteratively evaluated by the solver for different values of $\Delta\boldsymbol{\alpha}$, and for each value of $\Delta\boldsymbol{\alpha}$, the full nonlinear reduced plant equations are calculated over the entire prediction horizon. *fminunc* is a gradient-based optimisation solver and uses the Jacobian, which is the first-order derivative, of the cost function to identify the direction of search for the optimal solution. The Jacobian of the cost function is given by:

$$\frac{\mathrm{d}J}{\mathrm{d}\boldsymbol{\alpha}} = 2(q_e(\boldsymbol{y}_s - \boldsymbol{r}_e)^T\boldsymbol{\Theta} + q_\alpha\boldsymbol{\alpha}^T) \tag{3.84}$$

3.5 Simulation Study of Nonlinear Model

Compared with the linear driver-steering-vehicle model described in Section 3.2, steering system friction is implemented as a nonlinear component in the plant, and an EKF and a MPC method are used to represent the human drivers' state estimation and gamma activation, and control for the nonlinear plant. In this section, the effects of the nonlinear steering system friction on the steering properties are investigated through simulations of the open-loop nonlinear steering-vehicle model first. Then the performance of the nonlinear driver model is compared with that of the linear driver model through simulations of the closed-loop driver-steering-vehicle model.

3.5.1 Simulation Study of Friction Model Parameters

In this section, the open-loop steering-vehicle model with nonlinear steering system friction is simulated. A diagram showing the nonlinear steering system model with a steering wheel torque input from the driver T_{sw} is presented in Figure 3.28. Like Section 3.3.1, there is no assist torque from the driving assist system and no steering column torque disturbance. The values of the steering-vehicle system parameters are given in Table 3.1.

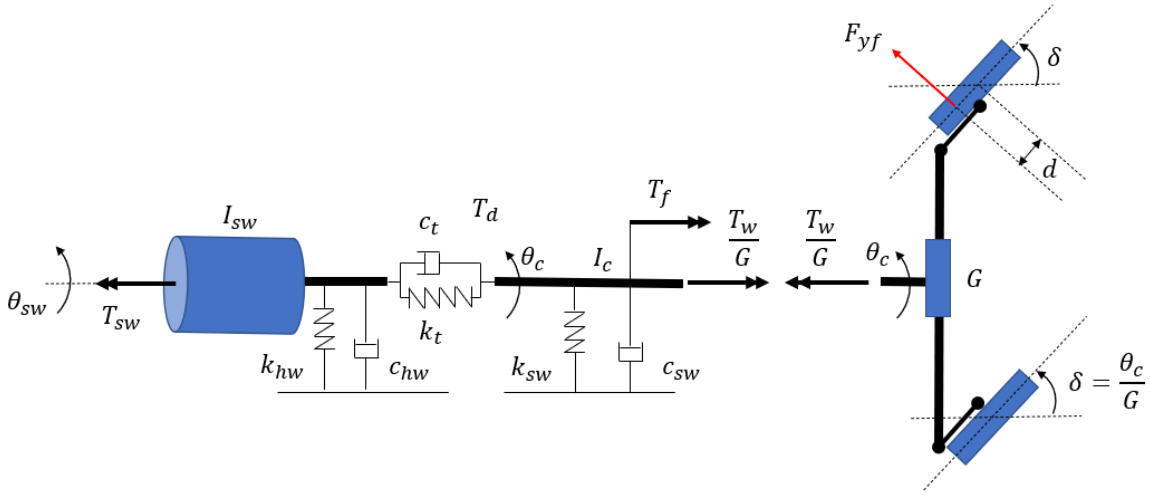

Figure 3.28: Nonlinear steering system model with external steering wheel torque input. The springs and dampers act in rotation.

Figure 3.29 show the cross-plots of the steering wheel torque input and two states of the steering-vehicle system, namely steering wheel angle θ_{sw} and vehicle lateral acceleration a_y, with various values of steering system friction magnitude F_c. The basic friction level is around 1.6Nm as suggested by [131] from TME. The steering-vehicle system is subject to a 0.2Hz sinusoidal steering wheel torque input with an amplitude of 2Nm. On examining these cross plots, the friction effect is noticed immediately by the widening of the hysteresis of the cross-plots containing the applied steering wheel torque T_{sw} and by the decrease in the maximum values of the system states. This is consistent with what is expected since part of the applied steering wheel torque T_{sw} is offset by the steering system friction torque T_f and hence more steering wheel torque needs to be applied to the steering wheel for the same level of steering-vehicle system response magnitude. In addition, it is noticed that there is a significant torque difference for an infinitesimal change in the value of system states at each end of the hysteresis curves. This is because as the steering wheel angular velocity changes sign, the friction torque goes from around $+F_C$ to $-F_c$, resulting in an immediate change in steering torque. The observed effects of steering system friction are comparable with those found by Harnett [33] and Pfeffer [58], who analysed the objective assessment of steering feel with nonlinearities in the steering system.

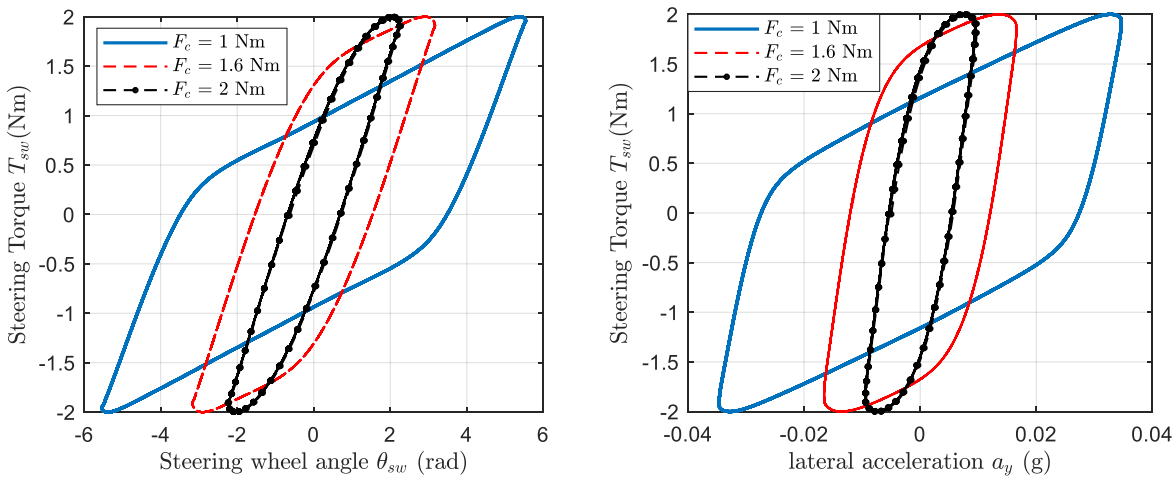

Figure 3.29: Cross-plots of the states of the steering-vehicle system operated at 2Nm steering torque and 0.2Hz. The hysteresis loops are formed clockwise.

3.5.2 Comparison between the Linear and Nonlinear Driver Models

In this section, simulations are carried out with various combinations of state estimators and controllers derived in Section 3.2 and Section 3.4, in order to evaluate the performance in terms of both state estimation and path-following accuracy, as well as to evaluate the computational load of each combination. In all simulations, nonlinear steering system friction with magnitude $F_c = 2$Nm is applied to the steering model, and the task for the driver is to reject the disturbances acting on the steering-vehicle system and/or follow a randomly moving target path for 30 seconds. There is no process or measurement noise in the simulation. The simulation conditions are summarised in Table 3.7. The closed-loop driver-steering-vehicle model parameters are given in Table 3.1 and Table 3.2.

Table 3.7: Summary of simulation conditions

	Disturbance amplitudes			
Sim. condition	W_r(m)	W_F(N)	W_M(N)	W_T(Nm)
1	8	0	0	0
2	0	2190	0	0
3	0	0	2160	0
4	8	0	0	4
5	8	2190	2160	4

Different combinations of state estimators and controllers implemented in each of the simulation conditions are summarised in Table 3.8. In combinations C1 and C2, LQR and a linear Kalman filter

are used. However, unlike the case where the actual plant is linear, the linear Kalman filter here is time-varying. The detailed derivations of the time-varying linear Kalman filter are similar to EKF1, which are given by equations 3.68 to 3.72, and therefore not repeated here. In these two combinations, the internal mental model of the driver-steering-vehicle dynamics must be linear. In C1, the internal mental model is set equal to the linear part of the nonlinear plant, which means the steering system friction torque is 0Nm. In C2, the internal mental model is set equal to the linear part of the nonlinear plant plus an equivalent damping term $C_{sw}{}'$ of the steering system friction. The damping term $C_{sw}{}'$ is placed in parallel with C_{sw}, which is between the inertia of the rack and the front wheels I_c and the ground, as shown in Figure 3.5. The value of $C_{sw}{}'$ is chosen by equating the dissipated energy from the nonlinear friction, assuming that the steering-vehicle system is operated at 1Hz, which is a normal operating frequency of a human driver in disturbance rejection tasks. The details about how $C_{sw}{}'$ is calculated are given by (3.85) and (3.86).

By assuming that the steering action is a sinusoidal signal, the energy dissipated over each cycle W_f is:

$$W_f = 4F_c\Theta_{sw} \tag{3.85}$$

where Θ_{sw} is the steering wheel angle amplitude and can be approximated through preliminary simulations. Meanwhile, the energy lost per cycle in a damper in a harmonically forced system could be expressed as:

$$W_d = 2\pi^2 C_{sw}{}' f \Theta_{sw}^2 \tag{3.86}$$

Therefore, the equivalent viscous damping constant is given by:

$$C_{sw}{}' = \frac{2F_c}{\pi^2 f \Theta_{sw}} \tag{3.87}$$

In C3, C4 and C5, different combinations of extended Kalman filters (EKF1 and EKF2) and MPC methods (LMPC and NMPC) are implemented. In these cases, the internal mental model of the driver-steering-vehicle dynamics is set equal to the actual nonlinear plant. The MPC preview horizon T_p is set to 3s in the simulation. This could make the finite-horizon MPC approximate an infinite-horizon controller and make the MPC and the LQR controllers perform similarly to each other when the cost function weight on the path-following error q_e is set to the same value for the linear models.

Table 3.8: Combinations of the state estimators and controllers with corresponding internal models

Combination	Internal model of the plant	Controller and state estimator
C1	The linear part of the nonlinear plant only	LQR with LKF
C2	The linear part of the nonlinear plant plus an equivalent damping term of the steering system friction $C_{sw}{}'$	LQR with LKF
C3	Real nonlinear plant	LMPC with EKF1
C4	Real nonlinear plant	LMPC with EKF2
C5	Real nonlinear plant	NMPC with EKF2

To assess the performance of each combination of state estimator and controller, the RMS value of the state estimation error for each sensory measurement and the RMS value of the path-following error over each simulation are found. The results for different simulation conditions are summarised in Figure 3.30- 3.34. As expected, it is shown that the nonlinear driver models (C3, C4 and C5) perform much better than the linear ones (C1 and C2) overall as more accurate internal mental models of the nonlinear plant are able to be implemented. When comparing the results of C3 and C4, the two extended Kalman filters perform very similarly, although EKF2 gives the smallest state estimation errors for the three measured signals in all the simulation conditions. In terms of controller performance, the NMPC is generally the best performing controller as the full nonlinear dynamics is captured, which is evidenced by the smallest path-following errors under all the simulations. However, the LMPC performs similarly to the NMPC in all the conditions. This suggests that the linearisation method used in the LMPC could properly approximate the nonlinear dynamics. The computational time is another important factor when considering which state estimator and controller combination should be used for practical engineering applications. The averaged computational time required for each state estimator and controller combination over all the simulation conditions is recorded in Table 3.9. There are significant differences in the orders of magnitudes of the computational time between the several proposed combinations of state estimator and controller. The slowest combination C5 takes about 4000 times longer time to run compared with the fastest combination C1. In general, it is shown in Figure 3.30- 3.34 that there is an inverse relationship between the state estimation and control accuracy and the computational speed of each combination. C5 achieves the smallest state estimation and path-following errors due to that the full nonlinear dynamics is considered as expected, however C3 with the linearised system dynamics performs as well as C5 in all the conditions and is much faster. Therefore, C3 can be used to represent the state estimation and control of a driver capturing the full nonlinear dynamics in an accurate and computationally efficient way.

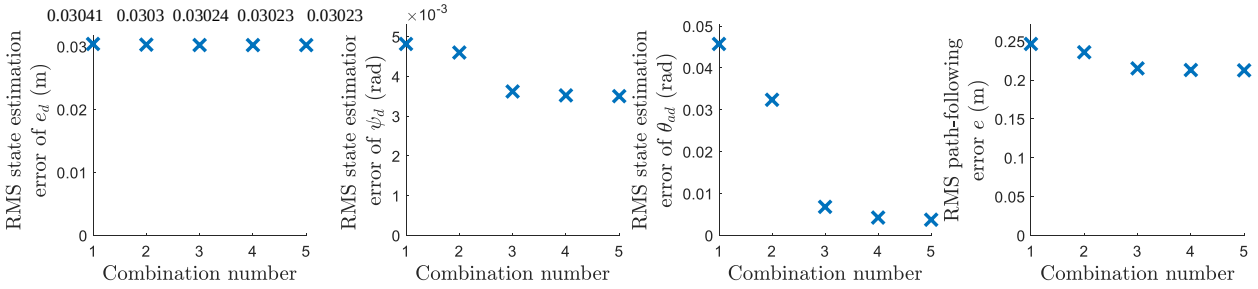

Figure 3.30: State estimation and path-following performance for different combinations listed in Table 3.8 in simulation condition 1.

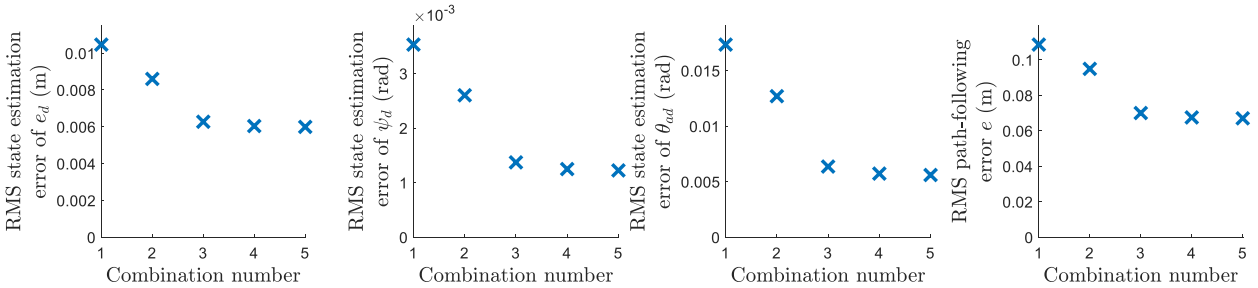

Figure 3.31: State estimation and path-following performance for different combinations listed in Table 3.8 in simulation condition 2.

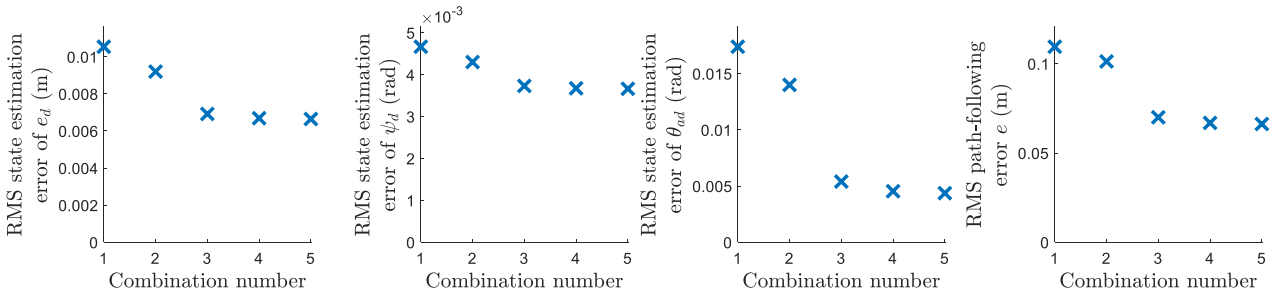

Figure 3.32: State estimation and path-following performance for different combinations listed in Table 3.8 in simulation condition 3.

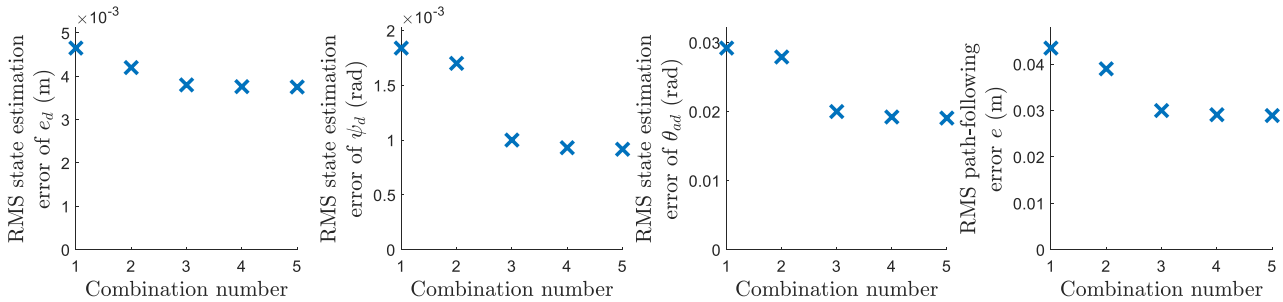

Figure 3.33: State estimation and path-following performance for different combinations listed in Table 3.8 in simulation condition 4.

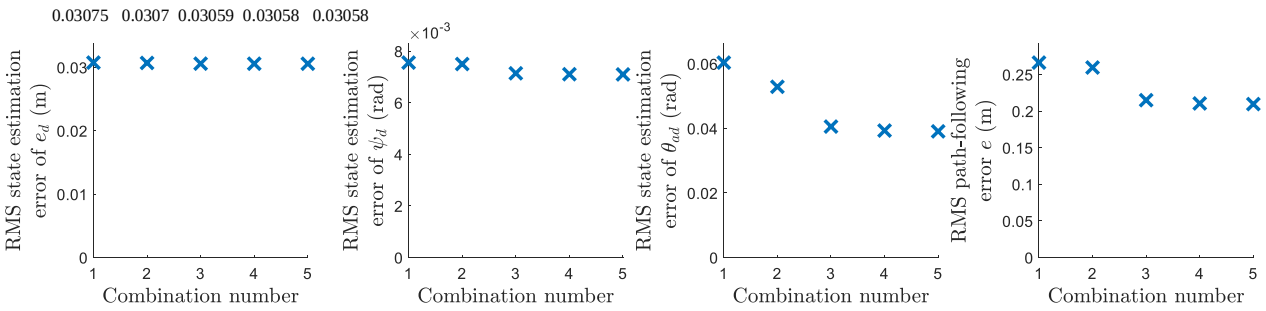

Figure 3.34: State estimation and path-following performance for different combinations listed in Table 3.8 in simulation condition 5.

Table 3.9: Computation time required for each combination.

Combination	C1	C2	C3	C4	C5
Simulation time	3.07 s	4.22 s	68 s	80 s	192 min

3.6 Conclusions

A new driver-steering-vehicle model incorporating steering torque feedback and state estimation has been developed, and then been extended to control a vehicle with nonlinear steering dynamics, especially steering system friction. The novelty of the model is the inclusion of the three important brain functions of perception, cognition and action, all three of which are governed by a single internal model of the plant. The model was conceived to provide a theoretical understanding of the human driver's subjective responses to steering torque feedback, especially in the on-centre regime. A comprehensive parameter study was conducted to investigate the effects of the model parameters on the model behaviours.

The effects of steering system parameters on the dynamic behaviour of the steering-vehicle system and the objective steering feel metrics (Table 3.4) have been demonstrated by using the steering-vehicle model, which can provide some initial guidelines for the steering system design. These results are consistent with published literature.

The neuromuscular dynamics has been modelled with the stretch reflex. The modelling of tensing (co-contracting) the muscles are reflected by the variation of parameters in the neuromuscular dynamics model. The passive damping resisting stretching of the muscle fibre is able to damp out muscle torques across a wide range of frequencies and the magnitude of the torque transmitted by the muscle to the steering wheel is determined by the tendon stiffness. The stretch reflex gain in the model has the effect of increasing the stiffness of the arms and introducing a lightly damped resonance.

The LQG framework has been used to model the driver's cognitive behaviour for the linear model. The ratios between the values of the process and measurement noise covariance matrices in the Kalman filter indicate how the known input and sensory measurements are weighted in the state estimation: as one of the values in the noise covariance matrices increases, the corresponding signal will be trusted less, and the Kalman filter will rely more on the other signals for state estimation. A cost function in the LQR controller allows the trade-off between path-following accuracy and control effort to be set.

Simulations were run to compare various combinations of state estimator and controller for the nonlinear model. In general, there is a trade-off between computation time and state estimation and control performance. The EKF and MPC methods perform much better than the LQG framework as the nonlinear dynamics are considered in the internal mental model. However, the computational time of the nonlinear driver model is much longer than that of the linear driver model. In choosing the state estimator and controller combination for the nonlinear driver model, the two versions of EKF (EKF1 and EKF2) and the two versions of the MPC method (LMPC and NMPC) perform similarly based on the simulation results, however EKF2 and NMPC take much longer to run compared to EKF1 and LMPC. Therefore, it is sensible to implement the quickest combination (EKF1 and LMPC), which involves a linear approximation to the nonlinear dynamics for the nonlinear driver model as an accurate and computationally efficient way. These findings are in consistent with those obtained by Nash and Cole [20].

Chapter 4

Driving Simulator Experiments

4.1 Introduction

This chapter presents a series of driving experiments performed on a fixed-base driving simulator to replicate real-world driving scenarios. There were two primary purposes for collecting data from these experiments. Firstly, the objective and subjective experimental data were used to analyse the behaviour of test drivers when they try to steer vehicles with different steering properties to follow the randomly moving target path and compensate for the disturbances acting on the steering-vehicle system, especially in the on-centre operating regime. Secondly, the experimental data was also used to identify and validate the driver-steering-vehicle model developed in Chapter 3.

The hardware used for the driving simulator experiments is briefly introduced at the beginning of this chapter, including the fixed-base driving simulator, a force and torque transducer (load cell), and a servo-motor. The calibration work for the hardware is then presented. The software of the fixed-base driving simulator introduced in this chapter is mainly the test steering and vehicle system model. Following the introduction of the driving simulator hardware and software, procedures of the driving experiments are introduced. Eleven trials were included in the experiments and thirteen test subjects were involved. Each trial stands for a particular combination of disturbances acting on the steering and vehicle system and steering-vehicle configuration. The experimental data and corresponding discussions of these trials are presented in Section 4.4 and Section 4.5. The data reflect the responses of the vehicle and the driver during the driving tasks. During the experiments, the test drivers were also asked to rate several subjective criteria regarding the steering performance. The analysis of the subjective data and its correlation with objective metrics taken in the experiments is given in Section 4.6. Conclusions from the experiments are given in Section 4.7.

4.2 Driving Simulator Hardware and Software

4.2.1 Introduction

The driving simulator experiments were carried out mainly using the fixed-base driving simulator at the Department of Engineering, University of Cambridge (CUED). This simulator consists of three commercial 4K 65-inch Samsung displays providing the driver with a 138 degrees field of view of the road path, a host PC controlling the driving simulator program, a target PC and a graphics PC running the steering-vehicle system model and virtual reality world in real-time, respectively, a torque feedback steering wheel driven by a torque servo-drive motor, an encoder measuring the driver steering wheel angle, and a six-axis load cell measuring the forces and torques applied by the driver to the steering wheel. A schematic representation of the configuration of the fixed-base driving simulator is shown in Figure 4.1. The critical parts of this simulator are calibrated before carrying out the experiments. The experiments were also replicated using the fixed-base driving simulator at Toyota Motor Europe (TME). The same software is implemented in the TME simulator. However, compared to the CUED simulator, the TME simulator uses a different set of hardware.

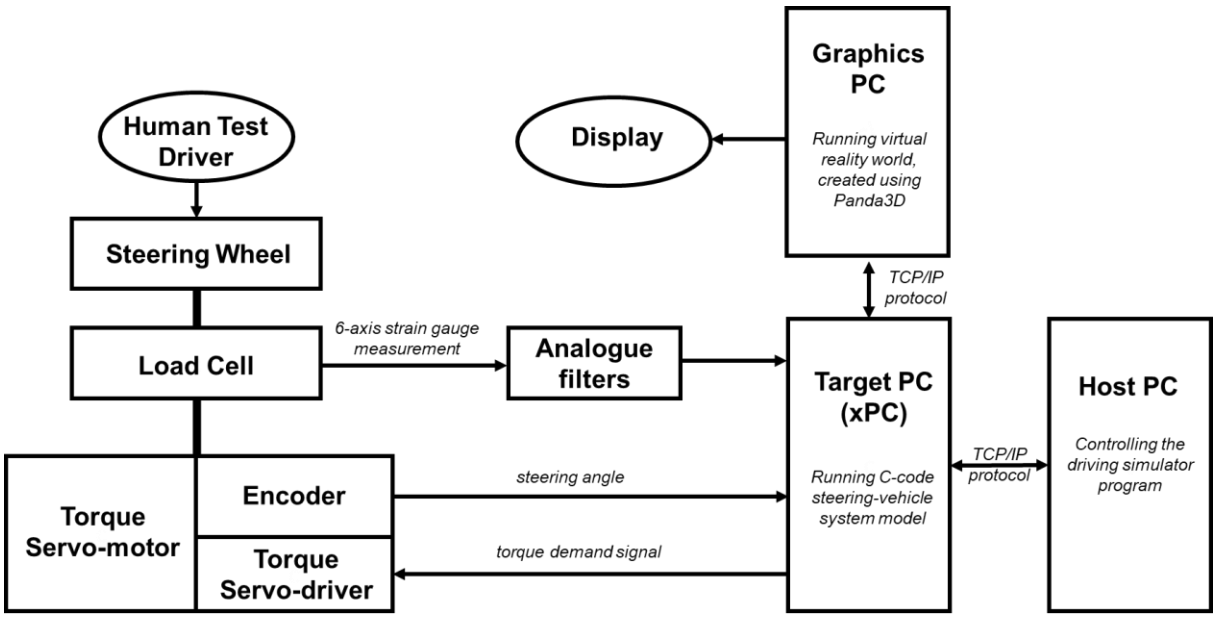

Figure 4.1: Diagram of the configuration of the CUED driving simulator.

4.2.2 Load Cell Calibration

The forces and torques applied by the driver were measured using a six-axis load cell installed on the steering column. Six pairs of strain gauges are positioned around the circle of the load cell, which has a thin-walled ‘top hat' design. Forces and torques can be measured in three orthogonal directions using

the six pairs of gauges. The outputs of all the gauges are processed by amplifiers with a gain of 2000, allowing the voltage signals to be easily collected. To ensure that the logged measured data is smoothed, the amplified signals are then processed through an analogue low-pass filter with a cut-off frequency of 100Hz.

The procedure reported by Pick [12] was carried out to calibrate the load cell. In this procedure, six different loading conditions were configurated by applying forces and torques to the load cell. The forces and torques were generated by hanging weights to a calibration lever, which replaced the steering wheel. An example of the loading condition is shown in Figure 4.2. To increase the calibration accuracy and remove any bias due to directions, a modification of the calibration procedure similar to that used by Wang [135] was adopted. This was accomplished by applying the hanging weights to the calibration lever in two directions during each loading configuration. There are a total of thirteen configurations used, which are detailed in Table 4.1. Seven different weights (including zero weight) were applied to each loading configuration, and strain gauge outputs were recorded. Loading weights were limited to 150N for direct forces and 20Nm for moments to avoid breaking the load cell. The centre of the orthogonal axis system was chosen as the mating face of the load cell and the steering wheel, as shown in Figure 4.2 as well.

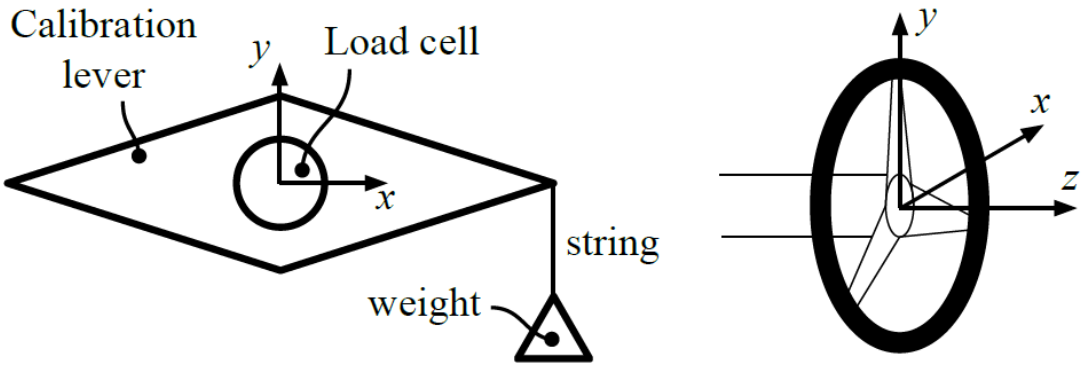

Figure 4.2: Load cell calibration set-up and orthogonal axis system of the steering wheel [135].

All six strain gauges' output voltages were combined into a voltage matrix $[V_1 \quad V_2 \quad V_3 \quad V_4 \quad V_5 \quad V_6]$ according to (4.1). In one loading condition, each row corresponds to a certain hanging weight in one direction. A force-torque matrix $[F_{hx} \quad F_{hy} \quad F_{hz} \quad M_{hx} \quad M_{hy} \quad M_{hz}]$ is used to represent the forces and torques applied by the hanging weight. As a result, using a multiple linear regression technique, a least-squared best fit to $[X]$ was obtained.

$$[V_1 \quad V_2 \quad V_3 \quad V_4 \quad V_5 \quad V_6][X] = [F_{hx} \quad F_{hy} \quad F_{hz} \quad M_{hx} \quad M_{hy} \quad M_{hz}] \tag{4.1}$$

where $[X]$ is a 6 by 6 calibration matrix; V_i is a 78-element column array (13 configurations multiplied by 6 different weights), containing the voltage outputs from the i_{th} strain gauge set in the load cell; $F_{hx,hy,hz}$ and $M_{hx,hy,hz}$ are also 78-elements column arrays containing the forces and torques applied to the load cell in x, y and z directions. It is worth noting that the voltage values when there is no loading are subtracted from each voltage reading to eliminate the effect of voltage offsets and self-weight of the calibration lever and the steering wheel. In linear regression models, the coefficient of determination (R-squared) is a goodness-of-fit measure and measures the strength of the relationship between the linear regression model and the forces and torques on a convenient 0% – 100% scale. In this analysis, all the channels achieved R-squared values larger than 97%, with the exact R-squared value for each individual of the channels shown in Table 4.2. The actual forces and moments applied to the load cell were compared with values of the forces and moments obtained by applying the calibration matrix to the measured voltages. The results showed that the forces and moments applied by the driver to the steering wheel could be accurately measured by the load cell with the identified calibration matrix, especially for steering torque measurement M_{hz}, the average error of the measurements of which is 0.30%.

Table 4.1: Loading configurations for load cell calibration.

Configuration number	F_{hx}	F_{hy}	F_{hz}	M_{hx}	M_{hy}	M_{hz}
1			+			
2		−				+
3		−				
4	+					+
5	+					
6			+		+	
7		−				−
8		+				
9	+					−
10	−					
11			+		−	
12			+	−		
13			+	+		

Note: + denotes loaded axis in positive direction, - denotes loaded axis in negative direction, F_{hi} denotes force and M_{hi} denotes moments, where i is selected from x, y or z.

Table 4.2: R-squared values of the multiple linear regression model for each individual channel

	F_{hx}	F_{hy}	F_{hz}	M_{hx}	M_{hy}	M_{hz}
R-squared	99.97%	99.99%	97.04%	99.76%	99.94%	99.88%

4.2.3 Servomotor Calibration

The servo-drive performs closed-loop control of the servomotor current in response to an analogue torque demand signal sent from the steering and vehicle system model in the target PC through the I/O card. The generated motor torque is proportional to the servomotor current. As a device for providing the feedback torque, the servomotor was calibrated. The servomotor was calibrated to find a factor that can describe the relationship between the torque demand signal and the actual motor torque by conducting an experiment. During the experiment, a sine wave torque demand signal (2V amplitude and 0.5Hz frequency) was sent to the motor. The steering wheel was rotated slowly with constant angular velocity, and the actual torque measured by the calibrated load cell was recorded. The cut-off frequencies for all the analogue low-pass filters were set to the same value, 100Hz, chosen to be low enough to prevent aliasing when the signals are sampled, and high enough to prevent significant gain or phase change in the frequency range of interest. The recorded torques and the torque demand signals were then used to generate a least-squared fitting line, as shown in Figure 4.3, and the slope of it was the calibration factor (0.986Nm/V). To check the bandwidth of the calculated calibration factor, another set of experiments was conducted, during which a series of sine wave torque demand signals with different frequencies were sent to the motor and the actual torque was measured by the calibrated load cell. The comparison between these two quantities showed that the servomotor can correctly generate the demanded steering torque for a wide range of frequencies, as shown in Figure 4.4.

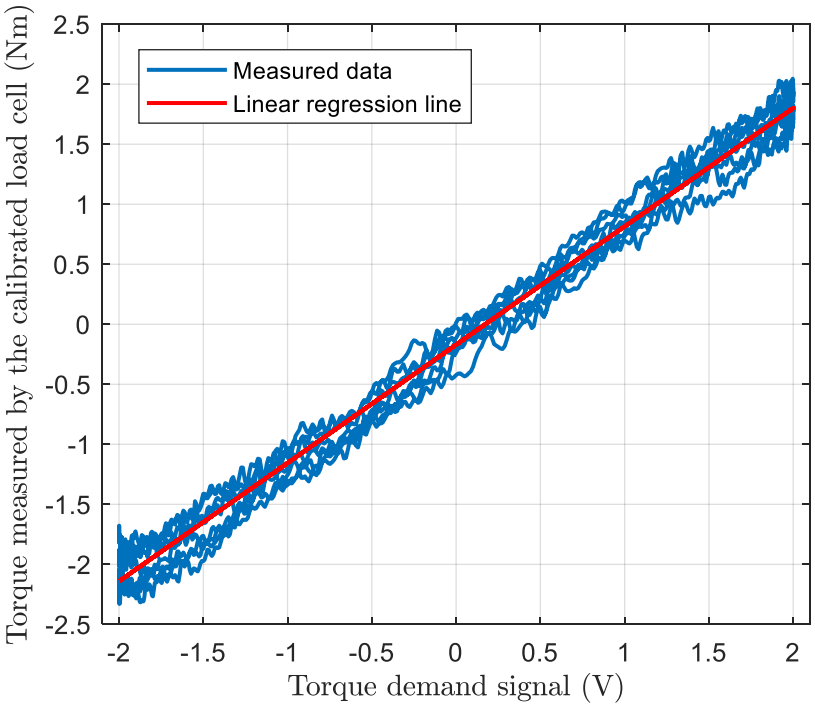

Figure 4.3: Torque demand signal (a sinusoidal signal with 2V amplitude and 0.5Hz frequency) vs. torque measured by the calibrated load cell.

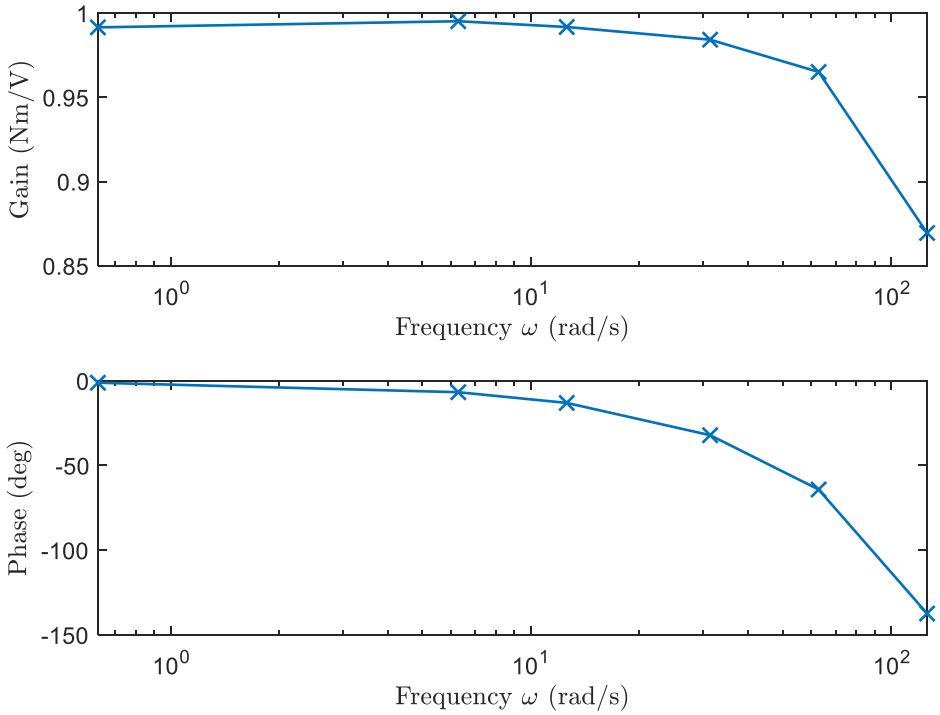

Figure 4.4: Gain and phase plots of the calibration factor in a wide range of frequencies. The measured data points are shown by the cross marks.

4.2.4 Test Steering-Vehicle Systems

The test steering-vehicle systems are realised by implementing the steering and vehicle models introduced in Chapter 3 using Matlab and Simulink in the driving simulator with a sampling frequency of 1000Hz, as shown in Figure 4.5. The PCI-6621 National Instrument Data Acquisition card (NIDA card) is used to exchange signals with the hardware. The steering wheel angle is measured by an optical quadrature encoder (Wachendorff WDGI58B) with 25,000 pulses per revolution. The output of the encoder is counted by the NIDA card to give an angular resolution of 0.0036 degrees. The measured steering wheel angle signal θ_{sw} is recorded and is differentiated to calculate steering wheel angular velocity $\dot{\theta}_{sw}$. However, the recorded wheel angle signal θ_{sw} is processed by a second-order Butterworth low-pass filter with a cut-off frequency 100Hz first to reduce the quantisation effect of the encoder. The simulated torque demand signal T_{demand} is also filtered by another by a second-order Butterworth low-pass filter with a cut-off frequency 100Hz before being sent to the servo-motor as an analogue signal via the NIDA card. Results from preliminary testing demonstrated that the practical effect of implementing these filters on the phase shift of the raw signals is negligible.

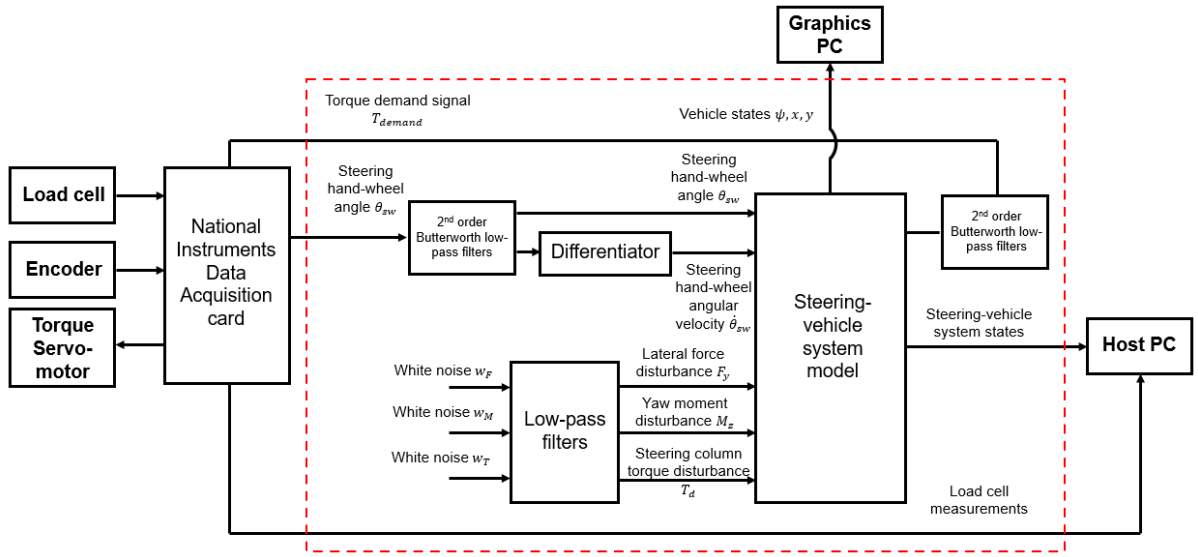

Figure 4.5: Structure of the Simulink model (enclosed by the dashed rectangle) operated by the Target PC in driving simulator and its interfaces with the hardware, the Host PC and the Graphics PC.

In terms of the steering-vehicle system model block, the vehicle model is the two-degree-of-freedom lateral-yaw 'bicycle' model with a lateral force disturbance F_y and a yaw moment M_z applied at the centre of mass, as described by Section 3.2.1 in Chapter 3. The steering model is the one described by Section 3.5.1 in Chapter 3 with assist torque from the driving assist system T_m and steering column disturbance T_d. To avoid any confusion, the steering model is shown in Figure 4.6 in this section again.

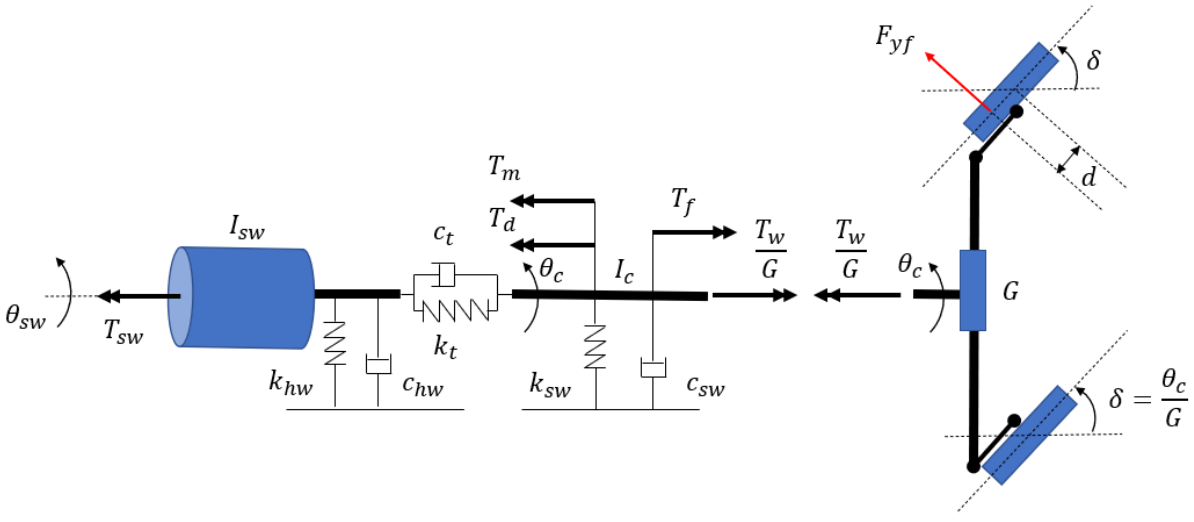

Figure 4.6: Steering system model used in the driving simulator experiments. The springs and dampers act in rotation.

Different from Chapter 3, the state-space equations of the steering-vehicle system are formulated by taking the steering wheel angle θ_{sw} as the system input and the torque demand T_{demand}, which is the

torque across the steering column stiffness k_t and the torsion bar damping c_t, as the system output. This formulation makes it more convenient to integrate this steering-vehicle system model into the driving simulator since the steering wheel angle is treated as an input to the model, and the demanded torque is treated as an output of the model. The demanded torque is fed to the servo-drive of the driving simulator's steering wheel to provide steering torque feedback to the driver. Therefore, the state-space form of the steering-vehicle system block shown in Figure 4.5 is expressed as:

$$\begin{Bmatrix} \dot{x}(t) \\ \dot{y}(t) \\ \dot{v}(t) \\ \dot{\psi}(t) \\ \dot{\omega}(t) \\ \dot{\theta}_c(t) \\ \ddot{\theta}_c(t) \end{Bmatrix} = \begin{bmatrix} 0 & 0 & 0 & 0 & 0 & 0 & 0 \\ 0 & 0 & 1 & U & 0 & 0 & 0 \\ 0 & 0 & -\dfrac{2C_f + 2C_r}{mU} & 0 & -U - \dfrac{2C_f a - 2C_r b}{mU} & \dfrac{2C_f}{Gm} & 0 \\ 0 & 0 & 0 & 0 & 1 & 0 & 0 \\ 0 & 0 & -\dfrac{2C_f a - 2C_r b}{IU} & 0 & -\dfrac{2a^2 C_f + 2b^2 C_r}{IU} & \dfrac{2C_f a}{GI} & 0 \\ 0 & 0 & 0 & 0 & 0 & 0 & 1 \\ 0 & 0 & G_1 & 0 & G_2 & G_5 & G_6 \end{bmatrix} \begin{Bmatrix} x(t) \\ y(t) \\ v(t) \\ \psi(t) \\ \omega(t) \\ \theta_c(t) \\ \dot{\theta}_c(t) \end{Bmatrix}$$

$$+ \begin{bmatrix} 0 & 0 & 0 & 0 & 0 & 0 & 0 & 1 \\ 0 & 0 & 0 & 0 & 0 & 0 & 0 & 0 \\ 0 & 0 & 0 & \dfrac{1}{m} & 0 & 0 & 0 & 0 \\ 0 & 0 & 0 & 0 & 0 & 0 & 0 & 0 \\ 0 & 0 & 0 & 0 & \dfrac{1}{I} & 0 & 0 & 0 \\ 0 & 0 & 0 & 0 & 0 & 0 & 0 & 0 \\ G_3 & G_4 & 0 & 0 & 0 & \dfrac{1}{I_c} & -\dfrac{1}{I_c} & 0 \end{bmatrix} \begin{Bmatrix} \theta_{sw}(t) \\ \dot{\theta}_{sw}(t) \\ \ddot{\theta}_{sw}(t) \\ F_y(t) \\ M_z(t) \\ T_d(t) \\ F_C \tanh\left(c\dot{\theta}_c(t)\right) \\ U \end{Bmatrix} \tag{4.2}$$

$$T_{demand} = [0 \quad 0 \quad 0 \quad 0 \quad 0 \quad -k_t \quad -c_t] \begin{Bmatrix} x(t) \\ y(t) \\ v(t) \\ \psi(t) \\ \omega(t) \\ \theta_c(t) \\ \dot{\theta}_c(t) \end{Bmatrix}$$

$$+ [k_t + k_{hw} \quad c_t + c_{hw} \quad 0 \quad 0 \quad 0 \quad 0 \quad 0 \quad 0] \begin{Bmatrix} \theta_{sw}(t) \\ \dot{\theta}_{sw}(t) \\ \ddot{\theta}_{sw}(t) \\ F_y(t) \\ M_z(t) \\ T_d(t) \\ F_C \tanh\left(c\dot{\theta}_c(t)\right) \\ U \end{Bmatrix} \tag{4.3}$$

where $G_1 = \frac{2C_f d}{GUI_c}$, $G_2 = \frac{2C_f ad}{GUI_c}$, $G_3 = \frac{(1+C_{boost})k_t}{I_c}$, $G_4 = \frac{(1+C_{boost})c_t}{I_c}$, $G_5 = -\left[\frac{(1+C_{boost})k_t + k_{sw}}{I_c} + \frac{2C_f d}{G^2 I_c}\right]$, $G_6 = -\frac{(1+C_{boost})c_t + c_{sw}}{I_c}$. Because small time steps could be used in the driving simulator, instead of being presented by Specker's dynamic friction model [78] as in Chapter 3, the steering system friction

torque T_f is modelled as a Coulomb friction, which is dependent on the steering column angular velocity $\dot{\theta}_c$, to replicate more realistic friction behaviour. A hyperbolic tangent function is chosen to represent the Coulomb friction model, as described by (4.4), to avoid the discontinuities when the steering column angular velocity changes from positive to negative.

$$T_f(t) = F_C \tanh\left(c\dot{\theta}_c(t)\right) \tag{4.4}$$

where F_C is the magnitude of the friction torque, and the value of the constant c can be chosen to give the desired steepness of the friction torque against the steering column angular velocity curve near zero steering column angular velocity. In this study, the value of c is chosen as 50s/rad to achieve the trade-off between the feasibility of the simulation and the accuracy of friction modelling. Figure 4.7 shows the Coulomb friction model with the magnitude of the friction torque F_C set to 2Nm as an example. Figure 4.8 shows the cross-plots of the steering wheel angle measured by the encoder against the steering torque measured by the load cell, and the steering wheel angle measured by the encoder against the simulated torque demand signal from the steering-vehicle system with the implemented Coulomb friction, the magnitude of which is 2Nm. The influence of steering system friction on the cross-plots is visible as a significant torque difference for an infinitesimal change in the steering wheel angle at each end of the hysteresis curves, as explained in Chapter 3.

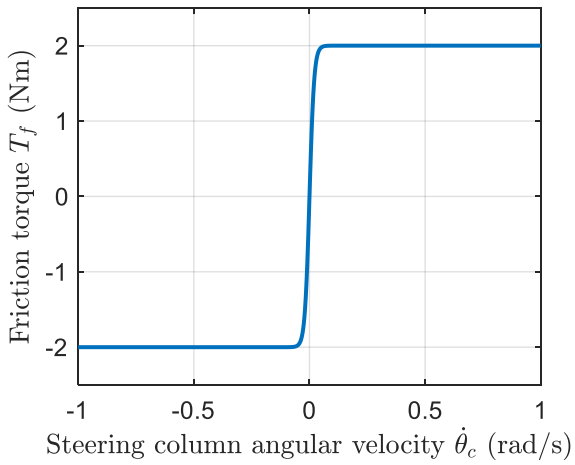

Figure 4.7: Coulomb friction model with F_C equal to 2Nm and c equal to 50s/rad.

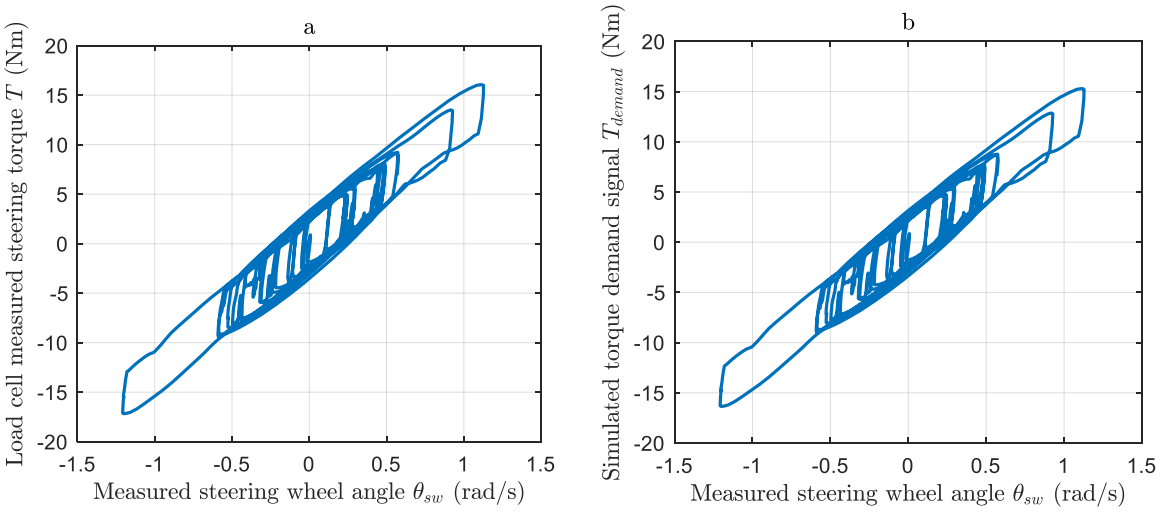

Figure 4.8: Cross-plots of torque against angle of the steering-vehicle system with Coulomb friction in the driving simulator (a: measured steering wheel angle vs. load cell measured steering torque; b: measured steering wheel angle vs. simulated torque demand signal).

All the states, outputs and inputs in the state-space equations (4.2) and (4.3), along with the white noise signals before the low-pass filters, are recorded by the Target PC and fed to the Host PC for storage through TCP/IP protocol. The simulated vehicle yaw angle ψ, vehicle longitudinal position x and vehicle lateral position y in the global coordinate system are sent to the Graphics PC to simulate the motion of the vehicle in the virtual reality world also via TCP/IP protocol.

Suitable values of the steering and vehicle model parameters were either identified by fitting the responses of the steering-vehicle model to data from an actual vehicle, which was provided by TME [124], using a least-square method with the same steering wheel angle input level, or selected from previous literature publishing accurate corresponding parameter values of the steering and vehicle system [1]. In addition, the torsion bar damping coefficient c_a and the damping coefficient of the steering system c_{sw} were adjusted during preliminary experiments to provide necessary stability of the software-hardware open-loop system while representing realistic steering system properties. A consequence of the fact that these parameter values are not from a single source is that not all of the parameter values of the steering-vehicle model are close to the corresponding parameter values of a real vehicle. However, comments from experienced test drivers, and the comparison between the simulated steering and vehicle responses and the actual steering and vehicle responses of an actual vehicle confirmed that the steering-vehicle model gave a realistic steering response. The steering and vehicle parameters used in the Simulink model are summarised as the 'base' in Table 3.1 in Chapter 3. However, the values of some of these parameters are altered during different experimental trials. The details are addressed in later sections.

4.2.5 Graphics and Display Setup

As mentioned in Section 4.2.1, there are three 4K 65-inch displays showing the driver the virtual reality world to replicate the driver's view in real-world driving scenarios. The horizontal width and the vertical height of an individual physical display screen are 144cm and 81cm, respectively, giving an aspect ratio of 1.7778. The seat is positioned so that the perpendicular distance from the driver's eye to the displays is 170cm, then the field of view for each display is 46 degrees, and the total field of view provided by the three displays is 138 degrees. Figure 4.9 is a sketch plan view showing how the displays are positioned relative to the driver's head. For the TME simulator, there is just one single display with a width of 82cm and a height of 35cm, however, the graphics and the seat were adjusted to give the same field of view as the CUED simulator.

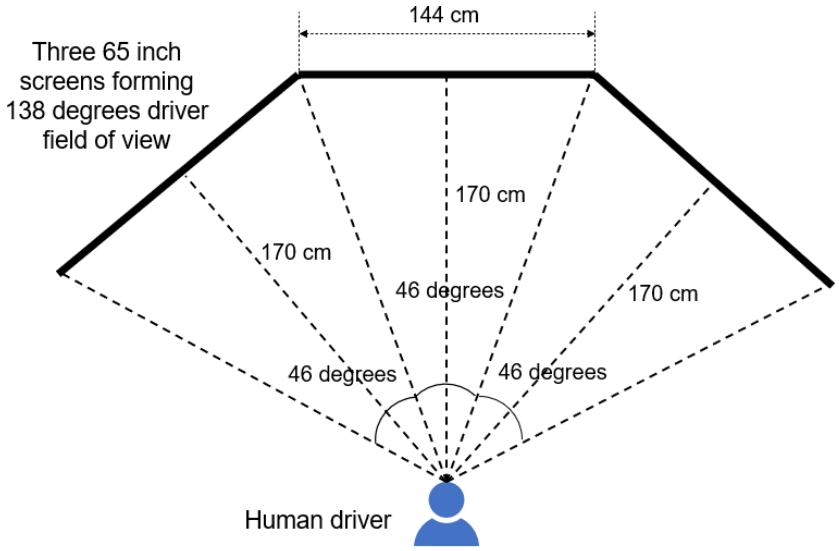

Figure 4.9: Plan view of the relative position of the driver's head to the three displays.

The virtual reality world is created using a Python package called Panda3D [136] and consists of a target path, a vehicle that the human driver steers, a double-lane road formed by the gray and white grids with boundary lines, and a sky with white clouds. The aspect ratio of the displays, the field of view, the positions and angles of the cameras are set to the values matching the real-world settings. The vehicle is represented by a 5m long and 2m wide box, while the width of each road lane is 4m. The distance of the viewpoint behind the vehicle is set to 4.2m. A plan view diagram showing the geometry of the virtual reality world settings is shown in Figure 4.10. The motion of the vehicle with respect to the road in the virtual world is controlled by the simulated vehicle yaw angle ψ, and the vehicle longitudinal position x and vehicle lateral position y signals from the Target PC in real-time. However, there is time delay of the displays and Ethernet, which has been found to be 60ms in total in preliminary experiments. It is important to note that in this driving simulator setup, the driver's view is outside of the vehicle, which means that the human driver sits outside of the vehicle and controls the vehicle

remotely. As the base of the driving simulator is fixed, the primary purpose of this setup is to make sure that there are no conflicts between the driver's visual and physical (vestibular) measurements, which could lead to motion sickness, and lead to unrealistic weightings of different sensory cues by the driver [117].

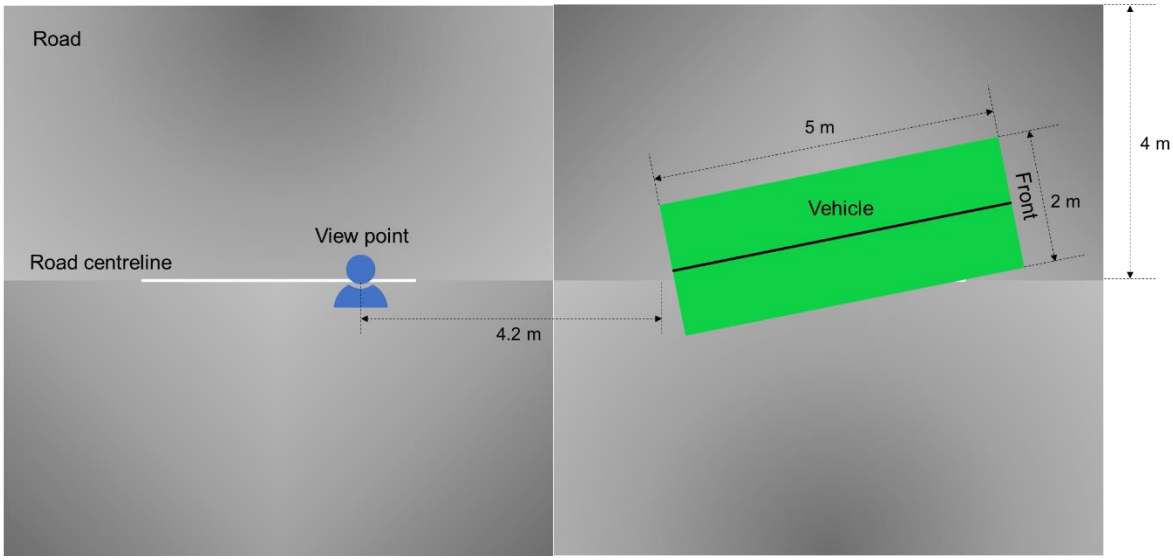

Figure 4.10: Plan view diagram of the virtual reality world settings, including the road with its centreline, the vehicle and the human driver's viewpoint.

4.3 Experimental Procedure and Results

4.3.1 Steering Control Tasks

The steering control task performed in the experiments was the same as the task described by the model in Chapter 3 (shown in Figure 3.1). The vehicle moved at constant longitudinal speed of 60km/h and the drivers were asked to steer the vehicle to follow a randomly moving target line r as closely as possible while rejecting the disturbances acting on the steering and vehicle system. The disturbances F_y, M_z and T_d were added as lateral force, yaw moment and steering column torque acting on the steering-vehicle system as shown in Figure 3.1. However, not all the disturbances are applied in the experiments described in this chapter and detailed experimental conditions are given in Section 4.3.2. The randomly moving target line r and the disturbances were generated using filtered Gaussian white noise to match the formulation of the driver model. White noise signals w_F, w_M, w_T and w_r were generated in discrete time by choosing random numbers from a zero-mean normal distribution, as suggested by Nash and Cole [116]. The variances W_F^2, W_M^2, W_T^2 and W_r^2 of these signals were tuned to give a suitable trade-off between achieving a high signal-to-noise ratio and a comfortable experience for the test subjects during preliminary testing. Large signal amplitudes are desirable to allow the drivers to generate control actions with a high signal-to-noise ratio so that the level of uncertainty in the

identification results can be reduced; however, the steering control task will become demanding when the disturbance amplitudes are large.

The cut-off frequencies of the low-pass filters $H_{fF}(s)$, $H_{fM}(s)$ and $H_{fT}(s)$ for the disturbances acting on the steering-vehicle system were also tuned during preliminary testing to ensure that the human drivers are not excited beyond the frequencies of interest and that the disturbances in the range of frequencies are not uncomfortable for the human drivers. The corresponding cut-off frequencies f_{cF}, f_{cM} and f_{cT} were set to 1Hz, 1Hz and 10Hz, for $H_{fF}(s)$, $H_{fM}(s)$ and $H_{fT}(s)$, respectively. The transfer function $H_{fr}(s)$ was implemented by combining a high-pass filter, to attenuate low frequencies and a low-pass filter to restrict the bandwidth of the target line, as in [116]. Because the range of the frequencies that the human driver can generate is limited, any component of the randomly moving target line with a higher frequency that the human driver cannot react to should be attenuated. The filter was chosen to have 40dB/decade roll-off at high and low frequencies, with upper and lower cut-off frequencies of 1rad/s and 0.05rad/s, respectively, as given in (4.5).

$$H_{fr}(s) = \left(\frac{s}{s+0.05}\right)^2 \left(\frac{1}{s+1}\right)^2 \tag{4.5}$$

Bode diagrams of the filters are shown in Figure 4.11, and examples of the time-domain of the randomly moving target line and the disturbances after being processed by the filters are shown in Figure 4.12.

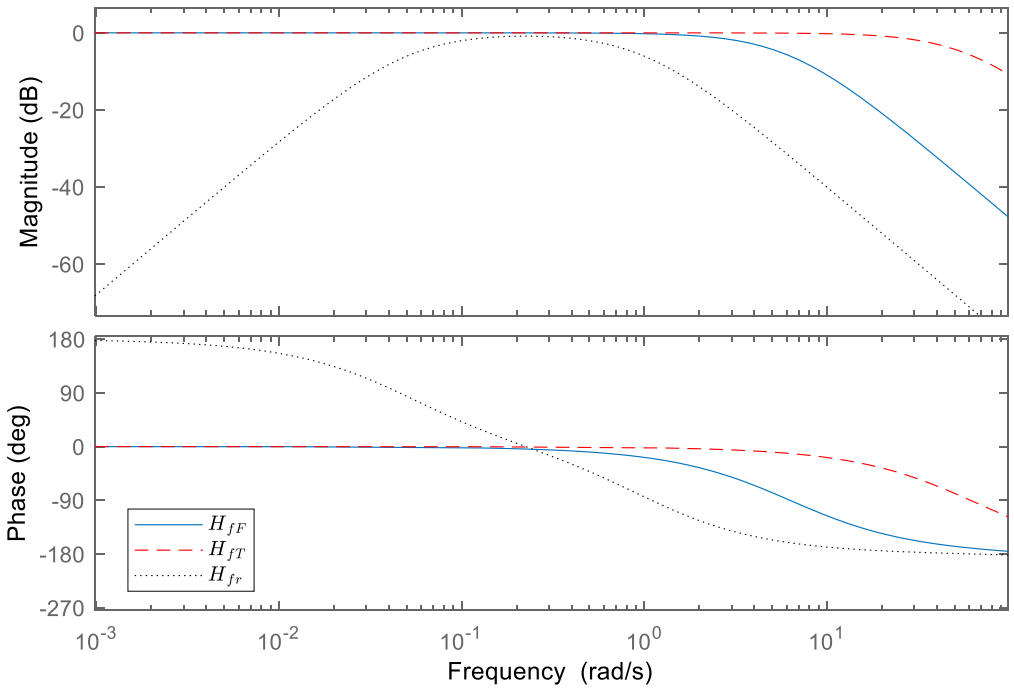

Figure 4.11: Bode diagram of the filters used in the experiments

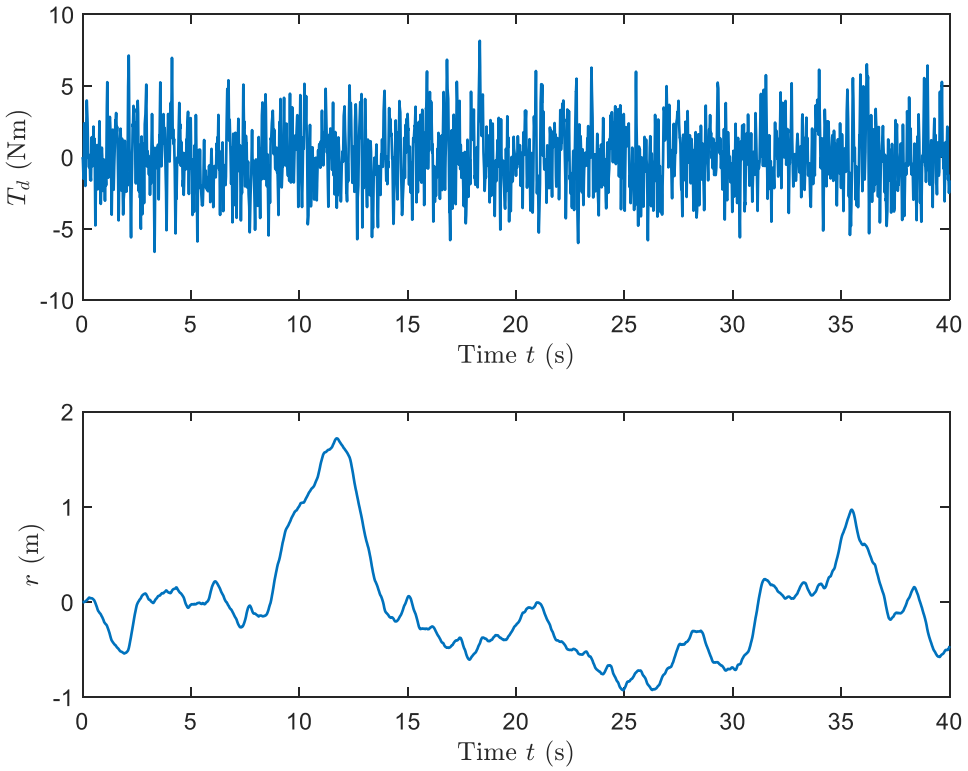

Figure 4.12: Time histories of the steering column torque disturbance T_d and the randomly moving target line r used in some of the experimental trials

In the experiments, the 'no preview' display used by Nash and Cole [116] was applied to replicate the steering control task described by the closed-loop driver-steering-vehicle model in Chapter 3. An example of the display is shown in Figure 4.13. The vehicle moved along the straight road with boundary lines of the road, and the gray and white grids were used as visual cues for the test drivers to assess depth and speed. In the experimental trials where the drivers were asked to follow a randomly moving target line, a straight red line moved laterally across the road, with the lateral displacement of each point on this line equal to $r(t)$ at time t. In this case, the driver can only see the current value of r without knowing any additional information about future values of the target line.

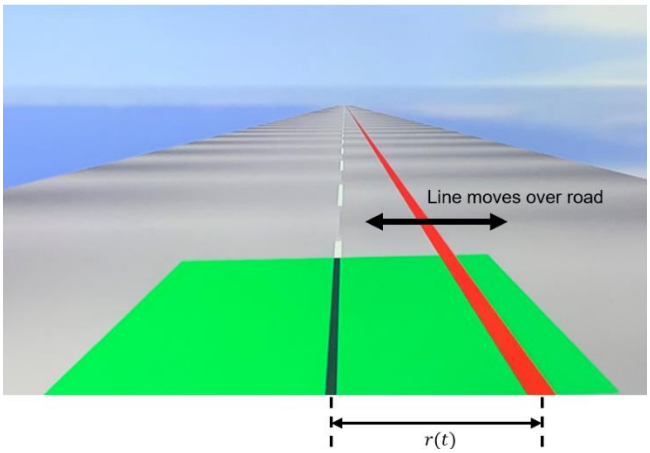

Figure 4.13: Visual display example showing the randomly moving target line r at time t.

4.3.2 Experiment Procedure and Trials

Based on the hardware calibration, including the load cell and the servomotor, and the implementation of the software, a series of driving simulator experiments were designed and carried out on the CUED driving simulator, as shown in Figure 4.14. The experiments were also replicated using the TME simulator. Each test subject sat in the driver seat of the driving simulator and was presented with a virtual driving environment (in the three 4K 65-inch screens) consisting of a target path (the red line) to follow and a vehicle (the green rectangle, with the black line representing the centre line of the vehicle) to steer. The complete set of experiments consisted of eleven trials to explore the driver's control behaviours under a wide range of conditions. Each trial stands for a particular combination of disturbances acting on the vehicle and steering properties configuration. Most of the trials just involve the randomly moving target path without adding disturbances on the steering-vehicle system. This is to avoid disturbances that can be effectively compensated solely by co-contracting, and therefore stiffening, the arm muscles. Disturbances of the target path are not effectively compensated using co-contraction, and instead require active control by the driver using their internal model. After each trial, the drivers were asked to provide a subjective assessment of the steering feel for that trial by using criteria listed on a questionnaire. The conditions of the trials are summarised in Table 4.3. The first three trials form the 'linear phase' of the experiments, where the steering and vehicle dynamics are entirely linear. In trials 4 to 7, different levels of steering system friction torque are applied to the steering system and in trials 8 to 11, some assist torque from the driving assist system is added to the steering system in addition to the steering system friction torque in order to make the test subjects' overall physical torque effort level similar to that in trial 3. An appropriate value of boost curve coefficient C_{boost} for each trial is chosen by making the measured steering torque level similar to that in trial 3 when the steering wheel angle control action level applied in each trial is the same as that in

trial 3. This aims to examine if the test subject's subjective assessment of the nonlinear (steering system friction) characteristic is affected by the overall level of physical effort required to steer the vehicle.

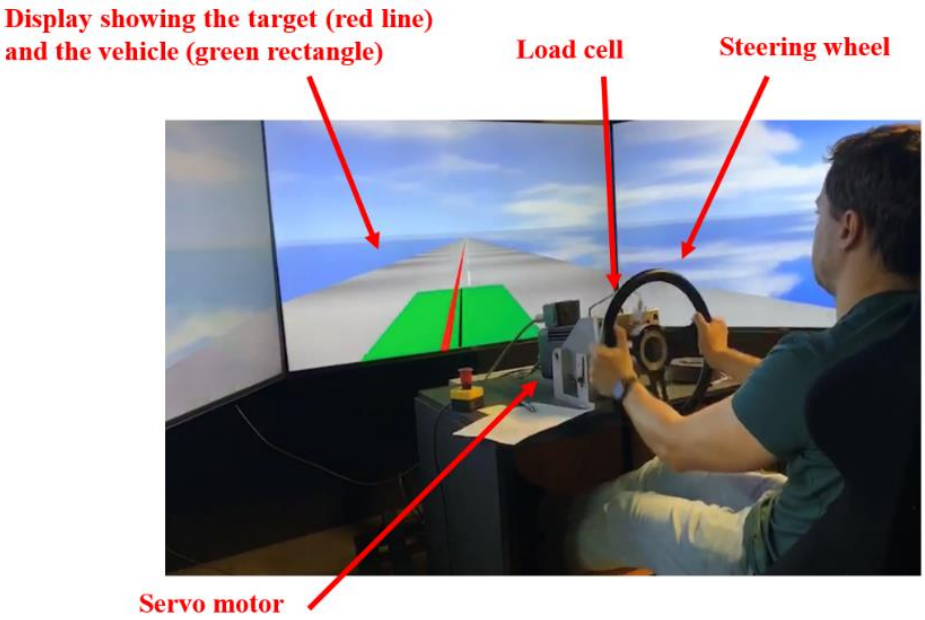

Figure 4.14: CUED driving simulator with test subject.

The dataset comprised thirteen test subjects, including eight Cambridge University drivers tested on the CUED driving simulator and five Toyota drivers tested on the TME driving simulator. The eight Cambridge drivers are 7 male drivers and 1 female driver aged between 21 and 30. All eight drivers possessed driving licences and have some experience driving a car and are familiar with steering torque feedback. Most of them were members of Cambridge University Automobile Club (CUAC) or vehicle dynamics engineering students. The five Toyota drivers are 4 male drivers and 1 female driver aged between 24 and 27. All five drivers are professional vehicle dynamics engineers. Detailed information about the test drivers is given in Table 4.4. Previous literature [137] [138] found that reaction times and sensory threshold have been found to increase with the increase of age. Therefore, choosing test subjects with a narrow range of age should improve the validity of combining datasets from different drivers to increase the signal-to-noise ratio before attempting model identification.

Before performing the experiments, the test subjects were given a leaflet with general information about the experiments and the instructions for operating the driving simulator safely. The test subjects were asked to familiarize themselves with the information before the experiments. General questions raised by the test subjects were answered regarding the experiment, the protocol, etc. After that, the test subjects were verbally instructed and demonstrated how to hold and turn the steering wheel. Then, a 10-minute training session consisting of practice runs of several of the trials was conducted to reduce the learning effect and help the test subjects become familiar with the driving simulator, the steering

task, the different disturbances, and the steering-vehicle system dynamic characteristics. The test subjects were told to use the same control strategy and keep the muscle conditions the same for all the trials.

During the experiments, linear trials 1, 2, and 3 were presented to the drivers first in order. For Cambridge drivers, the nonlinear trials 4 to 11 were divided into two groups: trials 4 to 7 and trials 8 to 11. Trials 8 to 11 were then presented to the drivers, followed by trials 4 to 7. In each of the two groups, the order was randomised. However, all the nonlinear trials 4 to 11 were presented to the drivers together in one single group with randomised order for Toyota drivers. Each trial ran for 5 minutes. Before the experiment began, each driver was told how the conditions might vary between the trials; however, to avoid biasing their expectations, they were not told anything about the specific conditions of each trial.

In experimental trials 3 to 11, the drivers were asked to provide subjective feedback of the steering feel for each trial by using the criteria listed in the questionnaire. The complete questionnaire on subjective assessment of steering feel is presented in Table 4.5. There are two types of subjective criteria, with the first type being estimation: judging how large/small or high/low the criterion is, such as the friction level and the yaw delay, and the second type being evaluation: judging how good/bad the criterion is, for examples, how easy is it to follow the randomly moving target path and how helpful is the steering torque feedback for the task. Each criterion on the questionnaire was evaluated using a unipolar discrete 1 - 10 rating scale. Trial 3 was used as the baseline trial, and every criterion about trial 3 was rated 5 as a reference to provide better data for the evaluation. The drivers then set their ratings in relation to this reference trial, which means the subjective ratings were relative ratings instead of absolute ratings. Before the experiments, a short training session regarding the concept and the importance of steering feel was also delivered. Such training has been recommended [10] because it can be used to familiarize the test subjects with the vocabulary concerning steering feel, which could increase the reliability of the answers and shorten the experiment time. The subjective assessment questionnaire was also presented to the test subjects during the training session to make sure they knew what they were going to assess during the experiments, and the test subjects were allowed to ask for clarifying information if they were uncertain about the meaning of some of the criteria listed on the questionnaire. However, no further clarification was given on the strategies of evaluating specific criteria. During the experiment, trial 3 was presented to the test subjects for a short time (30 seconds – 1 minute) quite often (e.g., after every two trials) to remind them of the conditions of the baseline trial frequently in order to ensure their use of the scale is constant across all the different trials. Each test subject was allowed to do some free driving (any manoeuvre) after the 5 minutes for each trial. This allowed the test subjects to ignore the instruction to follow the randomly moving target path and gave them the opportunity to evaluate all the criteria of steering feel in an unconstrained manner with more confidence.

Although a training session has been conducted before the experiments, the drivers may also have taken some time to get familiar with the new steering-vehicle dynamics and work out the conditions of each trial during the experiments. By taking account of this learning behaviour of the drivers, Nash and Cole [44] discarded the first 15s data of each trail. The interview responses of the test drivers indicate that 30s - 40s is sufficient to learn the dynamics of the system and settle on a control strategy. Therefore, the first minute of each trial is excluded from the data to eliminate the influence of the learning process.

Table 4.3: Experimental conditions for each trail

Exp. condition	**Disturbance amplitudes**			F_c(Nm)	Trail distance d (m)	Boost coefficient C_{boost}
	W_r(m)	W_F(N)	W_T(Nm)			
1	0	0	4	0	0	0
2	8	0	0	0	0	0
3	8	0	0	0	0.059	0
4	8	0	0	0.5	0.059	0
5	8	0	0	1	0.059	0
6	8	0	0	2	0.059	0
7	8	0	0	4	0.059	0
8	8	0	0	0.5	0.059	0.01
9	8	0	0	1	0.059	0.03
10	8	0	0	2	0.059	0.1
11	8	0	0	4	0.059	0.4

Table 4.4: Detailed information about the test drivers: age, gender, and experience

Source	No.	Age	Gender	Driving experience (years)	Other
University of Cambridge	1	25	Male	5	Vehicle dynamics expert
	2	25	Male	7	CUAC member, car/karting racing experience
	3	29	Male	18	CUAC member, car/karting racing/testing experience
	4	22	Male	3	Vehicle dynamics engineering student, racing experience
	5	21	Male	4	Vehicle dynamics engineering student
	6	21	Male	4	Vehicle dynamics engineering student
	7	21	Male	5	Vehicle dynamics engineering student
	8	24	Female	5	/
Toyota Motor Europe	9	24	Female	0	Vehicle dynamics engineer
	10	24	Male	6	Vehicle dynamics engineer
	11	24	Male	6	Vehicle dynamics engineer
	12	26	Male	8	Vehicle dynamics engineer
	13	27	Male	7	Vehicle dynamics engineer

Table 4.5: Questionnaire asking for the test subjects' subjective assessment of steering feel in the experiment.

Subjective criteria	Trial number										
	1	2	3	4	5	6	7	8	9	10	11
Q1. Friction level (1 to 10: low to high)?			5								
Q2. How easy is it to follow the randomly moving target path (1 to 10: difficult to easy)?			5								
Q3. Physical effort level (how hard is it to turn the steering wheel) (1 to 10: low to high)?			5								
Q4. Stability of the steering-vehicle system (1 to 10: unstable to stable)			5								
Q5. Yaw delay (between vehicle yaw velocity and steering wheel angle) (1 to 10: low to high)?			5								
Q6. Yaw gain (vehicle yaw velocity to steering wheel angle) (1 to 10: low to high)?			5								
Q7. Yaw linearity (1 to 10: linear to nonlinear)?			5								
Q8. How connected does it feel (1 to 10: disconnected to connected)?			5								
Q9. How helpful is the steering torque feedback for the task (1 to 10: useless to helpful)?			5								

4.4 Analysis and Discussion of the Linear trials

In the experiments, trial 3 is used as the baseline trial, where the steering torque feedback information is provided to the test subjects without being affected by any steering system friction. In contrast, in trial 2, the tyre trail distance is set to 0mm while all the other steering-vehicle properties and experimental conditions are set identical to those in trial 3. This means that there is no self-aligning moment generated between the front tyres and the ground, and the torque transmitted to the driver through the steering system is only due to the equivalent stiffness and damping of the steering system itself in trial 2. Therefore, the influence of steering torque feedback on the drivers' control performance can be determined by directly comparing trial 2 and trial 3 for each driver. Specifically, the following objective metrics are compared: measured steering torques, measured path-following errors and measured steering wheel angles. Detailed statistical analysis is conducted to determine if there are significant differences in the objective metrics between the two trials. Initially, a Shapiro-Wilk test is conducted to demonstrate that the values of each objective metric for each trial across all the test subjects follow a normal distribution with a normal probability plot. The mean and standard deviation of each metric over all the test subjects are then found based on the properties of a normal distribution. The statistical significance of the differences in the objective metrics is verified by using a paired t-test and an f-test comparing the two trials. In addition, the subjective ratings are analysed for each driver to examine the importance of steering torque feedback.

4.4.1 Steering Torque Analysis

Figure 4.15 and Figure 4.16 show the values of Root-Mean-Square (RMS) steering torque measured during the experiments for trial 2 and trial 3, respectively. It is shown that in trial 3, where there is steering torque feedback, Driver 4 and Driver 5 had the smallest steering torques with the RMS values below 4Nm, while Driver 12 and Driver 13 had the largest steering torques with the RMS values above 6Nm. In addition, the RMS steering torque level of trial 3 is significantly larger than that of trial 2, which is apparently due to the resistance caused by the self-aligning moment generated between the front tyres and the ground.

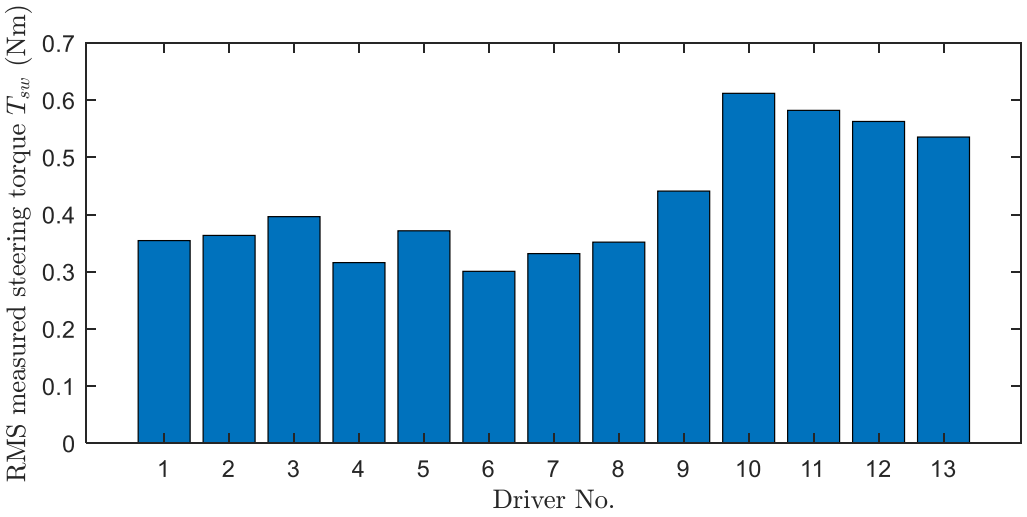

Figure 4.15: Values of RMS steering torque in trial 2 for each driver.

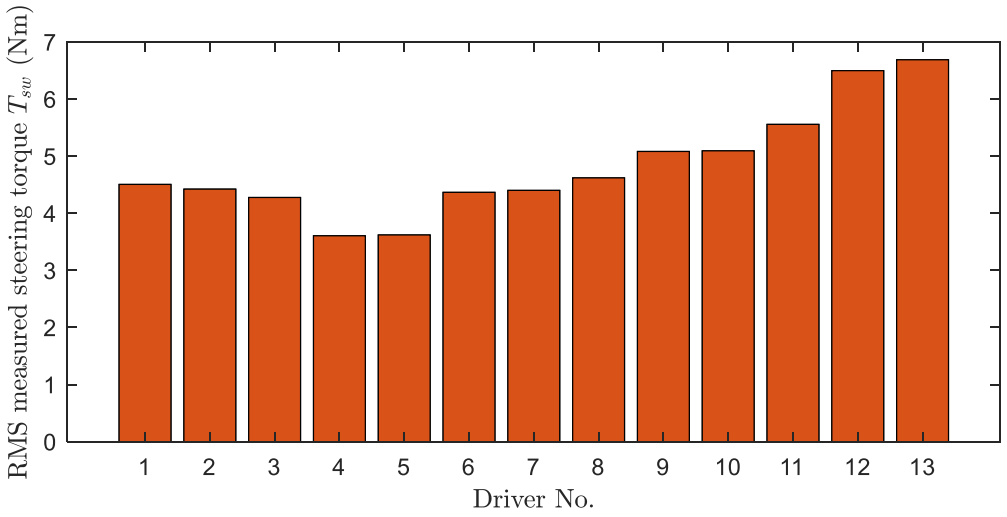

Figure 4.16: Values of RMS steering torque in trial 3 for each driver.

4.4.2 Path-following Performance Analysis

To investigate the effect of steering torque feedback on the path-following performance, the values of RMS path-following error in trial 2 and trial 3 for each driver are presented in Figure 4.17. Figure 4.17 demonstrates that most test drivers achieved small path-following errors with the RMS values below 0.4m. Driver 13 achieved the best path-following performance, while Driver 6 had the largest tracking errors. Figure 4.18 shows the time histories of the vehicle lateral displacements during trial 3 performed by Driver 13 and Driver 6. The solid black line presents the randomly moving target line, while the blue and red dashed lines represent the time history of Driver 13 and Driver 6, respectively. The time phase difference between the randomly moving target and the vehicle lateral displacement is smaller for Driver 13 than for Driver 6. This might be because Driver 13 reacted to the target more aggressively by

applying more steering effort. This finding suggests different driving styles, which are further examined in the steering wheel angle data. The percentage change in RMS path-following error when steering torque feedback was hidden in trial 2 with respect to trial 3 for each driver is shown in Figure 4.19, along with the median and mean values over the thirteen drivers.

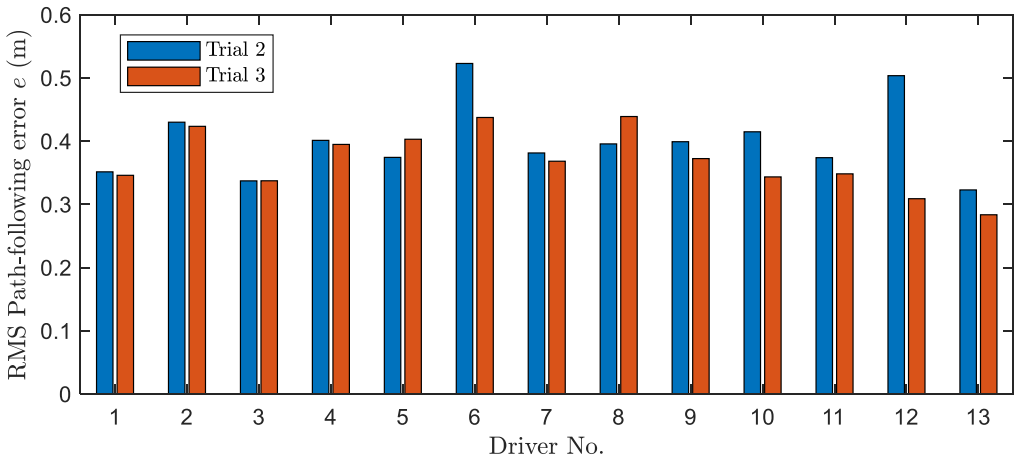

Figure 4.17: Values of RMS path-following error in trial 2 and trial 3 for each driver.

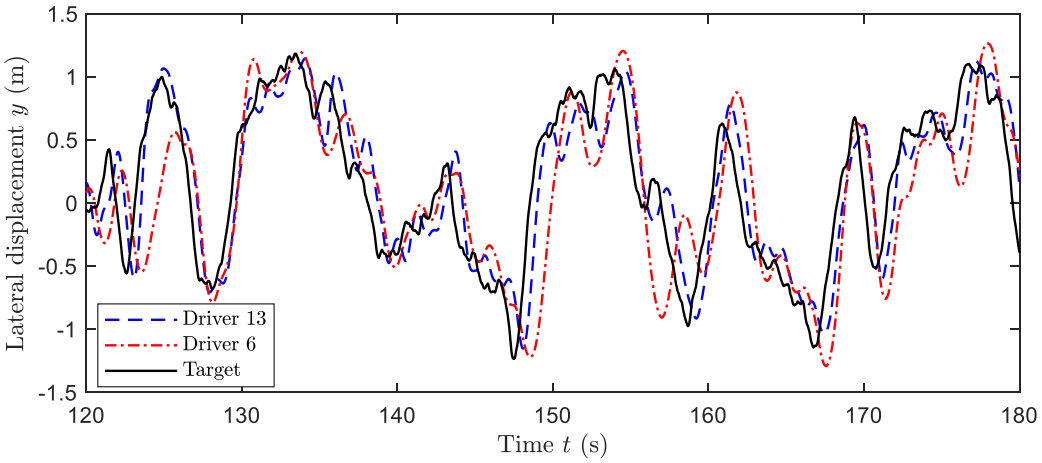

Figure 4.18: Time histories of the vehicle lateral displacements during trial 3 for Driver 13 and Driver 6 with the randomly moving target line.

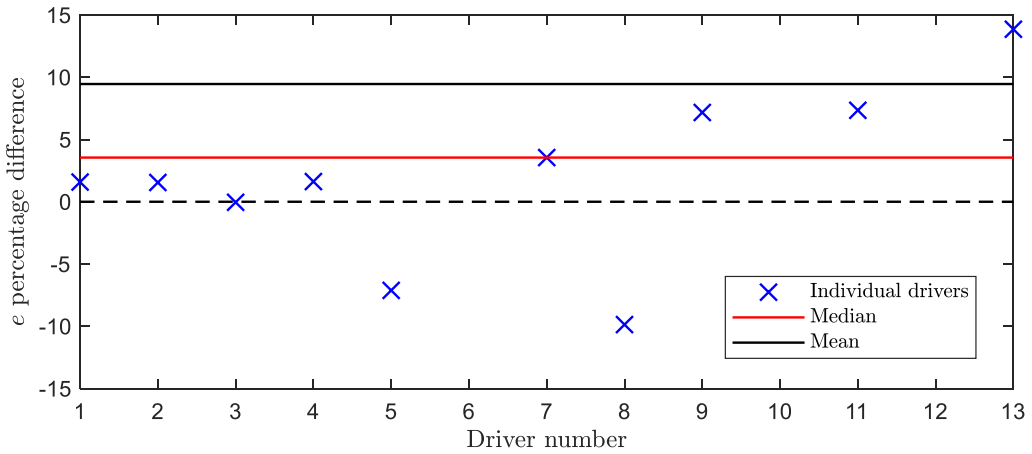

Figure 4.19: Change in RMS path-following error without steering torque feedback. Percentage differences are plotted for each driver and the median and mean over the thirteen drivers.

Figure 4.19 shows that the absence of steering torque feedback causes the path-following error to increase in general. However, to conduct detailed statistical analysis to determine if the difference in the RMS path-following error is statistically significant, it is necessary to know whether the values of RMS path-following error for each trial across all the drivers follow a normal distribution or not. Given the relatively small number of test subjects in this study, it is not easy to detect if the values are normally distributed via histograms. Instead, normal probability plots are graphics tools that can be used for this purpose. In normal probability plots, the values of RMS path-following error in each trial are plotted against a theoretical normal distribution, as shown in Figure 4.20. The horizontal axes are the values of RMS path-following error in each trial for all the drivers, and the vertical axes are the theoretical values of the cumulative probability for the RMS values. Theoretically, if the RMS values are normally distributed for each trial, they will be plotted approximately on a straight line. In order to check the linearity of the scattered data points, a solid reference line connecting the first and third quartiles of the data, and a dashed reference line extending the solid line to the ends of the data are also shown in Figure 4.20. If the data has a normal distribution, then the data points appear along the reference line. A distribution other than normal introduces curvature in the data plot. Figure 4.20 shows that most scattered points fall on the red straight line although there are one or two points sightly off, indicating the values of RMS path-following error for each trial follow a normal distribution. In addition to the normal probability plots, a Shapiro-Wilk test (sw-test) with a significant level of 5% is conducted to determine if the null hypothesis of a normal distribution is a reasonable assumption regarding the distribution of the RMS values for each trial. The p values, the probability of observing a test statistic as extreme as, or more extreme than, the observed value under the null hypothesis for the Shapiro-Wilk test, are shown in Table 4.6. The large p values indicate that the null hypothesis of a normal distribution is not rejected.

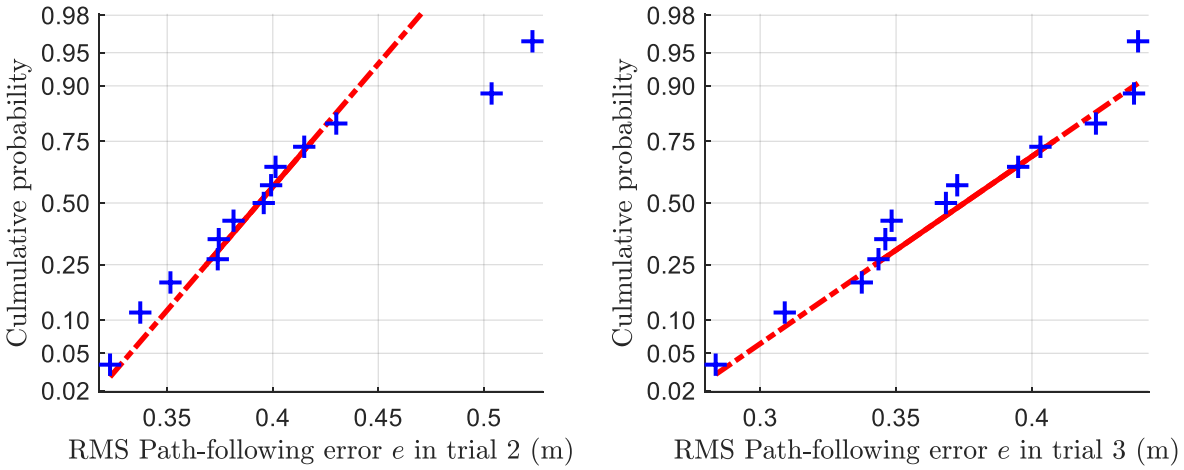

Figure 4.20: Normal plots for the values of RMS path-following error in trial 2 and trial 3.

Having demonstrated that the values of RMS path-following error in each trial for all the test subjects approximately follow a normal distribution, the mean values over the thirteen drivers for trial 2 and trial 3 are found, as shown in Table 4.7. The corresponding standard deviations for trial 2 and trial 3 are also calculated by using (4.6):

$$\sigma_e = \sqrt{\frac{1}{n_d - 1}\sum_{i=1}^{n_d}\left(\mathrm{RMS}(e_i) - \overline{\mathrm{RMS}(e)}\right)^2} \tag{4.6}$$

where n_d is the number of drivers and $\overline{\mathrm{RMS}(e)}$ is the mean RMS of path-following error over all the drivers, and the results are also shown in Table 4.6.

Statistical significance of the difference in the mean RMS path-following error between trial 2 and trial 3 is verified using a paired t-test, since the two trials were conducted by the same group of drivers. However, before the paired t-test, an f-test was conducted first to check the statistical significance of the difference in the variance of the values of RMS path-following error between trial 2 and trial 3 to ensure the robustness of the test results. The null hypothesis of the f-test is that the RMS values for trial 2 and trial 3 come from normal distributions with the same variance, while the null hypothesis of the paired t-test is that the difference in the RMS values between trial 2 and trial 3 comes from a normal distribution with a mean of zero and unknown variance. Any outlier was removed from the dataset. The p values for f-test and t-test are also summarised in Table 4.6. The small p values indicate that both the paired t-test and the f-test null hypotheses are rejected at a 5% significance level. This suggests that with steering torque feedback, the drivers could follow the target line more closely and achieve greater consistency of the path-following performance. These results agree with findings obtained by Wang [135], who studied the steering torque interaction between driver and vehicle, that steering torque

feedback information is helpful to drivers as it gives the drivers extra information which they can use to estimate the states and learn the system dynamics more accurately.

Table 4.6: Mean and standard deviation (in brackets) of RMS path-following error across all thirteen drivers for trial 2 and trial 3

Criteria	Trial 2	p (sw-test)	Trial 3	p (sw-test)	p (f-test)	p (t-test)
RMS path-following error e	0.401 m (0.0584 m)	0.1330	0.370 m (0.0382 m)	0.7479	0.0216	0.0446

4.4.3 Steering Wheel Angle Analysis

To investigate the effect of steering torque feedback on the steering wheel angle, comparisons between the RMS values of the steering wheel angle for trial 2 and trial 3 are shown in Figure 4.21. The values of RMS steering wheel angle vary across the test subjects. Driver 9 to 13 had larger overall steering wheel angle inputs than the other drivers, with values of RMS steering wheel angle larger than 0.4rad for both the two trials, while Driver 4 and Driver 5 consumed the smallest level of steering wheel angle inputs among the test drivers, with values of RMS steering wheel angle below 0.4rad. This is consistent with the corresponding steering torque levels shown in Figure 4.16. Figure 4.22 shows the spectrum of steering wheel angle in trial for Driver 13 and Driver 6 corresponding to the analysis conducted in Section 4.4.2. Comparison between the two lines shows that Driver 13 generated much higher frequency steering control actions than Driver 6. These differences suggest that Driver 13 reacted to the randomly moving target line more aggressively to meet the path-following requirements better. In contrast, Driver 6 completed the steering control task in a more 'relaxed' way, weighting less on the lateral displacement than the control inputs by applying lower-frequency small magnitude steering wheel angles. The driving styles shown by the steering wheel angle are consistent with the observation of difference in path-following accuracy shown in Figure 4.18. Figure 4.23 shows the percentage change in RMS steering wheel angle when steering torque feedback was hidden in trial 2 with respect to trial 3 for each driver, along with the median and mean values over the thirteen drivers. In general, the drivers had larger steering wheel angle input without steering torque feedback information.

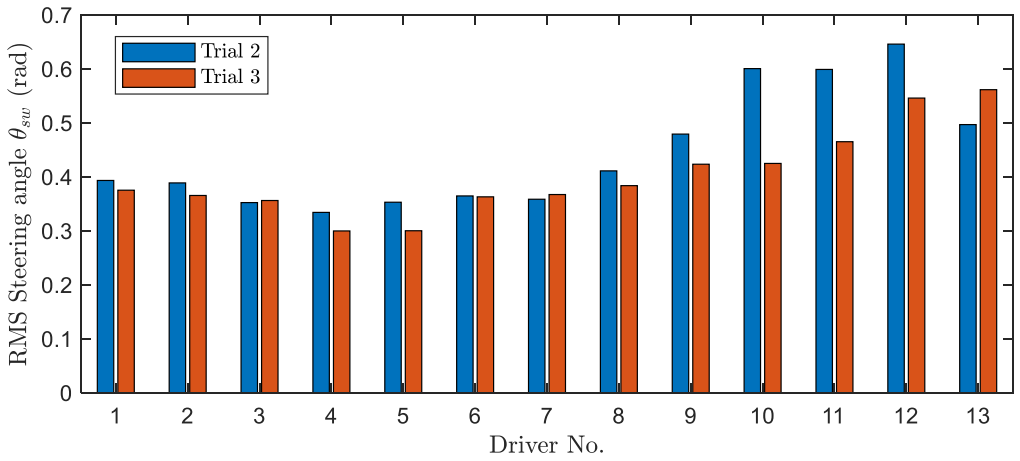

Figure 4.21: Values of RMS steering wheel angle in trial 2 and trial 3 for each driver.

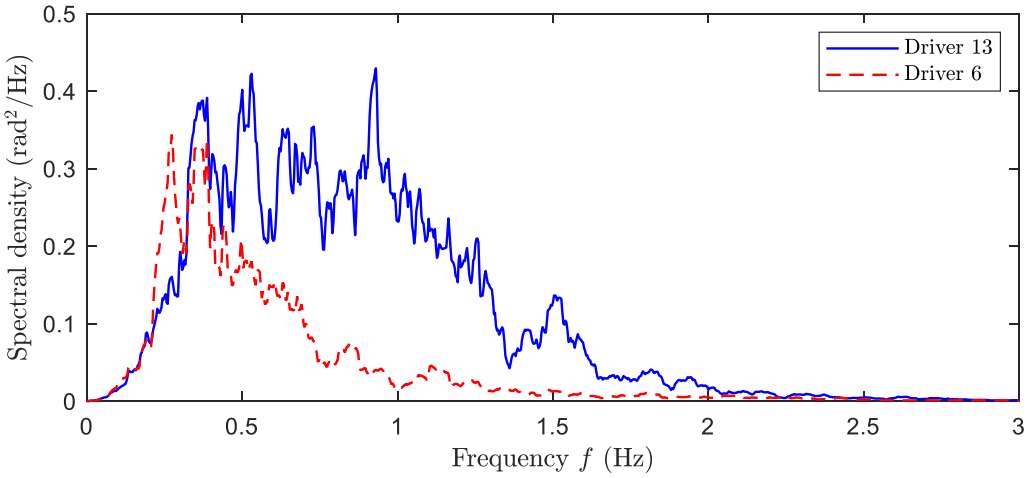

Figure 4.22: Spectrums of the steering wheel angle during trial 3 for Driver 13 and Driver 6.

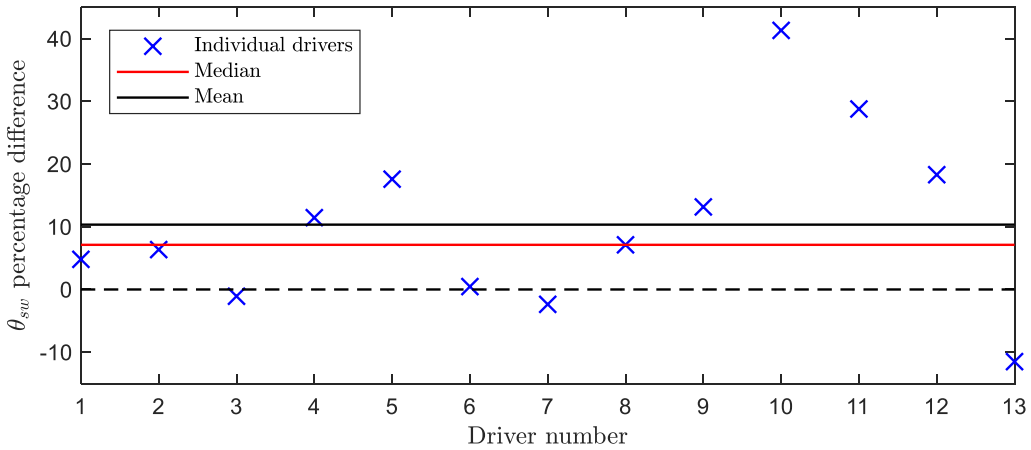

Figure 4.23: Change in RMS steering wheel angle without steering torque feedback. Percentage differences are plotted for each driver and the median and mean over the thirteen drivers.

Normal probability plots showing the values of RMS steering wheel angle in each trial against a theoretical normal distribution are presented in Figure 4.24. Although some scattered points are away from the reference line, the assumption of normal distribution is plausible considering the small number of drivers. In addition, the large p values from the Shapiro-Wilk test results, shown in Table 4.7, also indicate that the null hypothesis of a normal distribution is not rejected at a 5% significant level.

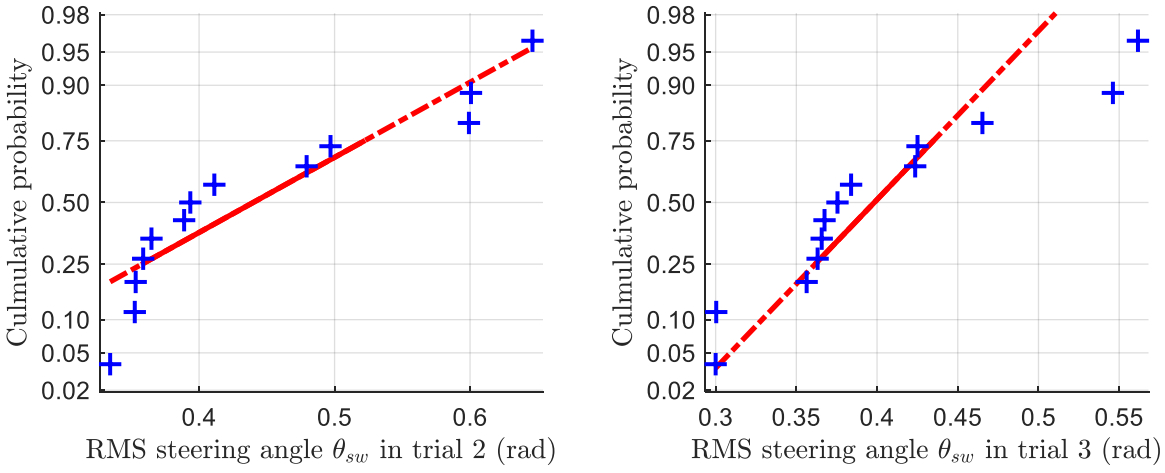

Figure 4.24: Normal plots for the values of RMS steering wheel angle in trial 2 and trial 3.

The calculated mean values and standard deviations of RMS steering wheel angle over the thirteen drivers following the properties of a normal distribution for trial 2 and trial 3 are presented in Table 4.7, along with the paired t-test and f-test results showing the statistical significance of the difference in the mean values and standard deviations of RMS steering wheel angle between the two trials. The small p value from the paired t-test suggests that the drivers had smaller steering wheel angle input with steering torque feedback at over 95% significance level. In addition, the small p value from the f-test suggests that the standard deviation of the steering wheel angles with steering torque feedback is also smaller than that without steering torque feedback at over 95% significance level.

Table 4.7: Mean and standard deviation (in brackets) of RMS steering wheel angle across all thirteen drivers for trial 2 and trial 3

Criteria	Trial 2	p (sw-test)	Trial 3	p (sw-test)	p (f-test)	p (t-test)
RMS steering wheel angle θ_{sw}	0.457 rad (0.109 rad)	0.1227	0.410 rad (0.081 rad)	0.1120	0.0172	0.0176

4.4.4 Subjective Assessment Analysis

The test drivers' subjective ratings on four questions in the subjective questionnaire for trial 2 and trial 3 are compared, and the results are shown in Figure 4.25.

- Q2: How easy is it to follow the randomly moving target path: 1 (difficult) to 10 (easy):

All the drivers gave lower ratings in trial 2 compared with trial 3. This indicates that the drivers found it is more difficult to follow the randomly moving target path without steering torque feedback. This is consistent with the findings from the objective data in Section 4.4.2 and Section 4.4.3 that the drivers had greater tracking accuracy with a smaller amount of steering wheel angles with the aid of steering torque feedback information.

- Q3: Physical effort level (how hard is it to turn the steering wheel): 1 (low) to 10 (high):

All the drivers gave lower ratings in trial 2 compared with trial 3, suggesting that the drivers can easily tell the overall physical effort level difference between the two trials. The difference in steering torque level between the two trials has also been demonstrated by Figure 4.15 and Figure 4.16 in Section 4.4.1.

- Q8: How connected does it feel: 1 (disconnected) to 10 (connected) & Q9: How helpful is the steering torque feedback to the task: 1 (useless) to 10 (helpful):

All the drivers gave the lowest ratings in trial 2, which agrees with the expectation that without steering torque feedback, the drivers felt like their control inputs are only loosely connected to the motion of the vehicle. Ratings in Q9 also further demonstrate that steering torque feedback information is helpful.

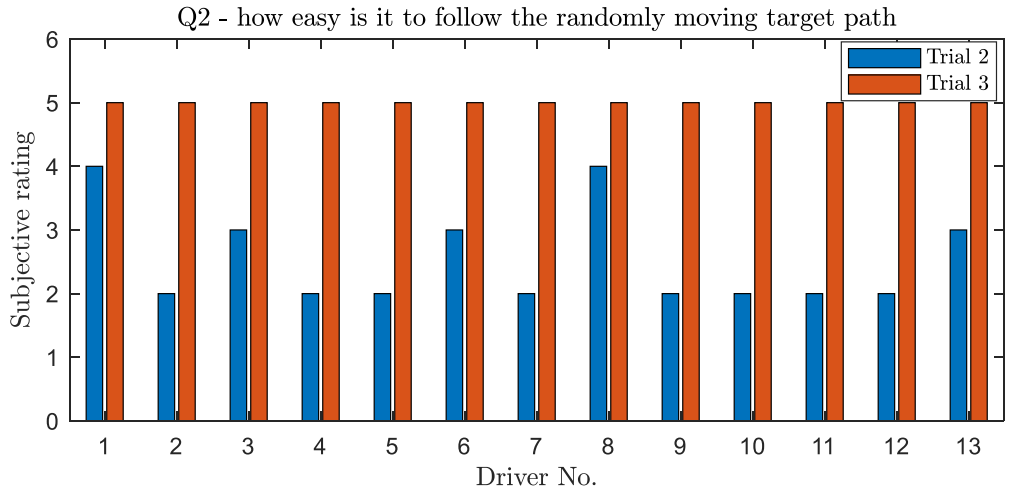

Figure 4.25: Subjective ratings on four questions for trial 2 and trial 3 for each driver. (from top to bottom: Q2 – how easy is it to follow the randomly moving target path; Q3 - physical effort level; Q8 - how connected does is feel; Q9 - how helpful is the steering torque feedback for the task)

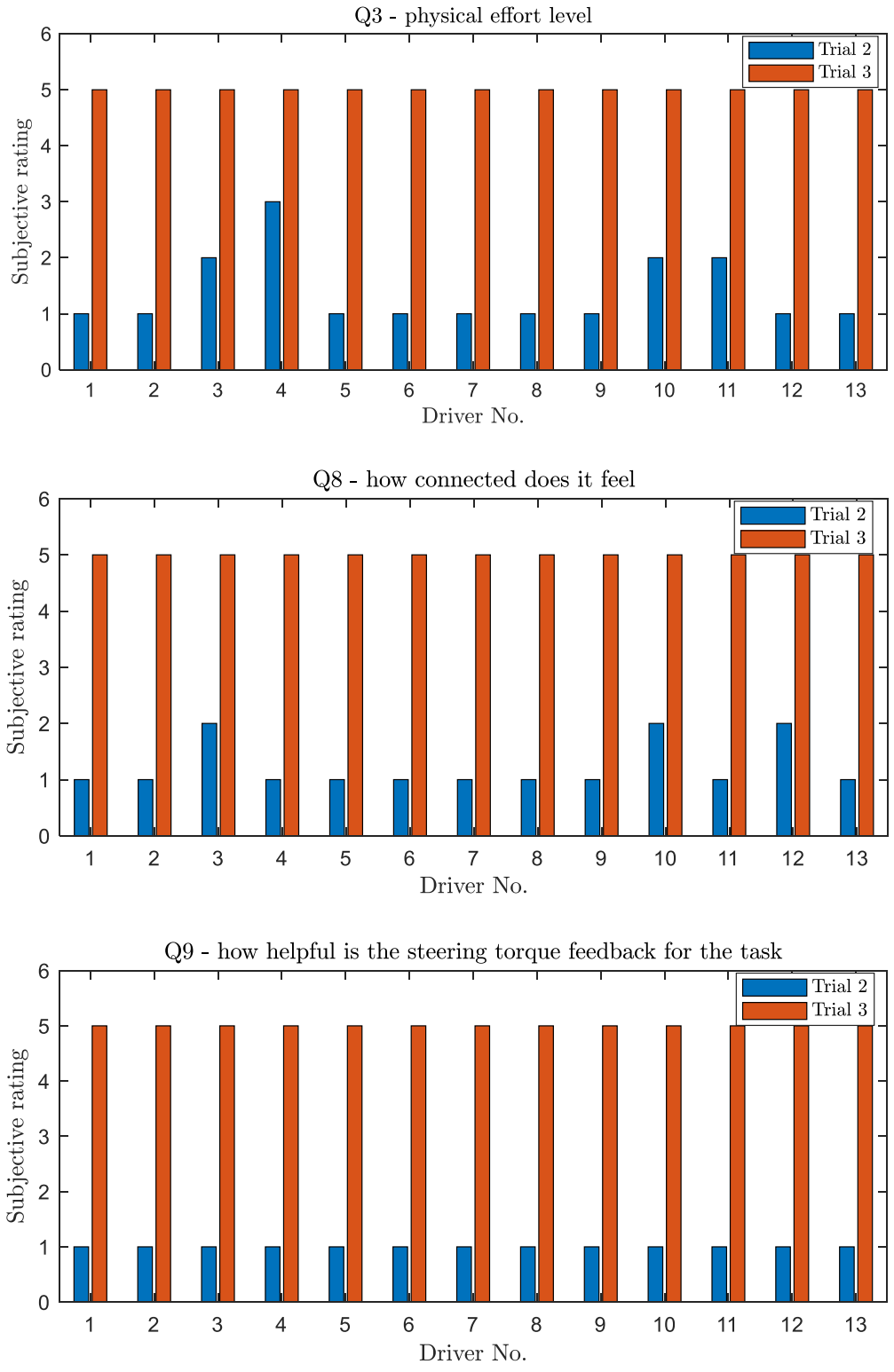

Figure 4.25(continued): Subjective ratings on four questions for trial 2 and trial 3 for each driver. (from top to bottom: Q2 – how easy is it to follow the randomly moving target path; Q3 - physical effort level; Q8 - how connected does is feel; Q9 - how helpful is the steering torque feedback for the task)

4.5 Analysis and Discussion of the Nonlinear trials

In the nonlinear phase of the experiments, different levels of steering system friction torque are applied to the steering system. In this section, the results of the nonlinear trials 4 to 11 are analysed to investigate the influence of steering system friction on the drivers' control performance. Specifically, the following objective metrics are compared between different trials: measured path-following errors, measured steering wheel angles, measured steering torques and measured steering reversal rates. Detailed statistical analysis is conducted to determine if there are significant differences in the objective metrics between the trials. Initially, similar to Section 4.4, a Shapiro-Wilk test is conducted to demonstrate that the values of each objective metric for each trial across all the test subjects follow a normal distribution with a normal probability plot. The mean and standard deviation of each metric over all the test subjects are then found accordingly. Statistical significance of the differences in the objective metrics is then verified using a one-way ANOVA test comparing all the different trials. To ensure the robustness of the comparison, a Bartlett's test for equal variances between the trials is conducted.

4.5.1 Path-following Performance Analysis

To investigate the effect of steering system friction on path-following performance, the values of RMS steering wheel angle in the nonlinear trials are plotted for each driver in Figure 4.26. The values vary across test drivers and trials. Similar to the observation in Section 4.4.2, Driver 13 had the smallest values of RMS path-following error, while Driver 6 had the largest. The percentage changes in RMS path-following error with respect to trial 3 when different levels of steering system friction were implemented are shown in Figure 4.27, along with the median and mean values over the thirteen drivers for each nonlinear trial. Figure 4.27 shows that an increase in friction level in the steering system incurred a decrease in path-following accuracy in general. However, a small amount of friction may be beneficial as it provides damping to stabilise the steering-vehicle system. This can explain the negative percentage changes with respect to trial 3 for trial 4 and trial 8.

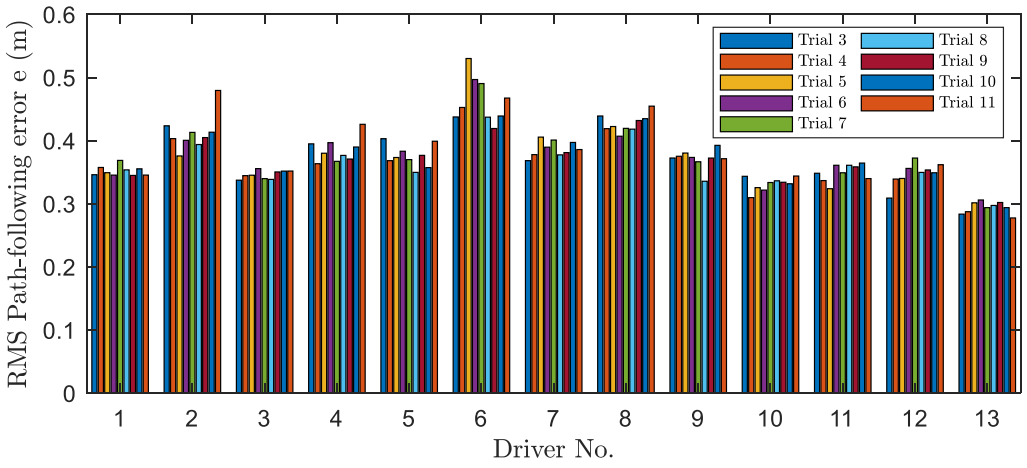

Figure 4.26: Values of RMS path-following error in trials 3 to 11 for each driver.

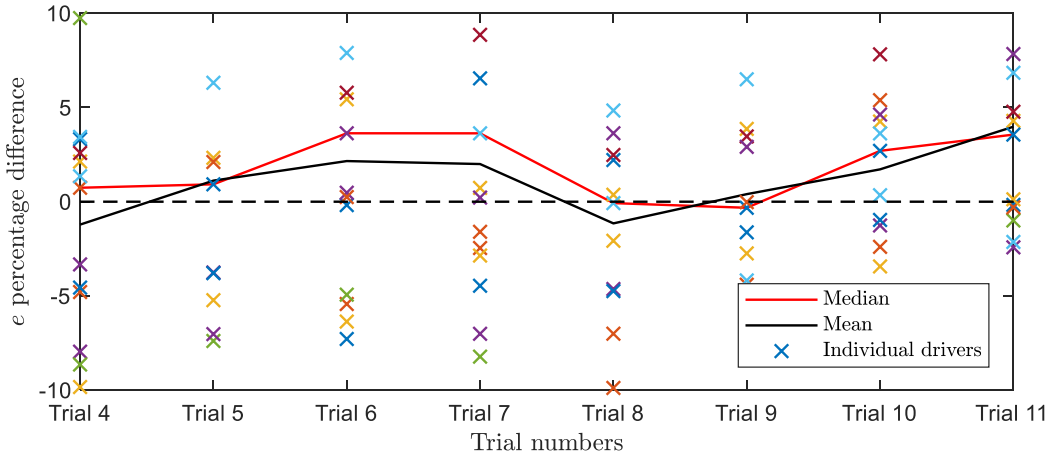

Figure 4.27: Change in RMS path-following error with different levels of steering system friction compared to trial 3. Percentage differences are plotted for each driver and the median and mean over the thirteen drivers.

Detailed statistical analysis is conducted to determine if there are statistically significant differences in RMS path-following error between different trials. In normal probability plots, the values of RMS path-following error for different drivers in each trial are plotted against a theoretical normal distribution to check the normality of the distribution of the RMS values. Examples of the plots for trial 7 and trial 11 are shown in Figure 4.28. It is shown that most scattered points are closely aligned with the red straight line, justifying the normal distribution assumption for these RMS values. The results for the RMS values of the other trials are similar to those shown in Figure 4.28. Additionally, a Shapiro-Wilk test (sw-test) with a significant level of 5% is conducted for each trial, and the results are shown in Table 4.8. The large p values also indicate that the null hypothesis of a normal distribution is not rejected.

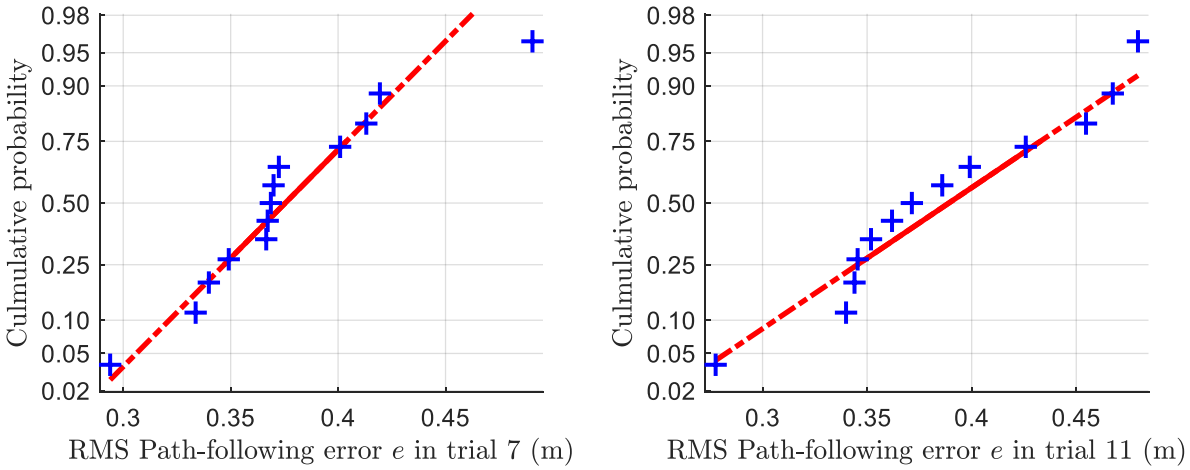

Figure 4.28: Normal plots for the values of RMS path-following error in trial 7 and trial 11.

Table 4.8: Results of Shapiro-Wilk test on the values of RMS path-following error for trials 3 to 11

Criteria	Trial 3	Trial 4	Trial 5	Trial 6	Trial 7	Trial 8	Trial 9	Trial 10	Trial 11
RMS path-following error e	0.7479	0.9897	0.1230	0.0888	0.1736	0.7120	0.9587	0.8317	0.5907

The mean and standard deviation of RMS path-following error over the thirteen drivers for each trial are shown in Table 4.9, calculated based on the properties of a normal distribution. Box plot of RMS path-following error of all thirteen drivers in trials 3 to 11 is shown in Figure 4.29, with the black asterisks indicating the mean values for each trial and red plus signs indicating the outliers. An outlier here is defined as a data point that is located outside 1.5 times the interquartile range above the upper quartile and below the lower quartile. Statistical significance of the difference in the mean RMS path-following error between the trials was verified by using a one-way ANOVA test, which is commonly used to determine whether there are any statistically significant differences between the means of three or more groups of normally distributed data. Before the one-way ANOVA test, Bartlett's test for equal variances between the nine trials was conducted to ensure the robustness of the results. The null hypothesis of Bartlett's test is that the RMS values for all the trials come from normal distributions with the same variance, while the null hypothesis of the one-way ANOVA test is that the differences in the RMS values between all the trials come from a normal distribution with a mean of zero. Any outlier was removed from the dataset. The p values for the one-way ANOVA test and Bartlett's test are also summarised in Table 4.9. Although an increasing trend can be identified in the mean value of RMS path-following error for the increased steering system friction level, the large p values in the one-way ANOVA test suggest that there is no statistically significant difference in the means between different

trails. This might be due to the large standard deviation for each trial, resulting from the significant driver to driver variation in steering control behaviour.

Table 4.9: Mean and standard deviation (in brackets) of RMS path-following error across all thirteen drivers for trials 3 to 11

Criteria	**Trial 3**	**Trial 4**	**Trial 5**	**Trial 6**	**Trial 7**	F **(ANOVA)**	p **(ANOVA)**	p **(Bartlett)**
RMS path-following error e	0.373 m (0.0482m)	0.367 m (0.0441 m)	0.378 m (0.0581 m)	0.379 m (0.0471 m)	0.379 m (0.0481 m)	0.13	0.9689	0.9042
Criteria	**Trial 3**	**Trial 8**	**Trial 9**	**Trial 10**	**Trial 11**	F **(ANOVA)**	p **(ANOVA)**	p **(Bartlett)**
RMS path-following error e	0.373 m (0.0482 m)	0.365 m (0.0373 m)	0.371 m (0.0353 m)	0.377 m (0.0415 m)	0.389 m (0.0585 m)	0.42	0.7964	0.3952

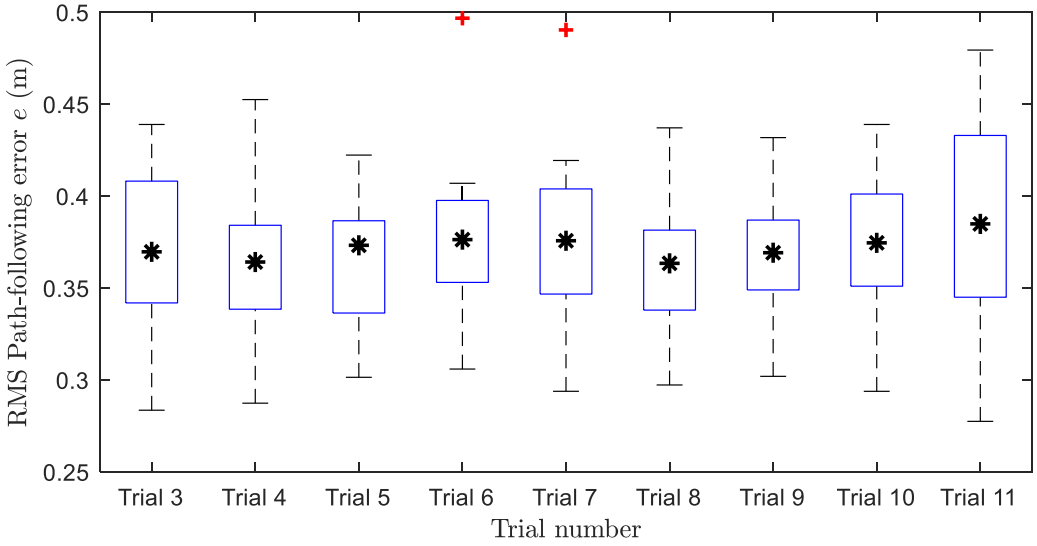

Figure 4.29: Box plot of RMS path-following error of all thirteen drivers in trials 3 to 11. The black asterisks indicate the mean of the RMS values for each trial, and the bottom and top edges of the box indicate the 25th and 75th percentiles, respectively. The dashed lines extend to the most extreme data points not considered outliers, and the red plus signs indicate the outliers.

4.5.2 Steering Action Analysis

To investigate the effect of steering system friction on steering action, values of RMS steering wheel angle and values of RMS steering torque for all thirteen drivers in trials 3 to 11 are plotted in Figure 4.30 and Figure 4.31, respectively. These steering action signals vary across the test drivers and trials. Driver 9 to 13 had larger overall steering wheel angle and torque inputs than the other drivers, while Driver 6 and Driver 7 used the smallest steering wheel angle and torque inputs among the test drivers. The percentage changes in RMS steering wheel angle and RMS steering torque with respect to trial 3

when different levels of steering system friction were implemented are shown in Figure 4.32 and Figure 4.33, respectively, along with the median and mean values over all thirteen drivers. Figure 4.32 shows a general increasing trend in RMS steering wheel angle with the increased level of friction presented in the steering system, which might indicate the difficulty of achieving accurate state estimation and internal mental model with steering torque feedback affected by friction. The influence of steering system friction on obtaining an accurate internal mental model and generating precise steering control actions and its reasons is further investigated in more details with the aid of the parametric driver model in Chapter 6. The drivers had smaller overall steering wheel angles in trials 4 to 7 compared to trials 8 to 11, and steering wheel angle levels in trials 4 to 6 are much lower than in trial 3. This could be because the addition of steering system friction increased the resistance in the steering system when there is no assist torque from the driving assist system. This is also the reason for the increasing steering torque level in trials 4 to 7, as shown in Figure 3.33. However, the drivers applied smaller steering torques in trials 4 and 5 compared to trial 3. This could be explained by that the drivers factor steering torque into their cost function more significantly in trials 4 and 5 where the resistance is relatively larger. In addition, although some assist torque is applied in trials 8 to 11 to make the drivers' overall physical torque effort level similar to that in trial 3 during preliminary experiments, there is still a slight increase trend for the steering torque in trials 8 to 11, which is consistent with the increased level of steering wheel angles.

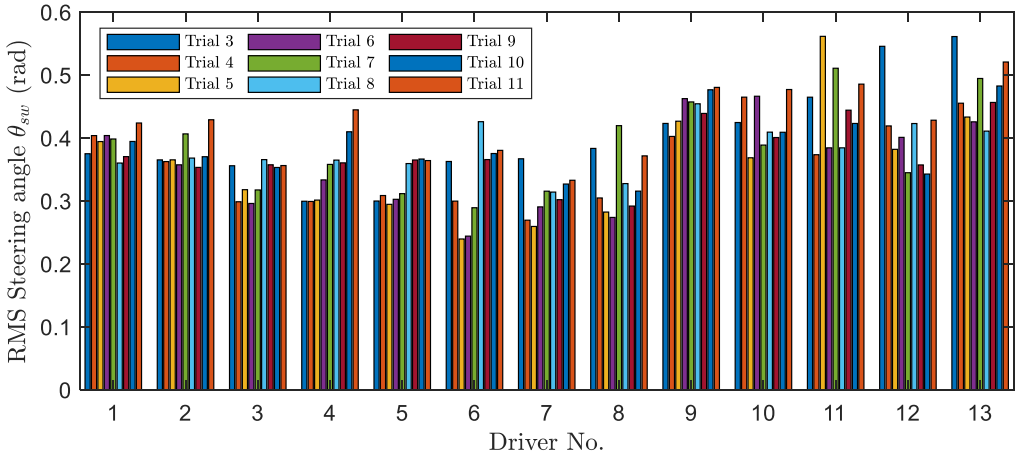

Figure 4.30: Values of RMS steering wheel angle in trials 3 to 11 for each driver.

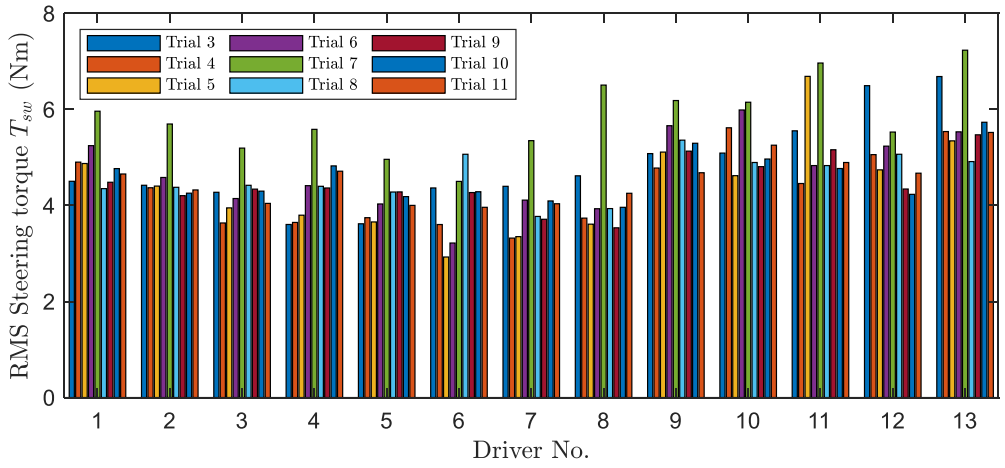

Figure 4.31: Values of RMS steering torque in trials 3 to 11 for each driver.

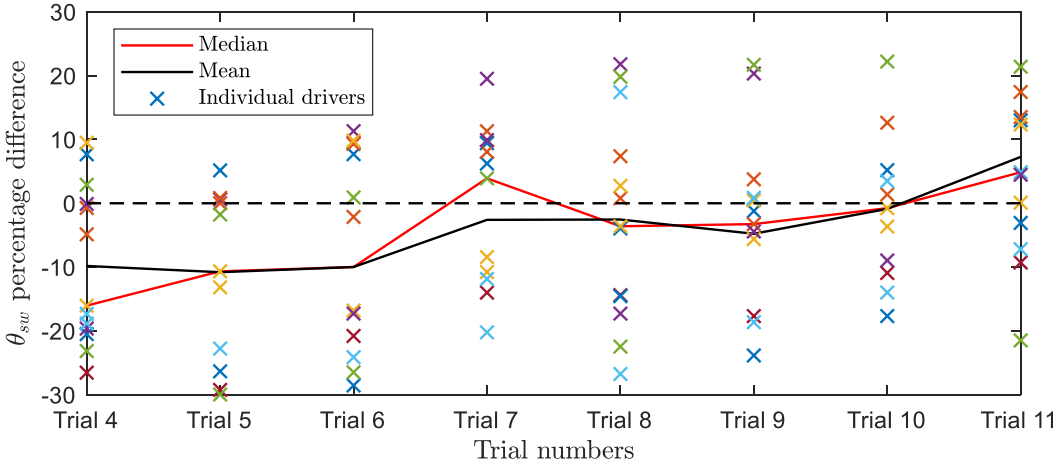

Figure 4.32: Change in RMS steering wheel angle with different levels of steering system friction compared to trial 3. Percentage differences are plotted for each driver and the median and mean over the thirteen drivers.

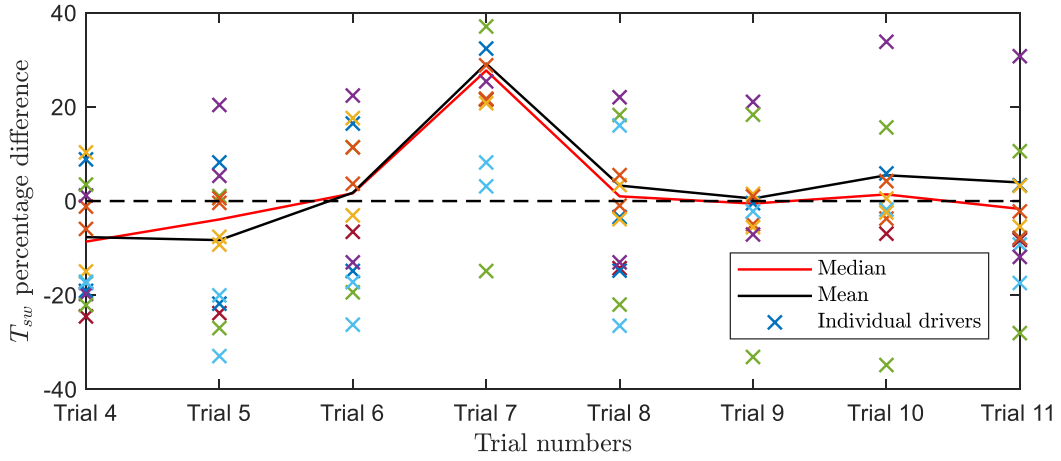

Figure 4.33: Change in RMS steering torque with different levels of steering system friction compared to trial 3. Percentage differences are plotted for each driver and the median and mean over the thirteen drivers.

Examples of the normal probability plots showing the values of RMS steering wheel angle and RMS steering torque against a theoretical normal distribution for trial 7 and trial 11 are presented in Figure 4.34 and Figure 4.35. Most of the scattered points are closely aligned with the red straight line, suggesting that the RMS values for each trial follow a normal distribution. The results for the RMS values of the other trials are similar to these two figures. In addition, the large p values from the Shapiro-Wilk test results, shown in Table 4.10, also indicate that the null hypothesis of a normal distribution is not rejected at a 5% significant level.

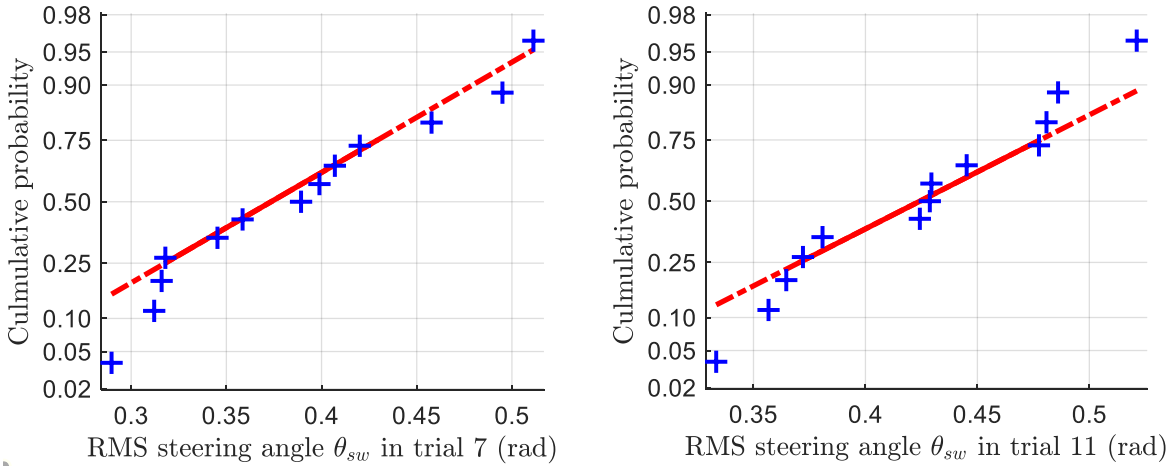

Figure 4.34: Normal plots for the values of RMS steering wheel angle in trial 7 and trial 11.

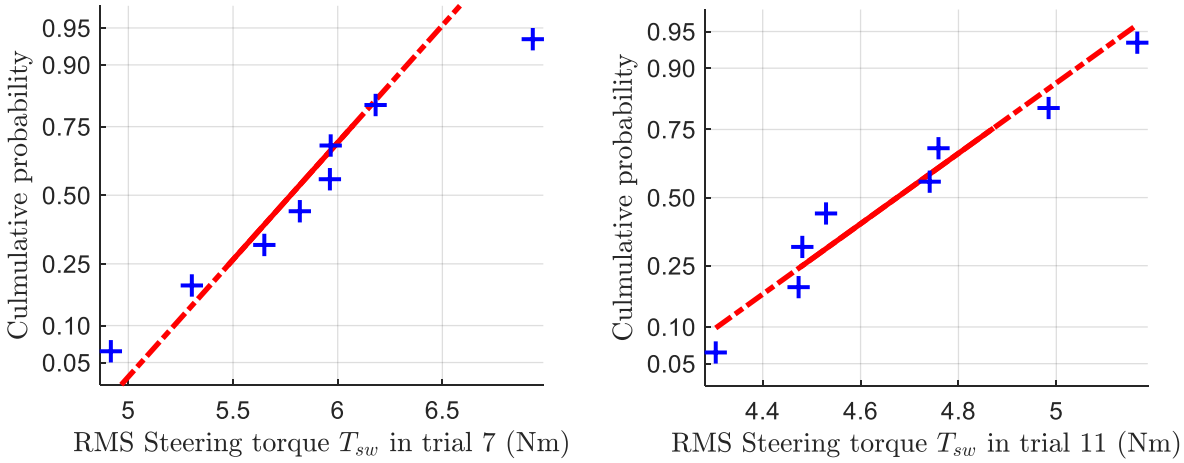

Figure 4.35: Normal plots for the values of RMS steering torque in trial 7 and trial 11.

Table 4.10: Results of Shapiro-Wilk test on the values of RMS steering wheel angle and RMS steering torque for trials 3 to 11

Criteria	Trial 3	Trial 4	Trial 5	Trial 6	Trial 7	Trial 8	Trial 9	Trial 10	Trial 11
RMS steering wheel angle θ_{sw}	0.1120	0.1519	0.2971	0.5785	0.4905	0.7708	0.2011	0.5197	0.6550
RMS steering torque T_{sw}	0.1292	0.1558	0.4621	0.8623	0.9943	0.6376	0.4663	0.1378	0.2233

The means and standard deviations of RMS steering wheel angle and RMS steering torque over all thirteen drivers for each trial calculated based on the properties of a normal distribution are shown in Table 4.11. Box plots of the RMS steering wheel angle and the RMS steering torque of all thirteen drivers in trials 3 to 11 are shown in Figure 4.36 and Figure 4.37, respectively. The results of statistical tests for investigating the significance of the difference between the trials are also summarised in Table 4.11. Although an increasing trend is identified in the mean value of RMS steering wheel angle for the increased steering system friction level, the large p values in the one-way ANOVA tests suggest that the statistical significance of the difference is small, which could be caused by the significant driver-to-driver variation in steering control behaviour. However, the differences in steering torque between trials 3 to 7 are statistically significant.

Table 4.11: Mean and standard deviation (in brackets) of RMS steering wheel angle and RMS steering torque across all thirteen drivers in trials 3 to 11

Criteria	**Trial 3**	**Trial 4**	**Trial 5**	**Trial 6**	**Trial 7**	F **(ANOVA)**	p **(ANOVA)**	p **(Bartlett)**
RMS steering wheel angle θ_{sw}	0.403 rad (0.0812 rad)	0.359 rad (0.0661 rad)	0.356 rad (0.0876 rad)	0.358 rad (0.0730 rad)	0.386 rad (0.0714 rad)	0.98	0.4249	0.8853
Criteria	**Trial 3**	**Trial 8**	**Trial 9**	**Trial 10**	**Trial 11**	F **(ANOVA)**	p **(ANOVA)**	p **(Bartlett)**
RMS steering wheel angle θ_{sw}	0.403 rad (0.0812 rad)	0.383 rad (0.0406 rad)	0.375 rad (0.0499 rad)	0.389 rad (0.0518 rad)	0.423 rad (0.0582 rad)	1.41	0.2420	0.1677
Criteria	**Trial 3**	**Trial 4**	**Trial 5**	**Trial 6**	**Trial 7**	F **(ANOVA)**	p **(ANOVA)**	p **(Bartlett)**
RMS steering torque T_{sw}	4.54 Nm (0.424 Nm)	4.17 Nm (0.532 Nm)	4.13 Nm (0.657 Nm)	4.58 Nm (0.602 Nm)	5.84 Nm (0.600 Nm)	11.97	<0.001	0.8447
Criteria	**Trial 3**	**Trial 8**	**Trial 9**	**Trial 10**	**Trial 11**	F **(ANOVA)**	p **(ANOVA)**	p **(Bartlett)**
RMS steering torque T_{sw}	4.54 Nm (0.424 Nm)	4.64 Nm (0.378 Nm)	4.51 Nm (0.351 Nm)	4.74 Nm (0.320 Nm)	4.48 Nm (0.289 Nm)	0.59	0.6730	0.8869

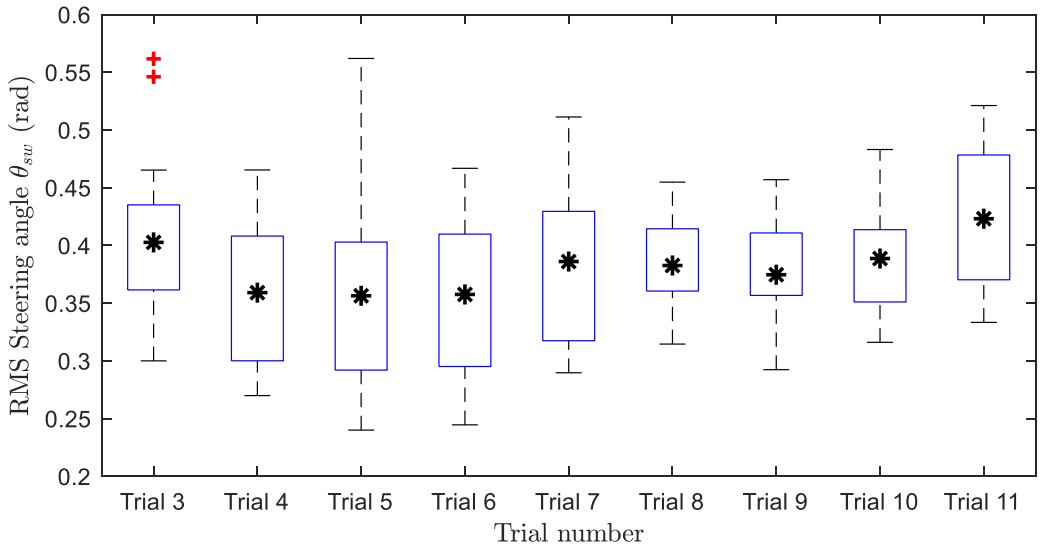

Figure 4.36: Box plot of RMS steering wheel angle of all thirteen drivers in trials 3 to 11. The black asterisks indicate the mean of the RMS values for each trial, and the bottom and top edges of the box indicate the 25th and 75th percentiles, respectively. The dashed lines extend to the most extreme data points not considered outliers, and the red plus signs indicate the outliers.

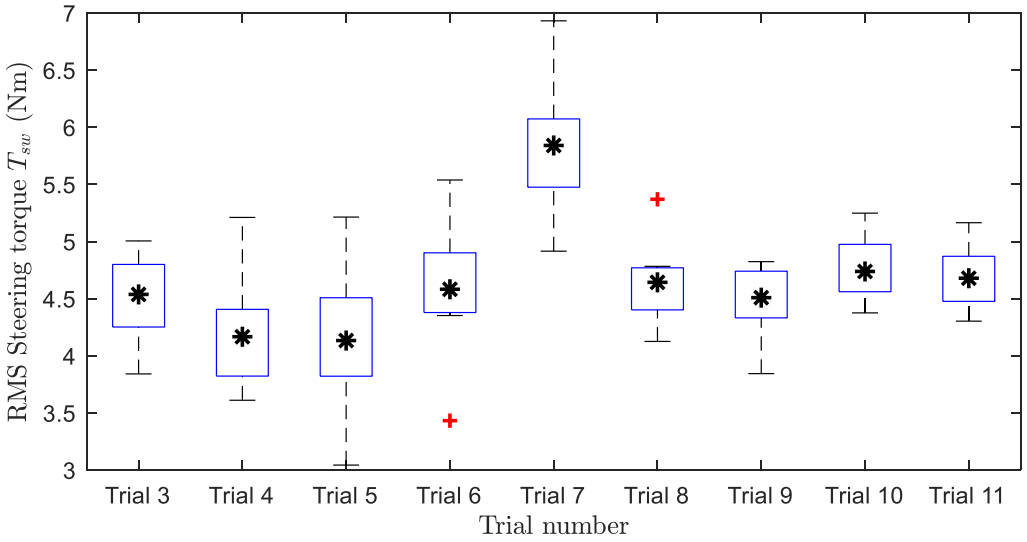

Figure 4.37: Box plot of RMS steering torque of all thirteen drivers in trials 3 to 11. The black asterisks indicate the mean of the RMS values for each trial, and the bottom and top edges of the box indicate the 25th and 75th percentiles, respectively. The dashed lines extend to the most extreme data points not considered outliers, and the red plus signs indicate the outliers.

4.5.3 Steering Reversal Rate Analysis

Steering reversal rate, SRR, counts the number of times the steering wheel changes direction per minute though an angle larger than a gap value 0.0524 radians; high values of SRR have been correlated with the increased level of difficulty of the steering task [139]. However, SRR could indicate how fast the drivers reacted to the moving target line in the randomly moving path following task. Values of RMS steering reversal rate for all thirteen drivers in trials 3 to 11 are plotted in Figure 4.38. The algorithm used for calculating the steering reversal rate is given in [140]. The steering wheel angle and steering angular velocity signals are processed by a second-order Butterworth filter with a cut-off frequency 2Hz to reduce high-frequency noise. The reversals in the steering wheel angle signal and the stationary points in the steering angular velocity signal in trial 11 for Driver 1 are shown in Figure 4.39 as an example. Driver 13 had the largest overall steering reversal rates compared to the others. This could be because Driver 13 employed a quite ‘aggressive’ control strategy to chase the moving target line by weighting less on the control inputs in the cost function. The values of steering reversal rate also vary with trials. The percentage changes in steering reversal rate with respect to trial 3 when different levels of steering system friction were implemented are shown in Figure 4.40, along with the median and mean values over the thirteen drivers for each nonlinear trial. Figure 4.40 shows that steering reversal rate is reduced when the friction level is increased in the steering system.

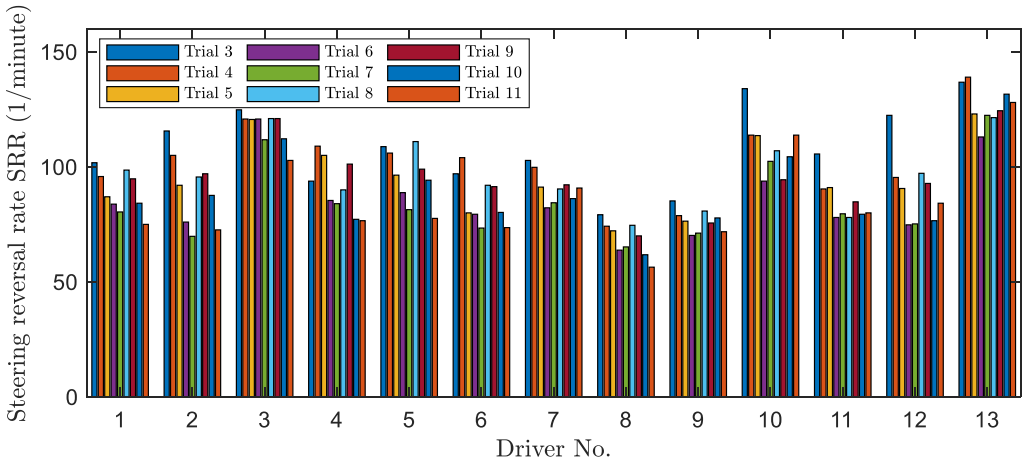

Figure 4.38: Values of steering reversal rate in trials 3 to 11 for each driver.

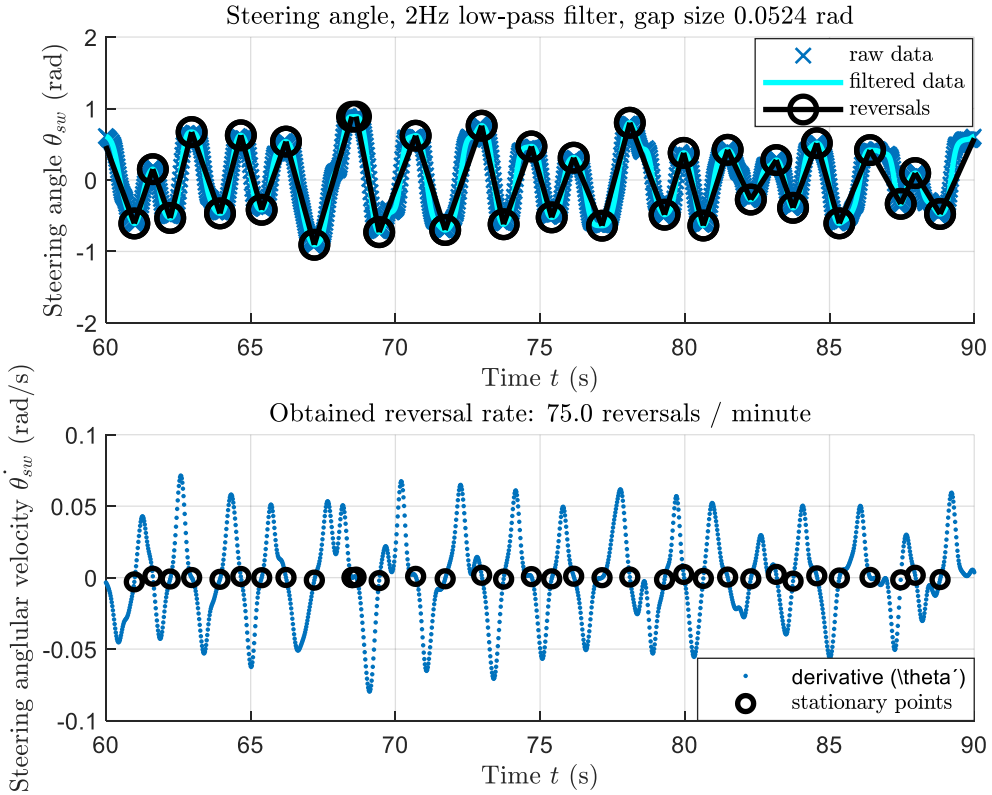

Figure 4.39: Example of steering wheel reversal in trial 11 for Driver 1.

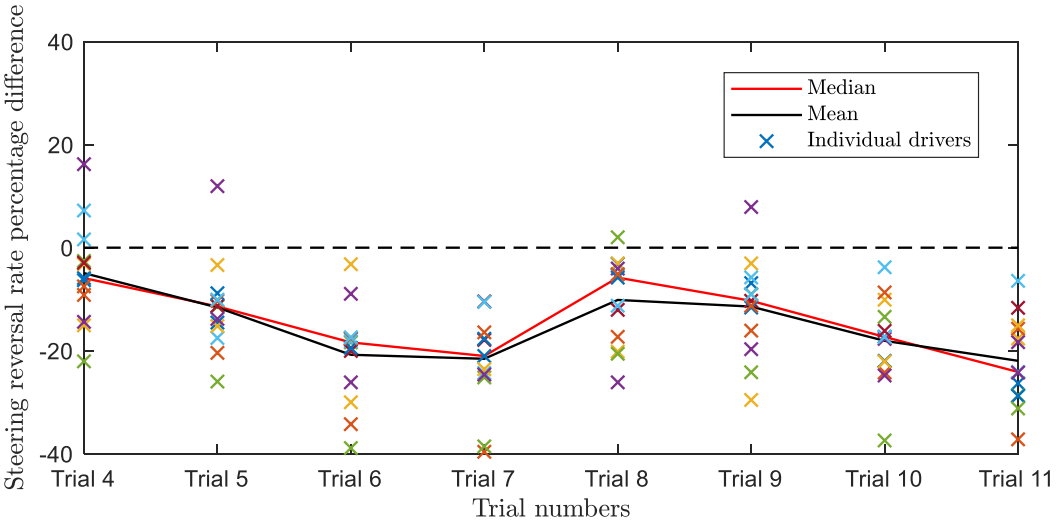

Figure 4.40: Change in steering reversal rate with different levels of steering system friction compared to trial 3. Percentage differences are plotted for each driver and the median and mean over the thirteen drivers.

Again, examples of the normal probability plots showing the values of steering reversal rate against a theoretical normal distribution for trial 7 and trial 11 are presented in Figure 4.41. Although there seems to be a curvature of the line formed by the scattered points, the p values from the Shapiro-Wilk test results, shown in Table 4.12, indicate that the normal distribution assumption is not invalid.

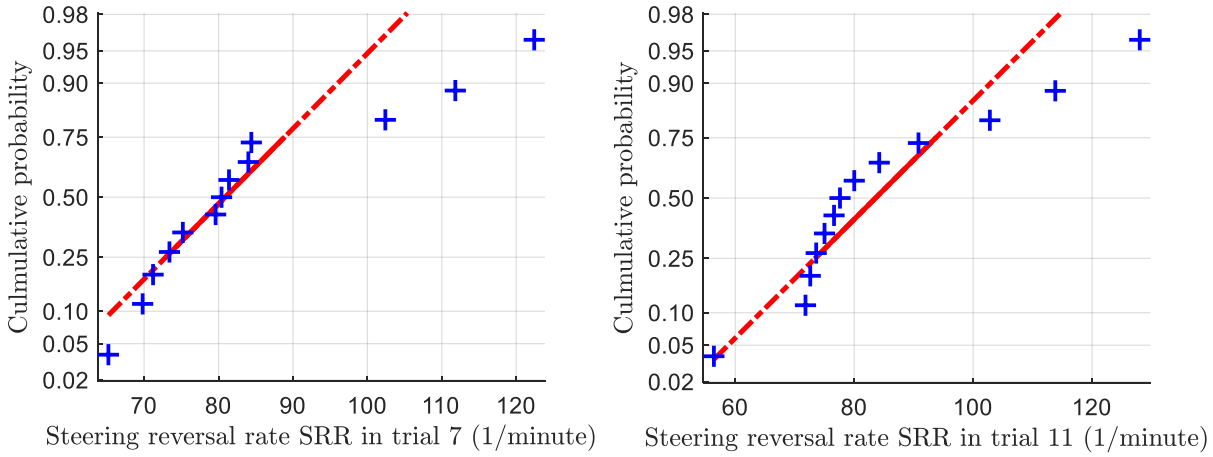

Figure 4.41: Normal plots for the values of steering reversal rate in trial 7 and trial 11.

Table 4.12: Results of Shapiro-Wilk test on the values of steering reversal rate for trials 3 to 11

Criteria	Trial 3	Trial 4	Trial 5	Trial 6	Trial 7	Trial 8	Trial 9	Trial 10	Trial 11
Steering reversal rate SRR	0.9195	0.6989	0.3752	0.0814	0.0681	0.5799	0.1829	0.0784	0.0717

The mean and standard deviation of steering reversal rate over the thirteen drivers for each trial are shown in Table 4.13. Box plot of steering reversal rate of all thirteen drivers is presented in Figure 4.42. The results of statistical tests for investigating the significance of the difference between the trials are also summarised in Table 4.13. The small p values in the one-way ANOVA tests suggest that the differences between the trials are statistically significant.

Table 4.13: Mean and standard deviation of the values of steering reversal rate across all thirteen drivers in trials 3 to 11

Criteria	**Trial 3**	**Trial 4**	**Trial 5**	**Trial 6**	**Trial 7**	F **(ANOVA)**	p **(ANOVA)**	p **(Bartlett)**
Steering reversal rate SRR	108 (17.8)	102 (17.0)	95.3 (16.1)	85.4 (16.1)	84.7 (17.1)	4.94	0.0016	0.9962
Criteria	**Trial 3**	**Trial 8**	**Trial 9**	**Trial 10**	**Trial 11**	F **(ANOVA)**	p **(ANOVA)**	p **(Bartlett)**
Steering reversal rate SRR	108 (17.8)	96.7 (15.0)	95.3 (15.1)	88.7 (18.2)	84.9 (19.5)	3.53	0.0118	0.8699

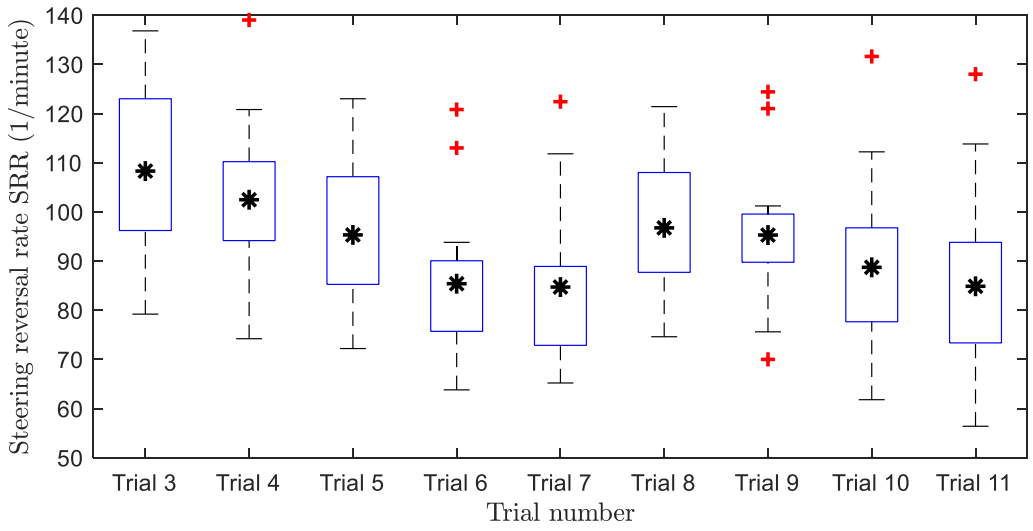

Figure 4.42: Box plot of steering reversal of all thirteen drivers in trials 3 to 11. The black asterisks indicate the mean of the RMS values for each trial. The black asterisks indicate the mean of the RMS values for each trial, and the bottom and top edges of the box indicate the 25th and 75th percentiles, respectively. The dashed lines extend to the most extreme data points not considered outliers, and the red plus signs indicate the outliers.

4.5.4 Trial Performance Comparison

The aim of the test subjects during each trial was to follow the randomly moving target path as closely as possible. Therefore, one way to quantify the test subjects' performance in each trial is to find the value of RMS path-following error. However, for a given test subject, the accuracy with which they

follow the randomly moving target also depends on their control effort, which could be reflected by the value of RMS steering torque. A test subject who decided to use more control effort may achieve a lower path-following error than a test subject who chose to steer less, which has been evidenced by the comparison of several objective metrics in earlier sections. Therefore, the value of RMS path-following error and the value of RMS steering torque need to be considered as a combination to assess the driving performance. The large spread of the RMS values shown in Figure 4.29 and Figure 4.37 indicate that the consistency between different test subjects' driving performance is poor. Therefore, the measured vehicle responses and driver steering actions for all thirteen drivers are concatenated to give a 'concatenated driver', which is used to assess the drivers' performance in different trials. The duration of the concatenated data is longer than that of the data for the individual drivers, allowing the RMS values to be less uncertain. An 'averaged driver' generated by averaging the time series data over the individual drivers is not used since the principle of superposition does not apply with nonlinear dynamics. The values of RMS path-following error and the values of RMS steering wheel angle in different trials for the 'concatenated driver' are shown as markers in Figure 4.43. Markers towards the lower left of the graph represent better overall performance where drivers achieved a lower path-following error with smaller steering torque inputs. By this metric, the 'concatenated driver' performed worse in trials with relatively high steering system friction level, which are represented by the red markers.

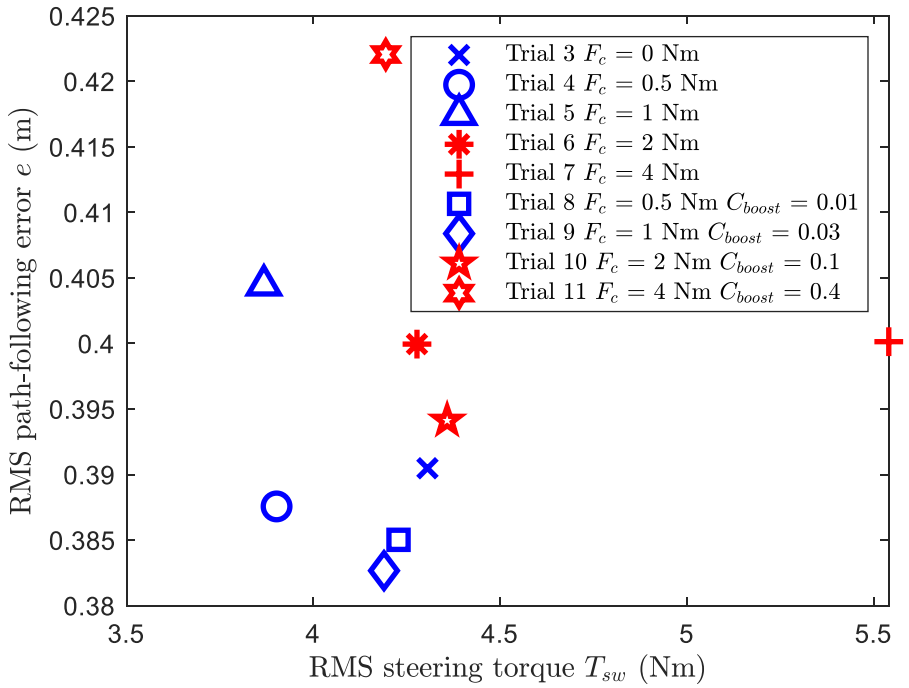

Figure 4.43: RMS path-following error against RMS steering torque for each of the trials for the 'concatenated driver'.

4.6 Analysis and Discussion of Subjective Ratings

In trials 3 to 11 where different levels of friction torque are applied to the steering system, the test subjects were asked to provide subjective ratings for each trial based on a questionnaire. This allows the influence of steering system friction on the drivers' subjective assessment of steering feel to be determined by directly comparing the subjective ratings between the trials. In this section, these subjective ratings are analysed in various ways. As recommended in [44], initial statistical analysis of the subjective ratings is conducted to understand how the test subjects used the judgement scales and set their ratings, and the ratings' spread. The subjective ratings are then normalised based on results of the initial analysis to allow the data analysis accuracy to be improved and more detailed statistical analysis and tests to be performed. Finally, correlations between the subjective and objective data are identified.

4.6.1 Overall Rating Distribution

In order to understand how the test drivers set their ratings during the experiments, a histogram showing their subjective rating distribution is generated by plotting the number of appearances of each rating for all drivers, all subjective questions and all trials, as presented in Figure 4.44a. Some descriptive statistics values, including the mean, the standard deviation, the median and the skewness of the ratings, are presented at the top of the figure. In addition, the normal probability plot of the subjective ratings to test whether the ratings follow a normal distribution or not is shown in Figure 4.44b. Figure 4.44a and Figure 4.44b show that the ratings on all subjective questions in all trials from all drivers form a slightly positively skewed distribution, which is somehow expected as when there was presence of steering system friction, most of the changes in the objective metrics reflected by the subjective questions or the subjective metrics themselves correspond to higher ratings compared to the linear trial 3.

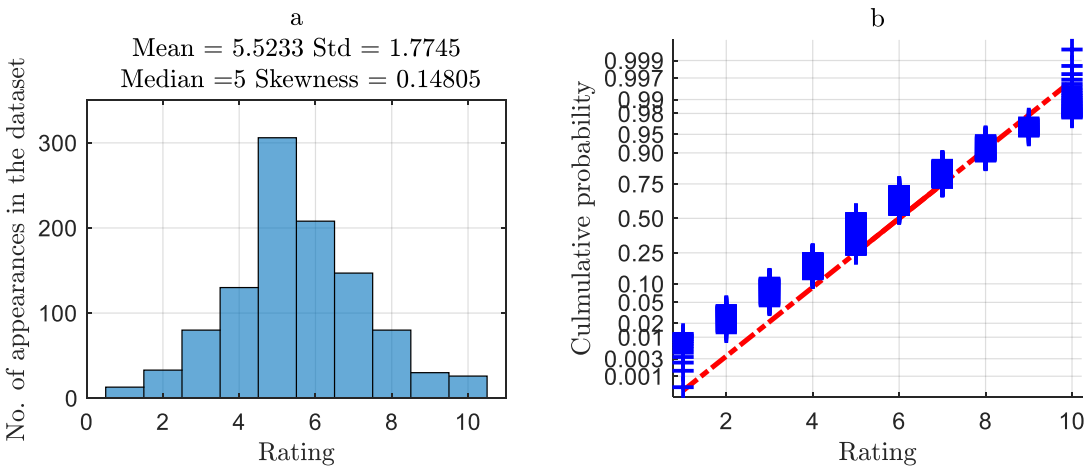

Figure 4.44: Subjective ratings distribution for all drivers, all questions, and all trials (a: histogram of subjective ratings with descriptive statistics; b: normal probability plot for the subjective ratings)

4.6.2 Driver Tendency and Normalisation

In order to understand the rating tendency for different test drivers, histograms showing the subjective rating distribution for each driver are generated by plotting the number of appearances of each rating for all subjective questions and all trials, as shown in Figure 4.45. Like Figure 4.44a, the mean, the standard deviation, and the median of the ratings are shown at the top of the figure. Figure 4.45 shows that the mean of each driver's ratings falls in the range between 4.86 to 6.32. The median of the range is around 5.59, which is close to the mean value 5.52 shown in Figure 4.44a. However, it is noticed that the rating tendency varies across the drivers. The means for Driver 2 and Driver 13 are comparably larger; the standard deviations for Driver 11, Driver 12, and Driver 13 are comparably lower. In Figure 4.46, subjective ratings are plotted for each driver for all subjective questions and trials, with the red dots representing the means for each question. The difference in the rating tendency between the test drivers is also identified in Figure 4.46. For example, the red dots for Driver 2 are usually seen at the top of the plot, while the blue circles for Driver 12 are distributed in a small range. Previous literature suggests that the discrepancy in the rating behaviours between drivers could be caused by the different driving experiences, the different professional vehicle dynamics experience, and the difficulty in setting the ratings in relation to the others [44]. No matter which is the root cause, the variation in rating tendency implies a risk for the data analysis: even when the different test drivers share similar impressions of the trials, it might not be reflected by the numerical ratings because of different use of the rating scale. To address this problem, a normalisation is conducted by normalising each test driver's ratings on each question to the average mean and standard deviation of the rating distribution of all ratings and all test subjects for that question, as suggested by [44] and shown in (4.7). The normalisation is conducted separately for each question, considering that the drivers might have different rating tendencies for different questions. Firstly, the ratings on each question for each test driver have their mean value subtracted and are divided by their standard error, resulting in a date set of standard normal distribution with a mean of zero and a variance of one. Then, the standard normal distribution is multiplied by the average standard deviation of all drivers' ratings on that question and adds to the average mean of all drivers' ratings on that question. In addition, the normalisation is conducted separately for trials 3 to 7 and for trials 3 and 8 to 11 in this study.

$$\hat{R}_{i,j,k} = \frac{(R_{i,j,k} - \bar{R}_{i,k})}{\sigma_{i,k}} \sigma_i + \bar{R}_i \tag{4.7}$$

where $R_{i,j,k}$ and $\hat{R}_{i,j,k}$ are the original rating and the normalised rating of driver k on question i for trial j, respectively; $\bar{R}_{i,k}$ and $\sigma_{i,k}$ are the mean value and the standard deviation of the ratings of driver k on question i over all the trials, respectively; $\bar{R}_i$ and σ_i are the mean value and the standard deviation of all drivers' ratings on question i, respectively.

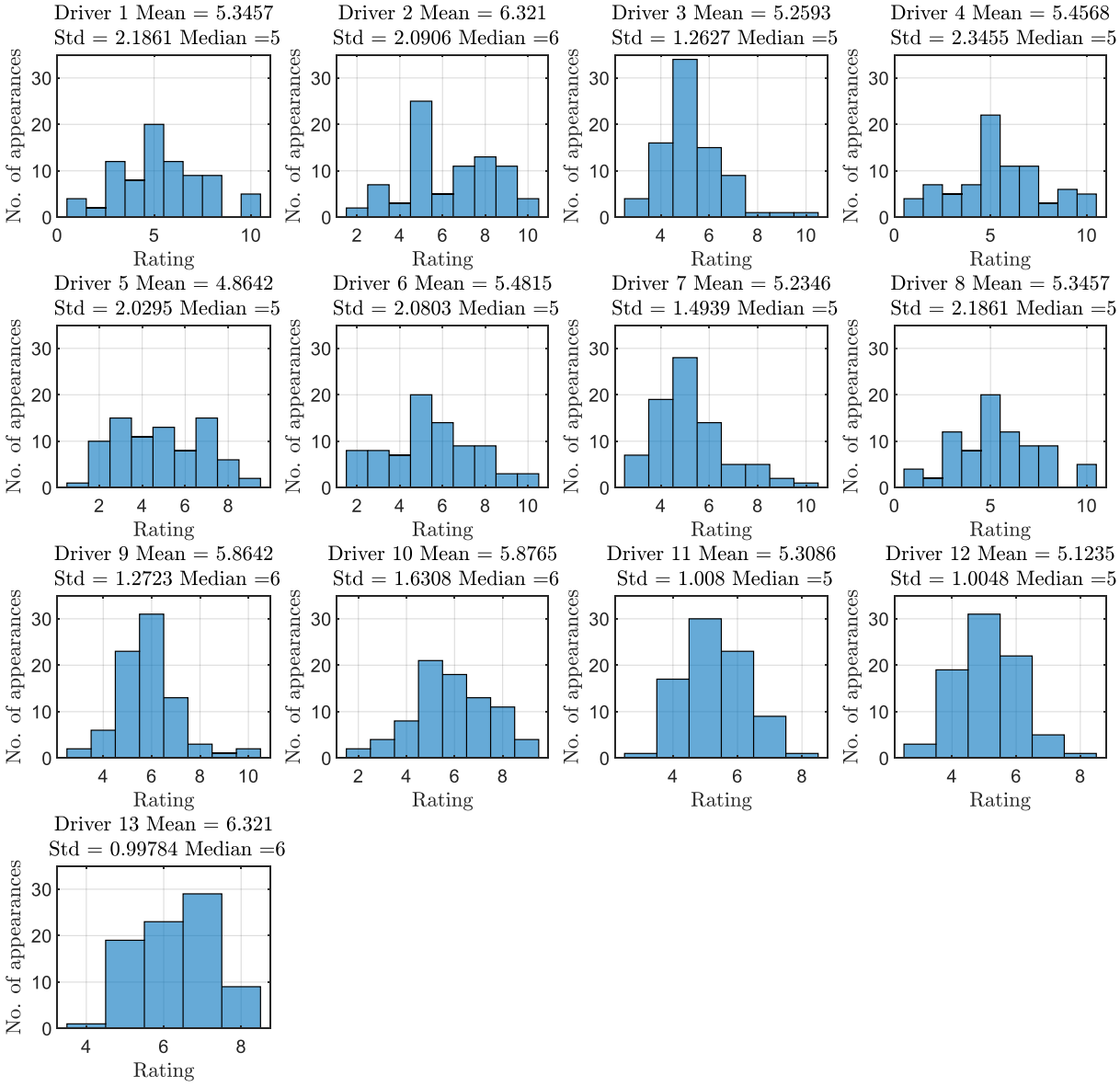

Figure 4.45: Subjective rating distribution on all questions in all trials for each driver with descriptive statistics.

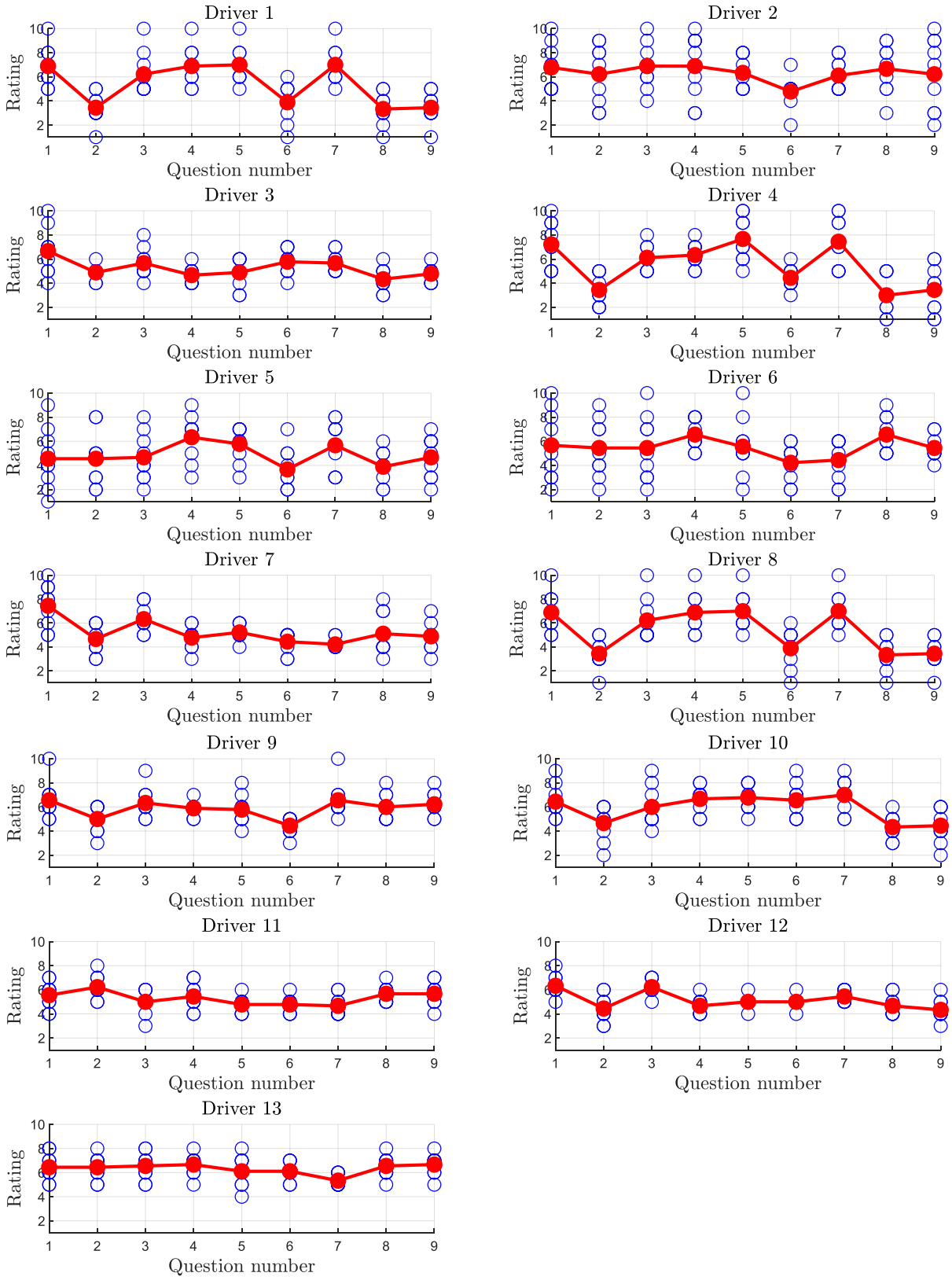

Figure 4.46: Subjective ratings on all questions in all trials for each driver, with blue circles representing the individual ratings and the red dots representing the values of mean of all trials.

4.6.3 Rating Distribution for Each Question

In order to conduct statistical analysis of the normalised subjective ratings, the Shapiro-Wilk test with a 5% significant level was conducted to determine if the normalised subjective ratings for each question and trial across all the drivers follow a normal distribution, with the resulting p values shown in Table 14 and Table 15. It is shown that there is a small number of p values which are smaller than 0.05. To visualise the non-normal characteristics, examples of the normal probability plots for the normalised subjective ratings for Question 1 Trial 11 and Question 3 Trial 7 are shown in Figure 4.47. It is also shown that there are several scattered points away from the red reference lines at the extremes. This deviation from the normal distribution is due to the finite range of the rating scale. However, it is encouraging that most of the p values are larger than 0.05, suggesting that the normal distribution assumption should not be rejected. To ensure the robustness of further statistical analysis results, the normalised subjective ratings are refined further by removing all the outliers. Again, an outlier is defined as a data point that is located outside 1.5 times the interquartile range above the upper quartile and below the lower quartile. The normality of the refined normalised subjective ratings was checked once more with the Shapiro-Wilk test, and all the resulting p values became larger than 0.05 after the data refinement.

Table 4.14: Results of Shapiro-Wilk test on the normalised subjective ratings in trials 3 to 7

Question No.	Trial 3	Trial 4	Trial 5	Trial 6	Trial 7
1	0.3340	0.5040	0.0077	0.1651	0.1891
2	0.3261	0.6816	0.6019	0.9104	<0.001
3	0.0017	0.9181	0.2795	0.0065	<0.001
4	0.1481	0.2139	0.1327	0.1244	0.0216
5	0.0080	0.9194	0.3351	0.0009	0.0189
6	0.2398	0.5039	0.7316	0.2907	0.1595
7	0.0796	0.0846	0.1073	0.2114	0.1439
8	0.1946	0.6190	0.5199	0.4113	0.1297
9	0.1379	0.3086	0.1314	0.9820	0.0902

Table 4.15: Results of Shapiro-Wilk test on the normalised subjective ratings in trials 3 and 8 to 11

Question No.	Trial 3	Trial 8	Trial 9	Trial 10	Trial 11
1	0.0309	0.6057	0.0444	0.3624	0.0104
2	0.4339	0.3419	0.1180	0.4760	0.0635
3	0.2139	0.2641	0.7920	0.0656	0.3270
4	0.1906	0.1476	0.2981	0.0071	0.0991
5	0.3358	0.5909	0.4979	0.1621	0.2061
6	0.4051	0.1615	0.2637	0.6171	0.1090
7	0.0549	0.5105	0.1684	0.3807	0.1116
8	0.2864	0.4826	0.3457	0.2682	0.0630
9	0.3457	0.7448	0.2121	0.1635	0.0839

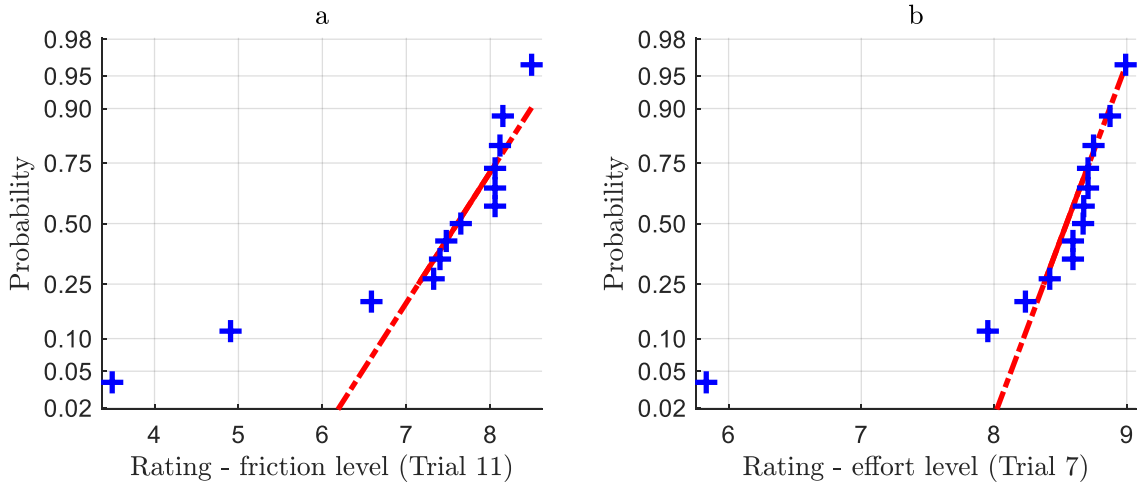

Figure 4.47: Normal plot for the subjective ratings of all drivers (a: Question 1 Trial 11; b: Question 3 Trial 7)

Based on the properties of a normal distribution, the mean of the normalised subjective ratings with the 95% confidence interval of the mean calculated based on the assumption of t-distribution for each trial and subjective question is plotted, as shown in Figure 4.48. Similar to the analysis of the influence of steering system friction on the objective metrics, the statistical significance of the difference in the mean normalised subjective rating between the trials was verified by using a one-way ANOVA test, complemented by Bartlett's test for equal variances to ensure the robustness of the results. The p values for these statistical tests conducted for trials 3 to 7 and for trials 3, 8 to 11 are summarised in Table 4.16 and Table 4.17, respectively.

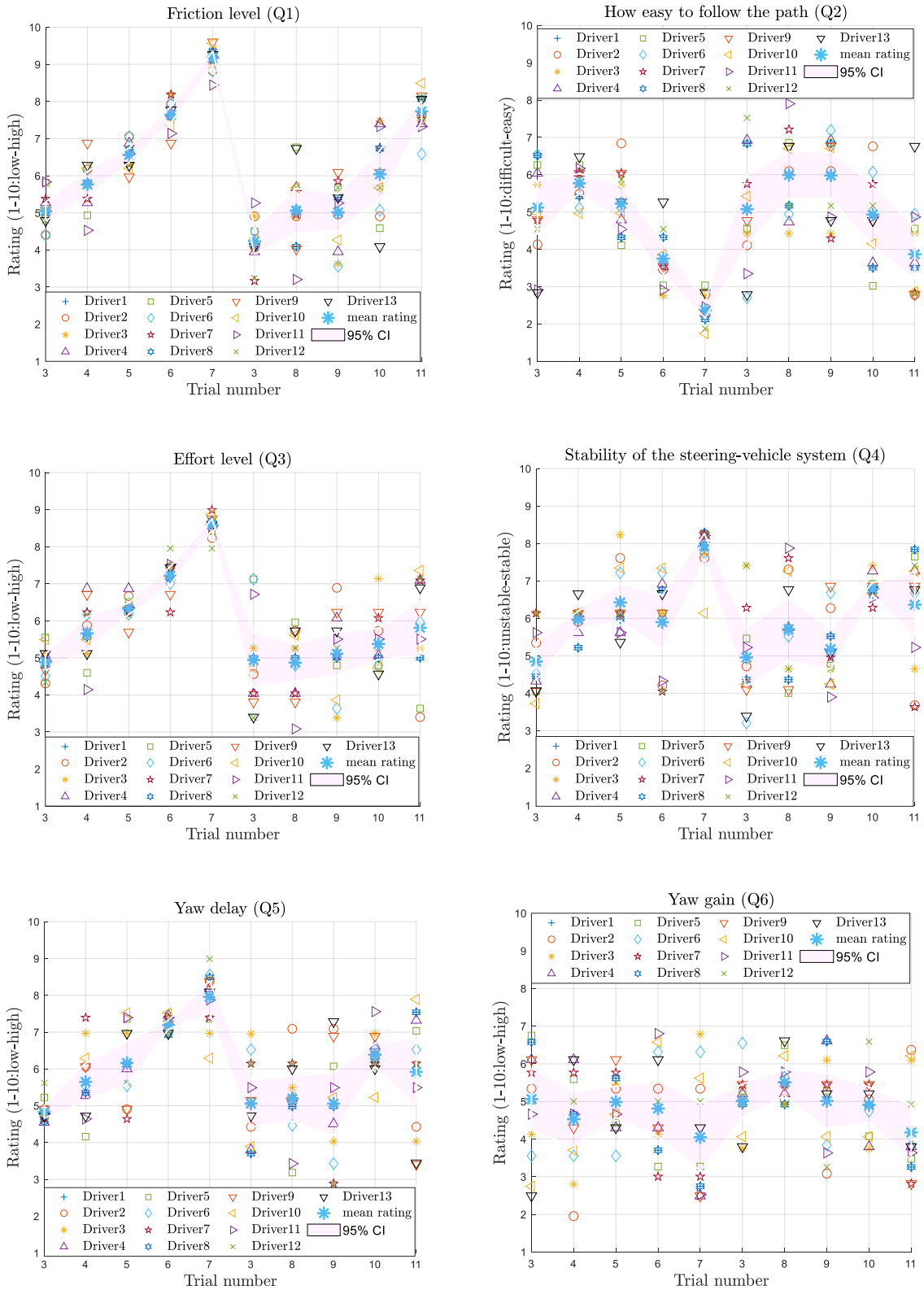

Figure 4.48: Normalised subjective ratings for all drivers in each trial for each question, with mean normalised subjective rating over all the drivers in each trial and its 95% confidence interval(CI).

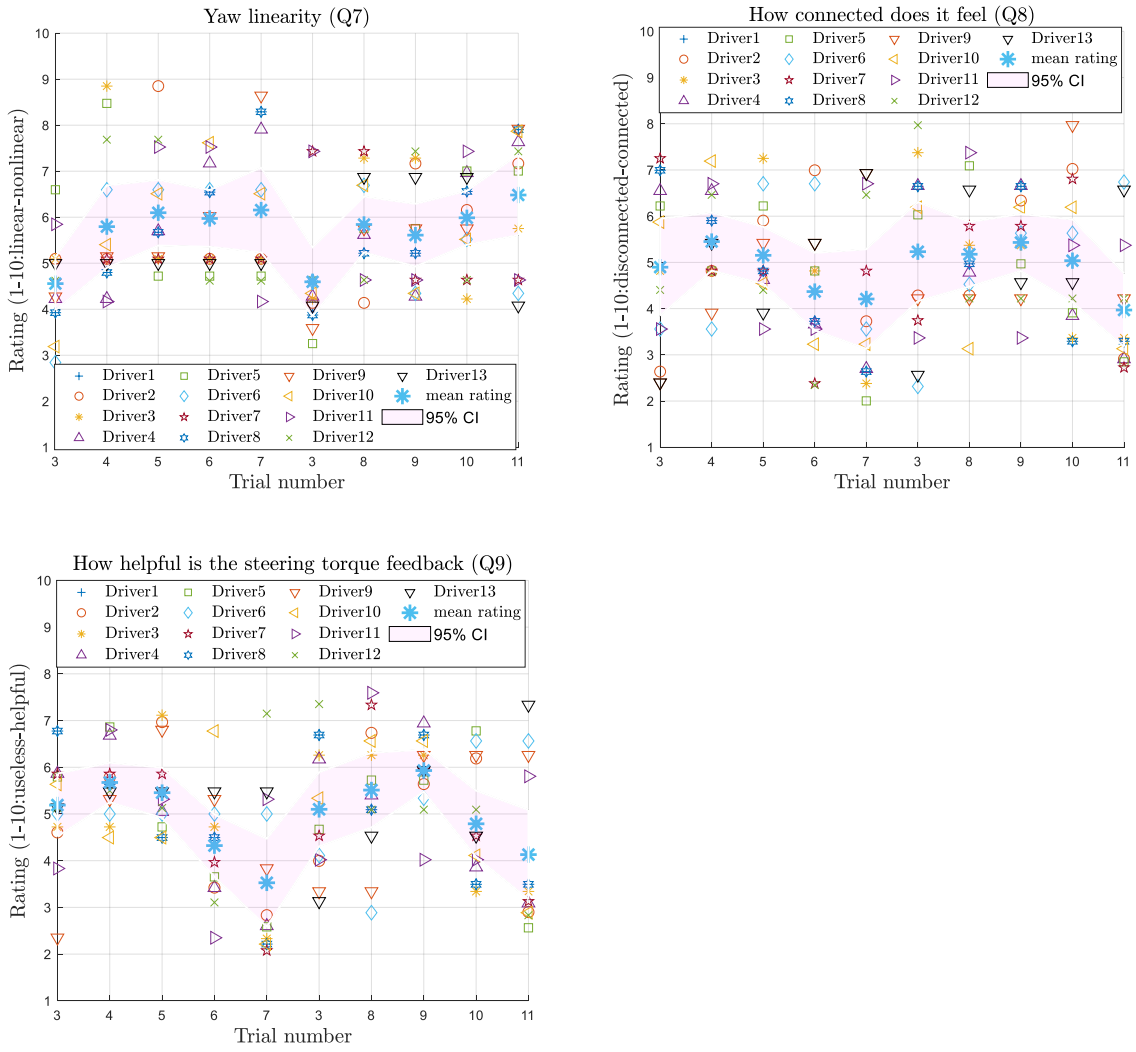

Figure 4.48(continued): Normalised subjective ratings for all drivers in each trial for each question, with mean normalised subjective rating over all the drivers in each trial and its 95% confidence interval(CI).

Table 4.16: Mean and standard deviation of the subjective ratings across all thirteen drivers in trials 3 to 7

Question No.	Trial 3	Trial 4	Trial 5	Trial 6	Trial 7	F (ANOVA)	p (ANOVA)	p (Bartlett)
1	5.05 (0.446)	5.92 (0.835)	6.70 (0.621)	7.54 (0.538)	9.17 (0.326)	97.16	<0.001	0.0265
2	5.12 (1.29)	5.77 (0.460)	5.23 (0.829)	3.92 (0.953)	2.66 (1.12)	21.43	<0.001	0.0193
3	5.08 (0.828)	5.66 (0.792)	6.35 (0.502)	7.06 (0.732)	8.39 (0.813)	38.78	<0.001	0.4964
4	4.85 (0.899)	6.12 (0.581)	6.43 (0.879)	5.90 (1.27)	7.40 (1.50)	9.55	<0.001	0.0210
5	4.87 (0.919)	5.65 (0.911)	6.16 (1.01)	7.08 (0.489)	7.71 (1.19)	18.93	<0.001	0.0776
6	5.06 (1.46)	4.53 (1.27)	4.99 (0.738)	4.81 (1.30)	4.05 (1.58)	1.3	0.2797	0.1551
7	4.88 (1.57)	5.80 (1.58)	6.10 (1.26)	5.97 (1.09)	6.16 (1.63)	3.18	0.0195	0.6181
8	4.90 (1.85)	5.45 (1.11)	5.15 (1.09)	4.37 (1.48)	4.21 (1.90)	1.52	0.2073	0.1709
9	4.93 (1.54)	5.49 (1.03)	5.46 (0.949)	4.32 (1.18)	3.53 (1.67)	5.28	0.001	0.2328

Table 4.17: Mean and standard deviation of the subjective ratings across all thirteen drivers in trials 3, 8 to 11

Question No.	Trial 3	Trial 8	Trial 9	Trial 10	Trial 11	F (ANOVA)	p (ANOVA)	p (Bartlett)
1	4.77 (1.55)	5.06 (1.05)	5.31 (1.35)	6.04 (1.13)	7.21 (1.45)	7.15	<0.001	0.6646
2	5.08 (1.63)	5.99 (1.11)	5.98 (1.09)	4.93 (1.47)	3.87 (1.20)	5.81	<0.001	0.5546
3	4.94 (1.31)	4.87 (0.878)	5.11 (1.03)	5.38 (0.741)	5.81 (1.33)	1.63	0.1777	0.2277
4	4.95 (1.36)	5.71 (1.47)	5.18 (0.945)	6.56 (0.704)	6.37 (1.53)	4.2	0.0046	0.0649
5	5.06 (1.13)	5.19 (1.08)	5.06 (1.50)	6.24 (0.780)	5.92 (1.61)	2.51	0.0443	0.1236
6	5.01 (0.788)	5.51 (0.609)	5.01 (1.30)	4.91 (0.831)	4.18 (1.28)	2.96	0.0267	0.0467
7	4.85 (1.60)	5.84 (1.07)	5.61 (1.20)	5.99 (1.03)	6.48 (1.55)	2.71	0.0382	0.4236
8	5.23 (1.89)	5.18 (1.24)	5.43 (1.09)	5.04 (1.58)	3.97 (1.40)	2.01	0.1041	0.3667
9	5.10 (1.40)	5.51 (1.41)	5.93 (0.797)	4.79 (1.25)	4.13 (1.69)	3.41	0.0140	0.1818

As mentioned in Section 4.3, there are two types of subjective questions listed in the questionnaire. The first type is judging the magnitude of the criteria: friction level, effort level, stability of the steering-vehicle system, yaw delay, yaw gain, and yaw linearity. The results of the statistical tests shown in Table 4.16 and Table 4.17 agree with most of the expected effects of steering system friction on the

corresponding objective metrics, indicating the drivers were able to detect the changes caused by steering system friction in these objective metrics. Detailed analysis of statistically significant results is presented below:

- Q1: Friction level: 1 (low) to 10 (high):

An increasing trend in the normalised subjective ratings is determined with the increased level of steering system friction. The normalised ratings in trials 8 to 11 are lower than those in trials 4 to 7, which is because of the reduction in friction level due to the existence of assist torque from the driving assisting system in trials 8 to 11. It is interesting to notice that the test drivers achieved greater consistency in the subjective evaluation in trials 4 to 7 compared to trials 8 to 11. This might be because it is more difficult for some drivers to assess the friction characteristics when the overall physical torque level is held similarly.

- Q3: Physical effort level (how hard is it to turn the steering wheel): 1 (low) to 10 (high):

The steering wheel is perceived as heavier to operate with an increase in steering system friction in trials 3 to 7, as the steering became more resistant with the implementation of steering system friction. A slight increase in the averaged rating is also observed in trials 8 to 11, although no significant difference in the perceived physical torque effort level is identified, as expected. This is because of the increased steering wheel angle magnitude caused by the increased steering system friction, which has been explained in Section 4.5.2. However, this could also be because some drivers related the change in the nonlinearity to the physical torque effort level, which could also explain the lower consistency in the ratings in trials 8 to 11 compared to trials 4 to 7.

- Q4: Stability of the steering-vehicle system: 1 (unstable) to 10 (stable):

The steering-vehicle system is perceived as more stable with an increase in steering system friction level. This is because of the damping effects of steering system friction.

- Q5: Yaw delay (between vehicle yaw velocity and steering wheel angle): 1 (low) to 10 (high) & Q7: Yaw linearity: 1 (linear) to 10 (nonlinear):

Increasing trends are observed for yaw delay and yaw linearity perceived by the drivers for increased steering system friction level. Friction is a direct source of nonlinearity in the steering-vehicle system and could incur delayed vehicle response due to its phase delay effect.

- Q6: Yaw gain (vehicle yaw velocity to steering wheel angle): 1 (low) to 10 (high):

In general, the yaw gain perceived by the drivers is similar in different trials, although the averaged normalised subjective rating in trial 11 is different from the others. This agrees with what is expected since the steering gear ratio is not affected by the steering system friction.

The second type of question is evaluating the properties of the steering-vehicle system based on purely subjective experience. Statistically significant differences in the normalised subjective ratings are observed between trials 3 to 7 and between trials 3 and 8 to 11 for the two questions: how easy is it to follow the randomly moving target path (Q2), and how helpful is the steering torque feedback for the task (Q9). The overall evaluation indicates that on average a steering-vehicle system with a small amount of friction around 0.5Nm to 1Nm is preferred. This could be because the small amount of steering system friction provides some damping to stabilise the steering-vehicle system. Segel [28] showed that low levels of damping in the steering response created unfavourable ratings. In addition, a similar finding is obtained by Skarzynska [141], who also investigated the influence of steering column friction on steering feel, that a steering system with a small amount of friction was preferred by the test drivers, although the preferred level was found to be around 0.15Nm. The drivers' satisfaction about the steering properties and the steering torque feedback drops when the friction level is increased further. A similar trend is identified for the averaged normalised subjective ratings for the question: how connected does it feel (Q8), which is evaluating the extent to which the rotation of the wheel is felt connected to the response of the vehicle. However, this effect is not statistically significant.

4.6.4 Correlations between Subjective and Objective Metrics

The normalised subjective ratings on most estimation questions are compared with the values of corresponding objective metrics measured in the experiments through a linear regression method, similar to that used in [10], to impartially evaluate the test drivers' subjective responses, as shown in Figure 4.49. The shaded area in each plot is the 95% confidence interval for the mean values of the normalised subjective ratings based on the assumption of t-distribution. There are three linear regression lines for each group of trials in each plot: the solid line represents the linear regression of mean values of the ratings, while the dashed lines represent the borders of the 95% confidence area. The correlation coefficient r for each of the linear regression lines is also shown in Figure 4.49. The objective metrics consisted of the following items which need specific clarification about how they are calculated:

- **Friction torque magnitude:** equivalent magnitude of the steering system friction torque acting on the steering wheel. A simulated torque demand signal is generated using the measured steering wheel angle processing a steering-vehicle model, where the friction element is placed directly at the steering wheel instead of the steering column. The value of the friction torque magnitude is estimated for each driver and trial by minimising the difference between the simulated torque demand signal and the actual torque demand signal recorded during the experiment. The known applied friction torque at the column is not directly used since the assist torque effectively reduces the magnitude of the applied friction torque.

- **Steering resistance level:** the ratio of RMS steering torque to RMS steering wheel angle (approximating the equivalent stiffness of the system).
- **Yaw delay:** time shift between steering wheel angle and vehicle yaw velocity. Initially, the cross-correlation between each pair of signals at all possible lags is found and then normalised. The estimated time delay is given by the negative of the lag for which the normalised cross-correlation has the largest absolute value. This algorithm is achieved by Matlab's '*finddelay*' function.
- **Yaw gain:** the ratio of RMS vehicle yaw velocity to RMS steering wheel angle.
- **Nonlinear torque ratio:** the ratio of friction torque magnitude to RMS torque demand signal.

Figure 4.49 shows clear correlations between the normalised subjective ratings provided by the test drivers and the corresponding objective metrics measured in the experiments, with five values of the absolute value of the correlation coefficient $|r|$ larger than 0.9, three values between 0.8 to 0.9, and one value between 0.7 to 0.8. Small values of $|r|$ are only seen for the correlations in yaw gain. However, the small range of the rating distribution agrees with the constant yaw gain across all trials. Moreover, the slope, the vertical position, and the spread of the linear regression lines fitting the data in trials 3 to 7 are different from those in trials 3 and 8 to 11. This could be because trials 4 to 7 and trials 8 to 11 were presented to some of the drivers in two different groups and the drivers used the rating scale in different ways in the two groups, which directly affects the distribution of the ratings when normalisation is performed separately for the two groups of trials.

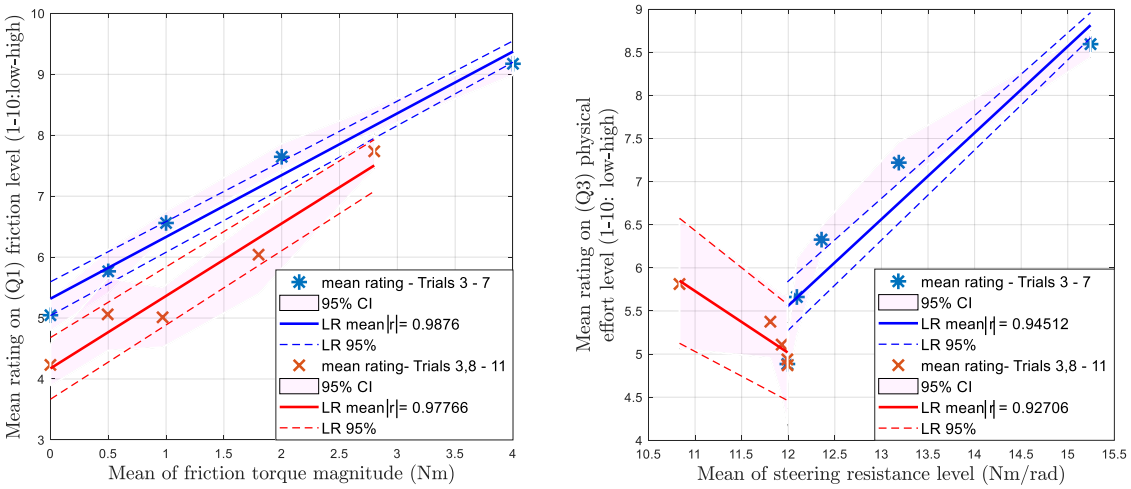

Figure 4.49: Correlations between normalised subjective ratings and objective metrics with their correlation coefficients. The shaded area represents the 95% confidence interval(CI) for the mean values of the normalised subjective ratings. The solid line represents the linear regression(LR) of mean values of the ratings and the dashed lines represent the borders of the 95% confidence area.

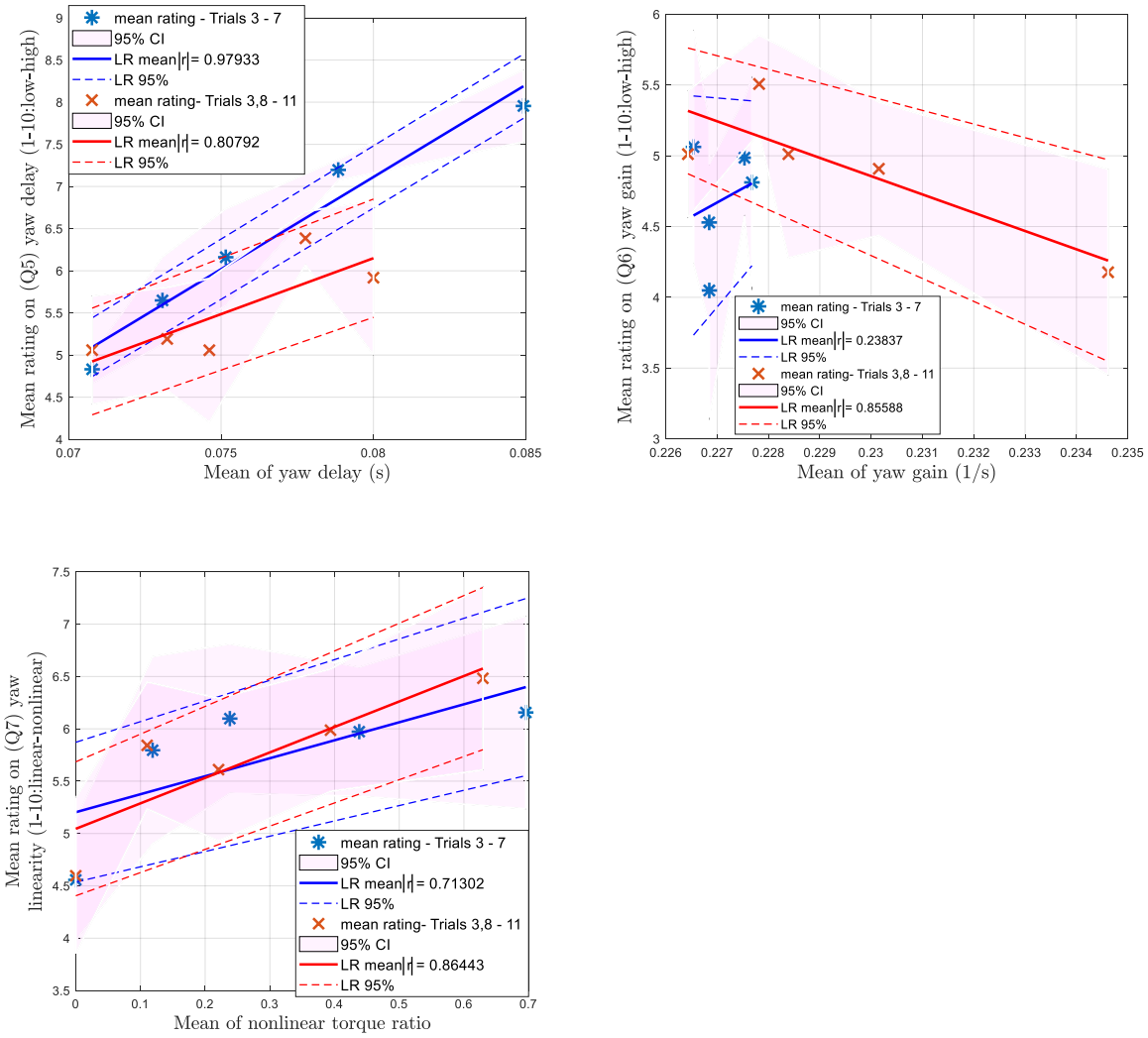

Figure 4.49(continued): Correlations between normalised subjective ratings and objective metrics with their correlation coefficients. The shaded area represents the 95% confidence interval(CI) for the mean values of the normalised subjective ratings. The solid line represents the linear regression(LR) of mean values of the ratings and the dashed lines represent the borders of the 95% confidence area.

The normalised ratings on the three evaluation subjective questions are also compared with some objective metrics measured in the experiments through linear regression, with the absolute values of the correlation coefficient for trials 3 to 7 and for trials 3 and 8 to 11 summarised in Table 4.18 and Table 4.19, respectively. The results show that the test drivers' subjective evaluation of steering feel correlates well with friction torque magnitude, nonlinear torque ratio, and steering resistance level for both groups of trials. Although there are some correlations between the ratings and other measured objective metrics, their coefficients are not as high as those for the three objective metrics mentioned above. Figure 4.50 showing the correlations between friction torque magnitude and rating for Q2 and for Q9 indicate that the subjective evaluation of steering feel is generally perceived as worse with an increase in friction torque magnitude. However, there is an optimal range of the friction torque magnitude, and linear

regression lines cannot capture this characteristic. As explained earlier, this could be because of the beneficial damping effect of friction.

Table 4.18: Absolute values of the correlation coefficient of evaluation subjective questions vs. objective metrics for trials 3 to 7

Objective metrics	Q2 (how easy is it to follow the path)	Q8 (how connected does it feel)	Q9 (how helpful is the steering torque feedback)
Friction torque magnitude (Nm)	0.9471	0.8067	0.9224
Nonlinear torque ratio	0.9249	0.8043	0.8477
RMS steering torque (Nm)	0.8965	0.8041	0.9194
Steering resistance level (Nm/rad)	0.9582	0.8205	0.9191
RMS steering wheel angle (rad)	0.3827	0.4277	0.4909
RMS path-following error (m)	0.7286	0.6828	0.6258
Steering reversal rate	0.8151	0.7518	0.7148
Yaw delay (s)	0.9732	0.7989	0.8587

Table 4.19: Absolute values of the correlation coefficient of evaluation subjective questions vs. objective metrics for trials 3, 8 to 11

Objective metrics	Q2 (how easy is it to follow the path)	Q8 (how connected does it feel)	Q9 (how helpful is the steering torque feedback)
Friction torque magnitude (Nm)	0.7390	0.8321	0.7275
Nonlinear torque ratio	0.7385	0.8361	0.7240
RMS steering torque (Nm)	0.1155	0.2414	0.1249
Steering resistance level (Nm/rad)	0.8607	0.9759	0.8188
RMS steering wheel angle (rad)	0.9455	0.8291	0.8973
RMS path-following error (m)	0.8463	0.9730	0.8117
Steering reversal rate	0.5029	0.6675	0.5294
Yaw delay (s)	0.8385	0.7667	0.6703

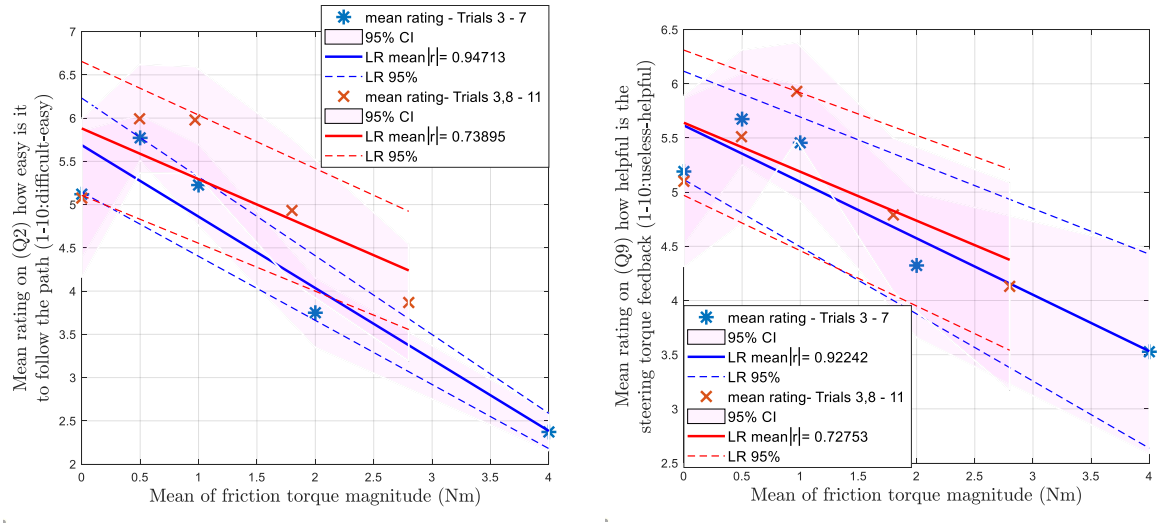

Figure 4.50: Correlations between friction torque magnitude and rating for Q2 and Q9.

Nash [126] suggests that assessing the steering performance of a human driver should consider both the path-following error and the steering effort. This trade-off is reflected by the controller cost function presented in Chapter 3. Therefore, a similar concept is adopted here, that is, the test drivers' subjective evaluation is correlated with RMS steering torque and RMS path-following error by using multiple linear regression. The coefficient of determination (R-squared) values of the regressions for trials 3 to 7 and for trials 3 and 8 to 11 are summarised in Table 4.20 and Table 4.21, respectively. Figure 4.51 shows the multiple linear regression results for Q2 as an example. It is shown that the test drivers found it easier to follow the path when a high tracking accuracy can be achieved using a small amount of steering effort.

Table 4.20: Coefficient of determination (R-squared) values of the multiple linear regressions of evaluation subjective questions vs. objective metrics for trials 3 to 7

Objective metrics	Q2 (how easy is it to follow the path)	Q8 (how connected does it feel)	Q9 (how helpful is the steering torque feedback)
1. RMS steering torque (Nm) 2. RMS path-following error (m)	0.9865	0.8173	0.9643

Table 4.21: Coefficient of determination (R-squared) values of the multiple linear regressions of evaluation subjective questions vs. objective metrics for trials 3, 8 to 11

Objective metrics	Q2 (how easy is it to follow the path)	Q8 (how connected does it feel)	Q9 (how helpful is the steering torque feedback)
1. RMS steering torque (Nm) 2. RMS path-following error (m)	0.9611	0.9725	0.8990

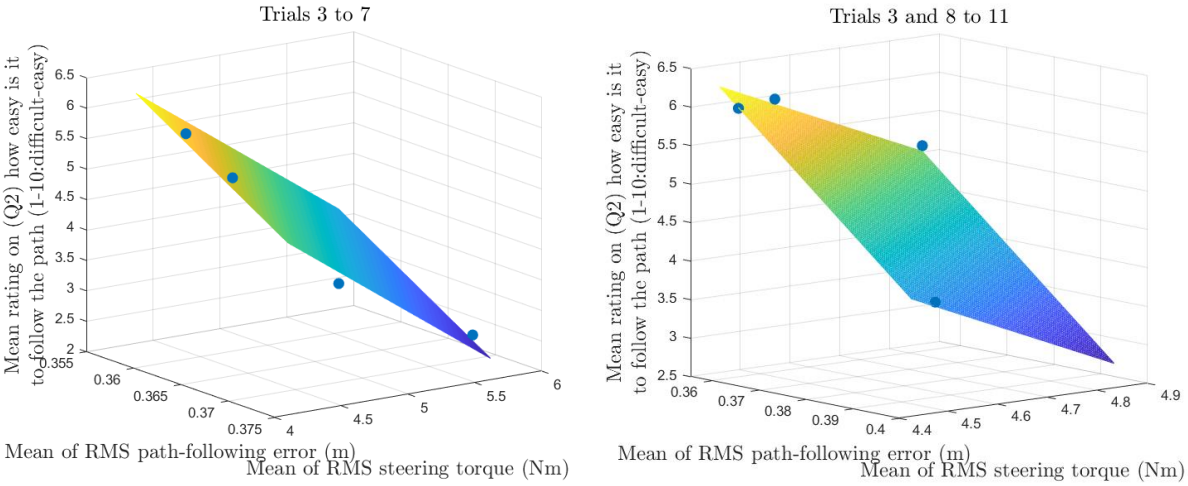

Figure 4.51: Multiple linear regression of RMS path-following error and RMS steering torque vs. how easy is it to follow the path. The blue dots are the data points, and the coloured curves represent the fitted multiple linear regression models.

4.7 Conclusions

A series of experiments have been performed on a fixed-base driving simulator, and the vehicle and driver responses and the driver's subjective ratings on steering feel questions were collected and analysed using rigorous statistical methods.

The addition of steering torque feedback was found to help the drivers follow the target path more accurately by applying smaller steering wheel angle inputs with greater consistency in steering control behaviour across drivers. This is consistent with the findings obtained by Wang [135] that steering torque feedback information is helpful to drivers as it gives the drivers additional information to estimate the states and learn the dynamics of the steering-vehicle system more accurately.

In general, a general increasing trend was found for RMS path-following error, RMS steering wheel angle and RMS steering torque with the increase in steering system friction level by comparing the mean values across all thirteen drivers. However, the identified trends are not statistically significant, resulting from the large driver to driver variation in steering control behaviour. The results from a 'concatenated driver' indicated the overall steering control performance deteriorated with the increase in steering system friction. In addition, the steering reversal rate was found to reduce with the increase in steering system friction in the randomly moving target path-following task.

The drivers' ratings for the subjective questions judging the magnitude of several objective metrics correlated well with their actual magnitudes, with five of the absolute values of the linear regression coefficient larger than 0.9 (for friction level, physical effort level, and yaw delay for trials 3 to 7), three values between 0.8 to 0.9 (for yaw delay for trials 3 and 8 to 11, yaw gain for trials 3 and 8 to 11, and yaw linearity for trials 3 and 8 to 11), and one value between 0.7 to 0.8 (for yaw linearity for trials 3 to

7). The large correlation coefficient values show the ability of the drivers to detect the changes caused by steering system friction in the objective metrics. In addition, the drivers' subjective evaluation of steering feel correlated well with friction torque magnitude, nonlinear torque ratio, and steering resistance level, with all the absolute values of the linear regression coefficient above 0.7. The subjective evaluation of steering feel is generally perceived as worse with an increase in steering system friction level. However, a steering-vehicle system with a small amount of friction around 0.5Nm to 1Nm was found to be preferred, as it may provide beneficial damping effects to stabilise the steering-vehicle system. Furthermore, the drivers also found it easier to follow the target path when a high tracking accuracy can be achieved with a small amount of steering effort.

Chapter 5

Linear Driver Model Identification

5.1 Introduction

A mathematical model of the driver-steering-vehicle system incorporating the vehicle and steering dynamics, the neuromuscular system, the sensory delays, and the human brain functions was proposed in Chapter 3, in order to provide a theoretical understanding of the human driver's subjective responses to steering torque feedback, especially in the on-centre region. The driver model performance depends on a large number of parameters. Although some of the parameter values are determined by the driving conditions or related to physical properties of the human driver, which can be obtained from relevant literature, there are several driver model parameters that are neither fixed in advance nor programmed into the driving simulator and therefore should be identified by using experimental results. In this chapter, an identification procedure used to find the key unknown parameter values of the linear driver model is presented, enabling the driver model to represent real driving behaviours, by searching for the best fit to the results of the three linear trials in the driving simulator experiments presented in Chapter 4. The linear model identification is based on the hypothesis that the human driver can learn an accurate internal mental model of the plant when the vehicle and steering dynamics are linear. The validity of the identified linear driver model in predicting realistic driving behaviours and the validity of the identification procedure in finding the model parameter values are also examined.

The details of the initial identification procedure for the linear model are presented in Section 5.2. The identification results, including model fit, identified parameter values, process noise properties, along with the driver model and identification procedure validations, are discussed in Section 5.3. The two additional experimental trials carried out to understand the properties of measurement noise and the corresponding results are presented in Section 5.4, and a single set of model parameter values is found to describe the human driver's steering control behaviour in a wide range of conditions in Section 5.5.

The one single set of model parameter values can serve as the basis for the identification of the driver model controlling a vehicle with nonlinear steering dynamics in Chapter 6. The overall results are discussed further in Section 5.6, and the main conclusions are summarised in Section 5.7.

5.2 Linear Driver Model Identification Procedure

An identification procedure developed based on the one used in [116] is applied for the linear driver model controlling a linear steering-vehicle system. The identification procedure consists of two stages, a Box–Jenkins nonparametric identification to find general polynomial transfer functions giving the best fit to the experimental results, and parametric identification to find the unknown parameter values of the linear driver model. There were thirteen test subjects involved in the driving simulator experiments in total, as mentioned in Chapter 4 and the identification procedure runs separately for each of the test drivers. However, the experimental data from each individual driver may comprise a significant amount of noise, which adds uncertainties to the identification results. Therefore, in addition to the thirteen drivers, a collection of 'averaged data', which is generated by averaging the time series data of the measured steering actions over all the individual drivers, is also used for identification. A set of more reliable parameter values is able to be found using the 'averaged data' based on the assumption that the drivers are using similar control strategies because averaging should reduce the contribution of the random noise of the individual steering actions. As described in Chapter 4, the driving simulator experimental data is collected for 5 minutes for each trial. The measured data is divided into three parts. The first minute of each trial is excluded from the data used for identification, as the drivers may have taken some time to learn the steering-vehicle system dynamics and the driving conditions before settling on a stable control strategy. The next three minutes of each trial are the data used for identification. The final minute of each trial is also excluded, so that it can be used to validate the identified driver model and to check if over-fitting exists. The last two separated parts of data are called the identification data and the validation data, respectively.

5.2.1 Box-Jenkins Identification

At the first identification stage, general transfer functions are fitted to the experimental data to estimate the portion of the measured steering actions caused by linear control behaviour. The identification results serve as a reference for the parametric driver model, as they effectively give an approximate upper prediction accuracy achievable by a linear mathematical model. The Box–Jenkins method estimates polynomial transfer functions between each of the model inputs: lateral force disturbance F_y, yaw moment disturbance M_z, steering column torque disturbance T_d and randomly moving target lateral position r, and the model output steering wheel angle θ_{sw} [142] [143]. This method also finds

a model $H_n(s)$ of the driver noise w_{sw} referred to the steering wheel angle signal. The structure of Box-Jenkins model is:

$$\theta_{sw}(t) = \frac{B_{F_y}(q)}{F_{F_y}(q)} F_y(t-n_1) + \frac{B_{M_z}(q)}{F_{M_z}(q)} M_z(t-n_1) + \frac{B_{T_d}(q)}{F_{T_d}(q)} T_d(t-n_2) + \frac{B_r(q)}{F_r(q)} r(t-n_3) + \frac{C_{sw}(q)}{D_{sw}(q)} w_{sw}(t) \quad (5.1)$$

where variables B_{F_y}, B_{M_z}, B_{T_d}, B_r, F_{F_y}, F_{M_z}, F_{T_d}, F_r, C_{sw} and D_{sw} are polynomials expressed in the time-shift operator q^{-1}, n_1, n_2 and n_3 are the input delays that characterise the transport delay for their corresponding input channel.

5th order polynomials are chosen for the Box-Jenkins identification in this study, as suggested by Nash and Cole [116], to balance variances and bias by considering the investigation results from Odhams and Cole [92]. The Box–Jenkins method also allows time delays between each input channel and the output, as represented by n_1, n_2 and n_3 in (5.1), to be found. To simplify the equation formulation, the time delays associated with the two model inputs lateral force disturbance F_y and yaw moment disturbance M_z are assumed to be the same, as these two inputs are both applied to the vehicle dynamics. However, the Box–Jenkins method does not estimate the values of these delays directly from the data, so they have to be set as known parameters. Therefore, the Box–Jenkins identification is carried out for a range of different delays, and the time delay values that give the optimal identification results are recorded. To achieve this, a genetic algorithm, starting with a population of 50 random combinations of the values of these time delays, is used to iterate towards the values which give the best fit to the experimental results. The mean-squared difference between the modelled steering wheel angle from the Box–Jenkins identification and the measured steering wheel angle is used to quantify the goodness of the fit of the identified model to the experimental results.

5.2.2 Parametric Identification

The linear parametric driver model performance depends on twenty-seven parameters in total, as described in Chapter 3. The amplitudes of the applied Gaussian white noise and their corresponding filters are known because they are programmed into the driving simulator. The other values relate to the physical properties of the human driver and need to be identified from the data recorded during the experiments. However, due to the large number of parameters involved in the driver model, the parameters which are not sensitive to the driving conditions are fixed following the results from the relevant literature, with details given in Section 3.2.10 in Chapter 3. As a result, there are eleven variable parameters that are neither fixed in advance nor programmed into the driving simulator, and these parameters are classified into three groups according to the functions they relate to:

- Neuromuscular parameters: damping resisting stretching of the muscle fibre c_a, arm inertia I_{arm}, reflex gain k_r
- Cognitive parameters: process noise standard deviation W, measurement noise standard deviations V_e, V_ψ, V_{θ_a}, path-following error cost q_e, cognitive controller time shift T_t
- Sensory delays: visual delay τ_{vi}, muscle angle sensory delay τ_{θ_a}

Upper and lower bounds are chosen for these parameters based on realistic physical limitations, as summarised in Table 5.1. The other fixed driver model parameters are summarised in Table 5.2.

Table 5.1: Upper and lower bounds for the identified parameter values

Parameter	c_a	I_{arm}	k_r	W	V_e	V_ψ	V_{θ_a}	τ_{vi}	τ_{θ_a}	T_t	q_e
Units	Nms /rad	kgm^2	Nm /rad	Nm	m	rad	rad	s	s	s	
Upper bound	6.0	0.3	80	10	1.5	0.2	10	0.5	0.5	1	1000
Lower bound	0.2	10^{-3}	0	1	10^{-3}	10^{-3}	0.01	0.1	0.1	-1	10^{-3}

Table 5.2: Fixed driver model parameters

	Description	Parameter	Value	Unit
Muscle model	Intrinsic muscle stiffness	k_p	0	Nm/rad
	Intrinsic muscle damping	c_p	0	Nms/rad
	Tendon stiffness	k_a	30	Nm/rad
Muscle activation	Motor neurons lag time constant	τ_1	30	ms
	Muscle activation and deactivation lag time constant	τ_2	20	ms
Stretch reflex	Reflex delay	τ_r	40	ms
LQR controller	Cost function weight on control input α	q_α	1	
Disturbance filters	Cut-off frequency for the low-pass filter H_{fy}	f_{cy}	1	Hz
	Cut-off frequency for the low-pass filter H_{fz}	f_{cz}	1	Hz
	Cut-off frequency for the low-pass filter H_{fd}	f_{cd}	10	Hz
	Cut-off frequency for the low-pass filter in H_{fr}	f_{crl}	1	rad/s
	Cut-off frequency for the high-pass filter in H_{fr}	f_{crh}	0.05	rad/s

There are two widely used methods for the identification of a parametric model incorporated in a closed-loop system, known as the direct and indirect methods [142]. The model is simulated in the open-loop in the direct identification, and is simulated in the closed-loop in the indirect identification. The pros and cons of these two methods in driver model identification have been extensively investigated by Keen [16], Odhams [14], Na [144] and Nash [126], and the indirect method has been found to be more suitable for identification using data from driving simulator experiments, as the feedback transfer function (the steering-vehicle system) is known. The indirect method can also result in lower bias compared to the direct identification method.

Following the framework of the indirect method for parametric identification, a prediction error minimisation approach is used. In general, the simulated steering wheel angle $\theta_{sw(sim)}$ and the measured steering wheel angle $\theta_{sw(exp)}$ are compared with each other, and the mean-square difference $\left(\theta_{sw(sim)} - \theta_{sw(exp)}\right)^2$ is minimised to find the optimum set of parameter values. There are two primary sources contributing to the difference $(\theta_{sw(sim)} - \theta_{sw(exp)})$. The first one is modelling error, which can be reduced by improving the accuracy of the driver model. The second one is the driver's random noise, which cannot be reduced. However, bias may be introduced to the identification results if the driver noise is not white. To address this problem, a modified version of the prediction error, a weighted prediction error ε, as defined in (5.2), is used as the term to be minimised in the identification, as suggested by Ljung [142], Odhams [14] and Nash and Cole [116].

$$\varepsilon(s) = \frac{1}{H_n(s)}\left(\frac{2\pi f_c}{s + 2\pi f_c}\right)^2 (\theta_{sw(sim)}(s) - \theta_{sw(exp)}(s)) \tag{5.2}$$

The weighted prediction error ε is obtained by filtering by the inverse of the noise model $H_n(s)$ found in the Box-Jenkins identification. However, this will result in an increased prediction error amplitude at high frequencies, which exceed the human driver's normal operating frequencies. To solve this problem, a low-pass filter is also included to reduce the high-frequency errors. The cut-off frequency f_c of the low-pass filter is set to different values for the three linear trials in the experiments: 5Hz for trial 1 and 3Hz for trials 2 and 3, based on the preliminary analysis of the measured steering control actions in the frequency domain.

The optimisation problem is likely to contain a large number of local minima and it is not feasible to convert the optimisation problem into a convex form due to the relatively large number of driver model parameters to be identified and the sophisticated relationships between them. Nash and Cole [116] has successfully utilised a genetic algorithm based minimisation method to find the global minimum solution to a similar problem with similar complexity. The genetic algorithm [145], which mimics the natural selection process to 'mute' and 'mutate' the best solutions, has been found to be an efficient way to find the global optimum solution to non-convex optimisation problems. As a result, the genetic

algorithm based two-stage stochastic minimisation method provided by Nash and Cole [116] is adopted to ensure the global minimum solution to be found:

1. Firstly, a genetic algorithm is used to find the global minimum solution of the minimisation problem. The entire space of interest is searched with 100 random combinations of parameter values between the upper and lower bounds set in Table 5.1 as the starting points. The solution converges towards the global minimum over 100 iterations based on a natural selection process that mimics biological evolution.
2. A gradient descent method is then carried out to ensure the global minimum solution is found, starting with the genetic algorithm solution. The Matlab function '*fmincon*' is used with the SQP algorithm to automatically search for an appropriate set of parameter values for this purpose.

Initially, single parameter sets are identified for each driver and the averaged driver by fitting the results of all three trials. However, it is always difficult to conduct optimisations over a multidimensional search space, and as the number of parameters increases, so does the uncertainties of the identified parameter values. Therefore, similar to the method used by Nash and Cole [116], the identification is conducted in several steps to limit the number of parameters to be identified at each step. The identification procedure is illustrated in the flow chart in Figure 5.1, and the conditions for each step are given in Table 5.3. The validity of the identification procedure in finding the correct model parameter values or say the global minimum solution are checked against the results of the simulation of identification described in Section 5.3.5.

In step 1, all the parameters are identified across all three linear trials. However, noise parameters W, V_e, V_ψ and V_{θ_a} not only affect the state estimation and control performance, but also represent the standard deviation of the driver's random noise. It is desirable for the noise standard deviation predicted by the model to match that found in the experiments. The model error is assumed to be negligible, so the driver noise is given by the difference between the measured steering wheel angle $\theta_{sw(exp)}$ and the modelled steering wheel angle $\theta_{sw(sim)}$. Preliminary simulations of the driver model showed that the predicted noise standard deviation is primally due to the process noise because the effect of measurement noise on the steering control actions has been eliminated by the state estimator, which has also been demonstrated by Nash and Cole [116]. Therefore, the process noise standard deviation W is scaled by the average ratio of the measured to the modelled noise standard deviations before step 2. In step 2, the process noise standard deviation W is then held constant while the remaining parameters are identified to fit the results of all three linear trials once more. In step 3, the three neuromuscular parameters are identified using all three linear trials, while the cognitive parameters and the sensory delays are fixed at the values identified in step 2. In step 4, the process noise standard deviation W and the cognitive controller time shift T_t are kept constant at the values found in step 2, the neuromuscular

parameters are kept constant at the values found in step 3, and the remaining six parameters are identified across all three linear trials by conducting a further optimisation. For the averaged data, the process noise standard deviation W is also scaled to match the standard deviation of the measured noise found in the data after step 1 and is then fixed at the following steps. However, the average of the scaled values of W for the thirteen drivers could also be used for the averaged driver after step 1 and is then used in the following steps. The difference between the two approaches of identifying the process noise standard deviation W for the averaged driver is discussed in Section 5.3.2.

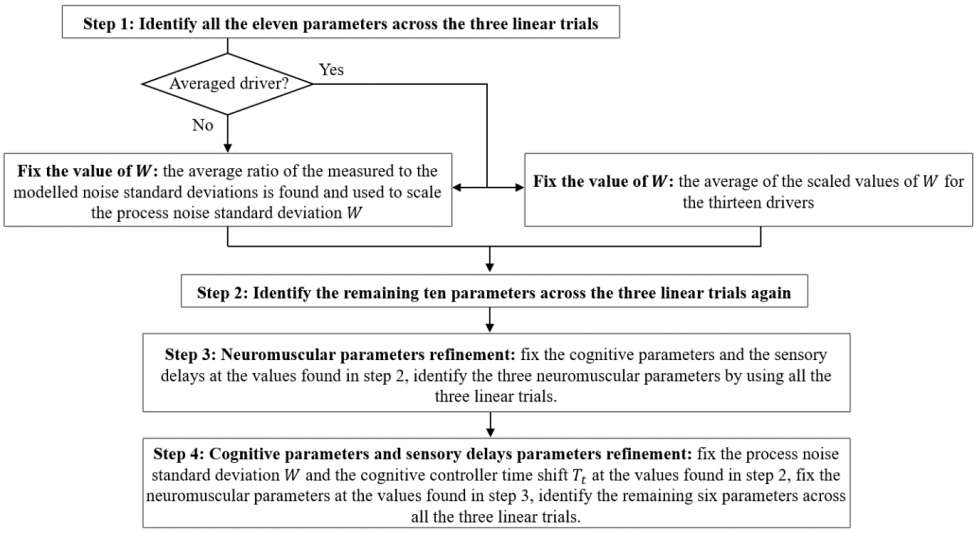

Figure 5.1: Identification procedure for finding one set of parameters for each driver and the averaged driver.

Table 5.3: Conditions for each step of the parametric identification procedure to find a single set of parameter values for each driver. × indicates parameters to be identified at each step.

		Neuromuscular parameters			**Cognitive parameters**						**Sensory delays**	
Step	**Trials**	c_a	I_{arm}	k_r	W	V_e	V_ψ	V_{θ_a}	T_t	q_e	τ_{vi}	τ_{θ_a}
1	1, 2, 3	×	×	×	×	×	×	×	×	×	×	×
2	1, 2, 3	×	×	×		×	×	×	×	×	×	×
3	1, 2, 3	×	×	×								
4	1, 2, 3					×	×	×		×	×	×

After a single set of parameter values fitting all three linear trials is found for each driver and the averaged driver, separate parameter sets are identified for each trial individually for each driver. Two

parallel identification steps are carried out, as illustrated by Figure 5.2, with conditions of each trial presented in Table 5.4. The driver noise levels predicted by the model are to be matched by those seen in the experiments. There is an amount of variation between different trials. Therefore, the values of process noise standard deviation W are scaled by the ratio of the measured to the modelled noise standard deviations for each trial, respectively, before either of the two identification steps. In step 5a, to reduce the computational time and simplify the optimisation problem, the process noise standard deviation W is then fixed at the value found in each individual trial, and the cognitive controller time shift T_t and the neuromuscular parameters are held constant using the values found for the single parameter set while the other cognitive parameters and sensory delays are identified for each trial individually. This may provide some insights into how the human drivers' cognitive parameters vary between different trials. In step 5b, another identification is carried out by fixing the process noise standard deviation W at the value found in each individual trial, fixing the arm inertia I_{arm} and the cognitive controller time shift T_t at the values found for the one single set of parameters for each driver, and identifying all the other parameters. This allows the variation in both the neuromuscular and cognitive systems between different linear trials to be studied. When identifying separate parameter sets for each individual trial, the upper bound of path-following error cost q_e is relaxed to 10^4.

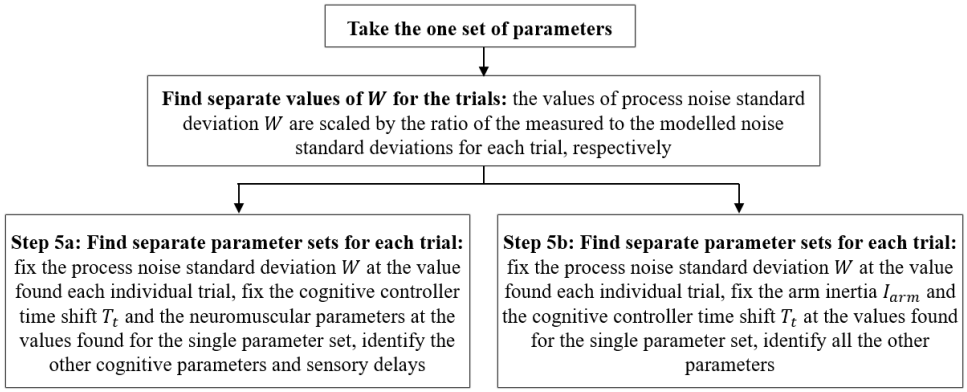

Figure 5.2: Identification procedure for finding separate parameter sets for each trial individually for each driver and the averaged driver.

Table 5.4: Conditions for each step of the parametric identification procedure to find separate parameter sets for each trial individually. × indicates parameters to be identified at each step.

	Neuromuscular parameters			**Cognitive parameters**						**Sensory delays**	
Step	c_a	I_{arm}	k_r	W	V_e	V_ψ	V_{θ_a}	T_t	q_e	τ_{vi}	τ_{θ_a}
5a					×	×	×		×	×	×
5b	×		×		×	×	×		×	×	×

5.3 Identification Results and Analysis

This section presents a comprehensive analysis of the model identification results. In Section 5.3.1, the fit of the identified models to the experimental results is investigated. In Section 5.3.2, the identified parameter values across different drivers and across different trials are shown and discussed. In Section 5.3.3, the driver noise levels predicted by the identified driver model are compared with those found in the experiments. In Section 5.3.4, the validity of the identified driver model in predicting driving behaviours is examined. In Section 5.3.5, the validity of the identification procedure is checked against simulation results.

5.3.1 Agreement between Model and Measurements

The goodness of the fit of the identified model to the experimental data is quantified using the 'variance accounted for' (VAF), which is the percentage of the variance in the measured steering wheel angle $\theta_{sw(exp)}$ matched by the modelled steering wheel angle $\theta_{sw(sim)}$, and is given by:

$$\mathrm{VAF} = \left(1 - \frac{\sum_k \{\theta_{sw(sim)}(k) - \theta_{sw(exp)}(k)\}^2}{\sum_k \{\theta_{sw(exp)}(k)\}^2}\right) \times 100\% \tag{5.3}$$

where k is the time-step index. VAF values of the identified linear parametric driver model are plotted in Figure 5.3 for each of the thirteen individual drivers as well as the averaged data. The lines connecting the markers represent variations of the agreement between experimental trials, rather than indicate a linear relationship or other similar interpretations between the trials. The fit of the Box–Jenkins model is also included as a benchmark for the fit of the parametric model, either using separate parameter sets to fit the results of each individual trial or a single parameter set fitting all three trials. It is seen that VAFs are largest for the Box–Jenkins model, which is expected as the Box–Jenkins model effectively gives an upper bound limit on the linear proportion of the steering wheel angle data. The VAFs for the separate parameter sets including both the results obtained in identification steps 5a and 5b are quite close or even equal to the VAFs for the Box-Jenkins model, indicating that the linear parametric driver model structure can explain the drivers' linear steering control behaviour quite well, although the VAFs for the separate parameter sets obtained in identification step 5a are slightly higher than the VAFs for the separate sets obtained in identification step 5b. The VAFs for the single parameter sets are close to the VAFs for the separate parameter sets, indicating that a fixed-parameter model is still able to provide a good approximation to the measured steering response across the range of conditions in the three trials. It is seen that there are several trials where the single parameter sets do not fit well for some drivers. This is because the drivers' control performance may vary between different trials. In addition, it is noticed that the VAFs are much higher for the averaged data than for any individual driver, supporting the hypothesis in [116] that the averaged data contains less random noise. The averaged VAF value for

all three trials using the averaged data is 75% for the one parameter set, and are 82% and 84% for the separate parameter sets obtained in identification steps 5a and 5b, respectively. These VAF values are comparably higher than those obtained by Nash and Cole [116], who employed five test subjects.

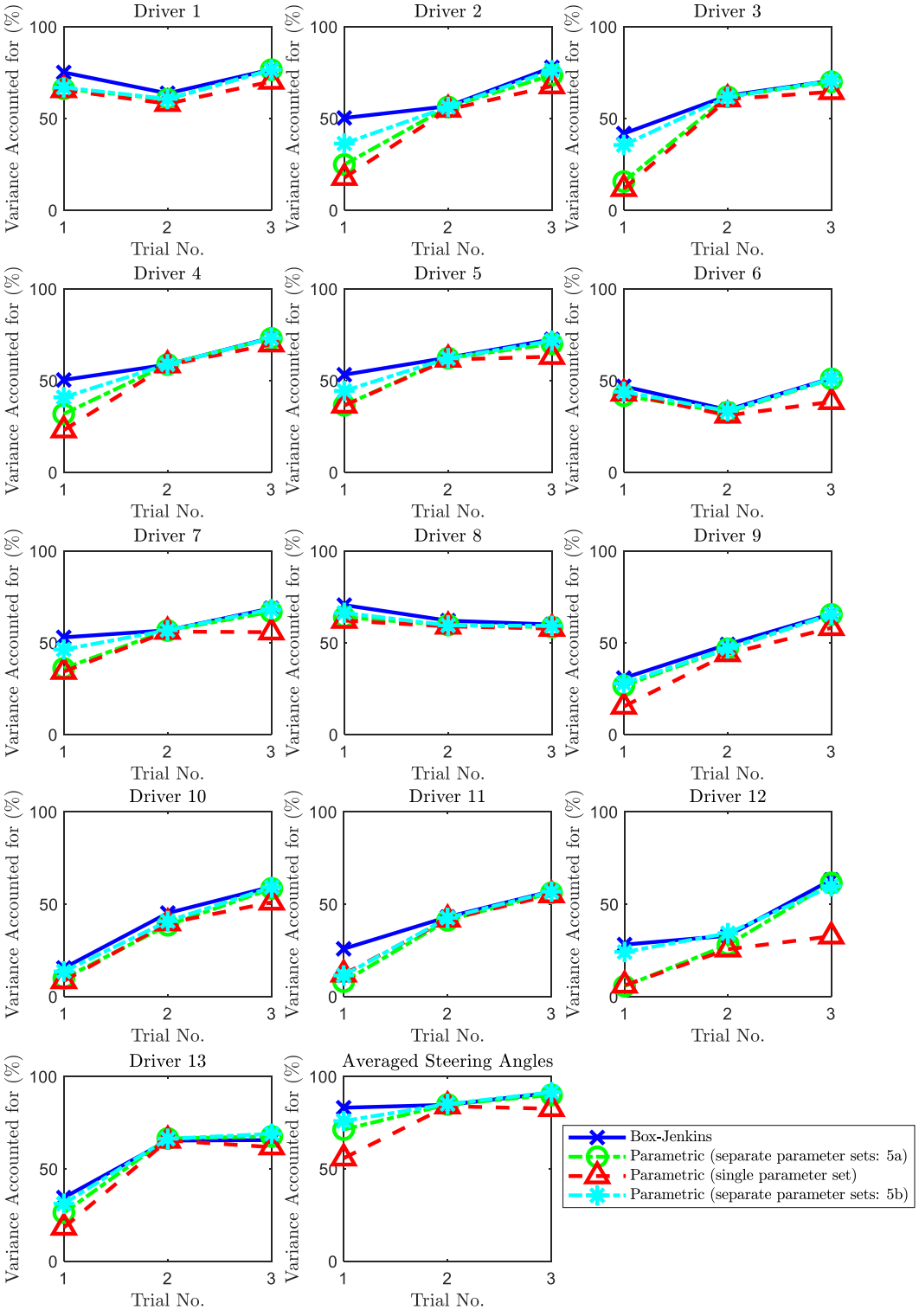

Figure 5.3: Agreement between parametric driver model predictions and experimental results. VAF value is plotted for each driver/trial combination, and for the averaged driver on each trial.

5.3.2 Identified Parameter Values

The identified single parameter set for each driver is shown in Figure 5.4. In general, the parameter values are broadly similar between the drivers, taking the complexity of the model and the number of unknown parameters, as well as the amount of noise in the measurements for each driver into account. The high similarity of the parameter values between different drivers suggests that the drivers had similar physical properties and were using similar control strategies, justifying the averaging of drivers' responses together to obtain a set of 'averaged data'. The parameter values identified using the averaged data all fall within the range for the individual drivers, suggesting that the averaged data is a valid representation of a typical driver's steering control behaviour.

The effects of these parameters on the driver model performance have been extensively investigated in Chapter 3. The arm inertia I_{arm} and the sensory delays τ_{vi} and τ_{θ_a} relate to each driver's internal physical properties, while the muscle damping c_a and the stretch reflex gain k_r are mainly determined by the muscle states the drivers used when they performed the experiments. It is likely that drivers with larger values of c_a and k_r tensed their muscles more than the others during the experiments. The path-following error cost q_e indicates the trade-off between the steering effort and the path following accuracy, while the cognitive controller time shift T_t describes which part of the vehicle is aligned with the target path. These two parameters are choices made by the human drivers during the experiments instead of being determined by physical properties. It is seen that the identified values of q_e for most of the drivers hit the upper bound limit of 1000. It is shown later that q_e was significantly larger for trial 1 than for trials 2 and 3. However, it is necessary to impose a constraint of 1000 on q_e to avoid biasing the other parameter values when identifying a single parameter set across all three trials. The details are discussed later in this section. The noise parameters W, V_e, V_ψ and V_{θ_a} appear in two places in the model: as variances of the added process and measurement noise; and as parameters of the state estimator. In Figure 5.4, the average of the scaled values of W for the thirteen drivers, with the corresponding identified values of V_e, V_ψ and V_{θ_a} for the averaged data are shown by the red dashed horizontal lines. As expected, the identified value of process noise standard deviation W is smaller than the average of the scaled values of W over the thirteen drivers, as the amount of random driver noise has been reduced by averaging the steering wheel angle actions over all the individual drivers. In addition, the values of the measurement noise standard deviations V_e, V_ψ and V_{θ_a} identified using the process noise standard deviation W scaled to match the standard deviation of the measured noise found in the measured data are also smaller than those identified using the average of the scaled values of W over the thirteen drivers. This is because it is the ratios between these noise parameters that affect the state estimator performance; the state estimator with a smaller value of one of these parameters also has smaller values of the others.

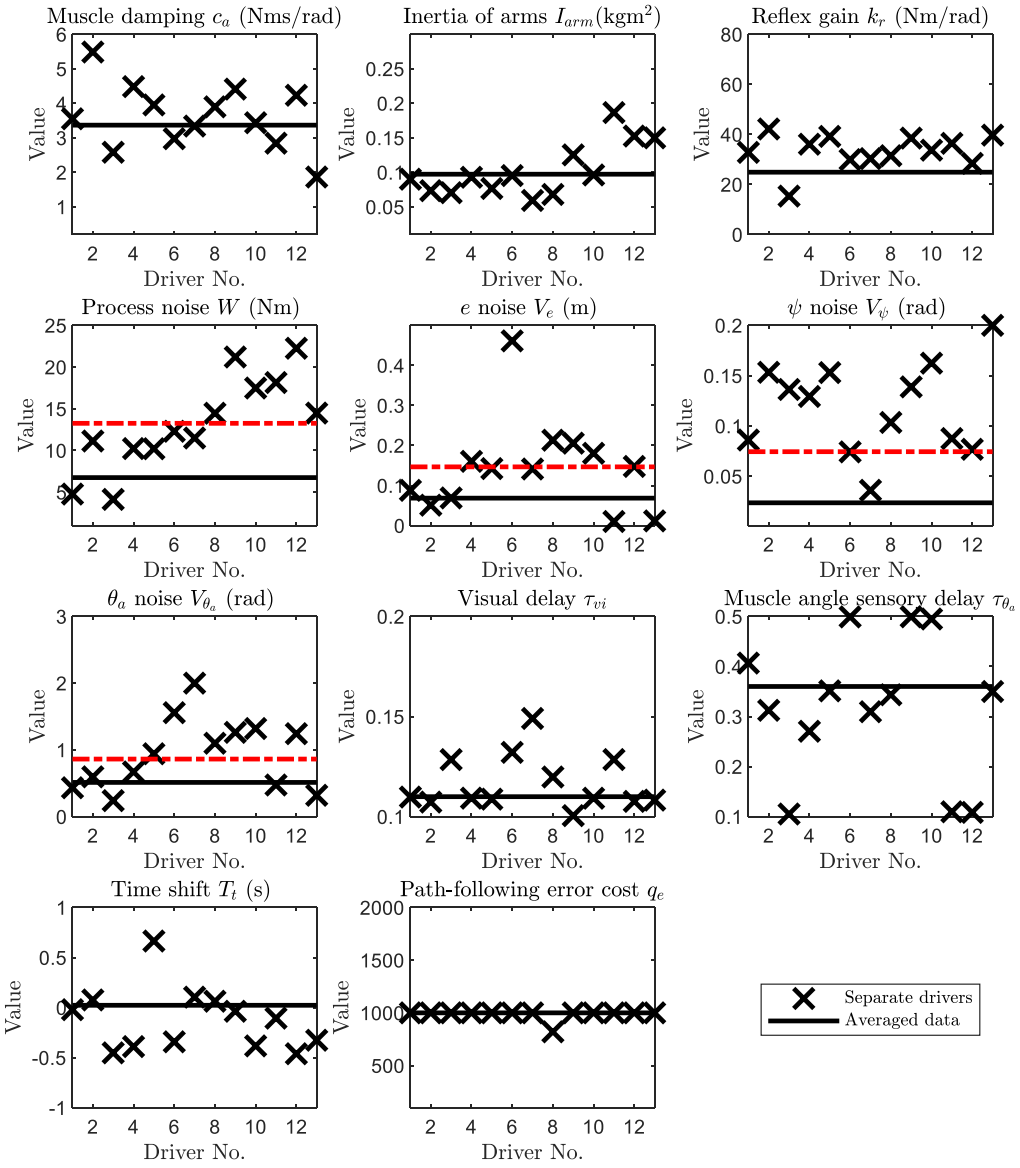

Figure 5.4: Identified single parameter sets fitting all three linear trials for the individual drivers (crosses) and the averaged data (solid horizontal lines). The average of the scaled values of W for the thirteen drivers, with the corresponding identified values of V_e, V_ψ and V_{θ_a} for the averaged data are shown by the red dashed horizontal lines.

To investigate whether the drivers' cognitive and neuromuscular parameters vary between the three linear experimental trials, separate parameter sets identified for each trial using the averaged data in identification step 5b are plotted in Figure 5.5. The cognitive parameters found in identification step 5a are similar to those identified in step 5b and therefore not repeated in the figure. The values of the arm inertia I_{arm}, process noise standard deviation W and the time shift T_t are fixed in this identification

step, so they are not discussed here. For some of the other parameters, there is a wide spread of identified values; this can be either because the parameter values are very sensitive to the type of trial or there is large uncertainty in the identified values.

The identified values of muscle damping c_a and stretch reflex gain k_r in experimental trial 1 are larger compared with those in trials 2 and 3. This is because the drivers tensed their arms more when reacting to high-frequency steering column disturbances than following a randomly moving target path with a relatively lower frequency of variation. In experimental trial 1, a very large value of visual noise standard deviation parameter V_e is identified. This is because the magnitude of the path-following error or say the lateral displacement of the vehicle is extremely small in trial 1 and when the noise level is much larger than the signal level, the driver places very little weight on the measurement. This suggests that there are thresholds below which drivers are unable to perceive each sensory signal. In addition, the large value of V_e represents a large amplitude of visual noise on the path-following error in the simulation, which results in a poor estimation of the target path as the large amplitude noise is directly fed to the human driver's visual system. This is compensated by a large value of controller cost function weight on path-following error q_e, as shown in the figure. Preliminary simulations showed that if the neuromuscular parameters are identified together with q_e, the identified values of c_a and k_r will be unrealistically large for a large value of q_e as the muscles often need to be tensed more to generate such aggressive steering control actions. This explains why the upper bound of q_e should be restricted in the identification procedure to find a single parameter set for each driver and the averaged data. It is also noticed that although the driving task is the same in trials 2 and 3, the identified measurement noise parameters are different. This suggests that the drivers weigh the sensory measurements in different ways when the steering-vehicle dynamics properties are different. However, the difference may also relate to the actual signal amplitudes. This relation is investigated in Section 5.4. There is also a wide spread of identified values of sensory delays for different experimental trials, as shown in the figure. Studies [116] [146] [147] [148] [149] have found that during an active control task with multiple stimuli presented together, humans develop accurate sensory estimates by optimally integrating the information they perceived over time in a sophisticated way. Therefore, it is difficult to accurately identify one single value of time delay for each sensory channel and separate the delays for different sensory channels. Considering this effect, the wide spread of identified values of sensory delays across different experimental trials is plausible.

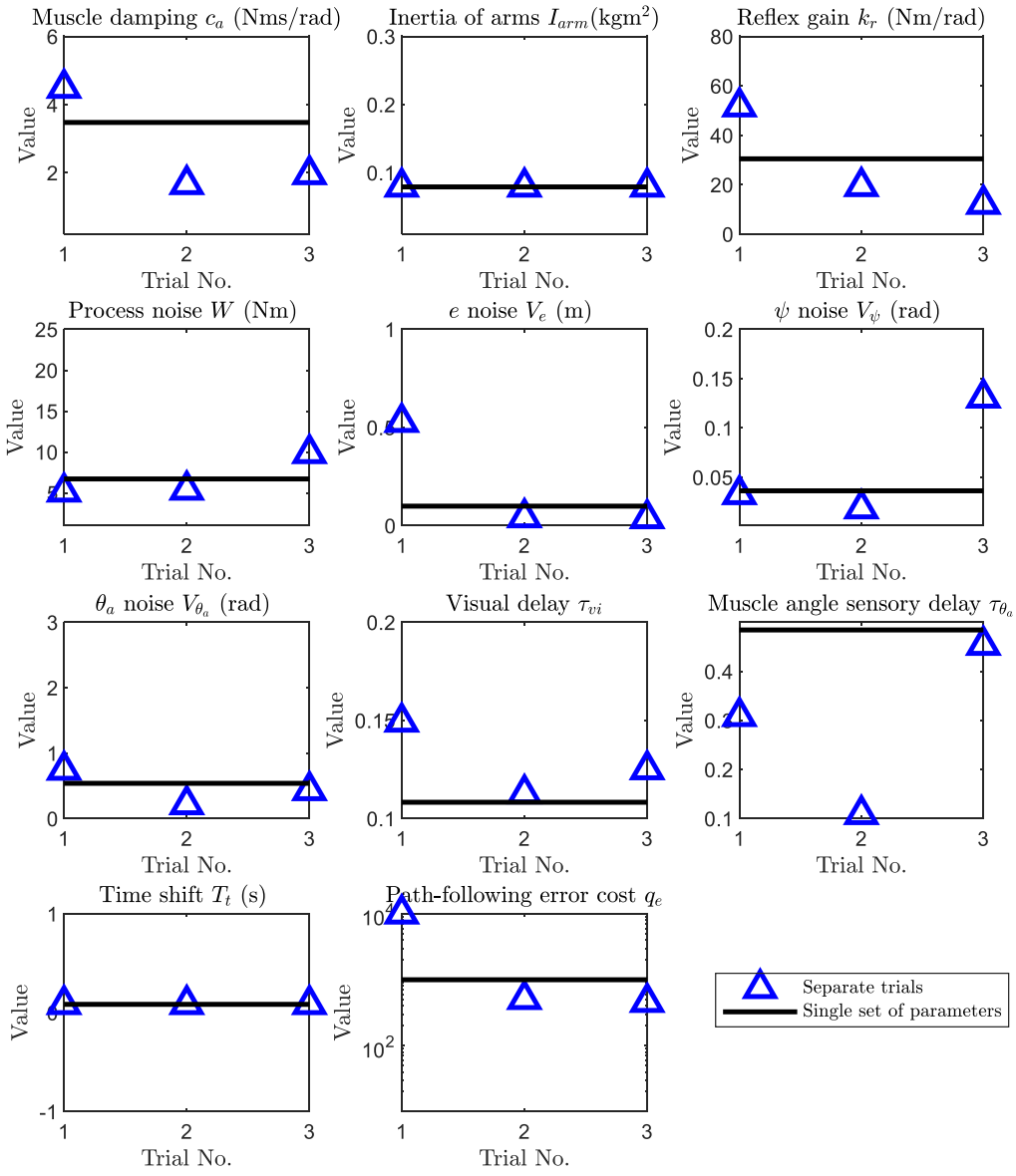

Figure 5.5: Identified parameter values for each trial separately using averaged data (triangles) and the identified single parameter set fitting all three linear trials for the averaged data (solid horizontal lines).

5.3.3 Measured and Modelled Driver Noise Amplitude

In the driver model, an optimal Kalman filtering algorithm is used to represent the human driver's sensory measurement integration by using statistically optimal methods to estimate the states of the plant. This requires the driver noise levels predicted by the driver model to be matched by those found in the experiments. Preliminary simulations of the driver model with process and measurement noise showed that most of the driver noise present in the steering wheel angle signal comes from the process

noise because the measurement noise has been reduced by the state estimator while the process noise is directly added to the human driver's control action. This conclusion is also supported by the study from Nash and Cole [116]. Therefore, the process noise standard deviation W is scaled based on the ratio between the measured and modelled noise standard deviations in the identification procedure described in Section 5.2.2. By assuming the modelling error is negligible, the driver noise is given by $(\theta_{sw(sim)} - \theta_{sw(exp)})$. The ratios between the measured and modelled noise standard deviations for each driver and trial combination are shown in Figure 5.6a, using the single parameter sets identified for each driver. It is seen that although there is an amount of variation between different trials, most of the ratios are close to 1, indicating the standard deviations of the modelled noise agree with those seen in the experiments overall. However, in order to identify separate parameter sets for each trial accurately as well as to investigate the reasons behind the variation in the ratios across the different trials, the value of W is scaled by the ratio of the measured and modelled noise standard deviations for each trial separately as well, as described in Section 5.2.2. The resulting new ratios between measured and modelled noise standard deviations are shown in Figure 5.6b. It is clearly seen that these ratios are drawn much closer to 1, indicating that the agreement between the measured and modelled noise standard deviations has been improved significantly.

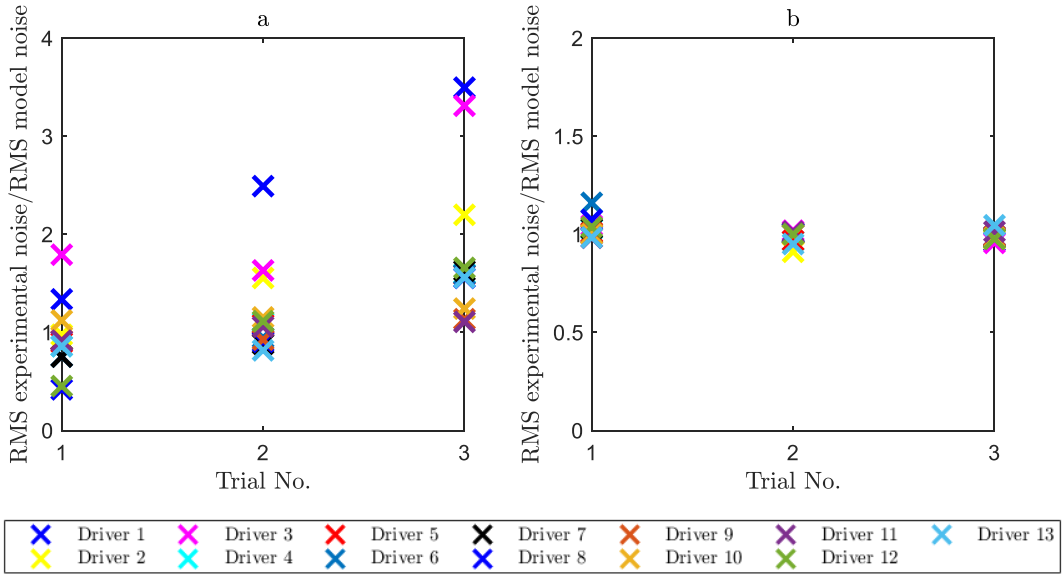

Figure 5.6: Ratio of the measured and modelled noise standard deviations. In (a), a constant value of W is used for each driver, while in (b) the values of W have been adjusted for each trial individually.

To determine if there is a relationship between the process noise level and the human driver's control action level, the adjusted values of W are to be compared with the amplitudes of the muscle activation torque T_a. However, the muscle activation torque signal T_a is not directly measured in the experiments. Therefore, a method is developed to estimate this signal by using the measured signals and the theoretical driver model:

1. A general transfer function fitting the simulated muscle angle signal $\theta_{a(sim)}$ to the simulated steering wheel angle $\theta_{sw(sim)}$ is identified for each trial by using the Box-Jenkins method with 5th order polynomials. The simulated muscle angle and steering wheel angle signals are generated by using the identified driver model with separate parameter sets for each trial. Similar to Section 5.2.1, the first minute is excluded from the data used for identification and the data in the last minute is used for validating the predictive power of the identified transfer function.
2. The actual muscle angle signal $\theta_{a(exp)}$ of the human driver in the experiment is estimated by using the measured steering wheel angle signal $\theta_{sw(sim)}$ and the transfer function identified at step 1 for each trial.
3. The actual muscle activation torque $T_{a(exp)}$ of the human driver in the experiment is calculated by using equation (3.6) describing the muscle dynamics in Chapter 3 for each trial:

$$T_{a(exp)}(k) = c_a\dot{\theta}_{a(exp)}(k) + k_a\left(\theta_{a(exp)}(k) - \theta_{sw(exp)}(k)\right) \tag{3.6}$$

The adjusted values of W are then plotted against the values of RMS estimated muscle activation torque $T_{a(exp)}$ in the experiment in Figure 5.7a. There is a clear linear relationship between these two variables, showing that process noise is signal dependent. The signal-to-noise ratio (SNR), which is defined as the ratio of RMS estimated muscle activation torque $T_{a(exp)}$ to W, is plotted for each driver in Figure 5.7b. It is shown that the values of SNR are broadly similar between different drivers. The averaged SNR value for the process noise W over all thirteen drivers is 0.47, which is comparable to the value obtained by Nash and Cole [116].

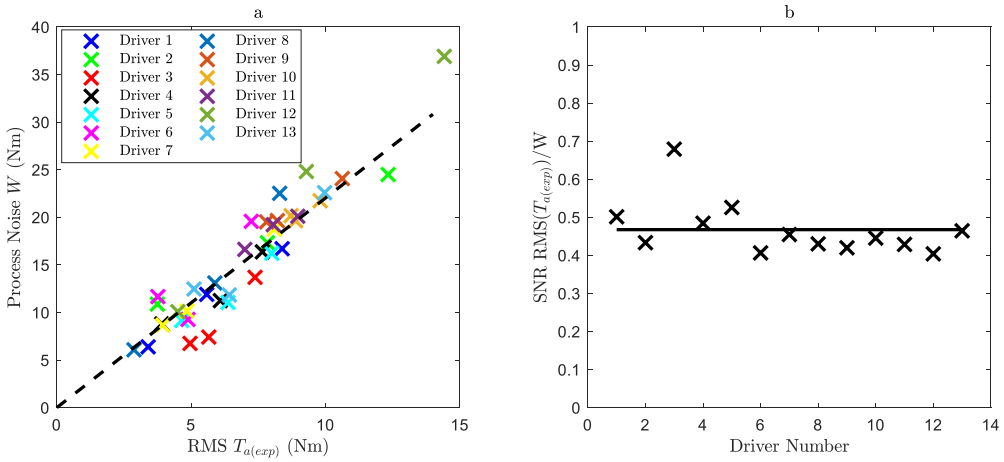

Figure 5.7: Investigation into signal-dependent process noise. In (a), the identified process noise standard deviation W is compared with the RMS estimated muscle activation torque $T_{a(exp)}$ in the experiment. In (b), the SNRs for the individual drivers (crosses) are compared and the averaged SNR (solid horizontal line) over all the drivers are calculated.

5.3.4 Driver Model Validation

Experimental data in the last minute is used to validate the identified models and to check if there is any over-fitting for any of these models. Over-fittings means that the fit of the model to the identification data is much better than the fit of the model to the validation data. This can be caused by the amount of data used for identification not being sufficient. To check this, the VAF values obtained from the identification data as well as those obtained from the validation data are plotted for each trial and driver including the averaged driver. The averaged VAF values calculated over all three trials are also calculated for each driver and the averaged driver. Figure 5.8, Figure 5.9 and Figure 5.10 show these VAF values for the Box-Jenkins model, the parametric driver model with separate parameter sets for each trial, and the parametric driver model with a single parameter set for each driver, respectively. In general, the VAF values in the validation data are similar to those in the identification data, indicating that the driver model is capable of predicting the human driver's behaviour accurately, and the amount of data used for identification is sufficient. However, over-fitting may have occurred in several trials for some drivers, such as in trial 1 for Drivers 1, 5, 7 and 13, trial 2 for Drivers 10, 11 and 13, and trial 3 for Drivers 2, 4, 6 and 12. These may be due to the identified models fitting to some random variations in each trial and may be also caused by the drivers not keeping the same driving behaviour during the trial. The results further suggest that the identified parameters found for these individual trial and driver combinations are unreliable. However, the VAF values in the identification data and the VAF values in the validation data are almost equal to each other for the averaged driver. This supports the hypothesis that averaging the measured data over all the individual drivers minimises over-fitting by reducing the amount of random noise in the data. Therefore, the parameter values identified by using the averaged data are more reliable than those for any individual driver.

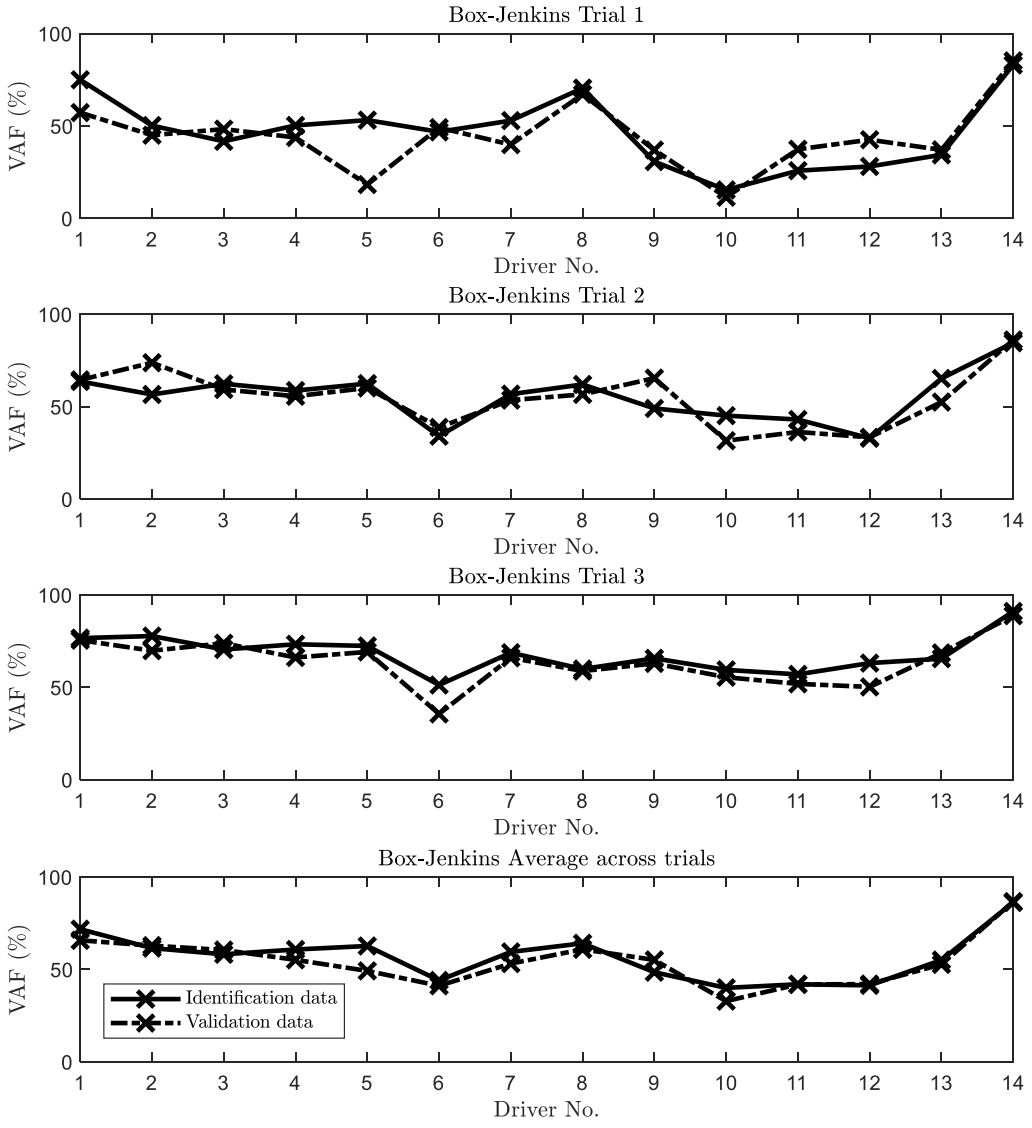

Figure 5.8: Validation of the Box-Jenkins model for each trial and driver including the averaged driver (Driver 14). The VAFs obtained from the identification data are represented by the markers on the solid lines, while the VAFs obtained from the validation data are represented by the markers on the dashed lines.

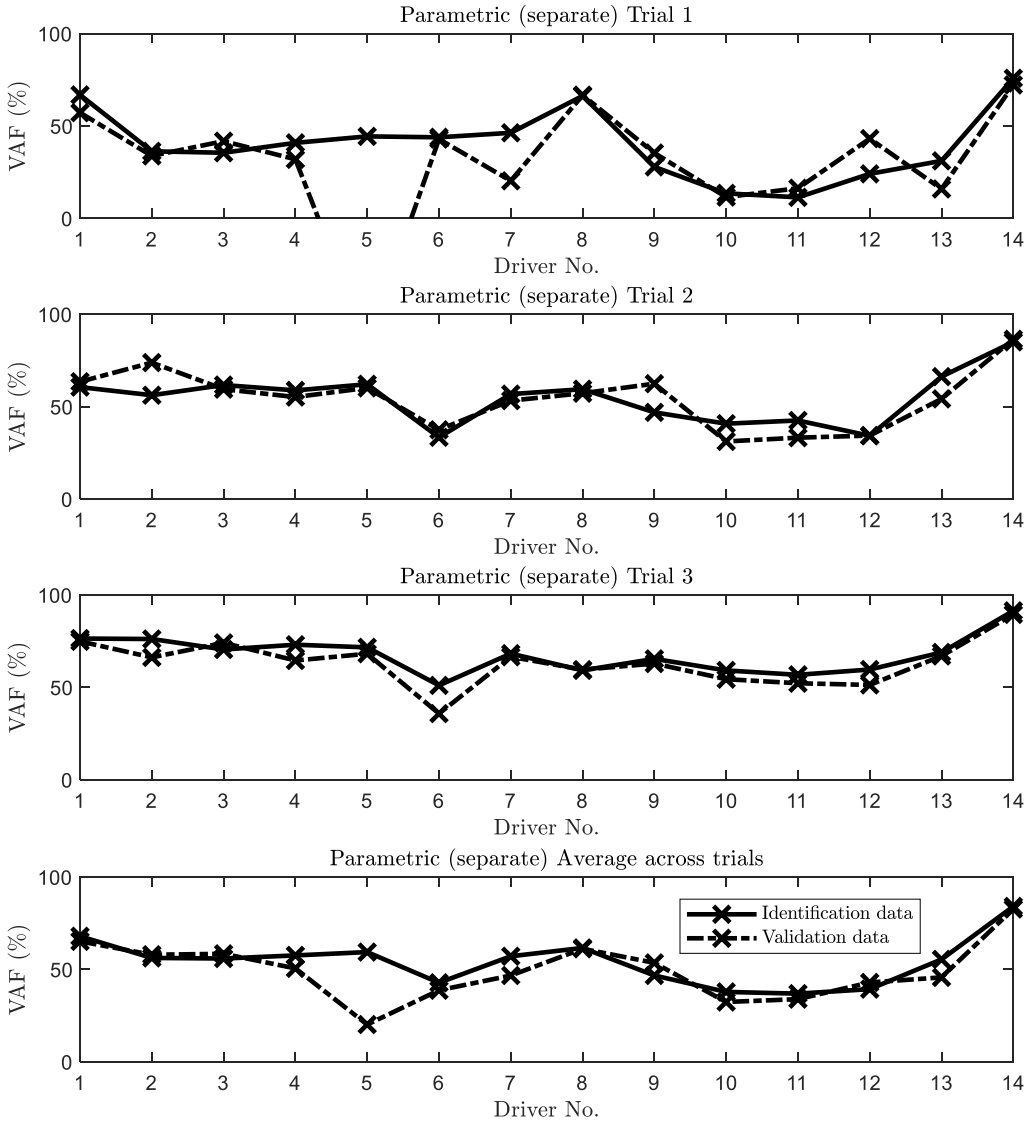

Figure 5.9: Validation of the parametric driver model (separate parameter sets for each trial identified at identification step 5b) for each trial and driver including the averaged driver (Driver 14). The VAFs obtained from the identification data are represented by the markers on the solid lines, while the VAFs obtained from the validation data are represented by the markers on the dashed lines.

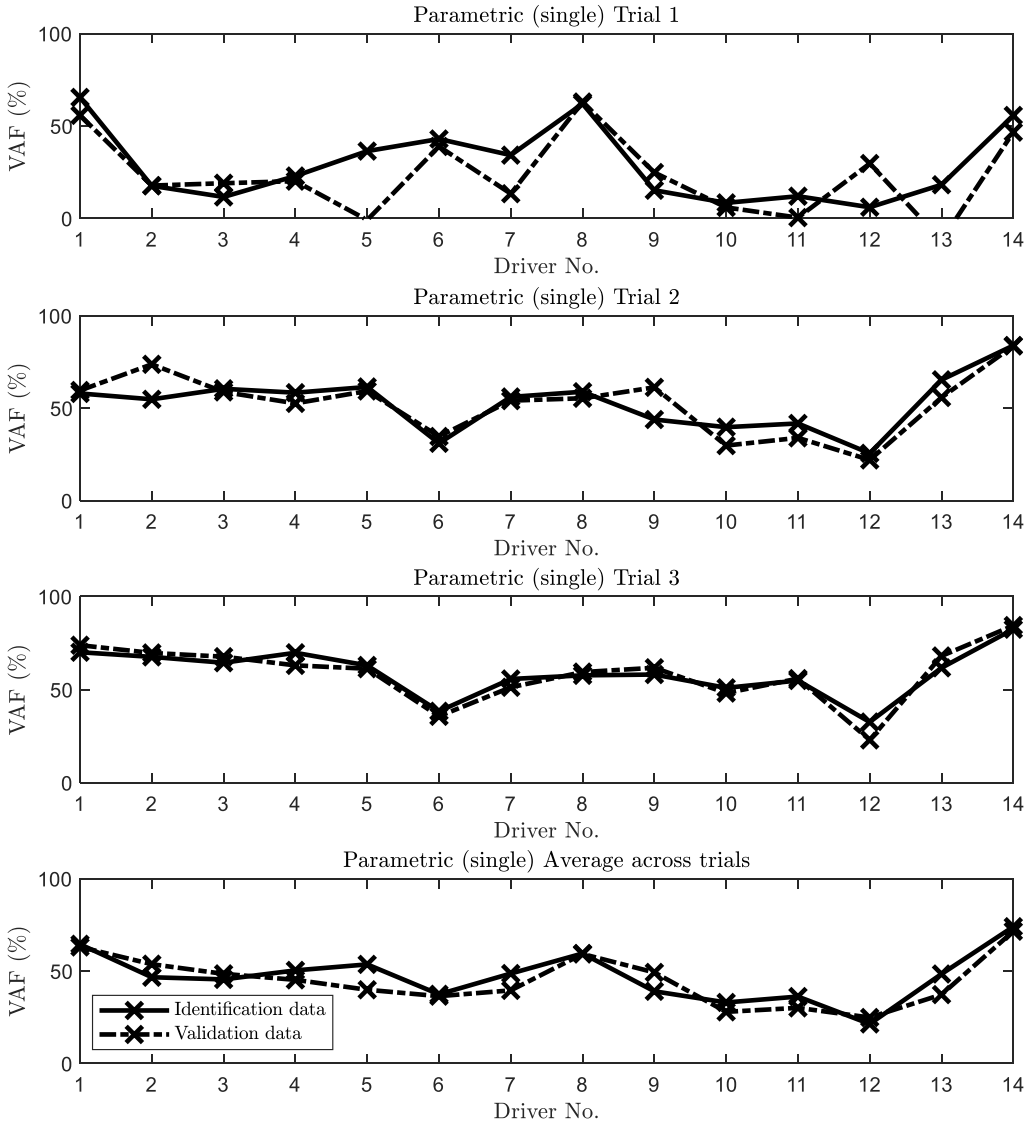

Figure 5.10: Validation of the parametric driver model (single parameter set for each driver) for each trial and driver including the averaged driver (Driver 14). The VAFs obtained from the identification data are represented by the markers on the solid lines, while the VAFs obtained from the validation data are represented by the markers on the dashed lines.

5.3.5 Identification Procedure Validation

To check that the parametric model identification procedure described in Section 5.2.2 could converge to the correct parameter values, a simulation of identification is conducted. Representative steering wheel angles are created by using the driver model with the one single set of parameters identified by using the averaged data. Process and measurement noise are also added to the simulation by implementing Gaussian white noise with the identified standard deviations, in order to match the actual driver noise seen in the experiments. Ten sets of representative steering wheel angles are generated for each of the three experimental trials with different random noise, and the identification procedure is exactly replicated for each set of simulated results. The single set of parameter values across all three trials for the ten different sets are shown in Figure 5.11.

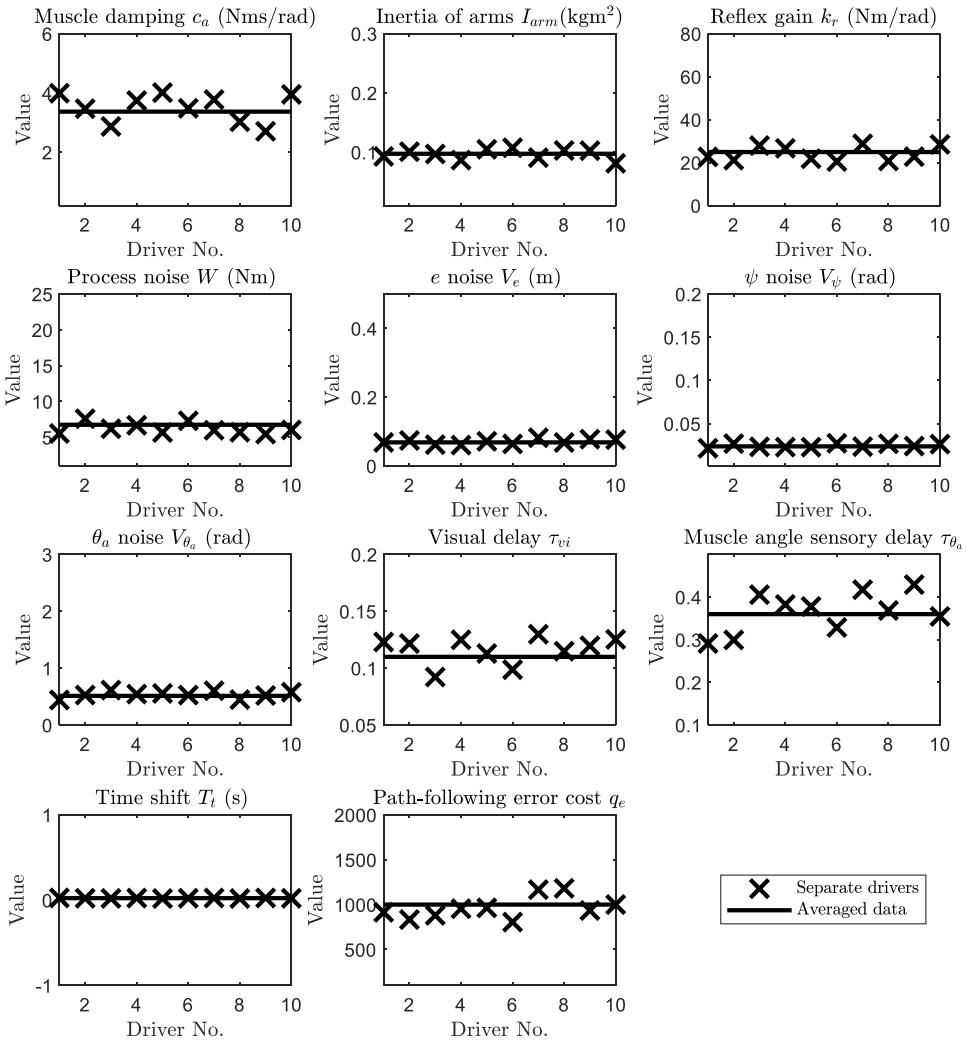

Figure 5.11: Validation of the identification. Identified single parameter sets fitting all three linear trials for each data set of the simulated results. Values found for the individual set are shown by markers, and actual parameter values used for generating the simulated results are shown by back solid horizontal lines.

5.4 Measurement Noise Analysis

It has been found in Section 5.3.3 that the value of process noise standard deviation W depends linearly on RMS muscle activation torque T_a and therefore can be described by using a constant signal-to-noise ratio SNR_W:

$$\mathrm{SNR}_W = \frac{\mathrm{RMS}(T_a)}{W} \tag{5.5}$$

It would be beneficial if the measurement noise is also signal-dependent so that the measurement noise standard deviation parameters V_e, V_ψ and V_{θ_a} can be related to the amplitudes of the signals measured in the experiments or estimated using experimental data through constant parameters. The noise parameters V_e, V_ψ and V_{θ_a} appear in two places in the model: as variances of the added noise; and as parameters of the state estimator to represent how the human driver places relative weights on different measurements. Because it is impossible to scale the values of V_e, V_ψ and V_{θ_a} to represent the actual levels of measurement noise of the drivers in the experiments as what is done for the process noise, the identified values of V_e, V_ψ and V_{θ_a} may represent weights placed by the drivers on different sensory channels. However, the drivers may have weighed them differently in trails with different steering-vehicle dynamics properties. Therefore, it is not reliable to draw conclusions about if the measurement noise is also signal-dependent by comparing ratios of the identified values of V_e, V_ψ and V_{θ_a} to the amplitudes of the corresponding signals in the three experimental trials. To solve this problem, additional linear experimental trials were carried out with five drivers to eliminate the effects of different steering-vehicle dynamics characteristics on the identified values of measurement noise standard deviations.

5.4.1 Linear Experiment Adjustments and Model Identification

Two additional trials were added to the linear phase of the experiments for Drivers 9 to 13. These two trials were performed directly after trial 3. The properties of the steering-vehicle dynamics in these two trials are kept the same as those in trial 3 but the amplitudes of the target path lateral distance variation are different. The conditions of the two new trials and trial 3 are summarised in Table 5.5.

Table 5.5: Experimental conditions for trail 3 and two new trials

Exp. condition	**Disturbance amplitudes**				**Trail distance** d (m)	**Boost coefficient** C_{boost}
	W_r(m)	W_F(N)	W_T(Nm)	F_c(Nm)		
3	8	0	0	0	0.059	0
3-1	6	0	0	0	0.059	0
3-2	10	0	0	0	0.059	0

In Section 5.2, the identification procedure was run for each of the individual drivers separately as well as for an averaged driver. It was found that differences between the drivers were small, and the identified parameter values for each trial were not reliable because of the high level of random noise in each trial. Therefore, in this section, the time domain steering wheel angles are averaged over the five drivers to give a set of average responses for each trial to reduce the amount of driver noise in the measurements, and the analysis was only carried out for the averaged data. The identification procedure is shown in Figure 5.12. Similar to Section 5.2.2, separate parameter sets are identified for each of the three trials (3, 3-1 and 3-2) individually for the averaged driver. However, before this, a single set of parameter values is found for this averaged driver by using trials 1, 2 and 3 following the identification procedure described in Section 5.2.2 and is used as the basis for the new identification. Initially, the values of process noise standard deviation W are scaled by the ratio of the measured to the modelled noise standard deviations for each trial, respectively. Then, the process noise standard deviation W is fixed at the value found for each individual trial, and sensory delays τ_{vi} and $\tau_{\theta a}$, the cognitive controller time shift T_t and the neuromuscular parameters are held constant using the values found for the single parameter set while the other parameters including V_e, V_ψ, V_{θ_a} and q_e are identified for each trial individually.

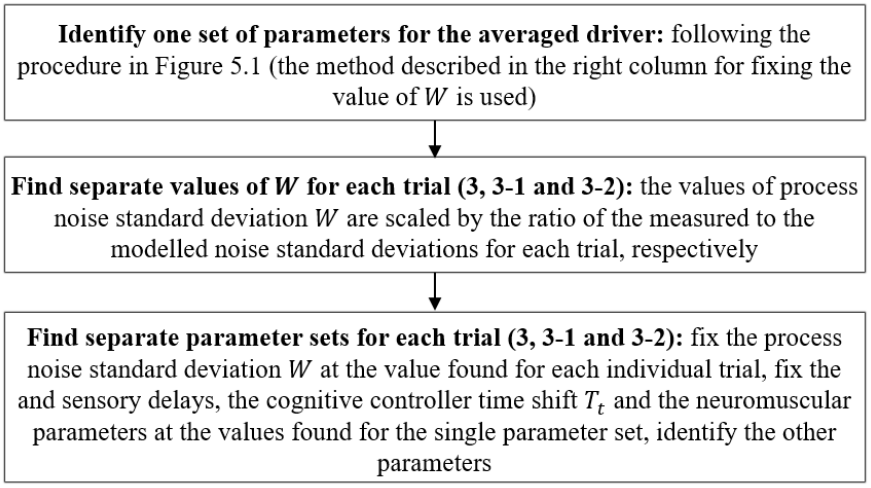

Figure 5.12: Identification procedure for finding separate parameter sets for each trial for the averaged driver.

5.4.2 Modelled Driver Measurement Noise

Identified measurement noise standard deviations for the three trials (3, 3-1 and 3-2) are plotted against RMS values of the corresponding signals in Figure 5.13. It is seen that there are clear linear relationships between them, indicating the measurement noise is also signal-dependent. In addition, the straight lines passing through the origin fit the scatters quite well, supporting that the patterns of the noise follow the

noise model, shown in Figure 5.14, used by Nash and Cole [117]. Overall, the noise standard deviation is proportional to signal amplitude with a zero intercept, but there is a threshold level under which humans cannot detect the signals. Therefore, the measurement noise standard deviations can be related to the amplitudes of the signals in the experiments by using constant SNRs when the levels of the signals are larger than the thresholds.

$$\mathrm{SNR}_e = \frac{\mathrm{RMS}(e)}{V_e} \tag{5.6}$$

$$\mathrm{SNR}_\psi = \frac{\mathrm{RMS}(\psi)}{V_\psi} \tag{5.7}$$

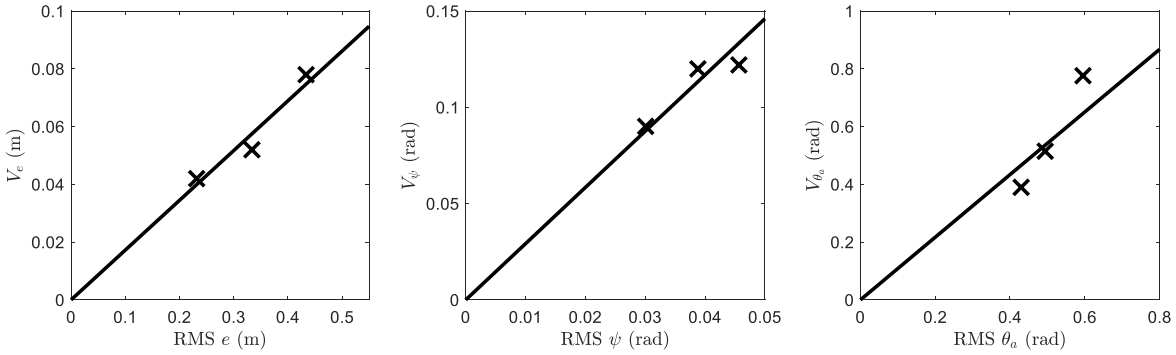

$$\mathrm{SNR}_{\theta_a} = \frac{\mathrm{RMS}(\theta_a)}{V_{\theta_a}} \tag{5.8}$$

Figure 5.13: The identified measurement noise standard deviations are compared with the corresponding RMS signal amplitudes. Straight lines passing through the origin are plotted to check the linearity of the plotted points.

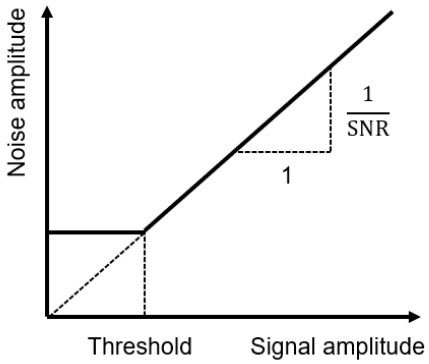

Figure 5.14: Signal-dependent noise model [117].

Although the scatters do not exactly lie on the straight lines, the identified signal-noise relationships are plausible by taking account that there is some uncertainty in the data although the level of noise has been reduced by averaging the experimental data. In addition, the averaged VAF value over all three

trials is 83% for the separate parameter sets, suggesting the driver model with the identified parameters fits the experimental results.

5.5 Single Set of Parameter Values

It has been found that the signal and noise amplitudes vary a lot between drivers and trials, where a constant noise standard deviation model would be inappropriate, and that the noise characteristics for the human driver's control action and each sensory measurement can be in principle be described by a SNR when the amplitudes of the signals are larger than certain levels. Therefore, instead of identifying the process and sensory measurement noise standard deviation parameters W, V_e, V_ψ and V_{θ_a} for the parametric driver model, a fixed set of parameters with SNRs has been fitted to the results from trials with random target path following task (trial 2 and trial 3) for each individual driver and the averaged driver. The experimental results from trial 1 are excluded from the data used for this identification, since the amplitudes of some relevant signals are below the thresholds that human drivers can detect and the experimental condition of trial 1 is very different to those of the other linear and nonlinear trials. SNRs are used to relate the noise standard deviations and the amplitudes of the signals measured in the experiments and therefore could provide the model with the predictive ability for a wide range of conditions. The parametric driver model now depends on the following eleven variable parameters:

- Neuromuscular parameters: damping resisting stretching of the muscle fibre c_a, arm inertia I_{arm}, reflex gain k_r
- Cognitive parameters: process noise SNR (SNR_W), measurement noise SNRs (SNR_e, SNR_ψ, SNR_{θ_a}), path-following error cost q_e, cognitive controller time shift T_t
- Sensory delays: visual delay τ_{vi}, muscle angle sensory delay τ_{θ_a}

where $\mathrm{SNR}_W = \frac{\mathrm{RMS}(T_a)}{W}$, $\mathrm{SNR}_e = \frac{\mathrm{RMS}(e)}{V_e}$, $\mathrm{SNR}_\psi = \frac{\mathrm{RMS}(\psi)}{V_\psi}$ and $\mathrm{SNR}_{\theta_a} = \frac{\mathrm{RMS}(\theta_a)}{V_{\theta_a}}$.

5.5.1 Identification Procedure

The identification process to a single set of parameters with SNRs is also carried out in several steps for each of the individual drivers and the averaged driver. The identification procedure is shown in Figure 5.15 and the conditions for each step are given in Table 5.6. It has been found in Section 5.3 that the identified value of path-following error cost q_e varies significantly between different trials since it is a choice of the driver rather than a physical parameter and depends on the condition of each trial, therefore an estimated value of q_e is found for each trial separately, by using a reasonable initial estimate of all the other parameter values: the neuromuscular parameters c_a, I_{arm}, k_r and the cognitive controller time shift T_t are chosen as the values found in the single set of parameters for each driver in Section 5.3.2, the process noise SNR_W is chosen as the value found for each driver in Section 5.3.3.

The value of q_e is then fixed in all the identification steps. To reduce the number of parameters to be identified, the neuromuscular parameters c_a, I_{arm}, k_r and the target time shift T_t are also fixed at the values found in the singe set of parameters for each driver in Section 5.3.2 in all the identification steps. In step 1, all the variable parameters including the SNRs and the sensory delays are identified across the two linear trials. As mentioned in Section 5.3, the process noise levels predicted by the model are to be matched by those seen in the experiments. Therefore, after step 1, the value of process noise SNR_W is scaled by using the average ratio of the measured to the modelled noise standard deviations. In step 2, the process noise SNR_W is then held constant while the remaining variable parameters are identified to fit the results of two linear trials again. However, the modelled noise standard deviation may vary with the change of the identified values of the SNRs in step 2. Therefore, steps 1 and 2 are repeated iteratively until the measured noise standard deviation equals the modelled noise standard deviation. For the averaged data, the process noise SNR_W is also scaled to match the standard deviation of the measured noise found in the measured data after step 1 and is then fixed in step 2. Again, similar to Section 5.2.2, the average of the scaled values of SNR_W over the thirteen drivers is also used for the averaged driver after step 1 and is then used in step 2. However, the two steps are only conducted once in this case.

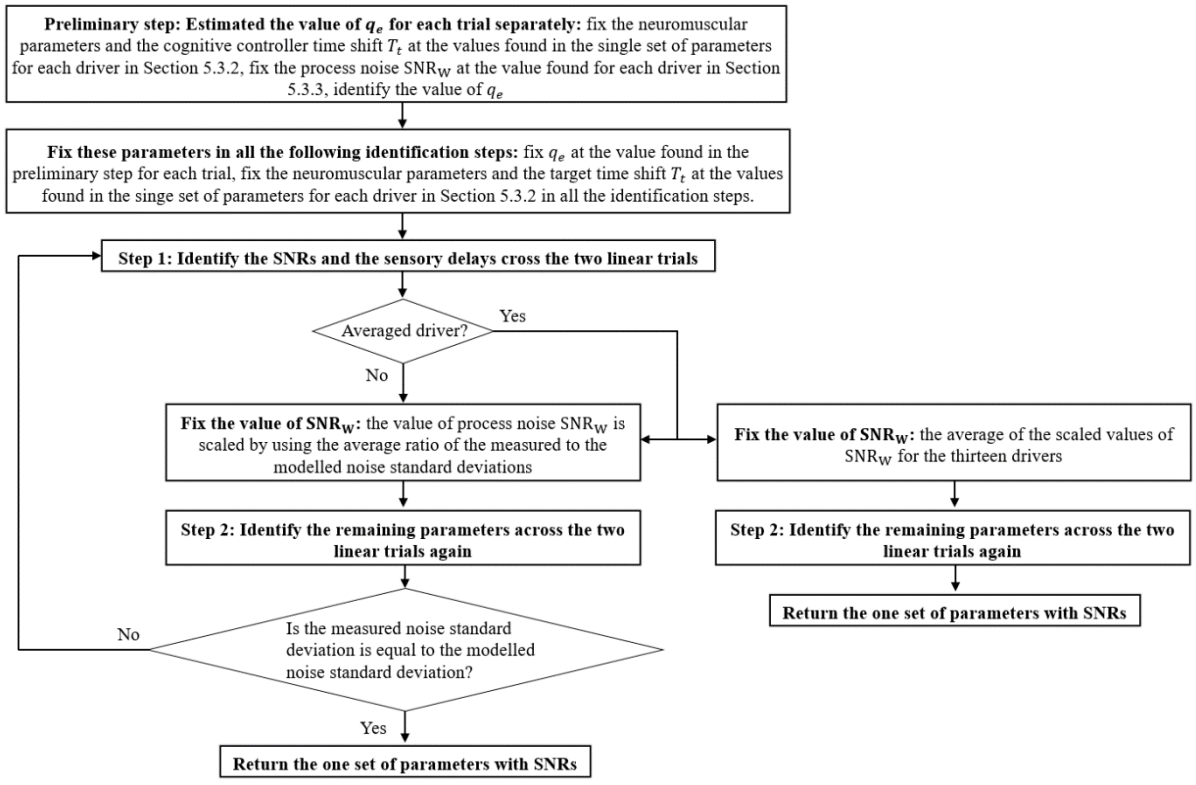

Figure 5.15: Identification procedure for finding one set of parameters with SNRs for each driver and the averaged driver.

Table 5.6: Conditions for each step of the new parametric identification procedure, to find a single set of parameter values for each driver. × indicates parameters to be identified at each step.

		Neuromuscular parameters			Cognitive parameters						Sensory delays	
Step	**Trials**	c_a	I_{arm}	k_r	$\mathrm{SNR_W}$	SNR_e	SNR_ψ	SNR_{θ_a}	T_t	q_e	τ_{vi}	τ_{θ_a}
1	2, 3				×	×	×	×			×	×
2	2, 3					×	×	×			×	×

There is a risk that the initial estimated values of q_e are not reliable because the measurement noise SNRs are identified along with q_e. To achieve better identification results, a more reliable estimated value of q_e is found again for each trial. Besides the fixed values of the neuromuscular parameters c_a, I_{arm}, k_r, the cognitive controller time shift T_t and the process noise SNR_W, the measurement noise SNRs are fixed at the values found for the averaged driver using the method described in the left column of Figure 5.15. The new estimated values of q_e are then held constant, and the identification steps 1 and 2 are performed again until the measured noise standard deviation is equal to the modelled noise standard deviation. The identification procedure described in the right column of Figure 5.15 is also conducted.

After a single set of parameter values fitting the two linear trials 2 and 3 is found for each individual driver and the averaged driver, separate parameter sets are identified for each trial individually for each driver. The process noise and measurement noise SNRs, the arm inertia I_{arm} and the cognitive controller time shift T_t are fixed at the values found for the one single set of parameters for each driver, while all the other parameters are allowed to be varied in the identification. The aim of this is to check for the greatest agreement between the model and the experimental results for each trial achievable by using the identified process and measurement noise SNRs.

5.5.2 Identification Results

The resulting VAF values of the identified linear parametric driver model with a single set of parameters with SNRs are plotted in Figure 5.16 for each driver and the averaged driver. The fit of the Box–Jenkins model is also included. As expected, the VAFs are the largest for the Box-Jenkins model. It is seen that the VAFs for the separate parameter sets are quite close or even equal to the VAFs for the Box-Jenkins model, and the difference between the VAFs for the single parameter sets and the VAFs for the separate parameter sets is negligible for most drivers and trials. This further supports that the linear parametric driver model structure can almost perfectly explain the drivers' linear steering control and it is a reasonable way to describe the process and measurement noise standard deviations in the parametric

driver model by using SNRs. For the averaged driver, the averaged VAF value over the two trials is 86.6% for the one parameter set and 86.8% for the separate parameter sets.

The single parameter set with the process and measurement noise SNRs identified for each driver is shown in Figure 5.17. The identified values of c_a, I_{arm}, k_r and T_t are fixed at the values shown in Figure 5.4, so they are not repeated here. Overall, the parameter values, especially the process and measurement noise SNRs, are similar between different drivers, and the values found using the averaged data all fall within the range of the parameter values found for the individual drivers, further supporting that the averaged data is a valid representation of a typical driver's steering control behaviour. Although the spread of the identified values for some of the parameters is large, it is reasonable by considering the model is fitting to some random noise for each individual driver. Therefore, the identified parameter values are more reliable for the averaged data.

In Figure 5.17, the average of the scaled values of SNR_W over the thirteen drivers, with the corresponding identified values of SNR_e, SNR_ψ and SNR_{θ_a} for the averaged data, are shown by the red dashed horizontal lines. The identified value of SNR_W is larger than the average of the scaled values of SNR_W over the thirteen drivers because the level of driver noise has been reduced by averaging the steering wheel angle actions over the drivers. In general, the values of SNR_e, SNR_ψ and SNR_{θ_a} identified by using SNR_W scaled to match the standard deviation of the measured noise found in the experimental data are also larger than those identified by using the average of the scaled values of SNR_W over the thirteen drivers. This is because that it is the ratios between the Kalman filter noise parameters that affect the state estimator performance. Therefore, the state estimator with a lower value of one of these noise parameters (higher value of one of the SNRs) also has lower values of the others (higher values of the other SNRs).

The identified parameter values for the averaged driver are shown in Table 5.7. The average of the scaled values of SNR_W over the thirteen drivers along with the corresponding identified values of SNR_e, SNR_ψ and SNR_{θ_a} are chosen since these values may represent a more typical driver. These parameters can be regarded as a single parameter set fitting the results of trials 2 and 3 across all drivers and can be used to simulate driver steering control under various conditions. The uncertainties of these parameters can be quantified by calculating the standard deviations of the identified parameters for each individual driver, which are also shown in Table 5.7. However, it is important to notice that the identified parameter values for the averaged driver are not equal to the average of the identified parameter values over the thirteen drivers.

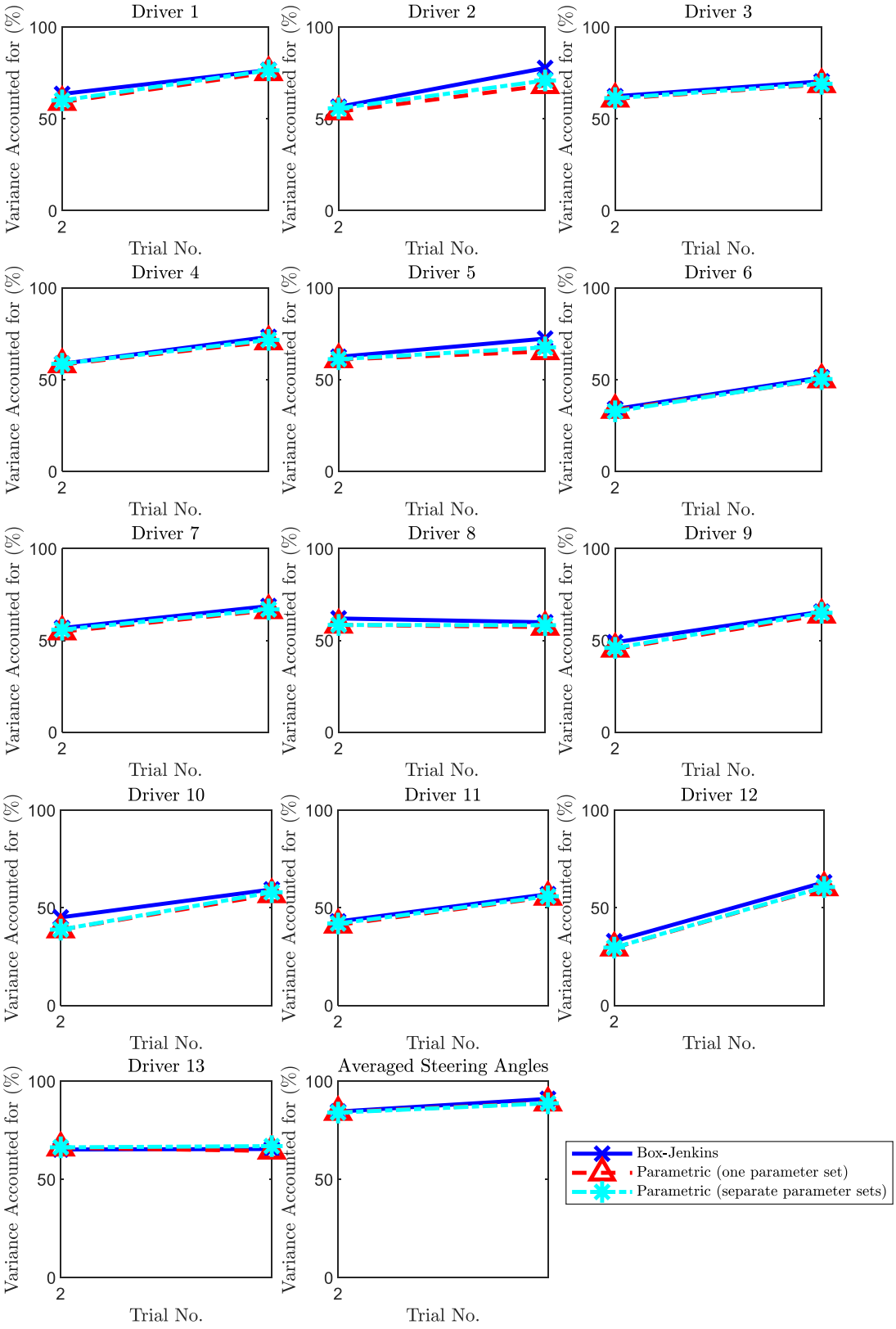

Figure 5.16: Agreement between parametric driver model (with SNRs) predictions and experimental results. VAF value is plotted for each driver/trial combination, and for the averaged driver on each trial.

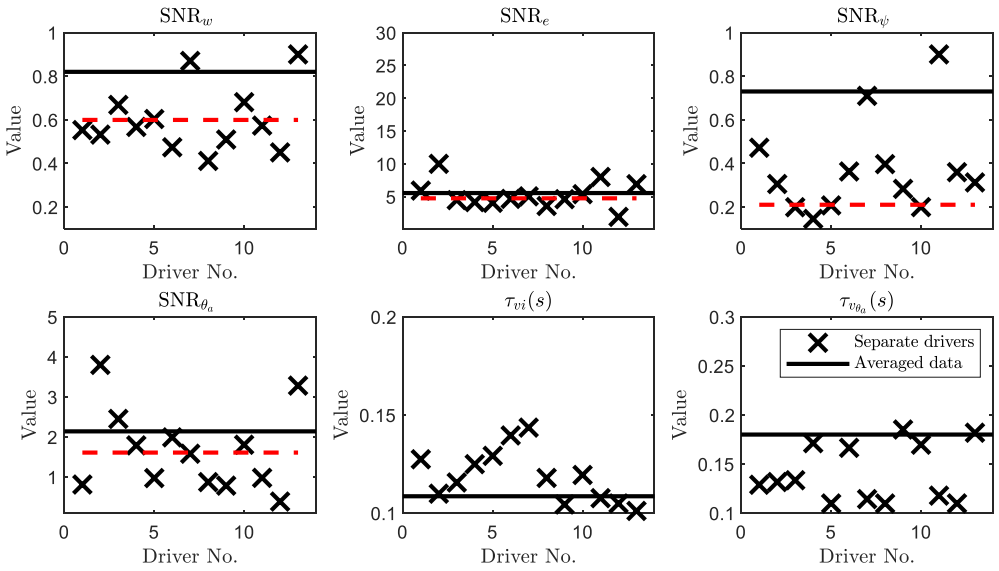

Figure 5.17: Identified single parameter sets fitting the linear trials 2 and 3 for the individual drivers (crosses) and the averaged data (solid horizontal lines). The average of the scaled values of SNR_W over the thirteen drivers, with the corresponding identified values of SNR_e, SNR_ψ and SNR_{θ_a} for the averaged data are shown by the red dashed horizontal lines.

Table 5.7: Single set of parameters identified to fit the results of all trials and all drivers.

Parameter	c_a	I_{arm}	k_r	SNR_W	SNR_e	SNR_ψ	SNR_{θ_a}	τ_{vi}	τ_{θ_a}	T_t
Units	Nms /rad	kgm^2	Nm /rad					s	s	s
Values	3.37	0.0973	24.9	0.600	4.75	0.210	1.61	0.109	0.180	0.023
Standard deviations	0.910	0.0375	7.00	0.154	1.99	0.228	0.995	0.0133	0.0303	0.308

In addition to generating noise-free steering wheel angle predictions, the parametric driver model can also estimate the standard deviation of the driver noise referred to the steering wheel angle. This estimate can be compared with the measured noise level to check if the identified SNRs are realistic. Again, by assuming a small modelling error, the measured driver noise is given by $(\theta_{sw(sim)} - \theta_{sw(exp)})$. The ratio between the measured and modelled driver noise standard deviations for each driver and trial combination is shown in Figure 5.18, using the single parameter set identified for each driver. Overall, the noise standard deviations match well between the model estimation and experimental measurement, indicating that the identified SNRs are capable of representing the actual driver noise seen in the experiments.

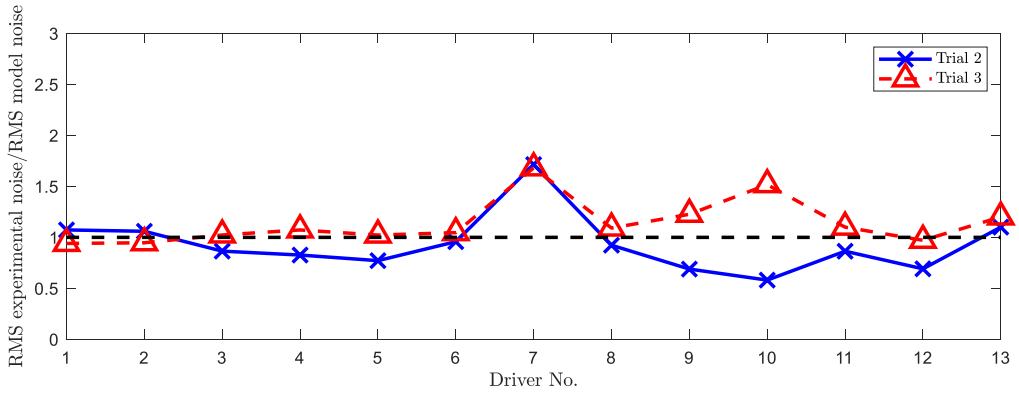

Figure 5.18: Ratio of the measured and modelled noise standard deviations for each driver and trial

Similar to Section 5.3.4, experimental measurements in the last minute are used to validate the predictive power of the parametric driver model with SNRs and to check if there is any over-fitting. The averaged VAF values over the two linear trials by using the identification data as well as those obtained by using the validation data are plotted for each driver and the averaged driver in Figure 5.19. The VAF values in the validation data are found to be similar to those in the identification data, and the VAF values in the identification data and the VAF values in the validation data are almost equal to each other for the averaged driver. This good agreement proves that the identified driver model with SNRs should be able to give a good approximation to the human driver's steering control behaviour.

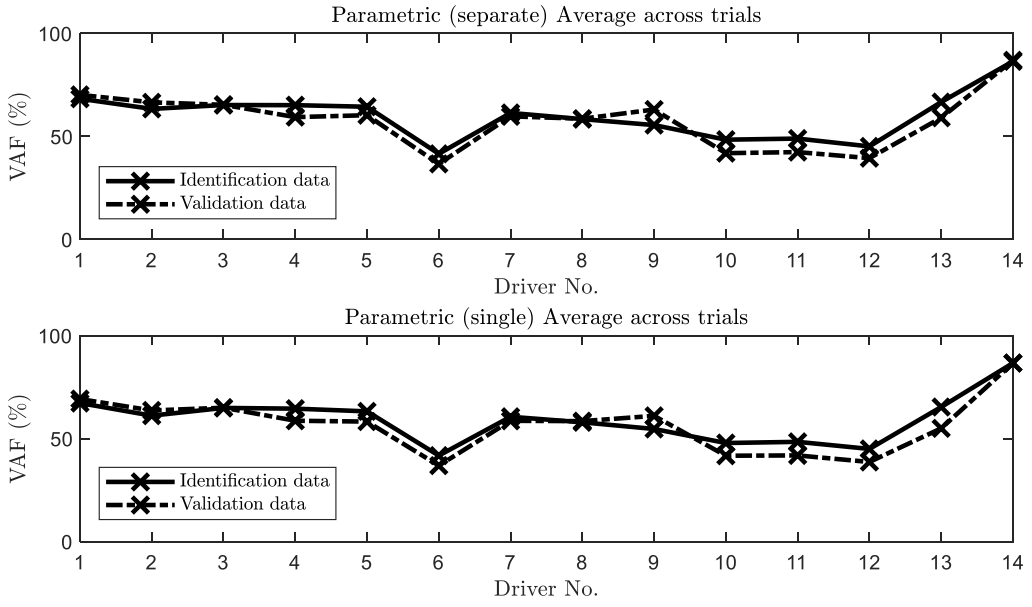

Figure 5.19: Validation of the parametric driver model with SNRs for each driver including the averaged driver (Driver 14). The VAFs obtained from the identification data are represented by the markers on the solid lines, while the VAFs obtained from the validation data are represented by the markers on the dashed lines.

5.6 Discussion

The identified parameter values can be compared with results from the literature to determine if each block of the parametric driver model can describe realistic functions of the corresponding sub-system. The parameters found by using the averaged data are used for the comparison, as shown in Figure 5.8.

The identified values of neuromuscular parameters are compared with those obtained by Hoult [17], who proposed a neuromuscular model for simulating driver steering torque and found ranges of values of the muscle damping, the arm inertia, and the stretch reflex for muscles with different states through experiments. It is seen that the identified stretch reflex gain k_r is within the range found by Hoult, while the identified muscle damping c_a and arm inertia I_{arm} are relatively larger than the corresponding values found by Hoult. However, the muscle model used in Hoult's studies is different from Hill's muscle model [121], and there is another non-zero damping term representing the intrinsic muscle properties. In addition, the values found by Hoult are identified through passive conditions and therefore, may not be applicable for the active steering control task. By taking these factors into account, the difference in the identified neuromuscular parameter values is plausible.

Nash and Cole [117] found a set of process and measurement noise SNRs in the study of human sensory feedback in car driving. The identified values of process noise SNR_W and visual vehicle yaw angle measurement noise SNR_ψ in this study are comparable with the those found by Nash and Cole, while the identified value of visual path-following error measurement noise SNR_e is much greater than the value found by Nash and Cole. However, the selected sensory measurement channels in the model developed by Nash and Cole are different from the ones selected in this study, which may influence the human driver's weighting on each sensory measurement for the state estimator.

The identified sensory delays can be compared against values summarised in [109]. As mentioned in Section 5.3.2, the sensory measurements used by humans for state estimation could include the information they perceived over a period and are optimally integrated in a sophisticated way, which makes it difficult to accurately identify separate time delays for different sensory channels. In addition, the cognitive delay is not included in the driver model explicitly, and thus the effect of this could also be incorporated in the sensory delay blocks. Therefore, it is not necessary for the identified sensory delays to match the literature. However, it is encouraging that the identified values are all within the ranges reported in [109].

Table 5.8: Comparison of identified parameter values with estimates from literature. Identified parameter values are obtained by using the averaged data.

Parameter	c_a	I_{arm}	k_r	SNR_W	SNR_e
Units	Nms/rad	kgm^2	Nm/rad		
Identified	3.37	0.0973	24.9	0.600	4.75
Literature	$0-1.25$	$0.0286-0.0446$	$0-50$	0.57	0.901
Source	[17]	[17]	[17]	[117]	[117]

Parameter	SNR_ψ	SNR_{θ_a}	τ_{vi}	τ_{θ_a}	T_t
Units			s	s	s
Identified	0.210	1.61	0.109	0.180	0.023
Literature	0.415	–	$0.100-0.560$	>0.034	–
Source	[117]		[109]	[109]	

5.7 Conclusions

The linear experimental results have been used to identify parameter values for a new parametric driver model incorporating steering torque feedback and state estimation. The fit of the identified model to the experimental results can achieve the upper bound limit given by the Box-Jenkins model, and a single set of parameter values has been found to fit the results from all linear trials well for most cases. The good agreement between the model and the experimental results supports the hypothesis that the identified parametric driver model is capable of representing the human driver's on-centre steering control behaviour.

The process noise standard deviation was found to be linearly dependent on RMS muscle activation torque, and this signal-dependence was also demonstrated to be valid for measurement noise. Using this linear relationship between signal magnitudes and noise standard deviations, a single set of parameter values with process and measurement noise SNRs was also identified for each driver and an averaged driver across the two linear trials with randomly moving target path. The averaged VAF value over the two trials is found to be 86.6% for the one parameter set found by using the averaged data. The high VAF value indicates that the identified driver model with the process and measurement noise SNRs can be used to simulate the driver's steering control behaviour in a wide range of conditions. The identified parameter values are found to be physically reasonable compared with the literature. The identification results in this chapter could serve as the basis for the nonlinear identification phase.

Chapter 6

Nonlinear Model Identification and Correlation with Subjective Assessment

6.1 Introduction

In Chapter 3, a novel mathematical model of the driver-steering-vehicle system has been developed, based on the hypothesis that a human driver learns an internal mental model of the driver-steering-vehicle dynamics and uses the internal model in sensory perception, cognitive control, and neuromuscular action. A linear model is developed first to enable a fundamental understanding of steering torque feedback to be obtained. The model is then extended to account for the human driver's steering control of a vehicle with nonlinear steering dynamics, especially nonlinear friction in the steering mechanism, by using an extended Kalman filter (EKF) and model predictive control (MPC) method, since the nonlinear steering system friction is thought to have a significant effect on the human driver's subjective assessment of steering torque feedback [1] [22] [33] [58]. These effects have also been demonstrated in Chapter 4, where a series of driving simulator experiments consisting of trials with different steering system friction levels are presented, and the correlations between the subjective assessment of steering torque feedback and objective metrics measured in the experiments are found. In Chapter 5, parameter values are found for the linear driver model using an identification procedure to fit results from the linear phase of the experiments and are compared with literature results. The model fits the experimental results well, and the parameter values are found to be physically plausible. In this chapter, a parametric identification procedure is used to fit the nonlinear driver-steering-vehicle model to the results of the nonlinear phase of the experiments described in Chapter 4. The procedure is adjusted to account for the challenges of finding parameter values for a nonlinear driver model based on the identification results of the linear model in Chapter 5. Simulations are then run by taking the identified driver model, and the meticulously selected simulated signals are compared with the test

drivers' subjective ratings to test the hypothesis that the human driver's subjective rating of steering feel is related to the driver's ability to predict the steering torque feedback using an internal mental model of the plant controlled by the driver and the known control input to the plant.

Details of the method used to identify the nonlinear model are presented in Section 6.2. The identification results along with the validations of the identified model and the identification procedure are discussed in Section 6.3. The investigation of the correlation between the model and the subjective ratings is presented in Section 6.4. A summary of the findings is given in Section 6.5.

6.2 Nonlinear Driver Model Identification

The identification procedure developed in Chapter 5 has been demonstrated to successfully find the eleven unknown parameters of the linear driver model. However, various adjustments to the identification procedure must be made to identify the nonlinear driver model. In Section 6.2.1, various assumptions of the human driver's internal mental model are justified. Details of the new identification procedure are given in Section 6.2.2. Similar to Chapter 5, the first minute of each trial is excluded from the data used for identification to eliminate the learning behaviour of human drivers, and the final minute of each trial is used to validate the identified driver model.

6.2.1 Perception of Nonlinear Steering Dynamics

The linear model identification described in Chapter 5 assumes that human drivers learn an accurate internal model of the driver-steering-vehicle dynamics, with any discrepancies between the model and the measurements represented by Gaussian process noise. However, previous literature [1] [22] [33] [58] found that higher steering system friction levels normally lead to subjectively worse steering feel. This suggests that human drivers in some circumstances may be unaware of the full nonlinear steering system friction dynamics or may use simplifications to reduce their mental load, resulting in the increased discrepancy between the predicted and measured driver-vehicle responses, which in turn causes unsatisfactory steering feel. To test this hypothesis, several variations of the human driver's internal mental model of the plant are proposed to represent different assumptions about how accurately the human driver can learn the characteristics of the steering-vehicle system with nonlinear friction.

The implemented driver model variations are summarised in Table 6.1. In driver model M0, the internal mental model is assumed to be equal to the linear part of the nonlinear plant, which means the modelled human driver ignores the friction in the steering system. In driver model M1, it is assumed that the internal mental model is equal to the linear part of the nonlinear plant plus an equivalent damping term $C_{sw}{}'$ of the steering system friction. The damping term $C_{sw}{}'$ is placed between the inertia of the rack

and the front wheels I_c shown in Figure 3.5 in Chapter 3 and the ground, and is identified for each driver and nonlinear trial by minimising the difference between the simulated torque demand signal $T_{demand(sim)}$ and the actual torque demand signal $T_{demand(exp)}$ recorded during the driving simulator experiment. The simulated torque demand signal $T_{demand(sim)}$ is generated by using the measured steering wheel angle $\theta_{sw(exp)}$ and the open-loop internal mental model. Driver model M1 indicates that the modelled human driver linearises the nonlinear steering system friction as viscous damping in the internal mental model. In driver model M2, the internal mental model of the driver-steering-vehicle dynamics is exactly the same as the actual plant, representing a modelled human driver who can precisely perceive the nonlinear steering characteristics. In driver models M0 and M1, the LQR method and a time-varying linear Kalman filter are used since their internal mental models are entirely linear, while in driver model M2, the MPC method (both LMPC and NMPC) and an extended Kalman filter (both EKF1 and EKF2) are used, as derived in Chapter 3.

Table 6.1: Variations of the human driver's internal mental model of the plant

Driver Model	Internal model of the plant	Controller and state estimator
M0	The linear part of the real nonlinear plant only	LQR with LKF
M1	The linear part of the real nonlinear plant plus an equivalent damping term of the steering system friction $C_{sw}{}'$	LQR with LKF
M2	Actual nonlinear plant	LMPC/NMPC with EKF1/EKF2

6.2.2 Identification Procedure

In the identification described in Chapter 5, parameter values are identified by maximising the fit of the linear driver model to experimental results using a two-stage minimisation method which comprises a genetic algorithm and a gradient search method to find the global optimal solution. This procedure has been demonstrated to successfully find optimal values of a large number of parameters at the same time. However, numerous simulations of the closed-loop driver-steering-vehicle are required in each optimisation in order to find reliable parameter values. The nonlinear models take much longer to simulate than the linear model, making it impractical to identify many parameter values in the same way. Therefore, where possible parameter values for the nonlinear driver models are taken from the linear identification phase, and only the necessary parameters are identified.

Signal-dependent relationships (SNRs) have been found for the driver process and measurement noise standard deviations in Chapter 5, allowing the noise standard deviations to be estimated based on the RMS values of the corresponding measured signal. Therefore, the noise parameters W, V_e, V_ψ and V_{θ_a} in the state estimator are calculated by:

$$W = \frac{\mathrm{RMS}(T_a)}{\mathrm{SNR}_W} \tag{6.1}$$

$$V_e = \frac{\mathrm{RMS}(e)}{\mathrm{SNR}_e} \tag{6.2}$$

$$V_\psi = \frac{\mathrm{RMS}(\psi)}{\mathrm{SNR}_\psi} \tag{6.3}$$

$$V_{\theta_a} = \frac{\mathrm{RMS}(\theta_a)}{\mathrm{SNR}_{\theta_a}} \tag{6.4}$$

where the path-following error e and the vehicle yaw angle ψ are directly recorded in the driving simulator experiments, while the muscle activation torque T_a and muscle angle θ_a are estimated by using the procedure described in Section 5.3.3. Because the simulated muscle angle $\theta_{a(sim)}$ in the first step of the estimation procedure is not available until the identified nonlinear driver model is known, the transfer function fitting the simulated muscle angle to the simulated steering wheel angle for experimental trial 3 is used for all the nonlinear trials by assuming the addition of nonlinear steering dynamics should not significantly affect the parameter values of the driver model, since the transfer function mainly describes the physical systems of the driver rather than the vehicle. In addition, the arm inertia I_{arm} and the cognitive controller time shift T_t do not vary between different trials, so the values of these two parameters are taken directly from the linear driver model identification results. Therefore, the linear driver models M0 and M1 now only depend on the following five parameters:

- Neuromuscular parameters: damping resisting stretching of the muscle fibre c_a, reflex gain k_r
- Cognitive controller parameter: path-following error cost q_e
- Sensory delays: visual delay τ_{vi}, muscle angle sensory delay τ_{θ_a}

For nonlinear driver model M2, the MPC prediction horizon T_p is set to 3s. As mentioned in Chapter 3, setting prediction horizon T_p to 3s could make the finite-horizon MPC approximate an infinite-horizon controller and provides a good trade-off between making MPC and LQR perform similarly to each other with the same value of path-following error cost q_e for linear models and saving computational time of MPC. There are two types of MPC developed for the human driver's nonlinear control, namely LMPC and NMPC, as described in Chapter 3. The simulation results in Chapter 3 show that NMPC, where the full nonlinear optimisation is carried out, is the best performing controller, although it is matched closely by LMPC, where the nonlinear system dynamics are linearised about the predicted state at each time step up to the full prediction horizon. However, LMPC is much faster to run than NMPC. In the identification of nonlinear driver model M2, both LMPC and NMPC are tested. Due to MPC and EKF taking much more computational time than LQR and LKF, it is not practical to identify five parameters for nonlinear driver model M2. Most of the parameters are thus set to the values identified for trial 3 in the linear identification phase in Chapter 5 for each nonlinear trial, and only the path-following error cost q_e is identified for nonlinear driver model M2.

The same identification strategy is also used for driver models M0 and M1 to enable direct comparisons between the three driver models. Since there is just one parameter to be identified, instead of using a rather complicated optimisation method, the closed-loop driver-steering-vehicle model is simulated with a range of manually selected values of q_e and the VAF between the modelled steering wheel angle and the measured steering wheel angle is calculated for each value of q_e. The highest VAF and the corresponding value of q_e are recorded. This identification method gives a reasonable estimate of q_e in a computationally efficient way.

However, in order to check if the parameter values adopted in Chapter 3 are appropriate for the nonlinear trials, another identification is conducted for driver models M0 and M1 separately by searching for the five parameters simultaneously. The identified parameter values and the VAFs are compared to those in the case where only the path-following error cost q_e is identified to justify the fixed parameter values. Nash [126] pointed out that the gradient search optimisation method cannot be applied because the optimisation cost function does not vary smoothly with the parameter values when simulating model with nonlinearity, and successfully used a genetic algorithm only with 10 iterations and an initial population of 12 to identify two unknown parameters of a nonlinear driver model controlling a vehicle with nonlinear tyre dynamics. In this work, a similar approach is taken. The five parameter values are identified using a genetic algorithm with 100 iterations and an initial population of 20 here. Preliminary simulations show that this is sufficient to give a reasonable estimate of the five optimal parameters in the trials.

Moreover, in Chapter 5, the measured steering actions are averaged over all the test drivers to give a set of 'averaged data', with lower noise levels compared to the individual drivers. However, this does not work for the nonlinear trials since the principle of superposition does not apply to nonlinear dynamics. Therefore, parameter values are only identified for each individual trial and driver separately.

Furthermore, Box-Jenkins models are also identified to fit the results of each nonlinear trial. However, this may not give an upper bound limit on the fit of the nonlinear parametric model since the relationship between the input and output signals of the Box-Jenkins model is restrained to be linear. Nevertheless, it can still be used as a benchmark for the parametric identification.

6.3 Identification Results and Analysis

This section presents a comprehensive analysis of the model identification results. In Section 6.3.1, the agreement between the identified models and the experimental results is investigated, and the identified parameter values are discussed. The validity of the identified parametric driver models in terms of predicting realistic driving behaviours is checked against experimental results and is justified via various ways including simulations of identification and coherence functions in Section 6.3.2. A deep

learning identification is conducted in Section 6.3.3 to investigate the parametric driver model structure error. A new driver noise model is proposed to make the spectrum of the driver noise predicted by the identified driver model match that found in the experiments with an identification procedure to find the new noise model parameters in Section 6.3.4.

6.3.1 Driver Model Fit

Various assumptions of the human driver's internal model of the real plant with the corresponding combination of state estimator and controller are proposed, as shown in Table 6.1. In Chapter 3, these different combinations were compared to each other through simulations. The simulation results show that the EKF and MPC method performs much better than the linear LQG framework. However, the computational time is sacrificed for the nonlinear driver model. The simulated results of the various driver models in Table 6.1 are compared with the experimental results simultaneously to investigate which one best describes the actual steering control behaviour of the human driver. In driver model M2, EKF1 and LMPC are chosen to save computational time as the simulation results in Chapter 3 show that the EKF1 and LMPC combination performs very similarly to the EKF2 and NMPC combination. Similar to Chapter 5, the 'variance accounted for' (VAF) is used to quantify the fit of a driver model to the experimental results. VAF values between the measured steering wheel angle and the simulated steering wheel angles of the identified driver models are plotted in Figure 6.1 for each driver and trial.

Figure 6.1 shows that the VAF values, especially those for driver model M2, are comparable to those achieved by the linear driver model in trial 3 in Chapter 5. This indicates that the proposed driver models can predict the measured driver steering behaviour well. To visualise the difference in the fit to the measured data between various identified driver models easily, the difference between the VAF value found for each driver model and that found for driver model M2 is plotted in Figure 6.2 for each driver and trial. Figure 6.2 shows that, overall, the VAF values for driver model M2 are the largest among the three proposed driver models, suggesting most drivers are able to capture the steering system friction characteristics in the experiments. However, the VAF values for the two linear driver models M0 and M1 are close to or even higher than those for driver model M2 when the friction level is relatively low, such as trials 4, 5, 8 and 9 for most drivers. This shows that the drivers might linearise the nonlinear steering system friction or even neglect the effect of friction and only used a linear internal mental model for the steering control task in those trials. In contrast, in trials 6, 7, 10 and 11, where the friction level is relatively high, the VAF values for driver model M2 are much larger than those for the linear driver models. This could be because that the effect of steering system friction was too significant to be compensated by a linear internal mental model in those trials so that the drivers had to learn the dynamics of the nonlinear friction as much as they could to follow the target path accurately. However, it is interesting to notice that for Drivers 2 and 5, the VAF values for the linear driver models are larger

than those for driver model M2 in most trials, and there is no significant difference in the performance between the various driver models even in trials where the highest VAF value is given by driver model M2. In addition, it is important to bear in mind that there is some uncertainty associated with the VAFs. Therefore, it cannot be confidently concluded which model best represents the actual driver when the VAF differences between the various driver models are small for some drivers and trials.

Identified values of the equivalent damping value $C_{sw}{}'$ of the steering system friction in driver model M1 for each driver and trial are shown in Figure 6.3. An obvious proportional relationship between the identified value of $C_{sw}{}'$ and the steering system friction is noticed, as expected. The identified values depend on the frequency bandwidth and the magnitude of the measured steering actions, which vary across drivers. Identified values of the path-following error cost q_e for each driver averaged over the eight trials and for each trial averaged over the thirteen drivers are shown in Figure 6.4. Although there is some variation in the identified values for different drivers and different trials, the orders of magnitude are quite consistent. The averaged identified value of q_e over all drivers and trials is around 7000.

Simulations are run for driver model M2 with EKF2 and NMPC by taking the identified values of q_e for each driver and trial combination. The simulated steering wheel angles and the corresponding VAF values are almost identical to those for driver model M2 with EKF1 and LMPC, suggesting that EKF1 and LMPC can approximate the full nonlinear state estimation and control. Another set of identification is conducted to search for the five parameter values for driver models M0 and M1, as mentioned in Section 6.2. There is some variation in the identified values for different trials for each driver. However, the VAF values are quite similar to those shown in Figure 6.1. This demonstrates that the fixed parameter values taken from the linear identification phase in Chapter 5 are appropriate for the nonlinear trials.

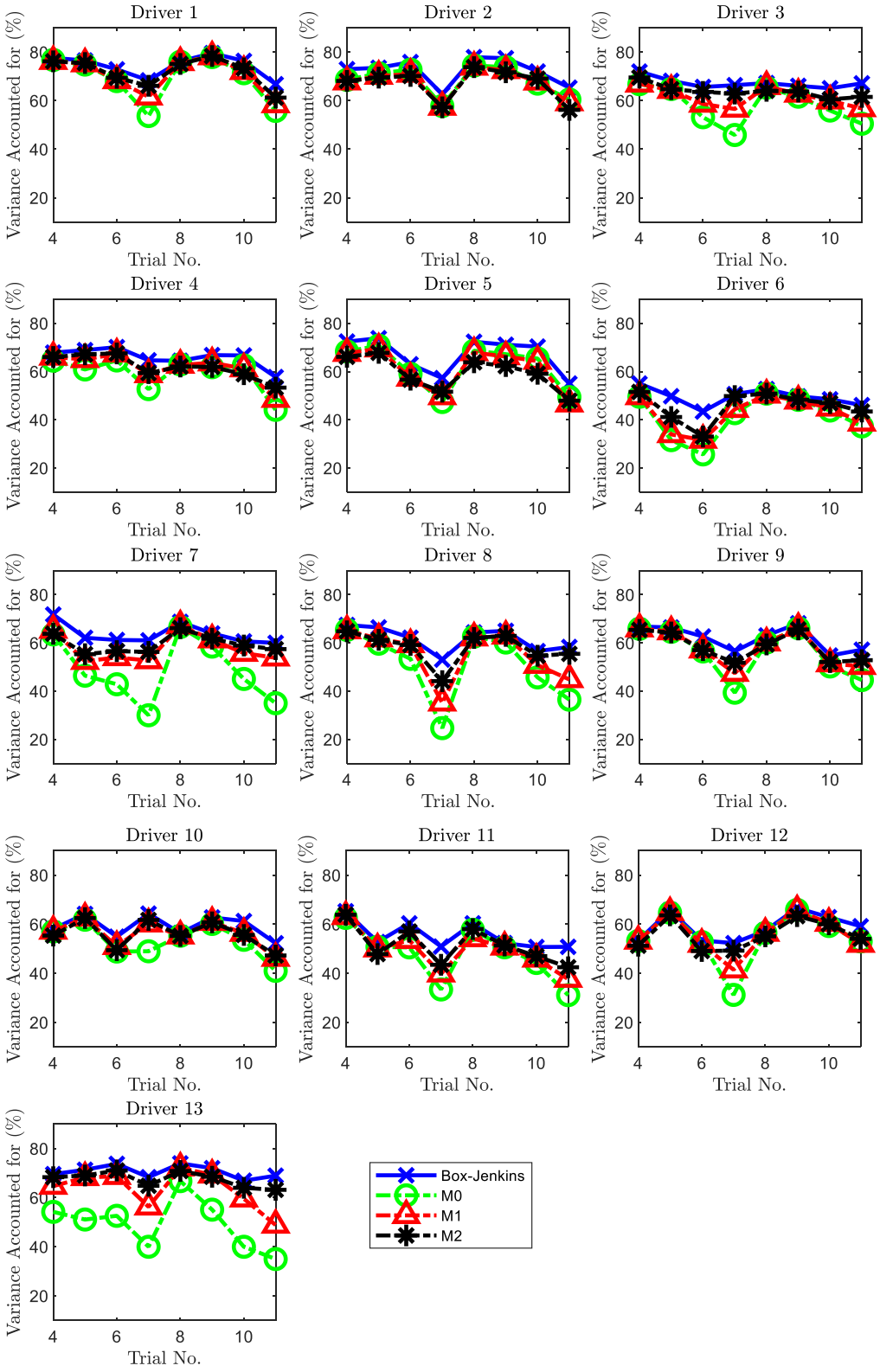

Figure 6.1: VAF values between the measured and modelled steering wheel angles for various driver models.

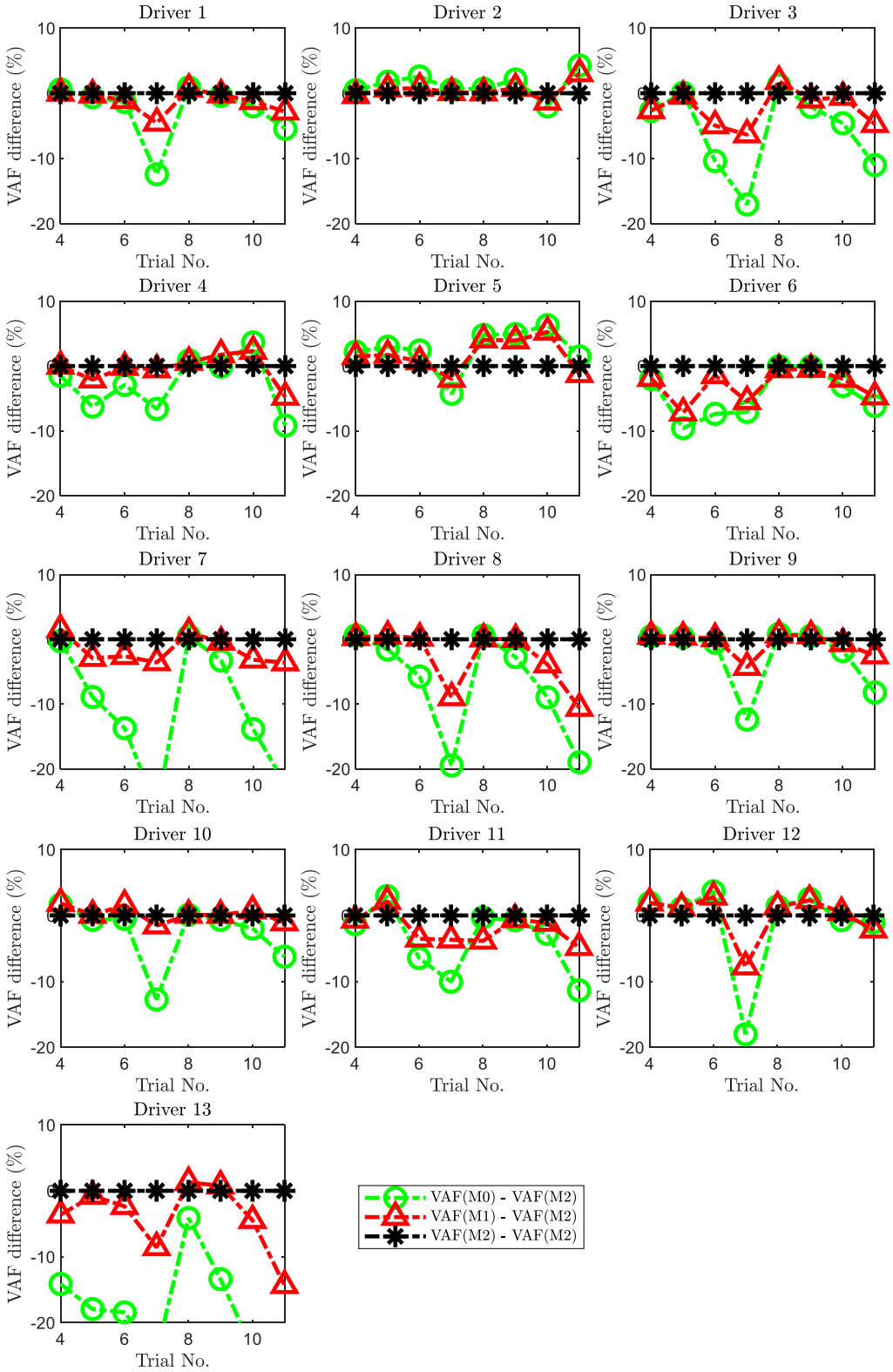

Figure 6.2: Difference between VAF values between the measured and modelled steering wheel angles with various driver models, and with driver model M2.

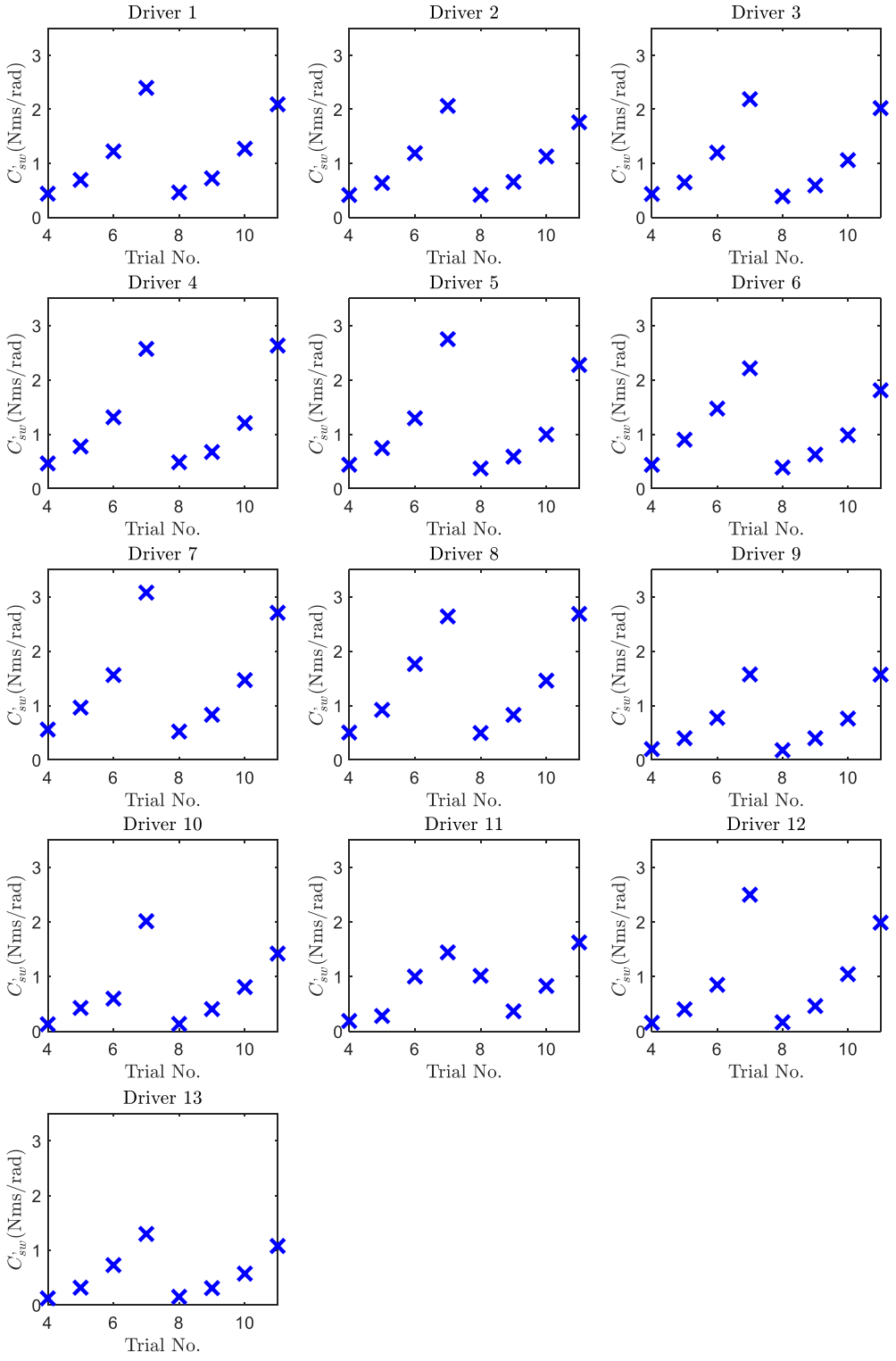

Figure 6.3: Identified equivalent damping value $C_{sw}{}'$ of the steering system friction in driver model M1 for each driver and trial.

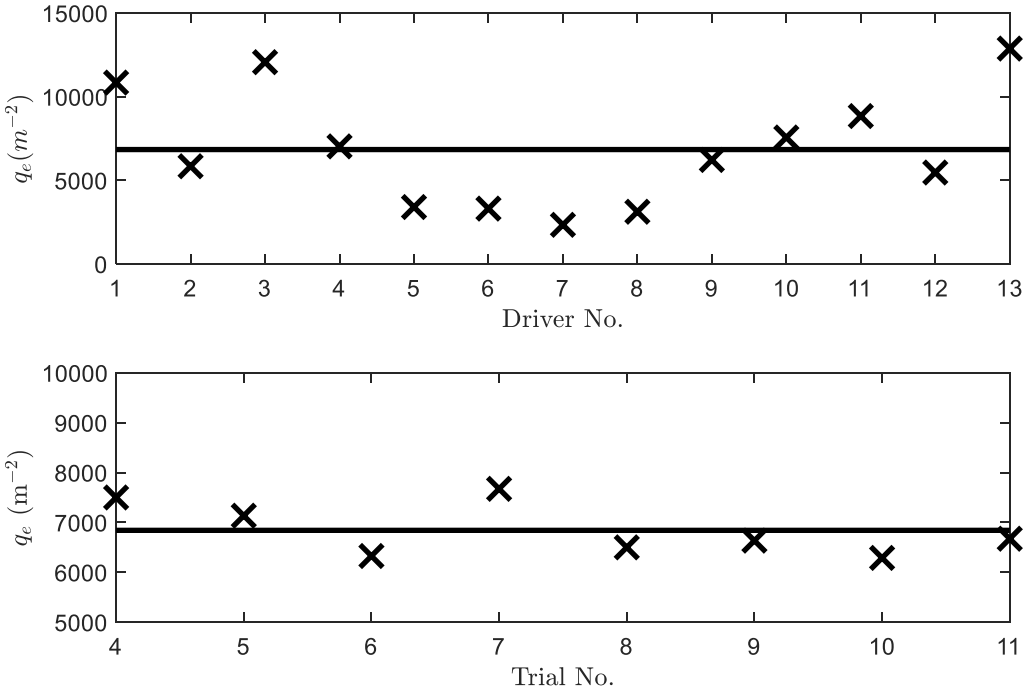

Figure 6.4: Identified values (crosses) of path-following error cost q_e for drivers averaged over all trials, and for trials averaged over all drivers. The average of the crosses is shown by the solid horizontal line in each subfigure.

6.3.2 Driver Model and Identification Validation

Switching the attention back to Figure 6.1, it is shown that the nonlinear driver model M2 does not give larger VAF values than the Box-Jenkins model even in trials with high friction levels. This could be because the steering system friction is a predictable source of disturbance that a human driver can compensate by additional muscle activation, and driver model M2 is able to successfully compensate the friction disturbance. Therefore, although the plant is nonlinear and the human driver's state estimator and control could exhibit nonlinear behaviour, the resulting driver-steering-vehicle response to random external disturbances would appear linear, and the VAF for the Box-Jenkins model would still be an upper bound on the VAF for driver model M2. To test this hypothesis, simulations of identification are conducted. Artificial steering wheel angles are created for each of the nonlinear trials using driver model M2 with the identified value of q_e for each driver. No process and measurement noise are added in the simulation, making all the steering actions be generated using the driver model. The identification is then conducted by fitting both the Box-Jenkins model and the driver-steering-vehicle model with driver model M2 to the artificial steering wheel angles, and the corresponding VAFs are recorded. For driver model M2, the VAFs will be 100%. The same simulation of identification procedure is also applied to driver models M0 and M1. The resulting VAF values between the artificial steering wheel angle and the simulated steering wheel angles of the known driver model and Box-

Jenkins model for Driver 1 are plotted in Figure 6.5 as examples, for each driver model. The results for the other drivers are similar to those for Driver 1. It is seen that the VAFs for the parametric driver models are 100%, as expected. The linear driver model M0 and M1 cause the VAF for the Box-Jenkins model to reduce, while the VAFs for the Box-Jenkins model are quite close to 100% in all trials generated by driver model M2. The results indicate that the nonlinear driver model M2 acts to fully linearise the closed-loop driver-steering-vehicle system, while the linear driver models M0 and M1 may also linearise the nonlinear steering dynamics to some extent.

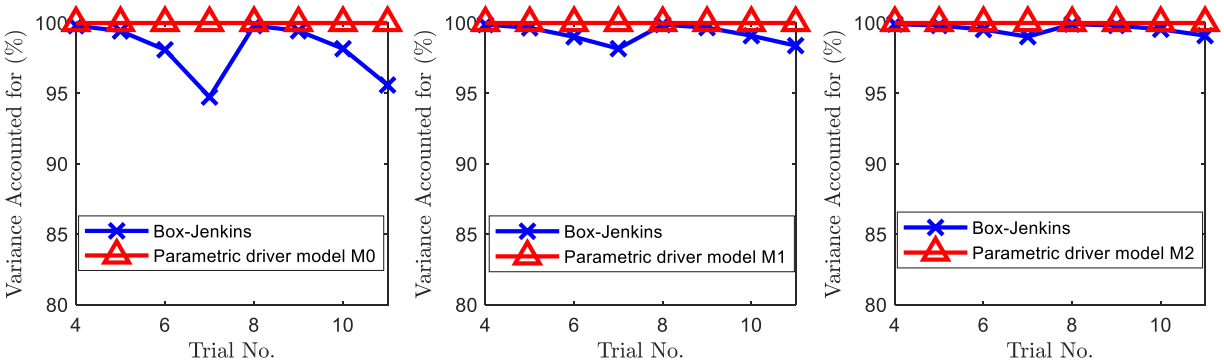

Figure 6.5: VAF values between the artificial and modelled steering wheel angles for Box-Jenkins model and the parametric driver models for Driver 1.

Moreover, the coherence function is used to quantify the linearity of the relationship between the artificial steering wheel angle and the randomly moving target path in a wide range of frequencies. A value of one across the frequency range implies there is no noise and no nonlinearity. Coherence functions relating the artificial steering wheel angles generated by the three identified parametric driver models and the randomly moving path for trial 11 with Driver 1 are plotted in Figure 6.6 as an example. The spectrum of the artificial steering wheel angles generated by each parametric driver model is also plotted in Figure 6.6. The results for the other drivers are similar to those for Driver 1. Figure 6.6 shows that the coherence function value for driver model M2 is very close to one, supporting the hypothesis that the nonlinear driver model M2 could fully linearise the nonlinear steering dynamics to make the closed-loop driver-steering-vehicle system response to external disturbances linear, at least at normal operating frequencies. In addition, the coherence function values for driver models M0 and M1 are slightly lower than for driver model M2. Again, this indicates that the linear driver models M0 and M1 may also linearise the nonlinear steering dynamics to some extent.

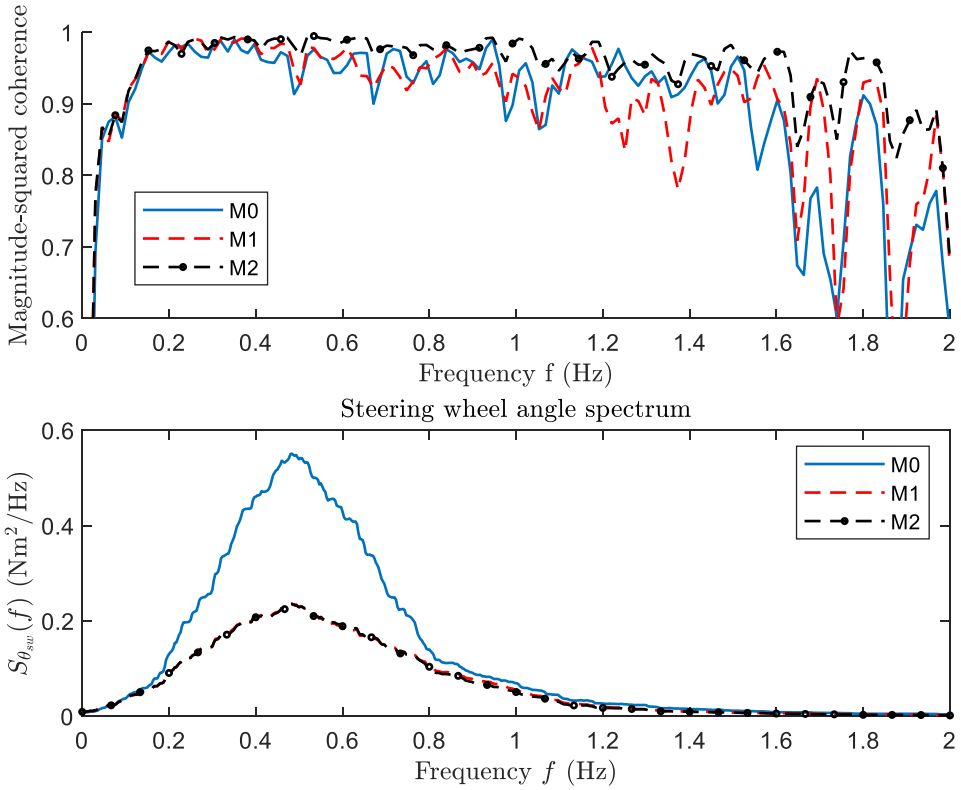

Figure 6.6: Coherence functions of the artificial steering wheel angles generated by the three identified parametric driver models and the randomly moving path for trial 11 with Driver 1, with spectrum of the artificial steering wheel angles.

Similar to Chapter 5, experimental measurements in the last minute are used to validate the identified models and check for over-fitting. The averaged VAF values calculated over all the eight nonlinear trials for each driver are presented in Figure 6.7 for each driver model. Overall, the VAF values in the validation data are similar to those in the identification data for all the identified models. However, some over-fitting may have occurred for several drivers, such as Drivers 4, 6 and 10. These may be due to the identified models fitting to some random variations and may also be because the drivers did not keep their control strategy constant in each trial.

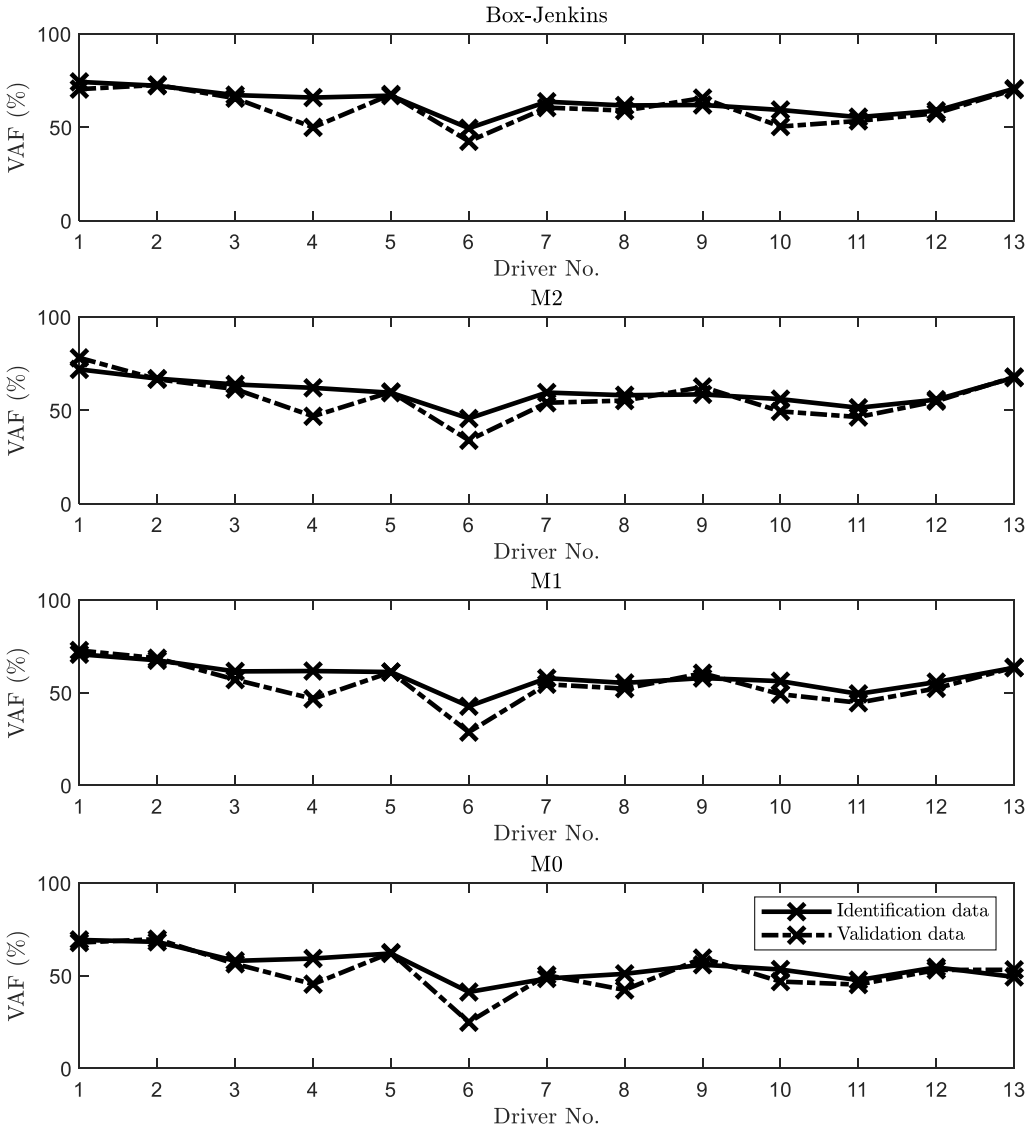

Figure 6.7: Validation of the identified models for each driver. Averaged VAF values over all the trials are compared. The VAFs obtained from the identification data are represented by the markers on the solid lines, while the VAFs obtained from the validation data are represented by the markers on the dashed lines.

6.3.3 Deep Learning Identification

The deep learning neural network, a data-driven Black Box modelling method, is an alternative to parametric-model methods for system identification [150] and can capture the underlying nonlinearity in the input-output relationship for complex systems according to Universal Approximation Theorem [151]. Recent studies [152] [153] [154] [155] show that Recurrent Neural Network (RNN) [156] [157],

a particular type of neural network emphasising the learning of features from a time sequence data, is an efficient modelling method to predict the time history response of dynamic systems as the system output is considered as a function of past values of system outputs, system inputs and prediction errors in this model. However, basic RNN could become unreliable for larger time sequences because the gradient of loss function will vanish gradually in the learning process so that the neural network cannot be optimised. Long Short-Term Memory (LSTM) [158], which is a complex form of basic RNN, addresses the vanishing gradient problem by adding additional components. The special memory states in LSTM allows the information from a given time step to be retained till the end of the time sequence. More about the explanation of the vanishing gradient issue and how LSTM avoids the problem is found in [158]. As a result, LSTM has been used to successfully identify the nonlinear dynamic system in [152] and [153], and Deep LSTM has been proved to be able to accurately predict dynamic system response in [154] and [155]. In this work, a Deep LSTM structure is used to fit the measured data to estimate the contribution of the driver's control behaviour to the measured steering actions. The identification results are compared with those from parametric model identification to investigate if there is any measured behaviour that is not captured by the identified parametric driver models, as the Deep LSTM gives an approximate upper bound limit of how well a model could be expected to fit. Figure 6.8 shows the architecture of Deep LSTM estimating the dynamic relationship between the model input randomly moving target lateral position r and the model output steering wheel angle θ_{sw}. The Deep LSTM structure includes a sequence input layer, multiple LSTM layers, fully connected layers, and a regression output layer.

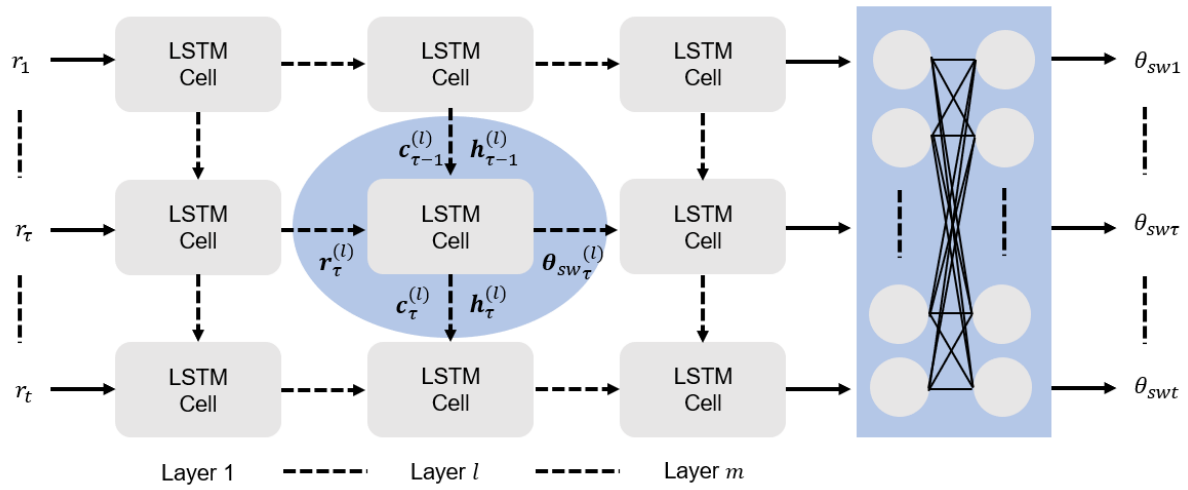

Figure 6.8: Schematic diagram of the Deep LSTM network mapping the model input randomly moving target lateral position r and the model output steering wheel angle θ_{sw} with m LSTM layers and fully connected layers.

The structure of each individual LSTM cell is shown in Figure 6.9. It comprises four units: a forget gate, an input gate, a tanh layer, and an output gate. The cell state retains the valuable information of the dynamic system carried by the time sequences with the help of the LSTM gates. Detailed explanations about how the gates work are found in [158].

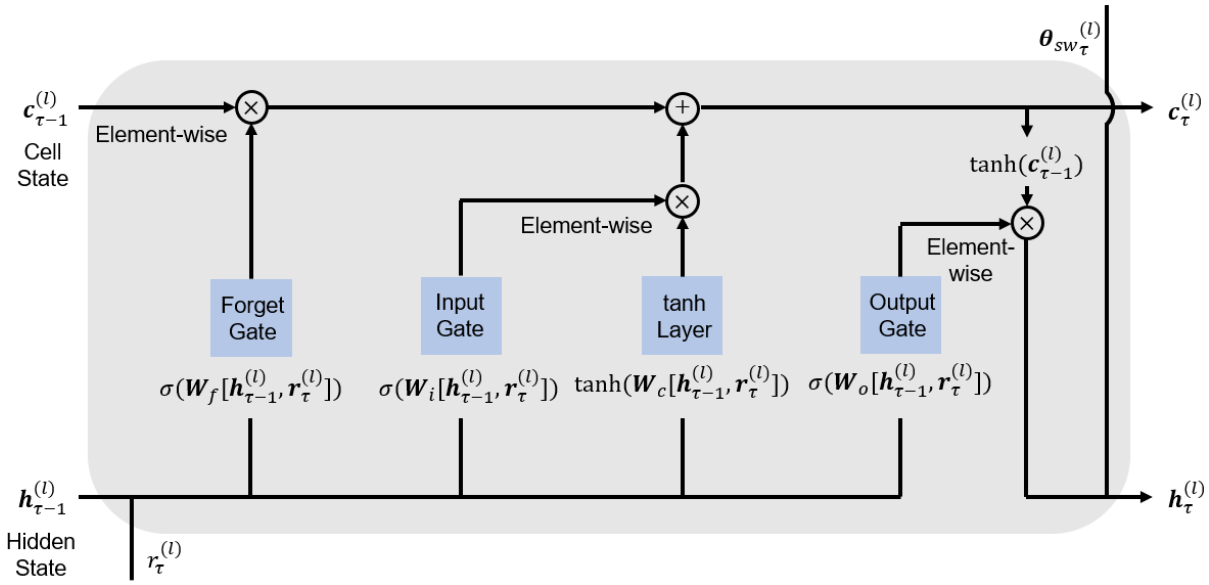

Figure 6.9: Schematic diagram of an individual cell of LSTM at layer l and time step τ, which depicts operations via the gates, cell state and hidden state.

The mathematical operations in the LSTM cell are as follows:

$$\boldsymbol{\Gamma}_f = \sigma\left(\boldsymbol{W}_{rf}^{(l)}\boldsymbol{r}_\tau^{(l)} + \boldsymbol{W}_{hf}^{(l)}\boldsymbol{h}_{\tau-1}^{(l)} + \boldsymbol{b}_f^{(l)}\right) \tag{6.5}$$

$$\boldsymbol{\Gamma}_i = \sigma\left(\boldsymbol{W}_{ri}^{(l)}\boldsymbol{r}_\tau^{(l)} + \boldsymbol{W}_{hi}^{(l)}\boldsymbol{h}_{\tau-1}^{(l)} + \boldsymbol{b}_i^{(l)}\right) \tag{6.6}$$

$$\boldsymbol{\Gamma}_o = \sigma\left(\boldsymbol{W}_{ro}^{(l)}\boldsymbol{r}_\tau^{(l)} + \boldsymbol{W}_{ho}^{(l)}\boldsymbol{h}_{\tau-1}^{(l)} + \boldsymbol{b}_o^{(l)}\right) \tag{6.7}$$

$$\tilde{\boldsymbol{c}}_\tau^{(l)} = \tanh\left(\boldsymbol{W}_{rc}^{(l)}\boldsymbol{r}_\tau^{(l)} + \boldsymbol{W}_{hc}^{(l)}\boldsymbol{h}_{\tau-1}^{(l)} + \boldsymbol{b}_c^{(l)}\right) \tag{6.8}$$

$$\boldsymbol{c}_\tau^{(l)} = \boldsymbol{\Gamma}_i * \tilde{\boldsymbol{c}}_\tau^{(l)} + \boldsymbol{\Gamma}_f * \boldsymbol{c}_{\tau-1}^{(l)} \tag{6.9}$$

$$\boldsymbol{h}_\tau^{(l)} = \boldsymbol{\Gamma}_o * \tanh\left(\boldsymbol{c}_\tau^{(l)}\right) \tag{6.10}$$

where $\boldsymbol{W}_{\alpha\beta}^{(l)}$ (with $\alpha = \{r, h\}$, $\beta = \{f, i, o, c\}$) denotes weightings on the corresponding states, $\boldsymbol{b}_\beta$ denotes bias vectors added to the functions, $*$ denotes element-wise multiplication, and σ denotes sigmoid function.

Hyperparameters including variables which determine the Deep LSTM network structure such as number of units (dimension of the hidden state) and number of layers, and variables which determine the training of the network such as the learning rate need to be tuned to prevent over-fitting and under-fitting while ensuring efficient computation in the training progress. In this study, a 7-layer Deep LSTM network with 300 units in each layer has been found to be able to represent the driver-steering-vehicle system dynamics well based on the results of preliminary simulations. The learning rate is set to 0.01 and the 'Adam' algorithm is chosen for the optimisation considering the complexity of the system to be identified. The 'Adam' algorithm, which combines the advantages of 'gradient descent with momentum' and 'RMSprop' algorithms, has been demonstrated to be able to produce the best optimisation results [159]. Similar to the Box-Jenkins identification and the parametric model identification, data in the last minute is used to validate the identified Deep LSTM model and to check for over-fitting and under-fitting, and VAF is used to quantify the fit of the model to the experimental results. The maximum number of epochs for the training is set to 600, and the model at the epoch where the VAF for the validation data is the maximum is selected.

Simulations of identification are conducted to test the capability of the Deep LSTM model to capture the target lateral position to steering wheel angle relationship if any nonlinearity does exist. Artificial steering wheel angles are created for each of the nonlinear trials using driver model M0 with the identified value of q_e for each driver without noise. The linear driver model M0 is chosen so that the closed-loop driver-steering-vehicle system still behave nonlinearly. Different from the artificial steering wheel angles generated using the same identified driver model M0 in Section 6.3.2, the bandwidth and the magnitude of the randomly moving target path input are adjusted to increase the proportion of nonlinearity in the data. The identification is then conducted by fitting both the Box-Jenkins and the Deep LSTM models to the artificial steering wheel angles, and the corresponding VAFs are recorded. The resulting VAF values between the artificial steering wheel angle and the simulated steering wheel angles of the Deep LSTM model and Box-Jenkins model for all the nonlinear trials with Driver 1 are plotted in Figure 6.10 as examples. The VAFs for the Box-Jenkins model drop with the increase in friction level, indicating an increasing trend of the contribution of nonlinear behaviour to the artificially generated steering actions. In contrast, the VAFs for the Deep LSTM model reach about 98% for all the trials for both the training data set and validation data set. This suggests that the Deep LSTM model is able to capture and predict the nonlinear relationship.

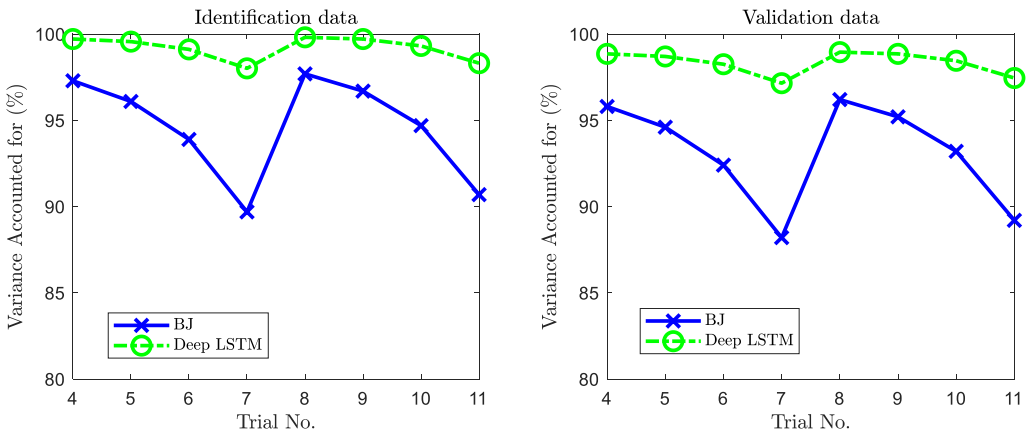

Figure 6.10: VAF values between the artificial and modelled steering wheel angles for Box-Jenkins model and Deep LSTM model for Driver 1.

Figure 6.11 compares the VAF for the Deep LSTM model with the highest VAF achieved by the previously identified models, either the Box-Jenkins model or the parametric driver models, for the validation data for each driver and trial. It is seen that VAFs are the largest for the Deep LSTM model, which is expected as the Deep LSTM model effectively gives an upper bound limit on the proportion of the steering wheel angle data that a model can predict. However, the maximum values of the VAFs for the other models are quite close or even equal to the VAFs for the Deep LSTM model. This indicates that the parametric driver models can explain the drivers' steering control of a vehicle with nonlinear steering friction quite well. However, there could be some driver control randomness that cannot be captured by the Deep LSTM model or the parametric driver-steering-vehicle model other than noise. For example, Johns and Cole [160] found that human drivers may use an intermittent control strategy, where they only apply control actions when some of the signals they perceived have exceeded a threshold, which may vary randomly during the driving. For simplicity, continuous driving is assumed and any characteristic that cannot be fitted by the Deep LSTM model is regarded as random noise in this study.

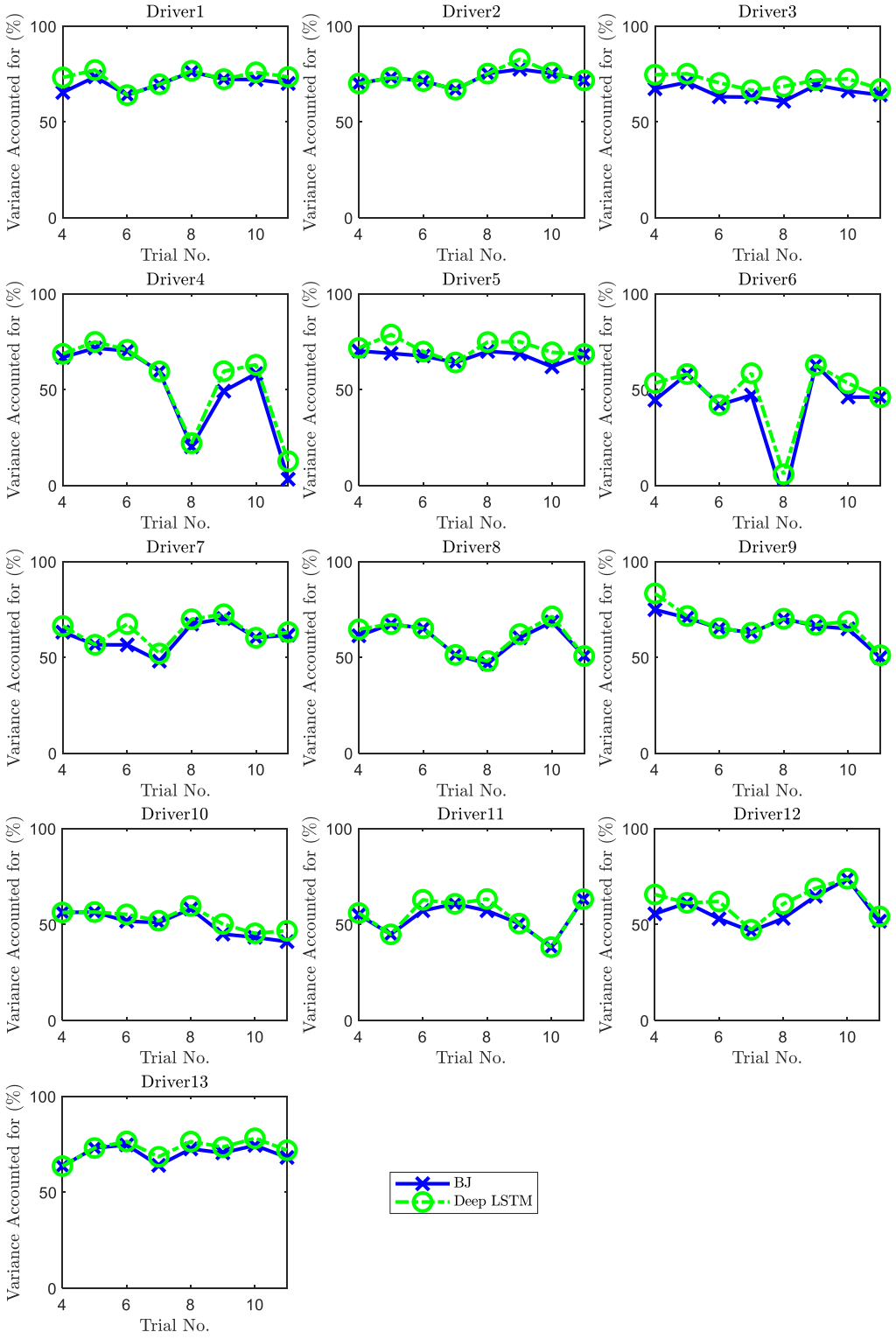

Figure 6.11: VAF values between the measured and modelled steering wheel angles for Box-Jenkins model and Deep LSTM model.

6.3.4 Measured and Modelled Driver Noise

Figure 6.1 shows that there is some variation in VAFs between different trials for each driver, and a decreasing trend is identified with the increase of friction level for most of the drivers. The deep learning identification results presented in Section 6.3.3 suggest that the parametric model error is small. Therefore, the variation in VAFs is predominantly due to the driver process noise because the effect of measurement noise is significantly reduced by the state estimator, as mentioned in Chapter 5. In this case, the driver process noise reflected in the steering wheel angle comes from the process noise added on the neural activation signal. The neural activation signal is processed by the neuromuscular dynamics and steering system dynamics, which varies with the steering system friction level. Therefore, the effect of the driver process noise on the variation in VAFs could be either due to the signal-to-noise ratio SNR_W being not constant cross different trials, or due to variation in the system dynamics for different trials with a relatively constant SNR_W. To investigate which one is the root cause of the variation in the experimental noise level, simulated driver noise referred to the steering wheel angle $w_{sw(sim)}$ is generated and compared with the experimental noise $\left(\theta_{sw(exp)} - \theta_{sw(sim)}\right)$. The identified driver model M2 is used in the simulations as it gives the highest VAF overall.

In order to have reliable simulations results, a deeper understanding of the driver's noise characteristics needs to be obtained. Figure 6.12 compares the spectrum of the experimental noise $\left(\theta_{sw(exp)}(s) - \theta_{sw(sim)}(s)\right)$ and with the spectrum predicted by the model $w_{sw(sim)}(s)$ with Gaussian white process noise added to the neural activation signal. Even though the RMS noise level on the steering wheel angle is similar in the simulation and the experiment, the modelled noise contains more high-frequency components while the experimental noise contains more low-frequency components. This suggests that the assumption of white process and measurement noise may be invalid, which was also noticed by Nash [126]. In order to have a realistic simulated driver's noise signal, the process noise model is revised based on the assumption that the noise spectrum should be similar in shape to the corresponding signal. Therefore, the Gaussian white process noise is processed by a filter H_{fw} before applied to the neural activation signal, as shown in Figure 6.13. The noise filter H_{fw} is defined as a combination of a second-order low-pass filter with a cut-off frequency f_{wl} and a second-order high-pass filter with a cut-off frequency f_{wh}:

$$H_{fw}(s) = \left(\frac{s}{s + f_{wh}}\right)^2 \left(\frac{f_{wl}}{s + f_{wl}}\right)^2 \tag{6.11}$$

For simplicity, this filter is not included in the human driver's internal mental model.

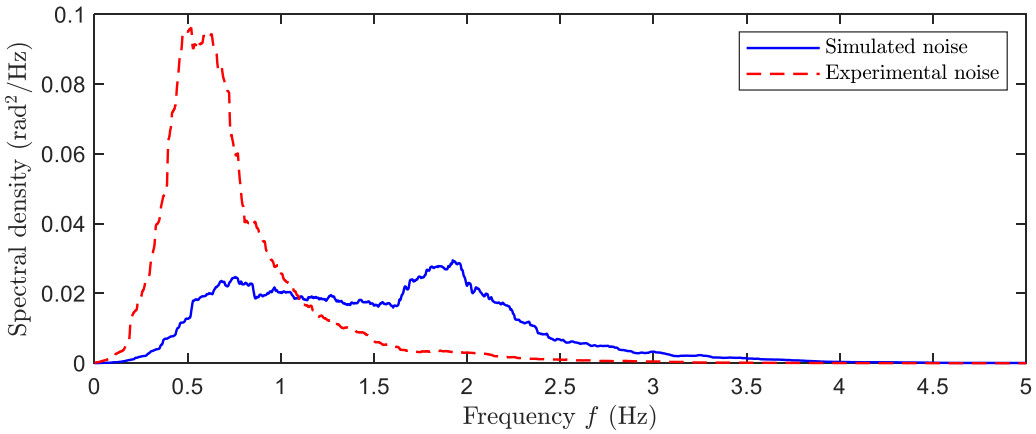

Figure 6.12: Spectrum of the driver noise referred to the steering wheel angle θ_{sw}, as found in the experiment and as predicted by the model for trial 4 with Driver 1, using the SNR_W obtained in the linear identification phase described in Chapter 5.

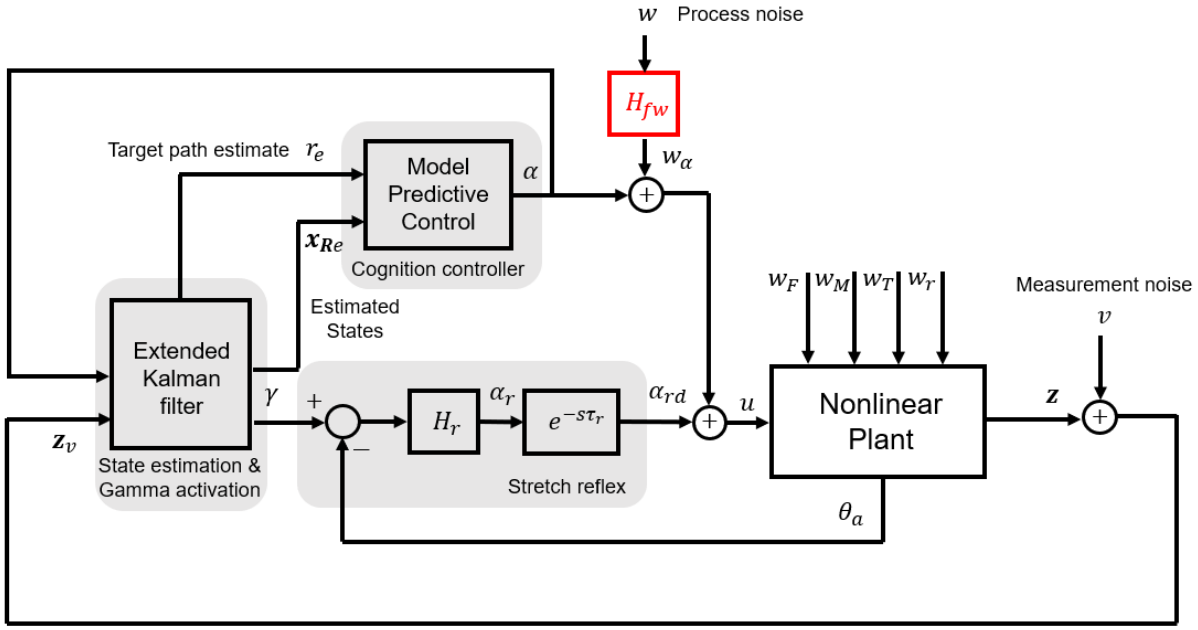

Figure 6.13: Schematic diagram of the nonlinear driver-steering-vehicle model with process noise filter H_{fw}.

There are three parameter values to be determined in the new process noise model: the white noise amplitude $\mathrm{RMS}(w)$, and cut-off frequencies f_{wl} and f_{wh} of the filter H_{fw}. An identification procedure is developed to find the values of these three parameters to make the spectrum of the filtered white noise w_α be similar to the spectrum of neural activation signal α in shape while ensuring the effect of the filtered white noise w_α is equivalent to that of the originally assumed white process noise w, the standard deviation of which is equal to the Kalman filter parameter W. The identification is conducted in several steps for each driver and trial combination separately:

1. The simulated neural activation signal α_{sim} is generated first by running a noise-free simulation of the identified driver-steering-vehicle model for the use of identification.
2. The spectrum of the simulated filtered process noise $w_{\alpha(sim)}(s)$ can be compared with the simulated neural activation signal $\alpha_{sim}(s)$ and the difference $\left(\alpha_{sim}(s) - w_{\alpha(sim)}(s)\right)$ is minimised to find the three parameter values simultaneously. This gives the simulated filtered white noise spectrum approximately the same as the simulated neural activation signal.
3. The values of cut-off frequencies f_{wl} and f_{wh} are then fixed. However, the value of RMS(w) needs to be adjusted because it is desirable for the steering wheel angle noise amplitude predicted by the model to match the noise amplitude found in the experiment. A process signal-to-noise ratio SNR_W has been determined for each driver to achieve this goal in Chapter 5 and been used in the nonlinear phase identification procedure, as described in Section 6.2.2. However, the previously determined SNR_W value for each driver needs to be adjusted as the noise model structure has been modified. The new value of SNR_W for each driver is determined using the linear trial 3 in several steps:
    a. Simulated driver noise referred to the steering wheel angle $w_{sw(sim)}$ is generated by using the identified linear driver-steering-vehicle model in Chapter 5 with the additional process noise filter H_{fw} identified in step 2 with process noise w only, where the amplitude RMS(w) = the identified value of W in the Kalman filter in trial 3.
    b. The simulated noise amplitude RMS$\left(w_{sw(sim)}\right)$ for trial 3 is calculated.
    c. The white noise amplitude RMS(w) for trial 3 is then scaled by using the ratio: the experimental noise amplitude RMS$\left(\theta_{sw(exp)}(s) - \theta_{sw(sim)}(s)\right)$ to the simulated noise amplitude RMS$\left(w_{sw(sim)}\right)$.
    d. The new value of SNR_W is defined as the ratio of the scaled white noise amplitude RMS(w) for trial 3 to the experimental muscle activation torque amplitude $T_{a(exp)}$, which is estimated using the procedure described in Section 5.3.3.

    The value of RMS(w) for each driver and trial is then calculated by:

$$\frac{\text{RMS}\left(T_{a(exp)}\right)}{\text{the new value of SNR}_W} \tag{6.12}$$

Figure 6.14 compares the spectrum of the filtered white noise $w_{\alpha(sim)}(s)$ generated using the identified parameter values in step 2 with the spectrum of the simulated neural activation signal $\alpha_{sim}(s)$. It is shown that the two spectrums match each other well, demonstrating the ability of the new noise model to replicate more realistic driver noise characteristics.

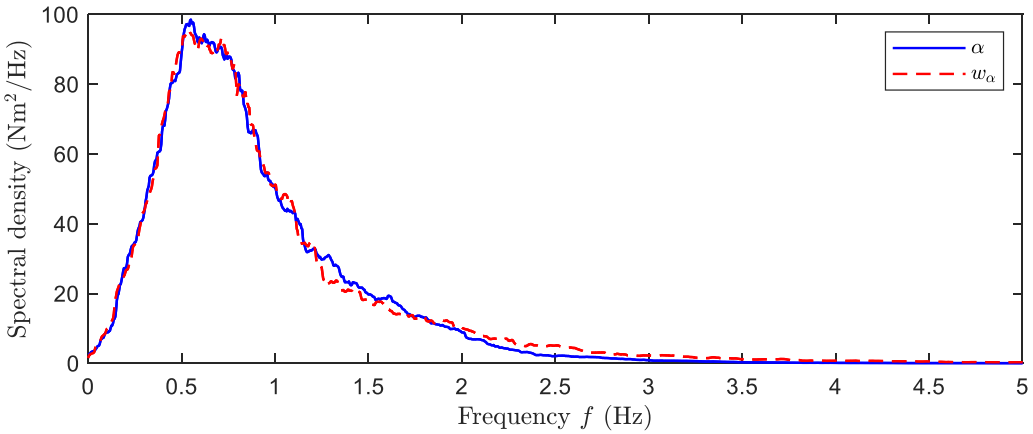

Figure 6.14: Spectrum of neural activation signal α predicted by the identified driver model M2, and the spectrum of filtered white noise w_α in step 2 for trial 4 with Driver 1.

Figure 6.15 compares the spectrum of the experimental noise $\left(\theta_{sw(exp)}(s) - \theta_{sw(sim)}(s)\right)$ with the spectrum predicted by the driver-steering-vehicle model $w_{sw(sim)}(s)$ with the modified noise model. The spectrums are similar in shape to each other. However, there is some discrepancy in the amplitudes, which suggests that the value of SNR_W might be affected by the steering system friction level.

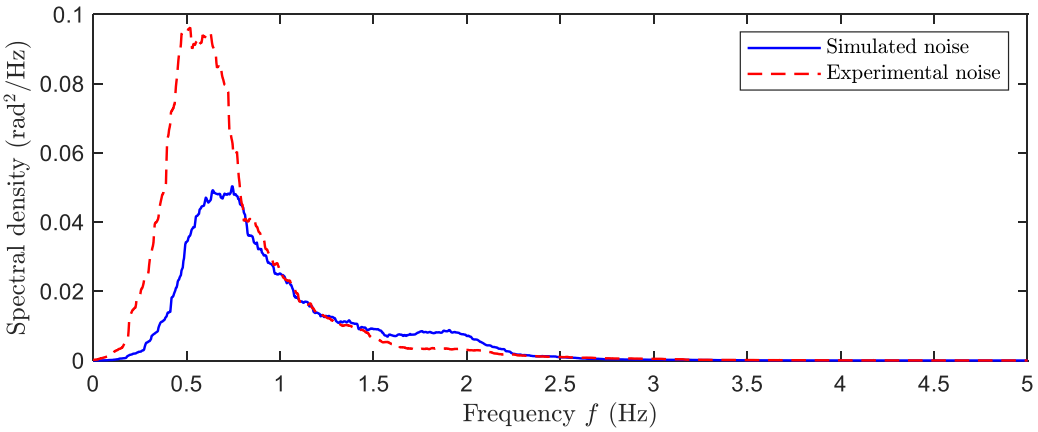

Figure 6.15: Spectrum of the driver noise referred to the steering wheel angle θ_{sw}, as found in the experiment and as predicted by the identified driver model M2 for trial 4 with Driver 1, using the modified noise model.

To further investigate how the VAF would vary between trials with a constant SNR_W, another set of simulations of identification is conducted. Artificial steering wheel angles are generated for each of the nonlinear trials using the identified driver model M2 for each driver. Filtered process white noise is added with the identified noise model parameter values. The identification of driver model M2 is run for the artificial steering wheel angles for each driver and trial. The resulting VAF is compared with the

corresponding VAF of driver model M2 fitting the actual experimental data, as shown in Figure 6.16. The discrepancy between the VAF values indicates that the values of SNR_W in the nonlinear trials are not always equal to that in the linear trials.

For easier comparison, the difference in VAF between the two sets of identification results is plotted in Figure 6.17 for each driver and trial. An apparent increasing trend in the VAF difference is noticed with the increase of steering system friction level. This suggests that the drivers had more process noise when there is more friction in the steering system. This might be because that the existence of friction prevents the actual system dynamics from being learnt by the drivers and therefore results in confusion in drivers' mind, which is also captured by process noise in the parametric model.

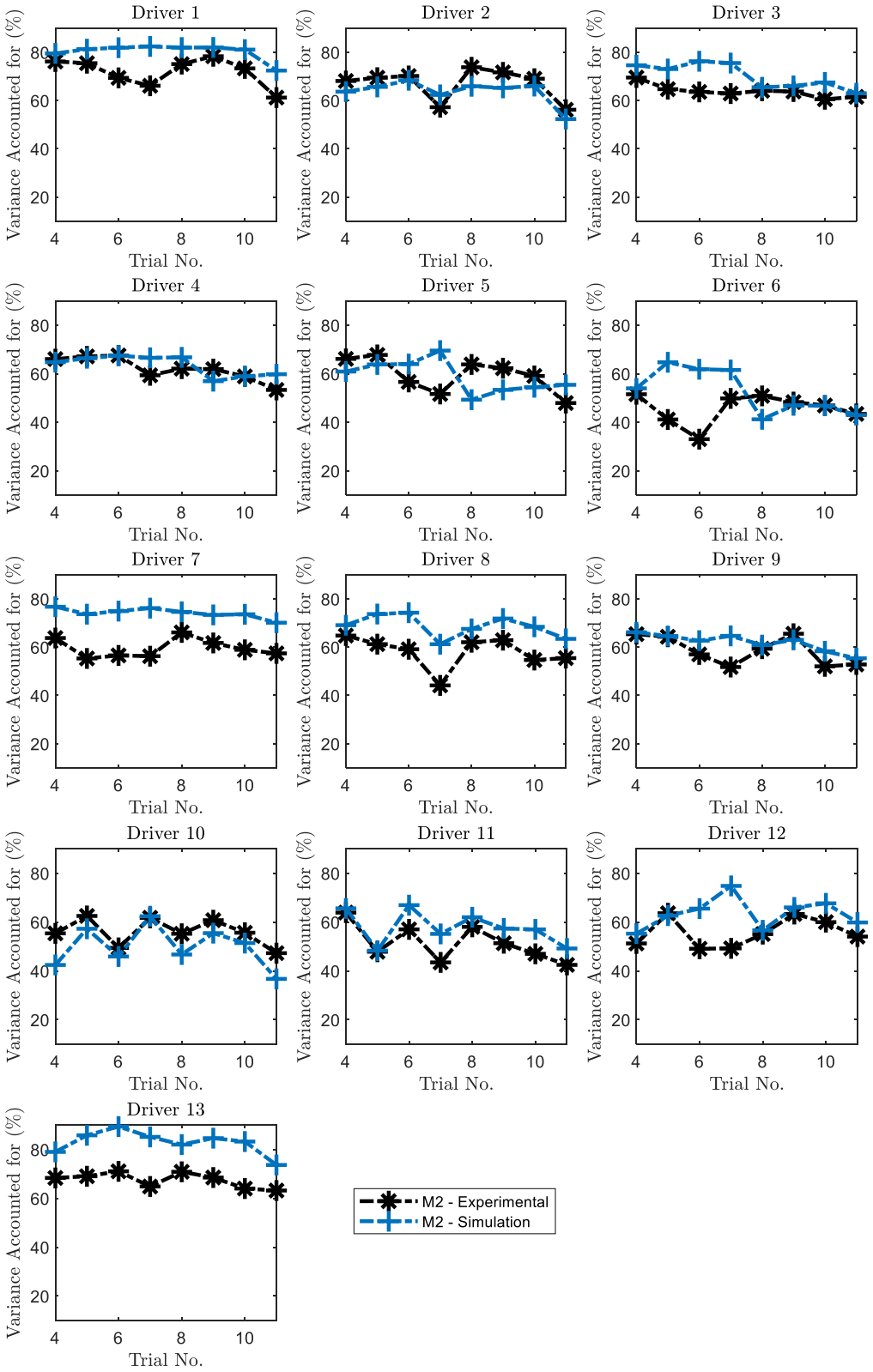

Figure 6.16: VAF values between the measured and modelled steering wheel angles for driver model M2, and VAF values between the artificially generated and modelled steering wheel angles for driver model M2.

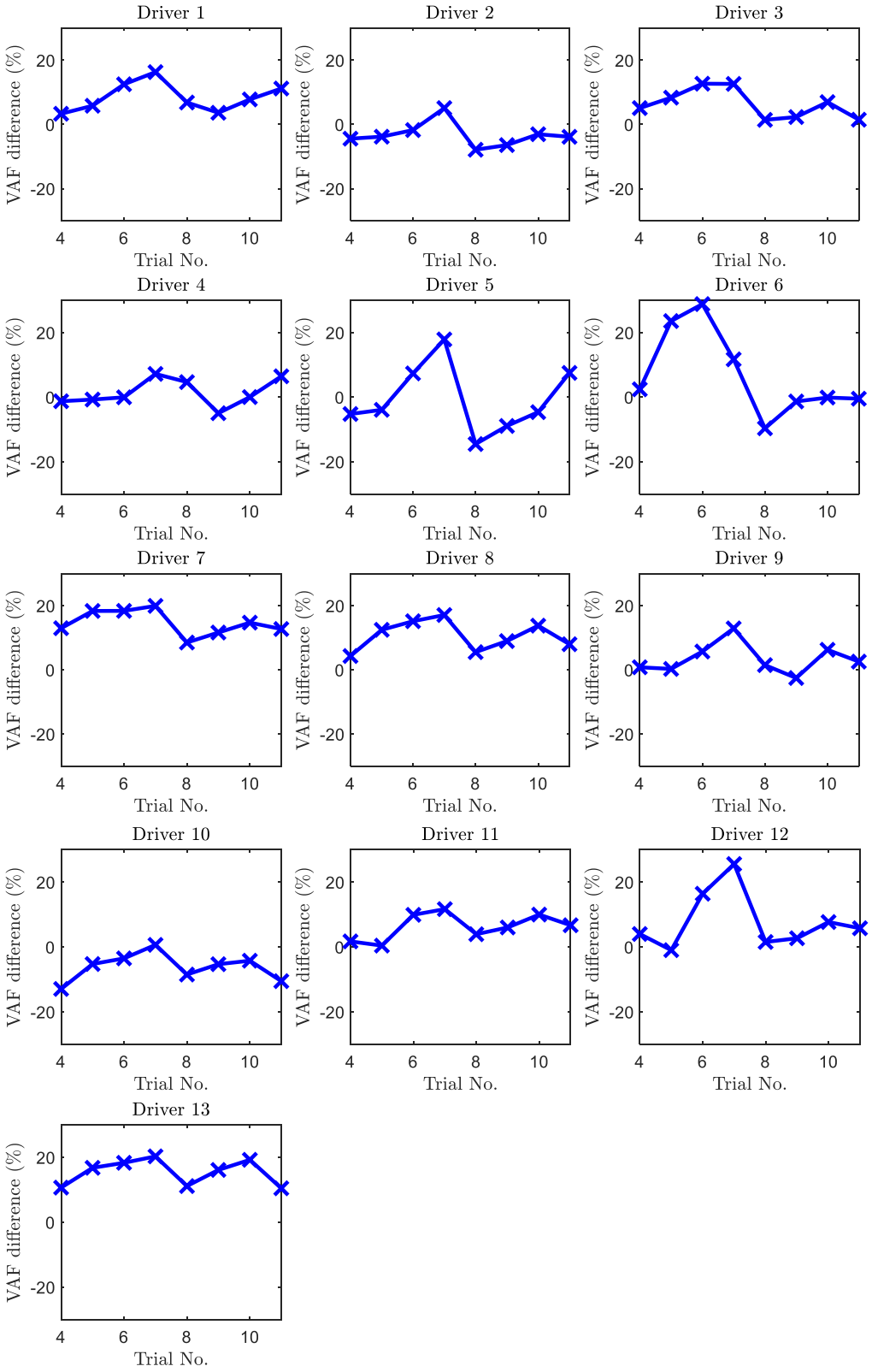

Figure 6.17: Difference between VAF values between the measured and modelled steering wheel angles with driver model M2, and between the artificially generated and modelled steering wheel angles for driver model M2.

6.4 Correlation between the Model and Subjective Assessment

In previous sections, the new parametric driver model structure is found to fit the experimental results from the nonlinear trials well, which has been justified by a comprehensive analysis of the identification results. In this section, the correlation between the parametric driver model and the human driver's subjective assessment of steering feel is explored through a series of simulations. To allow reliable simulations to be carried out, a rigorous method with multiple steps is developed by taking account of the variation in process noise signal-to-noise ratio in trials with different levels of steering system friction, as described in Section 6.4.1. The correlation results are presented in Section 6.4.2. These results highlight the potential of using the new parametric driver model structure to explain and predict the human driver's subjective responses to steering feel.

6.4.1 Simulation Techniques

Simulation is run by using the identified parametric driver model giving the highest VAF for each driver and trial with process noise, the standard deviation of which should be equal to the corresponding value of the noise parameter W in the state estimator, which can be determined by the value of RMS muscle activation torque T_a and the identified process noise signal-to-noise ratio SNR_W. However, it has been found in Section 6.3.4 that setting the value of SNR_W constant for all the nonlinear trials is not appropriate, and Gaussian white noise cannot represent the characteristics of a real driver's noise. Therefore, a modification to the identified parametric driver model is conducted through several steps to allow reliable simulation results to be collected:

- First, it is necessary for the noise amplitude predicted by the model $\mathrm{RMS}(w_{sw(sim)})$ to match the noise amplitude found in the experiment $\mathrm{RMS}(\theta_{sw(exp)} - \theta_{sw(sim)})$. Therefore, the value of process noise signal-to-noise SNR_W is scaled by using the ratio of the measured to modelled noise amplitudes and is used to update the value of the noise parameter W in the state estimator. This step is repeated iteratively until this ratio is almost equal to one.
- Second, it is also desirable for the spectrum of the noise predicted by the model $w_{sw(sim)}(s)$ to match the spectrum of noise found in the experiment $(\theta_{sw(exp)}(s) - \theta_{sw(sim)}(s))$. Therefore, the Gaussian white noise only process noise model is replaced by the new process noise model proposed in Section 6.3.4 and the three parameter values in the new noise model are found following the proposed identification method in that section. Different to the identification procedure described in Section 6.3.4, the white noise amplitude $\mathrm{RMS}(\mathrm{w})$ is found by matching the noise level in the trial itself, not in trial 3, in step 3 of the identification.

6.4.2 Correlation Results

As mentioned in Chapter 4, the subjective questions answered by the drivers can be divided into two categories, one is called estimation: judging the magnitude of an objective metric, and the other is called evaluation: assessing the properties of the steering-vehicle system based on purely subjective experience. Similar to Section 4.6.4 in Chapter 4, the normalised subjective ratings on most of the estimation questions are compared with the values of the corresponding test drivers' estimated objective metrics from simulations through linear regression, as shown in Figure 6.18. The shaded area in each plot is the 95% confidence interval for the mean values of the normalised subjective ratings based on the assumption of t-distribution. There are three linear regression lines for each group of trials in each plot: the solid line represents the linear regression of mean values of the ratings, and the dashed lines represent the borders of the 95% confidence area. The absolute value of the correlation coefficient $|r|$ for each linear regression line is also shown in Figure 6.18. The definitions of the objective metrics are similar to those defined in Section 4.6.4 in Chapter 4. However, the signals estimated by the state estimator from simulations are used instead of the signals measured in the experiments. In addition, the value of RMS steering torque is replaced by the value of RMS muscle activation torque in the calculation of steering resistance level and nonlinear torque ratio.

Overall, the normalised subjective ratings provided by the drivers correlate well with the values of the corresponding test drivers' estimated objective metrics from simulations, with six values of the absolute value of the correlation coefficient $|r|$ larger than 0.9 and three values between 0.8 to 0.9. The correlation results are comparable with those in Section 4.6.4, suggesting that the parametric driver model can reproduce the test drivers' steering behaviour. These results also show the capability of the parametric driver model structure to reflect the test drivers' subjective responses to the estimation questions. It is shown that the estimated yaw gain correlates with the rating of yaw gain inversely for trials 3 and 8 to 11. However, the range of the distribution for the ratings of yaw gain is quite small. Taking this into account, this correlation result is plausible.

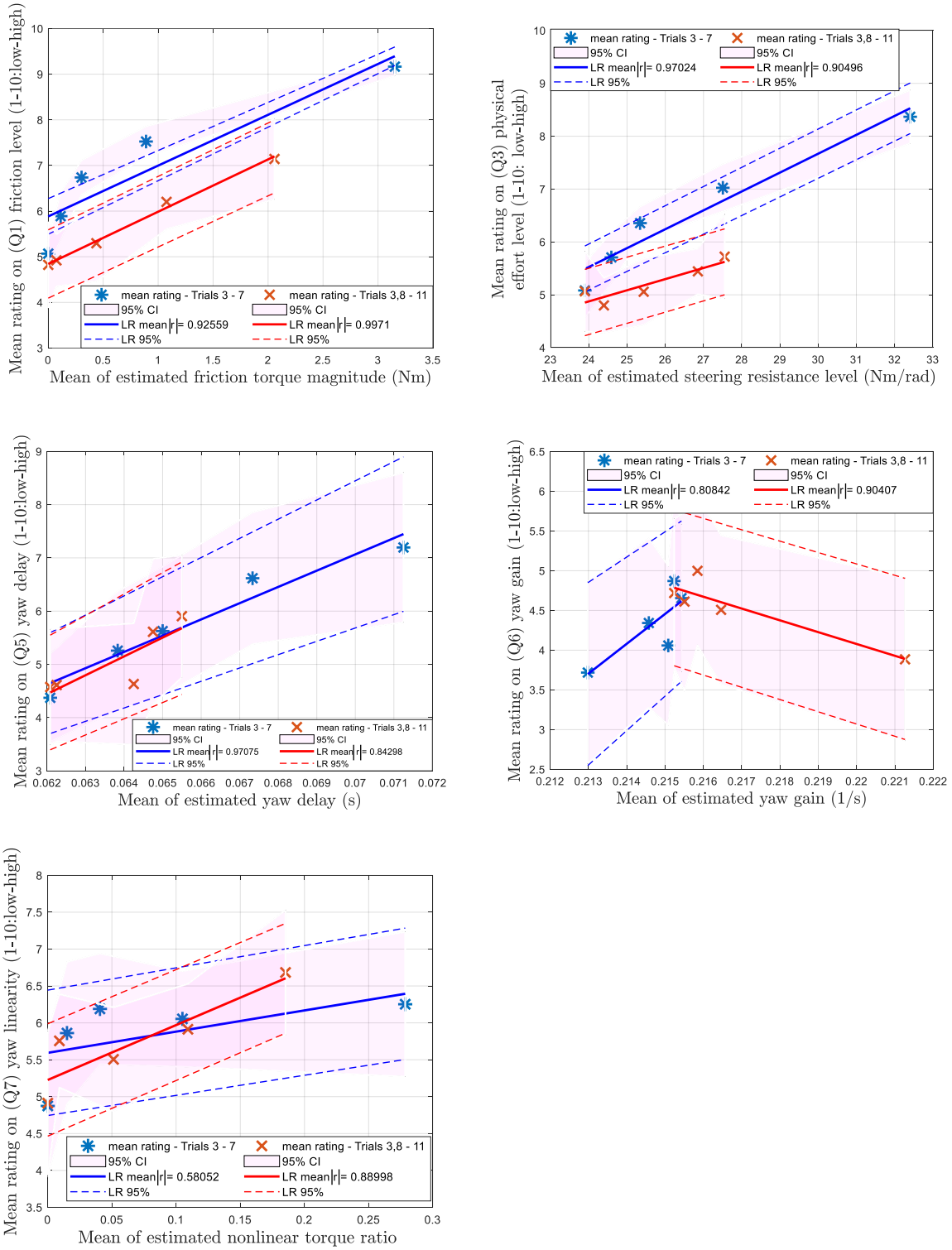

Figure 6.18: Correlations between normalised subjective ratings and simulated human drivers' estimated objective metrices with the correlation coefficients. The shaded area represents the 95% confidence interval(CI) for the mean values of the normalised subjective ratings. The solid line represents the linear regression(LR) of mean values of the ratings and the dashed lines represent the borders of the 95% confidence area.

It is hypothesised that the human driver's subjective rating of steering feel is related to the driver's ability to predict the steering torque feedback using an internal mental model and the known control input. To test this hypothesis, the normalised subjective ratings on the three evaluation questions are compared with the state estimator prediction error $\boldsymbol{z}(k) + \boldsymbol{v}(k) - \mathbf{C}\boldsymbol{x}_e(k|k-1)$, which represents the discrepancy between the predicted and the measured sensory feedback, from simulations. Again, the linear regression method is used, and the resulting absolute values of the correlation coefficient for trials 3 to 7 and trials 3 and 8 to 11 are summarised in Table 6.2 and Table 6.3, respectively. The average of all the correlation coefficients in the two tables is 0.9127. The large correlation coefficients suggest that the test drivers' subjective evaluation of steering feel correlates well with state estimator prediction error. Figure 6.19 illustrates the correlations for Q9 as an example. In general, the subjective evaluation is perceived as worse with an increase in state estimator prediction error, which is a combined effect of increased internal mental model inaccuracy and increased driver noise level. However, the test drivers gave the highest ratings in trials with a small non-zero steering system friction. As explained in Chapter 4, this could be because the test drivers perceived the steering-vehicle system as more stable compared with trial 3 as the small amount of steering system friction provides the essential damping effect to stabilise the system. To check this, the step response of the steering-vehicle system with the equivalent damping value C'_{sw} of the steering system friction shown in Figure 6.3 is plotted for each trial in Figure 6.20. The system is clearly shown to be less stable in trial 3 than in the other trials, evidenced by the larger overshoot and longer settling time for trial 3.

Table 6.2: Absolute values of correlation coefficient of evaluation subjective questions vs. state estimator prediction error for trials 3 to 7

Simulated signal	**Q2 (how easy is it to follow the path)**	**Q8 (how connected does it feel)**	**Q9 (how helpful is the steering torque feedback)**
State estimator prediction error for $e(k - N_{vi})$	0.8400	0.7852	0.7727
State estimator prediction error for $\psi(k - N_{vi})$	0.9751	0.9455	0.9841
State estimator prediction error for $\theta_a(k - N_{v\theta_a})$	0.9440	0.9624	0.9262

Table 6.3: Absolute values of correlation coefficient of evaluation subjective questions vs. state estimator prediction error for trials 3 and 8 to 11

Objective metrics	Q2 (how easy is it to follow the path)	Q8 (how connected does it feel)	Q9 (how helpful is the steering torque feedback)
State estimator prediction error for $e(k-N_{vi})$	0.8782	0.9364	0.8843
State estimator prediction error for $\psi(k-N_{vi})$	0.9679	0.9322	0.9640
State estimator prediction error for $\theta_a(k-N_{v\theta_a})$	0.8766	0.9577	0.8964

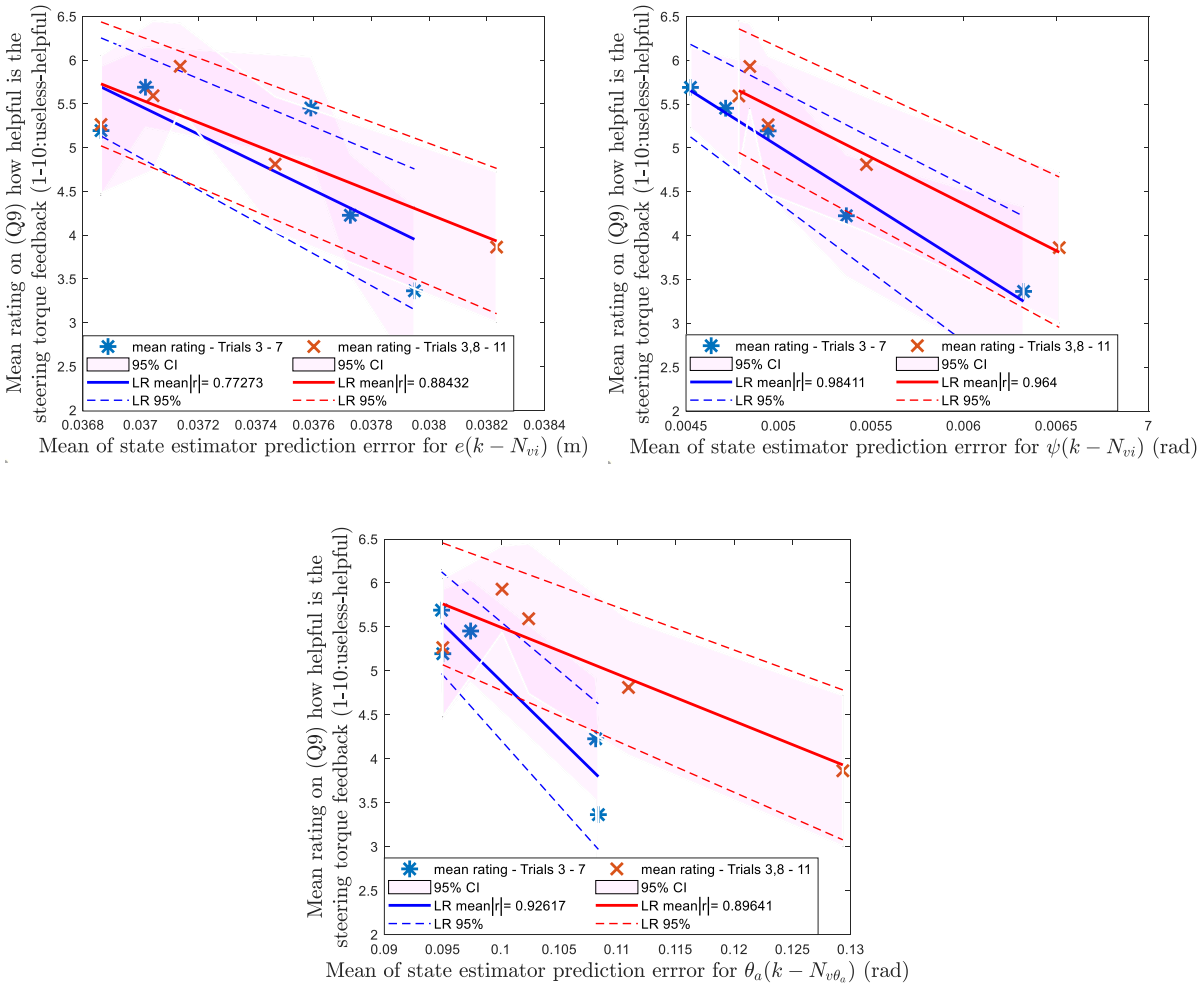

Figure 6.19: Correlations between normalised subjective ratings for Q9 and simulated state estimator prediction error signals with their correlation coefficients.

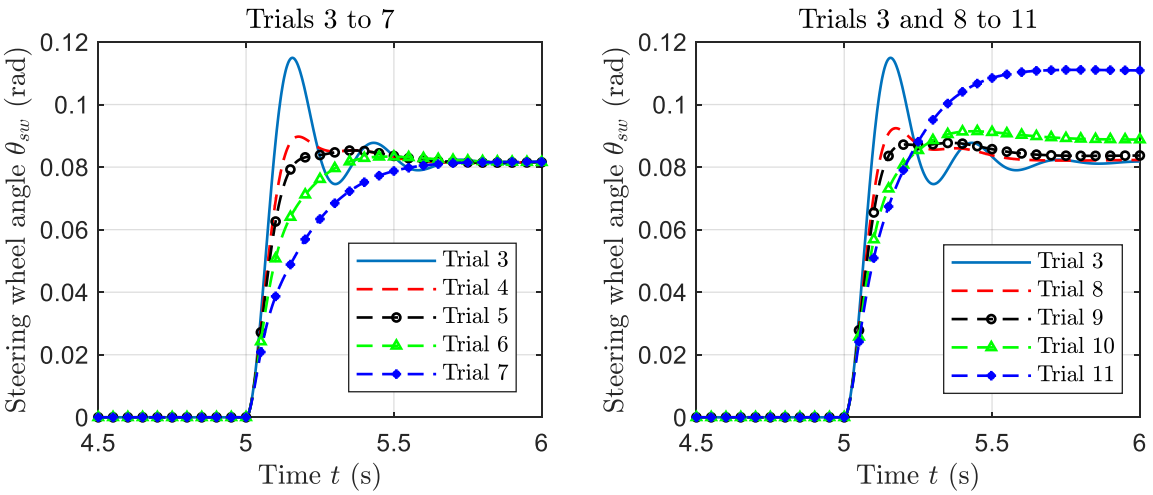

Figure 6.20: Step response of the steering-vehicle system with an equivalent damping value C'_{sw} of the steering system friction shown in Figure 6.3 for each trial for Driver 1.

6.5 Conclusions

The results from the nonlinear experiments have been used to identify parameter values and the internal mental model for a driver model controlling a vehicle with nonlinear steering system friction. The fit of the identified models to the experimental results can achieve the upper bound limit given by the Deep LSTM model, indicating that the model structure is able to accurately predict the deterministic component of the human driver's on-centre steering control of a vehicle with nonlinear steering system friction.

For most of the nonlinear trials, a nonlinear driver model accounting for the full nonlinear steering dynamics fits the measured results best. However, a driver model linearising the nonlinear steering system friction or even neglecting the effect of friction provides a similar or even higher agreement to the experimental results in trials with low friction levels. The driver model with an accurate nonlinear internal mental model has also been found to fully linearise the closed-loop driver-steering-vehicle system.

The assumption of Gaussian white noise for the driver's noise was found to be invalid, and a new process noise model developed based on the assumption that the noise spectrum should be similar in shape to the corresponding signal was found to fit the characteristics of the experimental driver noise well. In addition, the identified process noise level was found to increase with the increase in steering system friction level. Therefore, separate values of process noise signal-to-noise ratio SNR_W have been identified for each driver and trial combination, and the driver model structure has been updated by incorporating the new process noise model. However, it is possible that drivers may use an intermittent and threshold-driven control strategy which might not be represented by the neural network and the

current driver model structure and therefore might explain the increase in identified process noise level with the increase in steering system friction level.

Simulations were run to investigate the capability of the driver model to predict the human driver's subjective assessment of steering feel. The drivers' ratings for the subjective questions judging the magnitude of several objective metrics correlated well with the magnitudes of the corresponding signals from the state estimator, with six of the absolute values of the linear regression coefficient above 0.9 (for friction level, physical effort level, yaw delay for trials 3 to 7, and yaw gain for trials 3 and 8 to 11), and three values between 0.8 to 0.9 (for yaw delay for trials 3 and 8 to 11, yaw gain for trials 3 to 7, and yaw linearity for trials 3 and 8 to 11). These large correlation coefficient values show the capability of the driver model structure to reflect the drivers' ability to estimate the actual objective metrics. The drivers' subjective evaluation of steering feel correlated with the state estimator prediction error, which represents the discrepancy between the predicted and measured sensory feedback, with the averaged correlation coefficient being 0.9127. Overall, the subjective evaluation is perceived as worse with an increase in state estimator prediction error, which results from the increased internal mental model inaccuracy and/or the increased driver noise level. These results highlight the potential of using the driver model structure to explain and predict the human driver's subjective responses to steering feel. However, the limitation of the model is that the values of SNR_W were identified using the experimental results. Future work is necessary to understand why and how the identified process noise level depends on the steering and vehicle parameters.

Chapter 7

Conclusions and Future Work

7.1 Introduction

This thesis describes research on measuring and modelling human car driving with steering torque feedback, especially in the on-centre steering region. The aim of this research, defined in Chapter 1, was:

to improve theoretical understanding of the subjective assessment of steering feel, or steering torque feedback by measuring, understanding and modelling a driver's subjective and objective responses to steering torque feedback, especially for on-centre steering.

Four research objectives were proposed following the review of published literature, including (i) develop a mathematical driver-vehicle model incorporating steering feel, or steering torque feedback, for both linear and nonlinear steering dynamics, (ii) devise and perform experiments using a fixed-base driving simulator to provide the subjective and objective data necessary to identify and validate the driver-vehicle model, (iii) use the measured data to identify the unknown parameters of the mathematical model and the human driver's internal mental model, (iv) determine the relationship between: the subjective quality of steering torque feedback; the ability of the driver to learn an accurate internal model of the steering system and to generate optimal steering control actions; and the steering control performance that the human driver can achieve. Corresponding to these objectives, the main results and findings from previous chapters are summarised in this chapter. In addition, recommendations for potential future work to develop further understanding of steering torque feedback based on the findings discovered in this thesis are also made.

7.2 Summary of Findings

7.2.1 Literature Review (Chapter 2)

Published literature regarding existing steering feel assessment methods, steering system modelling techniques and works about driver models are reviewed. The findings are:

- The subjective-objective correlation method for the evaluation of steering feel has been criticised due to the little insight into the physical reasons and the wide range of objective parameters, subjective parameters, and test conditions.
- The steering system can be modelled with different levels of complexity depending on the aim of the study. The trade-off between computational efficiency and prediction accuracy favours a relatively simple steering mechanism model. Nonlinearities in the steering system such as friction require attention if accurate predictions are to be obtained. The development of advanced friction models has enabled the friction characteristics to be efficiently reproduced with high accuracy.
- An alternative approach likely to provide the necessary insight for the human driver's subjective evaluation of steering feel is to obtain a better understanding of the driver-vehicle system. Research in the field of motor neuroscience is relevant and applicable.

7.2.2 Driver-Steering-Vehicle Modelling (Chapter 3)

A new driver-steering-vehicle model incorporating steering torque feedback has been developed for both linear and nonlinear steering dynamics. The novelty of the model is the inclusion of the three important brain functions of perception, cognition and action, all three of which are governed by a single internal model of the plant. A comprehensive parameter study has been conducted, and the findings are:

- The influence of steering system parameters on the dynamic behaviour of the steering-vehicle system is demonstrated. The effects of steering system parameters on the objective steering feel metrics (Table 3.4) can provide some initial guidelines for the steering system design. The results are in consistent with published literature.
- The modelling of tensing (co-contracting) the muscles is able to be reflected by the variation of parameters in the neuromuscular dynamics model. The stretch reflex gain increases the stiffness of the arms and introduces a lightly damped resonance.
- The values of the process and measurement noise covariance matrices in the Kalman filter weigh the known input and sensory measurements in the state estimation, and the LQR cost function provides the trade-off between path-following accuracy and control effort.

- The EKF1 and LMPC methods, which involve a reasonable linear approximation to the nonlinear dynamics, can represent the state estimation and control of a driver capturing the full nonlinear dynamics in an accurate and computationally efficient way.

7.2.3 Driving Simulator Experiments (Chapter 4)

A series of driving simulator experiments and the analysis of the subjective and objective data collected during the experiments are presented. The findings are:

- Steering torque feedback is helpful for human drivers to achieve better tracking accuracy with a smaller steering input level. This in consistent with published literature.
- The steering reversal rate reduces with the increase in steering system friction in the randomly moving target path-following task.
- The drivers' steering control performance deteriorates with the increase in steering system friction overall.
- The drivers are able to detect the changes caused by steering system friction in objective metrics. The coefficients of the correlations between the drivers' ratings for the subjective questions judging the magnitude of the objective metrics and their actual magnitudes are large, with five values above 0.9, three values between 0.8 to 0.9, and one value between 0.7 to 0.8.
- The subjective evaluation of steering feel is generally perceived as worse with increased steering system friction level. The drivers' subjective evaluation of steering feel correlates well with friction torque magnitude, nonlinear torque ratio, and steering resistance level, with all the correlation coefficient values above 0.7.
- A small friction level of 0.5Nm to 1Nm may be preferred if it provides beneficial damping effects to stabilise the steering-vehicle system.
- The drivers may find it subjectively easier to follow the target path when a high tracking accuracy can be achieved with a low steering effort level.

7.2.4 Linear Driver Model Identification (Chapter 5)

An identification procedure has been developed to find parameter values for the new driver model using the linear experimental results. The findings are:

- The model fits the experimental results well, demonstrating its capability of representing the human driver's on-centre steering control behaviour.
- The process noise added to the driver's control action is signal-dependent, increasing linearly with RMS muscle activation torque.

- The measurement noise is also signal-dependent, increasing linearly with the corresponding RMS signal amplitudes when the signal amplitudes exceed the threshold.
- A single set of parameter values with process and measurement noise SNRs can be used to simulate drivers' steering control behaviour in a wide range of conditions. The model fits the results of the averaged driver with a variance account for value of 86.6% averaged over trials.
- The identified parameter values are physically reasonable compared with the literature.

7.2.5 Nonlinear Model Identification and Correlation with Subjective Assessment (Chapter 6)

The identification of the parameter values and the internal mental model of the driver model controlling a vehicle with nonlinear steering dynamics using the nonlinear experimental data and the correlation between the model and the human driver's subjective assessment of steering feel are presented. The findings are:

- The fit of the driver-steering-vehicle model to the experimental results agrees to that of the Deep LSTM model, demonstrating the capability of the driver-steering-vehicle model to represent the deterministic component of a human driver's on-centre steering control of a vehicle with nonlinear steering system friction.
- A nonlinear driver model accounting for the full nonlinear steering dynamics gives the best fit to the experimental results overall. It acts to fully linearise the closed-loop driver-steering-vehicle system.
- A driver model linearising the nonlinear steering system friction or even neglecting the effect of friction gives a similar or even higher fit to the experimental results in trials with low friction levels.
- A process noise model with a noise spectrum similar in shape to the driver's control signal fits the measured driver noise well.
- The identified process noise level increases with the increase of steering system friction level.
- An updated driver model accounting for the process noise level variation and the realistic process noise spectrum can reflect the drivers' ability to estimate the actual objective metrics. The coefficients of the correlations between the drivers' ratings for the subjective questions judging the magnitude of the objective metrics and the magnitudes of the corresponding signals from the state estimator are large, with six values above 0.9 and three values between 0.8 to 0.9.
- The subjective evaluation of steering feel is overall perceived as worse with an increase in state estimator prediction error, resulting from the increased internal mental model inaccuracy and/or the increased driver noise level. This highlights the ability of the driver model structure to

explain and predict the human driver's subjective responses to steering feel. The drivers' subjective evaluation of steering feel correlates well with the state estimator prediction error, with an averaged correlation coefficient of 0.9127.

- The limitations of the study include: the process noise level is identified using the experimental results for each trial separately; the possibility that the drivers may use an intermittent and threshold-driven control strategy which might explain the increasing trend for identified process noise level with the increase in steering system friction level is not examined.

7.3 Future Work

Future research work based on the findings and conclusions from this thesis is recommended as below:

- Investigate why and how the identified process noise signal-to-noise ratio depends on the vehicle and steering parameters. One limitation of the current study is that the identified process noise level is found to vary with the steering system friction level, so that a constant signal-to-noise ratio is not applicable. In order to use the model as a predictive tool for the assessment of the human driver's subjective evaluation of steering feel, various studies should be conducted to enable a better understanding of the physical reason for the variation in the identified process noise level. These studies might involve updating the driver model by incorporating the human driver's intermittency in cognitive control. The driver model currently uses the LQR and MPC methods to model the driver's cognitive control behaviour, which assumes that the driver uses a continuous control strategy. However, it has been found by Johns and Cole [160] that the human driver might use an intermittent control and threshold-driven control strategy, which the deep learning model may not capture. Therefore, updating the LQR and MPC methods with an intermittent control behaviour might help explain the increase in the identified process noise level.
- Update the driver model using an adaptive control method (such as the model-based reinforcement learning method). When a new steering-vehicle system is presented, the driver must undergo a period of adaptation to become familiar with the dynamics of the vehicle and then settle on a stable control strategy. This learning/adaptation process contributes to the human driver's subjective assessment of steering feel and might be more significant in the transition from automated control to human control for ADAS systems. To include such learning/adaptation behaviours in the driver model, an adaptive control method like the model-based reinforcement learning might be helpful.
- Review the design of the driving simulator experiments to improve the reliability and generalizability of the results. Future improvements might involve: include trials in which the drivers are allowed to preview the upcoming target path; tune the amplitudes of the disturbances

to replicate more realistic driving conditions; extend the duration of each trial to reduce the uncertainties regarding the objective data and subjective data collected during the experiments.

- Extend the model to include more nonlinear components in the steering-vehicle system and deal with the off-centre operating regime. Until now, the scope of the research has been limited to the on-centre operating regime, where the nonlinear steering system friction significantly affects the dynamic properties of the system. It is necessary to understand if the findings reported in this thesis still hold in the off-centre operating regime, where the nonlinear tyre dynamics and the nonlinear motor assist torque characteristics significantly impact the steering feel.

References

[1] M. Harrer and P. Pfeffer, *Steering handbook*. Springer International Publishing, 2016.

[2] D. J. Cole, "Occupant–vehicle dynamics and the role of the internal model," *Vehicle System Dynamics*, vol. 56, no. 5, pp. 661–688, May 2018.

[3] A. Ziebinski, R. Cupek, D. Grzechca, and L. Chruszczyk, "Review of advanced driver assistance systems (ADAS)," in *AIP Conference Proceedings*, 2017, vol. 1906.

[4] A. M. Lazcano, T. Niu, X. Carrera Akutain, D. Cole, and B. Shyrokau, "MPC-based haptic shared steering system: a driver modeling approach for symbiotic driving," *IEEE/ASME Transactions on Mechatronics*, vol. 26, no. 3, pp. 1201–1211, Jun. 2021.

[5] H. E. B. Russell, L. K. Harbott, I. Nisky, S. Pan, A. M. Okamura, and J. C. Gerdes, "Motor learning affects Car-To-Driver handover in automated vehicles," *Science Robotics*, vol. 1, no. 1, Dec. 2016.

[6] D. C. Chen, D. A. Crolla, C. J. Alstead, and J. P. Whitehead, "A comprehensive study of subjective and objective vehicle handling behaviour," *Vehicle System Dynamics*, vol. 25, no. SUPPL., pp. 66–86, 1996.

[7] D. A. Crolla, D. C. Chen, J. P. Whitehead, and C. J. Alstead, "Vehicle handling assessment using a combined subjective-objective approach," *SAE Transactions*. Paper 980226, 1998.

[8] M. Harrer, P. E. Pfeffer, and D. N. Johnston, "Steering feel - objective assessment of passenger cars - analysis of steering feel and vehicle handling," *Proceedings of FISITA 2006 World Automotive Congress*. 2006.

[9] M. Nybacka, X. He, Z. Su, L. Drugge, and E. Bakker, "Links between subjective assessments and objective metrics for steering, and evaluation of driver ratings," *Vehicle System Dynamics*, vol. 52, no. sup1, pp. 31–50, 2014.

[10] G. L. Gil Gómez, M. Nybacka, E. Bakker, and L. Drugge, "Objective metrics for vehicle handling and steering and their correlations with subjective assessments," *International Journal of Automotive Technology*, vol. 17, no. 5, pp. 777–794, Oct. 2016.

[11] R. S. Sharp, "Some contemporary problems in road vehicle dynamics," *Proceedings of the Institution of Mechanical Engineers, Part C: Journal of Mechanical Engineering*, vol. 214, no. 1, pp. 137–148, Jan. 2000.

[12] A. J. Pick, "Neuromuscular dynamics and the vehicle steering task," PhD thesis, University of Cambridge, 2004.

[13] J. J. Rix, "Identification of the closed-loop steering behaviour of a driver," PhD thesis, University of Cambridge, 2005.

[14] A. M. C. Odhams, "Identification of driver steering and speed control," PhD thesis, University of Cambridge, 2006.

[15] S. Rutherford, "Modelling driver nonlinear steering control," PhD thesis, University of Cambridge, 2007.

[16] S. D. Keen, "Modeling driver steering behavior using multiple-model predictive control," PhD thesis, University of Cambridge, 2008.

[17] W. Hoult, "A neuromuscular model for simulating driver steering torque," PhD thesis, University of Cambridge, 2009.

[18] N. Kim, “The role of steering torque feedback in a driver’s control of a nonlinear vehicle,” PhD thesis, University of Cambridge, 2011.

[19] R. S. Bigler, “Automobile driver sensory system modeling,” PhD thesis, University of Cambridge, 2013.

[20] C. J. Nash and D. J. Cole, “Modelling the influence of sensory dynamics on linear and nonlinear driver steering control,” *Vehicle System Dynamics*, vol. 56, no. 5, pp. 689–718, May 2018.

[21] F. O. Jaksch, “Driver-vehicle interaction with respect to steering controllability,” *SAE Transactions*. Paper 790740, 1979.

[22] D. G. Farrer, “An objective measurement technique for the quantification of on-centre handling quality,” *SAE Transactions*. Paper 930827, 1993.

[23] M. Rothhämel, J. Ijkema, and L. Drugge, “A method to find correlations between steering feel and vehicle handling properties using a moving base driving simulator,” *Vehicle System Dynamics*, vol. 49, no. 12, pp. 1837–1854, 2011.

[24] M. Rothhämel, “Characterisation and utilisation of steering feel in heavy trucks,” PhD thesis, Royal Institute of Technology, KTH Vehicle Dynamics, 2013.

[25] J. Aurell, N. Fröjd, and S. Nordmark, “Correlation between objective handling characteristics and subjective perception of handling qualities of heavy vehicles,” *Proceedings AVEC2000, 5th International Symposium on Advanced Vehicle Control*. Ann Arbor, Michigan, 2000.

[26] J. Kim and Y. S. Yoon, “Objectification of steering feel around straight-line driving for vehicle/tyre design,” *Vehicle System Dynamics*, vol. 53, no. 2, pp. 197–214, 2015.

[27] M. Nybacka, X. He, G. Gómez, E. Bakker, and L. Drugge, “Links between subjective assessments and objective metrics for steering,” *International Journal of Automotive Technology*, vol. 15, no. 6. pp. 893–907, 2014.

[28] L. Segel, “An investigation of automobile handling as implemented by a variable-steering automobile,” *Human Factors: The Journal of Human Factors and Ergonomics Society*, vol. 6, no. 4, pp. 333–341, 1964.

[29] K. D. Norman, “Objective evaluation of on-center handling performance,” *SAE Transactions*. Paper 840069, 1984.

[30] Anon, “Road vehicles -- Test method for the quantification of on-centre handling -- Part 1: Weave test.” ISO 13674-1:2003, 2003.

[31] J. Somerville, D. G. Farrer, and J. P. Whitehead, “Improvements in the quantification of on-centre handling quality,” *IMechE Conference on Vehicle Ride and Handling*. 1993.

[32] H. Sato, H. Osawa, and T. Haraguchi, “The quantitative analysis of steering feel,” *JSAE Review*, vol. 12, no. 2, pp. 85–87, 1991.

[33] P. Harnett, “Objective methods for the assessment of passenger car steering quality,” PhD thesis, Cranfield University, Cranfield, UK, 2002.

[34] J. Dang *et al.*, “Optimal design of on-center steering force characteristic based on correlations between subjective and objective evaluations,” *SAE International Journal of Passenger Cars - Mechanical Systems*, vol. 7, no. 3. pp. 2014-01–0137, 2014.

[35] K. Misaji, H. Tokunaga, Y. Shimizu, A. Uoi, and K. Shibata, “Vehicle dynamics analysis by ‘analytical method of equivalent linear system using the restoring force model of power function type,’” in *Vehicle System Dynamics*, 2004, vol. 42, no. 1–2, pp. 119–131.

[36] H. Tokunaga, K. Misaji, S. Takimoto, and Y. Shimizu, “Steer feel evaluation method based on

"analytical method of equivalent linear system using the restoring force model of power function type"," *Proceedings AVEC2002, 6th International Symposium on Advanced Vehicle Control*. 2002.

[37] H. Tokunaga, K. Misaji, and Y. Shimizu, "On-center steer feel evaluation based on non-linear vibration analytical method," *Vehicle System Dynamics*, vol. 41, no. SUPPL., pp. 391–400, 2004.

[38] J. Yu, J. Aston, C. Gilsinger, J. Shutway, and H. Tokunaga, "Vehicle dynamic feeling study with a focus on the on-center steering feeling of north American highway driving," *Proceedings AVEC2004, 7th International Symposium on Advanced Vehicle Control*. 2004.

[39] Anon, "Road vehicles -- Test method for the quantification of on-centre handling -- Part 2: Transition test." ISO 13674-2:2006, 2006.

[40] B. Siegler and C. Regan, "The effect of vehicle component changes on steering feel," in *Proceedings of FISITA 2006 World Automotive Congress*, 2006.

[41] M. Koide and S. Kawakami, "Analysis of 'steering feel' evaluation in vehicles with power steering," *JSAE Review*, vol. 9, no. 3, pp. 36–42, 1988.

[42] S. A. Peppler, J. R. Johnson, and D. E. Williams, "Steering system effects on on-center handling and performance," *SAE Transactions*. Paper 1999-01-3765, 1999.

[43] E. R. Hoffmann and P. N. Joubert, "Just noticeable differences in some vehicle handling variables," *Human Factors: The Journal of Human Factors and Ergonomics Society*, vol. 10, no. 3, pp. 263–272, 1968.

[44] G. L. Gil Gomez, M. Nybacka, E. Bakker, and L. Drugge, "Findings from subjective evaluations and driver ratings of vehicle dynamics: Steering and handling," *Vehicle System Dynamics*, vol. 53, no. 10, pp. 1416–1438, 2015.

[45] G. L. G. Gómez, M. Nybacka, E. Bakker, and L. Drugge, "Correlations of subjective assessments and objective metrics for vehicle handling and steering: A walk through history," *International Journal of Vehicle Design*, vol. 72, no. 1. pp. 17–67, 2016.

[46] "J1441: Subjective rating scale for vehicle ride and handling SAE International," *SAE International*. 2016.

[47] A. K. Zschocke and A. Albers, "Links between subjective and objective evaluations regarding the steering character of automobiles," *International Journal of Automotive Technology*, vol. 9, no. 4, pp. 473–481, 2008.

[48] G. L. Gil Gomez, E. Bakker, M. Nybacka, and L. Drugge, "Analysing vehicle dynamics objective and subjective testing in winter conditions," *The Dynamics of Vehicles on Roads and Tracks*, pp. 759–768, 2016.

[49] H. A. S. Ash, "Correlation of subjective and objective handling of vehicle behaviour," PhD thesis, The University of Leeds, 2002.

[50] M. Rothhämel, J. IJkema, and L. Drugge, "On the correlation between steering feel and handling in heavy trucks," *FISITA World Automotive Congress 2008, Congress Proceedings - Mobility Concepts, Man Machine Interface, Process Challenges, Virtual Reality*, vol. 1. pp. 311–317, 2008.

[51] G. Chen, W. Zhang, Z. Gong, and W. Sun, "A new approach to vehicle shift quality subjective evaluation based on fuzzy logic and evidence theory," *2009 4th IEEE Conference on Industrial Electronics and Applications*. 2009.

[52] R. P. King, D. A. Crolla, H. A. S. Ash, and J. Whitehead, "Identification of subjective-objective vehicle handling links using neural networks for the foresight vehicle," *SAE Transactions*. Paper 2002-01-1126, 2002.

[53] J. Baxter, “Analysis of stiffness and feel for a power-assisted rack and pinion steering gear,” *SAE Transactions*. Paper 880706, 1988.

[54] A. Wohnhaas and U. Essers, “Nonlinear modeling and simulation of a rack and pinion steering,” *Proceedings AVEC1992, 1st International Symposium on Advanced Vehicle Control*. Japan, 1992.

[55] J. W. Post and E. H. Law, “Modeling, characterization and simulation of automobile power steering systems for the prediction of on-center handling,” *SAE Transactions*. Paper 960178, 1996.

[56] U. Neureder, “Investigation into steering wheel nibble,” *Proceedings of the Institution of Mechanical Engineers, Part D: Journal of Automobile Engineering*, vol. 216, no. 4. SAGE PublicationsSage UK: London, England, pp. 267–277, 28-Apr-2002.

[57] E. Ueda, E. Inoue, Y. Sakai, M. Hasegawa, H. Takai, and S. Kimoto, “The development of detailed steering model for on-center handling simulation,” in *Proceedings AVEC2002, 6th International Symposium on Advanced Vehicle Control*, 2002.

[58] P. E. Pfeffer, M. Harrer, and D. N. Johnston, “Interaction of vehicle and steering system regarding on-centre handling,” *Vehicle System Dynamics*, vol. 46, no. 5, pp. 413–428, 2008.

[59] W. Kemmetmüller, S. Müller, and A. Kugi, “Mathematical modeling and nonlinear controller design for a novel electrohydraulic power-steering system,” *IEEE/ASME Transactions on Mechatronics*, vol. 12, no. 1, pp. 85–97, Feb. 2007.

[60] A. Dell’Amico and P. Krus, “Modeling, simulation, and experimental investigation of an electrohydraulic closed-center power steering system,” *IEEE/ASME Transactions on Mechatronics*, vol. 20, no. 5, pp. 2452–2462, Oct. 2015.

[61] A. Dell’Amico, “On electrohydraulic pressure control for power steering applications active steering for road vehicles,” PhD thesis, Linköping University, 2016.

[62] A. Zaremba and R. I. Davis, “Dynamic analysis and stability of a power assist steering system,” *Proceedings of the American Control Conference*, vol. 6. pp. 4253–4257, 1995.

[63] A. T. Zaremba, M. K. Liubakka, and R. M. Stuntz, “Control and steering feel issues in the design of an electric power steering system,” *Proceedings of the American Control Conference*, vol. 1, no. June. pp. 36–40, 1998.

[64] A. Badawy, J. Zuraski, F. Bolourchi, and A. Chandy, “Modeling and analysis of an electric power steering system,” *SAE Transactions*. Paper 1999-01-0399, 1999.

[65] C. Dannöhl, S. Müller, and H. Ulbrich, “H∞-control of a rack-assisted electric power steering system,” *Vehicle System Dynamics*, vol. 50, no. 4, pp. 527–544, 2012.

[66] T. Tamura, A. Maroonian, M. Higashi, and R. Fuchs, “Modeling and simulation for dynamic analysis of column type electric power steering,” *JTEKT Engineering Journal English Edition*, no. 1010, pp. 19–25, 2013.

[67] M. Parmar and J. Y. Hung, “Modeling and sensorless optimal controller design for an electric power assist steering system,” *IECON Proceedings (Industrial Electronics Conference)*, vol. 3. pp. 1784–1789, 2002.

[68] A. Marouf, C. Sentouh, M. Djemai, and P. Pudlo, “Control of an electric power assisted steering system using reference model,” *50th IEEE Conference on Decision and Control and European Control Conference*. 2011.

[69] V. Govender and S. Müller, “Modelling and position control of an electric power steering system,” *IFAC-PapersOnLine*, vol. 49, no. 11, pp. 312–318, 2016.

[70] K. Yamamoto, D. Koenig, O. Sename, and P. Moulaire, “A new control design for an optimized electric power steering system,” *20th IFAC World Congress*. Toulouse, France, 2017.

[71] C. Choi *et al.*, “Multi-domain modeling of electric power steering with PMSM drive system,” *Proceedings of IEEE International Electric Machines and Drives Conference, IEMDC 2007*, vol. 2. IEEE, pp. 1355–1360, May-2007.

[72] J. Song, K. Boo, H. S. Kim, J. Lee, and S. Hong, “Model development and control methodology of a new electric power steering system,” *Proceedings of the Institution of Mechanical Engineers, Part D: Journal of Automobile Engineering*, vol. 218, no. 9. pp. 967–975, 15-Sep-2004.

[73] L. Segel, “On the lateral stability and control of the automobile as influenced by the dynamics of the steering system,” *Journal of Manufacturing Science and Engineering, Transactions of the ASME*, vol. 88, no. 3, pp. 283–294, Aug. 1966.

[74] N. Zhang and M. Wang, “Dynamic modeling of hydraulic power steering system with variable ratio rack and pinion gear,” *JSME International Journal, Series C: Mechanical Systems, Machine Elements and Manufacturing*, vol. 48, no. 2 SPEC. ISS., pp. 251–260, 2005.

[75] K. Sakai, A. Yoneda, and Y. Shimizu, “Improvement in control performance of driver-vehicle system with EPS using cables to connect the steering wheel and gearbox,” *Proceedings of AVEC 2002, Hiroshima, Japan*, pp. 641–646, 2002.

[76] C. C. de Wit, P. Lischinsky, K. J. Åström, and H. Olsson, “A new model for control of systems with friction,” *IEEE Transactions on Automatic Control*, vol. 40, no. 3, pp. 419–425, 1995.

[77] C. Canudas-de-Wit and P. Lischinsky, “Adaptive friction compensation with dynamic friction model,” *IFAC Proceedings Volumes*, vol. 29, no. 1. Elsevier BV, pp. 2078–2083, 01-Jun-1996.

[78] T. Specker, M. Buchholz, and K. Dietmayer, “A new approach of dynamic friction modelling for simulation and observation,” *IFAC Proceedings Volumes (IFAC-PapersOnline)*, vol. 19. pp. 4523–4528, 2014.

[79] M. Plöchl and J. Edelmann, “Driver models in automobile dynamics application,” *User Modeling and User-Adapted Interaction*, vol. 45, no. 7–8, pp. 699–741, Jul. 2007.

[80] D. T. McRuer and E. S. Krendel, “The human operator as a servo system element,” *Journal of the Franklin Institute*, vol. 267, no. 5, pp. 381–403, May 1959.

[81] D. T. McRuer and E. S. Krendel, “The man-machine system concept,” *Proceedings of the IRE*, vol. 50, no. 5. pp. 1117–1123, May-1962.

[82] M. Kondo and A. Ajimine, “Driver’s sight point and dynamics of the driver-vehicle-system related to it,” *SAE Transactions*. Paper 790740, 1968.

[83] K. Yosimoto, “Simulation of driver/vehicle system including preview control,” *Journal of Mechanics Society of Japan*, vol. 71, 1968.

[84] K. Guo and H. Guan, “Modelling of driver/vehicle directional control system,” *Vehicle System Dynamics*, vol. 22, no. 3–4, pp. 141–184, Jan. 1993.

[85] A. Reński, “Identification of driver model parameters,” *International Journal of Occupational Safety and Ergonomics*, vol. 7, no. 1, pp. 79–92, Jan. 2001.

[86] C. C. MacAdam, “An optimal preview control for linear systems,” *Journal of Dynamic Systems, Measurement and Control, Transactions of the ASME*, vol. 102, no. 3, pp. 188–190, 1980.

[87] C. C. MacAdam, “Application of an optimal preview control for simulation of closed-loop automobile driving,” *IEEE Transactions on Systems, Man and Cybernetics*, vol. 11, no. 6, pp. 393–399, 1981.

[88] H. Peng, “Evaluation of driver assistance systems – a human centered approach,” *Proceedings of the 6th International Symposium on Advanced Vehicle Control, AVEC*. Hiroshima, Japan, 2002.

[89] R. S. Sharp and V. Valtetsiotis, “Optimal preview car steering control,” *Vehicle System Dynamics*, vol. 35, no. SUPPL. 1. pp. 101–117, 2001.

[90] D. J. Cole, A. J. Pick, and A. M. C. Odhams, “Predictive and linear quadratic methods for potential application to modelling driver steering control,” *Vehicle System Dynamics*, vol. 44, no. 3. pp. 259–284, Mar-2006.

[91] S. D. Keen and D. J. Cole, “Bias-free identification of a linear model-predictive steering controller from measured driver steering behavior,” *IEEE Transactions on Systems, Man, and Cybernetics, Part B: Cybernetics*, vol. 42, no. 2. pp. 434–443, Apr-2012.

[92] A. M. C. Odhams and D. J. Cole, “Identification of a driver’s preview steering control behaviour using data from a driving simulator and a randomly curved road path,” *Proceedings 10th International Symposium on Advanced Vehicle Control, AVEC 2010*. Loughborough, 2010.

[93] A. M. C. Odhams and D. J. Cole, “Identification of the steering control behaviour of five test subjects following a randomly curving path in a driving simulator,” *International Journal of Vehicle Autonomous Systems*, vol. 12, no. 1, pp. 44–64, 2014.

[94] S. D. Keen and D. J. Cole, “Steering control using model predictive control and multiple internal models,” *Proceedings 8th International Symposium on Advanced Vehicle Control, AVEC 2006*. Taiwan, 2006.

[95] N. Kim and D. J. Cole, “A model of driver steering control incorporating the driver’s sensing of steering torque,” *Vehicle System Dynamics*, vol. 49, no. 10, pp. 1575–1596, Oct. 2011.

[96] D. Cole and A. Pick, “Neuromuscular dynamics and the vehicle steering task,” *Vehicle System Dynamics*, vol. 41, no. SUPPL., pp. 182–191, 2004.

[97] A. J. Pick and D. J. Cole, “Neuromuscular dynamics in the driver-vehicle system,” *Vehicle System Dynamics*, vol. 44, no. SUPPL. 1, pp. 624–631, Jan. 2006.

[98] A. J. Pick and D. J. Cole, “Measurement of driver steering torque using electromyography,” *Journal of Dynamic Systems, Measurement and Control, Transactions of the ASME*, vol. 128, no. 4, pp. 960–968, Dec. 2006.

[99] A. J. Pick and D. J. Cole, “Driver steering and muscle activity during a lane-change manoeuvre,” *User Modeling and User-Adapted Interaction*, vol. 45, no. 9, pp. 781–805, Sep. 2007.

[100] A. J. Pick and D. J. Cole, “Dynamic properties of a driver’s arms holding a steering wheel,” *Proceedings of the Institution of Mechanical Engineers, Part D: Journal of Automobile Engineering*, vol. 221, no. 12, pp. 1475–1486, Dec. 2007.

[101] A. J. Pick and D. J. Cole, “A mathematical model of driver steering control including neuromuscular dynamics,” *Journal of Dynamic Systems, Measurement and Control, Transactions of the ASME*, vol. 130, no. 3, p. 031004, May 2008.

[102] W. Hoult and D. J. Cole, “A neuromuscular model for driver simulation,” *Proceedings of 20th IAVSD Symposium on the Dynamics of Vehicles on Roads and Tracks*. Berkeley, USA, 2007.

[103] D. J. Cole, “A path-following driver-vehicle model with neuromuscular dynamics, including measured and simulated responses to a step in steering angle overlay,” *Vehicle System Dynamics*, vol. 50, no. 4, pp. 573–596, Apr. 2012.

[104] C. G. I. Droogendijk, “A new neuromuscular driver model for steering system development,” Master thesis, Delft University of Technology, 2010.

[105] D. Katzourakis, C. Droogendijk, and D. Abbink, “Driver model with visual and neuromuscular feedback for objective assessment of automotive steering systems,” *International Symposium on Advanced Vehicle Control (AVEC)*. Loughborough, UK, 2010.

[106] D. J. Cole, “Influence of steering torque feedback and neuromuscular dynamics on driver and vehicle response to lateral force disturbance,” *Proceedings of 22nd IAVSD Symposium on the Dynamics of Vehicles on Roads and Tracks*. Manchester, UK, 2011.

[107] C. C. Macadam, “Understanding and modeling the human driver,” *Vehicle System Dynamics*, vol. 40, no. 1–3, pp. 101–134, Jan. 2003.

[108] R. S. Bigler and D. J. Cole, “A review of mathematical models of human sensory dynamics relevant to the steering task,” *22nd IAVSD Symposium on the Dynamics of Vehicles on Roads and Tracks*. Manchester, UK, pp. 1–6, 2011.

[109] C. J. Nash, D. J. Cole, and R. S. Bigler, “A review of human sensory dynamics for application to models of driver steering and speed control,” *Biological Cybernetics*, vol. 110, no. 2–3. pp. 91–116, 16-Jun-2016.

[110] C. M. Harris and D. M. Wolpert, “Signal-dependent noise determines motor planning,” *Nature*, vol. 394, no. 6695, pp. 780–784, Aug. 1998.

[111] J. Kang, J. Wu, A. Smerieri, and J. Feng, “Weber’s law implies neural discharge more regular than a Poisson process,” *European Journal of Neuroscience*, vol. 31, no. 6, pp. 1006–1018, Mar. 2010.

[112] F. Soyka, P. R. Giordano, K. Beykirch, and H. H. Bülthoff, “Predicting direction detection thresholds for arbitrary translational acceleration profiles in the horizontal plane,” *Experimental Brain Research*, vol. 209, no. 1, pp. 95–107, Mar. 2011.

[113] F. Soyka, P. R. Giordano, M. Barnett-Cowan, and H. H. Bülthoff, “Modeling direction discrimination thresholds for yaw rotations around an earth-vertical axis for arbitrary motion profiles,” *Experimental Brain Research*, vol. 220, no. 1, pp. 89–99, Jul. 2012.

[114] C. J. Nash and D. J. Cole, “Development of a novel model of driver–vehicle steering control incorporating sensory dynamics,” *Proceedings of 24th IAVSD Symposium on the Dynamics of Vehicles on Roads and Tracks*. Graz, Austria, 2015.

[115] J. L. Campos and H. H. Bülthoff, “Multimodal integration during self-motion in virtual reality,” in *The Neural Bases of Multisensory Processes*, 2011, pp. 603–627.

[116] C. J. Nash and D. J. Cole, “Identification and validation of a driver steering control model incorporating human sensory dynamics,” *Vehicle System Dynamics*, vol. 58, no. 4, pp. 495–517, Apr. 2020.

[117] C. J. Nash and D. J. Cole, “Measurement and modeling of the effect of sensory conflicts on driver steering control,” *Journal of Dynamic Systems, Measurement and Control, Transactions of the ASME*, vol. 141, no. 6, Jun. 2019.

[118] S. J. Blakemore, D. Wolpert, and C. Frith, “Why can’t you tickle yourself?,” *NeuroReport*, vol. 11, no. 11. pp. R11–R16, 2000.

[119] E. Donges, “A two-level model of driver steering behavior,” *Human Factors: The Journal of Human Factors and Ergonomics Society*, vol. 20, no. 6, pp. 691–707, Dec. 1978.

[120] T. Niu and D. J. Cole, “A model of driver steering control incorporating steering torque feedback and state estimation,” Technical Report ENG-TR 005, Department of Engineering, Uni-versity of Cambridge, 2020.

[121] J. M. Winters and L. Stark, “Muscle models: What is gained and what is lost by varying model complexity,” *Biological Cybernetics*, vol. 55, no. 6, pp. 403–420, Mar. 1987.

[122] R. E. Kalman, “A new approach to linear filtering and prediction problems,” *Journal of Fluids Engineering, Transactions of the ASME*, vol. 82, no. 1, pp. 35–45, 1960.

[123] M. S. Grewal and A. P. Andrews, *Kalman Filtering: Theory and Practice Using MATLAB®: Third Edition*. John Wiley and Sons, 2008.

[124] X. C. Akutain, “Email: Vehicle and steering parameters,” *Toyota Motor Europe*, 2018.

[125] T. Niu and D. J. Cole, “Experimental identification of a driver steering control model incorporating steering feel,” *Proceedings of 27th IAVSD Symposium on Dynamics of Vehicles on Roads and Tracks*. Saint-Petersburg, Russia, 2021.

[126] C. J. Nash, “Measurement and modelling of human sensory feedback in car driving,” PhD thesis, University of Cambridge, 2018.

[127] S. M. Erlien, S. Fujita, and J. C. Gerdes, “Shared steering control using safe envelopes for obstacle avoidance and vehicle stability,” *IEEE Transactions on Intelligent Transportation Systems*, vol. 17, no. 2, pp. 441–451, Feb. 2016.

[128] P. Falcone, F. Borrelli, H. E. Tseng, J. Asgari, and D. Hrovat, “Linear time-varying model predictive control and its application to active steering systems: Stability analysis and experimental validation,” *International Journal of Robust and Nonlinear Control*, vol. 18, no. 8, pp. 862–875, May 2008.

[129] M. Gerdts, S. Karrenberg, B. Müller-Beler, and G. Stock, “Generating locally optimal trajectories for an automatically driven car,” *Optimization and Engineering*, vol. 10, no. 4, pp. 439–463, Dec. 2009.

[130] A. Y. Ungoren and H. Peng, “An adaptive lateral preview driver model,” *Vehicle System Dynamics*, vol. 43, no. 4, pp. 245–259, Apr. 2005.

[131] I. Kushiro and M. Yamomoto, “Vehicle behavior under the influence of steering dynamics by means of low frequency torque input,” *SAE Transactions*. Paper 2006-01-0557, 2006.

[132] V. Lampaert, F. Al-Bender, and J. Swevers, “A generalized Maxwell-slip friction model appropriate for control purposes,” *2003 International Conference Physics and Control, PhysCon 2003 - Proceedings*, vol. 4. Institute of Electrical and Electronics Engineers Inc., pp. 1170–1177, 2003.

[133] J. Hartikainen, A. Solin, and S. Särkkä, “Optimal filtering with Kalman filters and smoothers - a manual for the Matlab toolbox EKF/UKF,” 2011.

[134] A. Wächter and L. T. Biegler, “On the implementation of an interior-point filter line-search algorithm for large-scale nonlinear programming,” *Mathematical Programming*, vol. 106, no. 1, pp. 25–57, May 2006.

[135] H. Wang, “Measurement and simulation of steering torque interaction between driver and vehicle,” PhD thesis, University of Cambridge, 2016.

[136] “A Panda3D hello world tutorial — Panda3D manual.” [Online]. Available: https://docs.panda3d.org/1.10/python/introduction/tutorial/index. [Accessed: 05-Jun-2021].

[137] I. J. Deary and G. Der, “Reaction time, age, and cognitive ability: Longitudinal findings from age 16 to 63 years in representative population samples,” *Aging, Neuropsychology, and Cognition*, vol. 12, no. 2, pp. 187–215, Jun. 2005.

[138] H. Kingma, “Thresholds for perception of direction of linear acceleration as a possible evaluation of the otolith function,” *BMC Ear, Nose and Throat Disorders*, vol. 5, no. 1, Jun. 2005.

[139] W. A. Macdonald and E. R. Hoffmann, “Review of relationships between steering wheel

reversal rate and driving task demand," *Human Factors*, vol. 22, no. 6, pp. 733–739, Nov. 1980.

[140] G. Markkula and J. Engstrom, "A steering wheel reversal rate metric for assessing effects of visual and cognitive secondary task load," *13th World Congress on Intelligent Transport Systems and Services*. pp. 1–12, Aug-2006.

[141] M. Skarzynska, "Influence of steering column friction on steering feel," Master thesis, Delft University of Technology, 2018.

[142] L. Ljung, "System identification: theory for the user (second edition)." Upper Saddle River, NJ, USA: Prentice Hall, 1999.

[143] B. Kleiner, G. E. P. Box, and G. J. Jenkins, "Time series analysis: forecasting and control," *Technometrics*, vol. 19, no. 3, p. 343, 1977.

[144] X. Na, "Game theoretical modelling of a driver's interaction with active steering," PhD thesis, University of Cambridge, 2013.

[145] P. M. T. Zaal, D. M. Pool, Q. P. Chu, M. M. V. Paassen, M. Mulder, and J. A. Mulder, "Modeling human multimodal perception and control using genetic maximum likelihood estimation," *Journal of Guidance, Control, and Dynamics*, vol. 32, no. 4, pp. 1089–1099, May 2009.

[146] A. A. Samji and L. D. Reid, "The detection of low-amplitude yawing motion transients in a flight simulator," *IEEE Transactions on Systems, Man and Cybernetics*, vol. 22, no. 2, pp. 300–306, 1992.

[147] V. V. Rodchenko, S. Y. Boris, and A. D. White, "In-flight estimation of pilots' acceleration sensitivity thresholds," in *Modeling and Simulation Technologies Conference*, 2000.

[148] A. R. V. Pais, D. M. Pool, A. M. De Vroome, M. M. Van Paassen, and M. Mulder, "Pitch motion perception thresholds during passive and active tasks," *Journal of Guidance, Control, and Dynamics*, vol. 35, no. 3, pp. 904–918, Aug. 2012.

[149] D. M. Pool, A. R. V. Pais, A. M. De Vroome, M. M. Van Paassen, and M. Mulder, "Identification of nonlinear motion perception dynamics using time-domain pilot modeling," *Journal of Guidance, Control, and Dynamics*, vol. 35, no. 3, pp. 749–763, Aug. 2012.

[150] K. Worden and P. L. Green, "A machine learning approach to nonlinear modal analysis," *Mechanical Systems and Signal Processing*, vol. 84, pp. 34–53, Feb. 2017.

[151] B. C. Csaji, "Approximation with artificial neural networks," Master thesis, Eotvos Lorand University, 2001.

[152] Y. Wang, "A new concept using LSTM Neural Networks for dynamic system identification," *Proceedings of the American Control Conference*. Institute of Electrical and Electronics Engineers Inc., pp. 5324–5329, 29-Jun-2017.

[153] J. Gonzalez and W. Yu, "Non-linear system modeling using LSTM neural networks," *IFAC-PapersOnLine*, vol. 51, no. 13. Elsevier B.V., pp. 485–489, 01-Jan-2018.

[154] R. Zhang, Z. Chen, S. Chen, J. Zheng, O. Büyüköztürk, and H. Sun, "Deep long short-term memory networks for nonlinear structural seismic response prediction," *Computers and Structures*, vol. 220, pp. 55–68, Aug. 2019.

[155] R. Zhang, Y. Liu, and H. Sun, "Physics-informed multi-LSTM networks for metamodeling of nonlinear structures," *Computer Methods in Applied Mechanics and Engineering*, vol. 369, p. 113226, Sep. 2020.

[156] L. Jain and L. Medsker, *Recurrent Neural Networks: Design and Appication*. CRC Press, 1999.

[157] D. P. Mandic and J. A. Chambers, *Recurrent Neural Networks for Prediction*. John Wiley &

Sons, Ltd, 2001.

[158] S. Hochreiter and J. Schmidhuber, “Long Short-Term Memory,” *Neural Computation*, vol. 9, no. 8, pp. 1735–1780, Nov. 1997.

[159] D. P. Kingma and J. L. Ba, “Adam: A method for stochastic optimization,” *3rd International Conference on Learning Representations, ICLR 2015 - Conference Track Proceedings*. 2015.

[160] T. A. Johns and D. J. Cole, “Measurement and mathematical model of a driver’s intermittent compensatory steering control,” *Vehicle System Dynamics*, vol. 53, no. 12, pp. 1811–1829, Dec. 2015.